WDL-TR2962
VOLUME III
ANTENNAS

FAN BEAM NAVIGATION SATELLITE STUDY

NASA-CR-85001

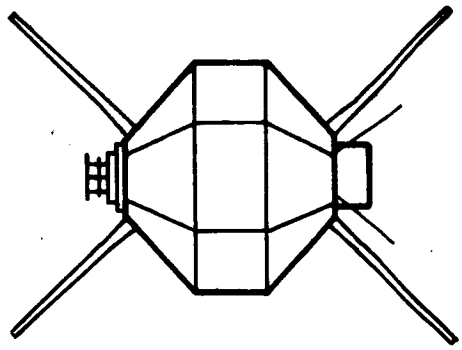

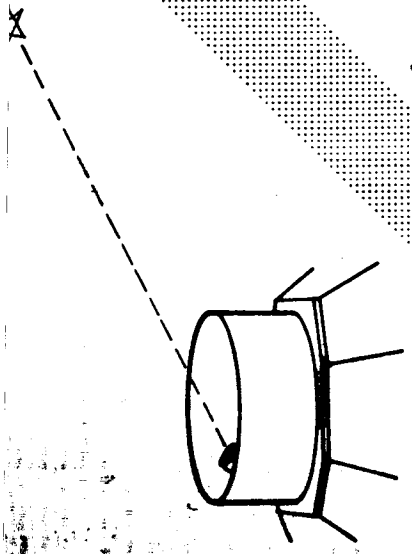

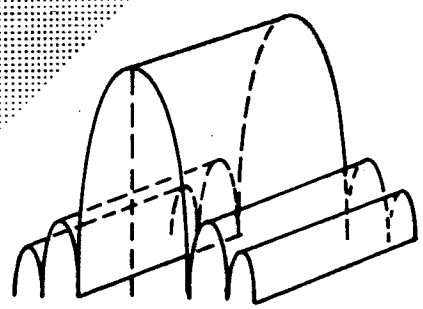

N67-31479

FACILITY FORM 602

(ACCESSION NUMBER) 203 (PAGES) CR-85001 (NASA CR OR TMX OR AD NUMBER)

(THRU) 1 (CODE) 21 (CATEGORY)

D PRICE $ _____

STI PRICE(S) $ _____

Hard copy (HC) 3.00

Microfiche (MF) .65

653 July 65

CONTRACT NUMBER NASW-1368

Submitted to

HEADQUARTERS NATIONAL AERONAUTICS AND SPACE ADMINISTRATION

WASHINGTON, D.C.

PHILCO
A SUBSIDIARY OF Ford Motor Company
WDL DIVISION
PALO ALTO-CALIFORNIA
HOUSTON-TEXAS

WDL TECHNICAL REPORT 2962

FAN BEAM NAVIGATION SATELLITE STUDY

Volume III

ANTENNA STUDIES

13 July 1966

Contract No. NASW-1368

Submitted to:

Headquarters
National Aeronautics and Space Administration
Washington, D.C.

Prepared by

PHILCO CORPORATION
A Subsidiary of Ford Motor Company
WDL Division
Palo Alto, California

TABLE OF CONTENTS

Section		Page
1	NAVIGATION SATELLITE ANTENNA STRUCTURAL ANALYSES	1-1
	1.1 Introduction and Summary	1-1
	1.2 Stresses and Deflections of DeHavilland Extendable Boom Antenna; Circular Cross-Section with Slit	1-2
	1.2.1 Axial Stress and Elongation	1-3
	1.2.2 Bending Stresses and Lateral Deflections	1-5
	1.2.3 Discussion	1-13
	1.3 Stresses and Deflections of Cantilevered Rectangular Honeycomb Boom Antennas	1-16
	1.3.1 Stresses and Deflections Due to Lateral Loading on Constant Section Beam	1-17
	1.3.2 Stresses and Elongation Due to Longitudinal Loading on Constant Section Beam	1-21
	1.3.3 Deflections Due to Lateral Loading on a Tapered Beam	1-23
	1.3.4 Stresses and Elongation Due to Longitudinal Loading on a Tapered Beam	1-26
	1.3.5 Investigation of Preliminary Design with Constant Cross-Section	1-27
	1.4 Stresses and Deflections of Guyed Rectangular Honeycomb Boom Antennas	1-44
	1.4.1 Computer Solution for Optimum Placement of Single Guywire	1-47
	1.4.2 Computer Model "B" of Propped Antenna	1-48
2	ANTENNA ELECTRICAL ANALYSIS	2-1
	2.1 Introduction	2-1
	2.2 Circular Waveguides	2-2
	2.3 Rectangular and Elliptical Waveguides	2-3
	2.4 Extendable Waveguide Arrays	2-4
	2.5 Array of Arrays	2-9
	2.6 Fan Beam Analysis	2-17
	2.7 A Measurement-Verification Scheme	2-21
	2.7.1 Introduction	2-21
	2.7.2 Technical Plan	2-23

TABLE OF CONTENTS (Continued)

Section			Page
	2.7.3	Deflection Curve and Array Design	2-25
	2.7.4	Array Design for Pattern Computation	2-26
	2.7.5	Results of Pattern Computation	2-27
	2.7.6	Array Design for Fabrication	2-31
	2.7.7	Range Geometry and Measurement Errors	2-31
3	COMPUTER SIMULATION		3-1
	3.1	Introduction	3-1
	3.2	Theoretical Development	3-1
	3.2.1	Antenna Deflection	3-1
	3.2.2	Cantilever Antenna	3-3
	3.2.3	Guyed Antenna	3-4
	3.2.4	Antenna Pattern Equations	3-5
	3.2.5	Co-ordinate Transformation	3-6
	3.2.6	Beam Maximum	3-9
	3.2.7	Beam Deflection	3-10
	3.3	Simulation	3-11
	3.3.1	Program Description	3-11
	3.3.2	Simulated Antenna Pattern	3-14
	3.3.3	Deflected Antenna Effects	3-22
	3.3.4	Single Antenna Study	3-22
	3.3.5	Double Antenna Study	3-24
Appendix A	CIRCULAR WAVEGUIDE ARRAY INVESTIGATION		A-1
Appendix B	EXPERIMENTAL STUDY OF PHASE SHIFT VS. BENDING OF RECTANGULAR WAVEGUIDE		B-1
Appendix C	DEFLECTED ANTENNA PATTERNS		C-1
Appendix D	DOUBLE ANTENNA PATTERNS		D-1

LIST OF ILLUSTRATIONS

Figure		Page
1-1	Antenna Lateral Deflection at Spin Rate Ω = 180 rpm	1-29
1-2	Antenna Lateral Deflection at Spin Rate Ω = 150 rpm	1-30
1-3	Antenna Lateral Deflection at Spin Rate Ω = 100 rpm	1-31
1-4	Maximum Lateral Deflection for Various Antenna Lengths and Spin Rates	1-32
1-5	Bending Stress vs Antenna Length	1-34
1-6	Deflected Shape for 100" Antennas Propped at 66, 70, 74, 78 inches, Spin Rate Ω = 180 rpm	1-49
1-7	Deflected Shape for 90" Antennas Propped at 58, 62, 66, 70, 74 inches, Spin Rate Ω = 180 rpm	1-50
1-8	Deflected Shape for 80" Antennas Propped at 54, 58, 60 62 inches, Spin Rate Ω = 180 rpm	1-51
1-9	Deflected Shape for 70" Antennas Propped at 46, 50, 52, 54 inches, Spin Rate Ω = 180 rpm	1-52
1-10	Optimum Prop Locations for Minimum Deflections, Spin Rate Ω = 180 rpm	1-53
1-11	Deflected Shape for 95.909" Antenna Propped at x = 72.421 inches, Spin Rate Ω = 100 rpm	1-55
1-12	Shear Diagram for 95.909" Antenna Propped at x = 72.421 inches, Spin Rate Ω = 100 rpm	1-56
1-13	Moment Diagram for 95.909" Antenna Propped at x = 72.421 inches, Spin Rate Ω = 100 rpm	1-57
2-1	Telescoping Guides Cross Sections	2-7
2-2	Choke Joint Cross Sections	2-7
2-3	Telescoping Array	2-10
2-4	Center Feed Schematic	2-11
2-5	Linear Array Co-ordinates	2-13
2-6	Planar Array Co-ordinates	2-13
2-7	Planar Array of Arrays	2-16
2-8	Computation Co-ordinate System	2-18
2-9	θ, ϕ Angular Positions of Peak of Fan Beam, Undeflected (ω = 0) and Deflected Arrays(ω=100,180 rpm)	2-22
2-10	Boresight View from Source	2-24
2-11	Computed Voltage Patterns for Deflected and Undeflected Arrays	2-28

LIST OF ILLUSTRATIONS (Continued)

Figure		Page
2-12	Projection of Peak of Fan Beam on X-Z Plane	2-29
2-13	Deflection Curve for 100-Element Array (ω = 100 rpm) and 40-Element Array	2-30
2-14	Fabrication Sketch—Slotted Waveguide Antenna Array	2-32
2-15	Antenna Range Geometry	2-34
3-1	Position of Antenna Relative to Spin Axis	3-2
3-2	Antenna Co-ordinate System	3-7
3-3	System Geometric Relationships	3-8
3-4	Flow Chart of Beam Analysis Program	3-12
3-5	Broad Dimension View ($\delta = 90^{o}$) of Undeflected Beam	3-15
3-6	Edge View of an Ideal Fan Beam	3-16
3-7	Contour Plot of Fan Beam	3-17
3-8	Beam Cross Section, Illustrating Defined Terms	3-19
3-9	"Top" View of Beam, Illustrating Defined Terms	3-19
3-10	Schematic View of a Beam Section	3-20
3-11	Relative Location of Various Beam "Centers" for Undeflected Antenna	3-21
3-12	Diagonal ($\delta = 45^{o}$) View of Broad Beam Profile	3-23
3-13	Dependence of Antenna Deflection on Spin Rate	3-25
3-14	Dependence of Antenna Deflection on Antenna Length	3-26
3-15	Dependence of Antenna Deflection on Mounting Angle	3-27
3-16	Deflection of a Guyed Antenna	3-28
3-17	Typical Plot Showing Residual Angular Deviation after Best Linear Correction for Particular Minimum θ	3-29
3-18	Residual in $\Delta\varphi$ Due to Beam Non-Planarity Optimized for $\theta_{min} = 81^{\circ}$ (Synchronous Altitude)	3-30
3-19	Residual in $\Delta\varphi$ Due to Beam Non-Planarity Optimized for $\theta_{min} = 66^{\circ}$ (5000 n. mi. Altitude)	3-31
3-20	Double Antenna Configuration Definition	3-33
A-1	Circular Waveguide Slotted Line	A-2
A-2	Flanges	A-3
A-3	Slot Test Section	A-4
A-4	Rectangular to Circular Transition	A-5

LIST OF ILLUSTRATIONS (Continued)

Figure		Page
A-5	Probe Carriage	A-6
A-6	Circular Waveguide Array Investigation Test Set-Up	A-8
B-1a	Bending in E Plane	B-5
B-1b	Bending in H Plane	B-5
B-2	Phase Shift Per Foot vs 1/R for E and H Plane Bending	B-7
C-1 through C-24	Unguyed Antenna Patterns	C-2 through C-25
C-25	Guyed Antenna Patterns	C-26
C-26	Guyed Antenna Patterns	C-27
C-27	Guyed Antenna Patterns	C-28
D-1	Normal Cross Section Showing Effects of Separation and Misalignment	D-2
D-2	Normal Cross Section Showing Effects of Separation and Misalignment	D-3
D-3	Normal Cross Section Showing Effects of Separation and Misalignment	D-4
D-4	Normal Cross Section Showing Effects of Separation and Misalignment	D-5
D-5	Normal Cross Section Showing Effects of Separation and Misalignment	D-6
D-6	Normal Cross Section Showing Effects of Separation and Misalignment	D-7
D-7	Normal Cross Section Showing Effects of Separation and Misalignment	D-8
D-8	Normal Cross Section Showing Effects of Separation and Misalignment	D-9
D-9	Normal Cross Section Showing Effects of Separation and Misalignment	D-10
D-10	Normal Cross Section Showing Effects of Separation and Misalignment	D-11
D-11	Normal Cross Section Showing Effects of Separation and Misalignment	D-12
D-12	Normal Cross Section Showing Effects of Separation and Misalignment	D-13
D-13	Normal Cross Section of Typical Interference Pattern	D-14

LIST OF ILLUSTRATIONS (Continued)

Figure		Page
D-14	Normal Cross Section of Typical Interference Pattern	D-15
D-15	Normal Cross Section of Typical Interference Pattern	D-16
D-16	Detail of Typical Interference Pattern	D-17
D-17	Wide Range View Showing the Reference Envelope of the Interference Pattern	D-18
D-18	Broad Beam Cross Section Showing How Misalignment Causes Interference in Long Dimensions	D-19
D-19	Broad Beam Cross Section of two Antennas with no Misalignment	D-20
D-20	Normal Cross Section of Antenna Pattern with no Misalignment	D-21
D-21	Normal Cross Section of Antenna Pattern with no Misalignment	D-22
D-22	Antenna Pattern Generated by a Sequence of Slot Pairs	D-23
D-23	Antenna Pattern with Phase Shift at Midpoint	D-24
D-24	Antenna Pattern with Phase Shift not at Midpoint	D-25

LIST OF TABLES

Table		Page
2-1	Slot Positions	2-33
3-1	Summary of Parametric Study	3-32
B-1	Data Summary	B-6

SUMMARY

The primary loads imposed on the boom antenna are due to the centrifugal forces which occur during spinning of the satellite. Structural analyses were performed on several boom antenna configurations under consideration for possible application in a navigation satellite. For each configuration stresses and deflections were determined for various lengths of antennas mounted on satellites spinning in the range of 100 to 180 rpm.

An extendible DeHavilland boom structure was initially considered because of its simplicity and compactness. Calculations showed that very large bending stresses and deflections and large torsional stresses and rotations occur at the spin rates under consideration. In addition, it was also shown that such a structure would have a local instability problem because of the thinness of the tube walls. This structure can only be used by drastically reducing the spin rate. Such a restriction is unwarranted because of other considerations.

Next, a rectangular honeycomb sandwich beam cantilevered antenna was examined. Such a section is inherently stronger and stiffer than a DeHavilland beam. As one might expect, the most severe loads occur with the longer antennas and the higher spin rates. Under the maximum loads the stresses and deflections are rather high but they can be reduced by considering slightly shorter antennas or lower spin rates. Hence, it was judged that this structural configuration is feasible.

To improve the structural performance of the cantilever beam, the use of intermediate supports in the form of guy wires was investigated. Stresses and deflections were greatly reduced from those of the pure cantilever, but this configuration is mechanically more complicated.

Thus, two feasible structural configurations were identified: the cantilevered honeycomb beam and the guyed cantilevered beam. The choice will naturally be determined by the electrical performance requirements of the antenna. If a shorter antenna or lower spin rate is allowable, then the cantilever beam would be the logical choice. On the other hand, if deflections are large enough to cause excessive degradation in electrical performance, then the guyed configuration must be used.

The electrical performance of deformed antennas was evaluated for several antenna lengths and spin rates as well as the guyed and unguyed configurations. It was found that for combinations of spin rate and antenna length such that the antenna was deflected no more than 3° (defined as the arc tangent of the deflection over the antenna length), an unguyed antenna performs as well as a guyed antenna. This is due to the fact that although the fan beam is deflected it remains substantially planar for small antenna deflections.

A lower bound on spin rate is imposed by satellite stability considerations and antenna deflection imposes an upper bound. Similarly, suitable beam definition requires that an antenna be at least a minimum length and deflection considerations impose a maximum length. The parametric evaluation performed shows that an unguyed antenna between 40 and 100 inches in length mounted on a satellite spinning between 100 and 120 rpm will give satisfactory electrical performance.

SECTION 1
NAVIGATION SATELLITE ANTENNA STRUCTURAL ANALYSES

1.1 INTRODUCTION AND SUMMARY

This section contains structural analyses performed on several configurations of boom antennas for possible application in a navigation satellite system. Antenna lengths up to 100 inches mounted on spacecrafts spinning in the range of 100 to 180 rpm are investigated.

In Section 1.2 a DeHavilland extendible boom antenna with circular cross section and lengthwise slit is examined. Analysis shows that stresses and deflections are several orders of magnitude too high.

A rectangular honeycomb cantilevered antenna is analyzed in Section 1.3. Calculations show that deflections and stresses are somewhat high but this configuration is structurally feasible.

To provide decreased deflections for electrical reasons, a guyed antenna is considered in Section 1.4. Deflections and stresses are well within allowable limits and it seems that this is the best theoretical solution. However there are some mechanical problems associated with the deployment of guyed structures. It appears that a detailed deployment study would help to delineate the trade-offs involved.

1.2 STRESSES AND DEFLECTIONS OF DE HAVILLAND EXTENDABLE BOOM ANTENNA; CIRCULAR CROSS-SECTION WITH SLIT

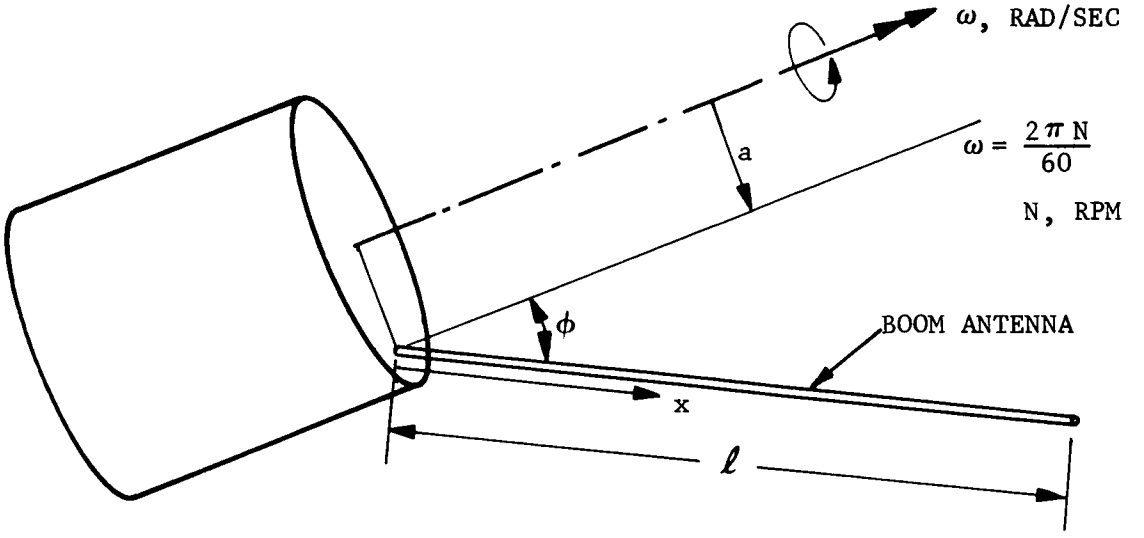

The antenna will experience centrifugal forces due to the spacecraft spin rate ω, rad/sec.

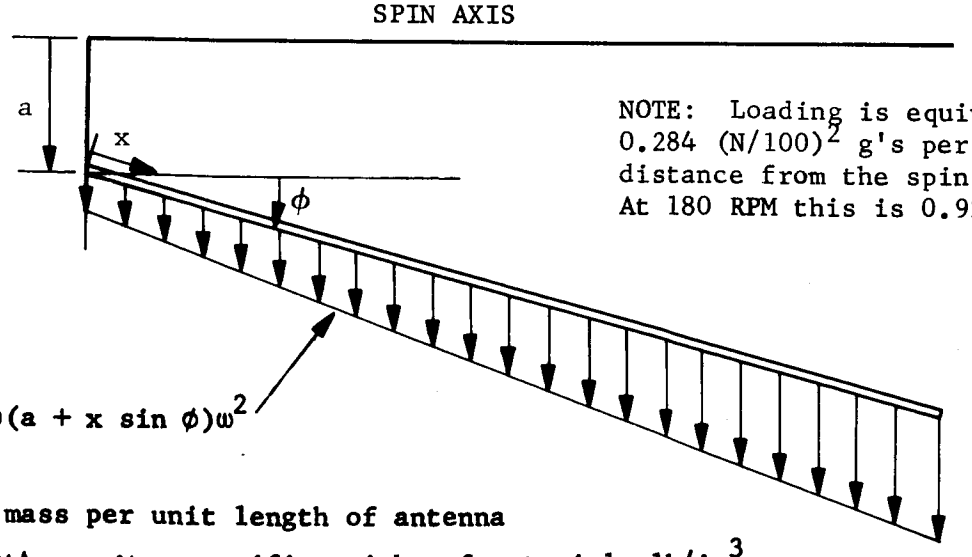

NOTE: Loading is equivalent to $0.284\ (N/100)^2$ g's per inch of distance from the spin axis. At 180 RPM this is 0.92 g/inch.

$p = \rho(a + x \sin \phi)\omega^2$

ρ is mass per unit length of antenna

$\rho = \frac{\gamma A}{386}$ γ = specific weight of material, lb/in^3
A = area of cross-section, in^2

The loading is separated into a component parallel to the antenna, $p_P = p \sin \phi$, which will produce axial stresses and elongation, and a component normal to the antenna, $p_N = p \cos \phi$, which will produce bending stresses and lateral deflections. We consider these two cases separately.

1.2.1 Axial Stress and Elongation

The component parallel to the antenna will produce an axial force, P, as sketched on the right. This force acts at the centroid of the cross-section and is found from equilibrium as sketched below.

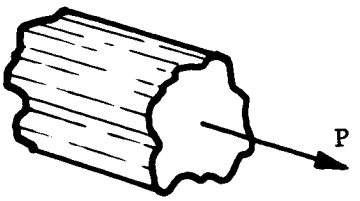

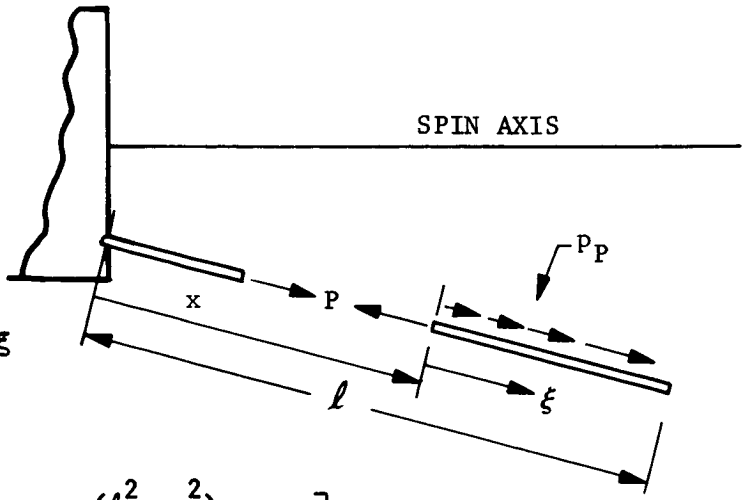

$$P = \int_x^{\ell} p \sin \phi \, d\xi$$

$$P = \frac{\gamma A}{386} \omega^2 \sin \phi \int_x^{\ell} (a + \xi \sin \phi) d\xi$$

$$P = \frac{\gamma A}{386} \omega^2 \sin \phi \left[a(\ell - x) + \frac{(\ell^2 - x^2)}{2} \sin \phi \right] \qquad (2)$$

The axial force, P, is the resultant of a uniform axial stress, σ, as sketched on the right. The magnitude of this stress is given by

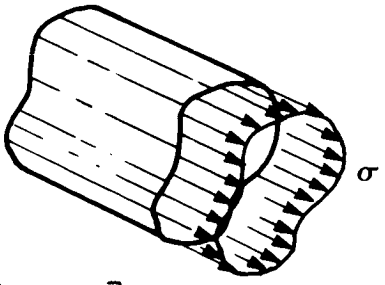

$$\sigma = \frac{P}{A} = \frac{\gamma \omega^2}{386} \sin \phi \left[a \, (\ell - x) + \frac{(\ell^2 - x^2)}{2} \sin \phi \right] \qquad (3)$$

which is independent of the bar cross-section. The maximum axial force, P, and axial stress, σ, occur at the base of the antenna (x = 0) where the values are

$$P_{max} = \frac{\gamma A}{386}\,\omega^2 \ell^2 \sin\phi \left[\frac{a}{\ell} + \frac{\sin\phi}{2}\right] \tag{4}$$

$$\sigma_{max} = \frac{\gamma\,\omega^2 \ell^2}{386} \sin\phi \left[\frac{a}{\ell} + \frac{\sin\phi}{2}\right] \tag{5}$$

EXAMPLE

$\gamma = 0.285$ lb/in^3 (steel)

$\phi = 45^\circ$, $a = 0$

$\omega = \frac{2\pi}{60} N$

$$\sigma_{max} = \frac{0.285}{386}\left(\frac{2\pi}{60}\right)^2 N^2 \ell^2 \frac{(.707)^2}{2}$$

$$\sigma_{max} = 202\left(\frac{N}{100}\right)^2 \left(\frac{\ell}{100}\right)^2$$

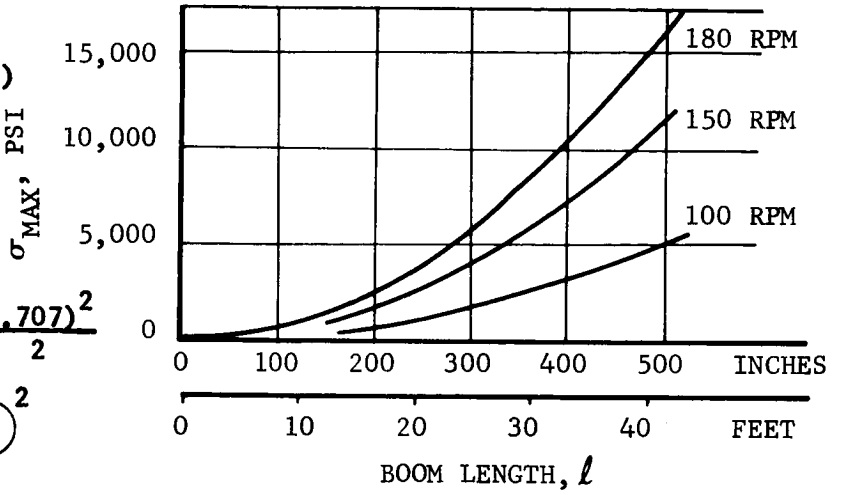

The axial elongation, δ is obtained by integrating the strain, $\epsilon = \frac{\sigma}{E}$, over the length of the bar

$$\delta = \int_0^x \frac{\sigma}{E}\,dx = \frac{\gamma\omega^2}{386\,E} \sin\phi \int_0^x \left[a\,(\ell - x) + \frac{\ell^2 - x^2}{2} \sin\phi\right] dx$$

$$\delta = \frac{\gamma\omega^2}{386\,E} \sin\phi \left[ax\left(\ell - \frac{x}{2}\right) + \frac{x}{2}\left(\ell^2 - \frac{x^2}{3}\right) \sin\phi\right] \tag{6}$$

The maximum elongation, which occurs at the outer end, ($x = \ell$), is given by

$$\delta_{max} = \frac{\gamma\omega^2}{386\,E}\,\ell^3 \sin\phi \left(\frac{a}{2\ell} + \frac{\sin\phi}{3}\right) \tag{7}$$

Note that, as for the stress, the axial elongation is independent of the cross section.

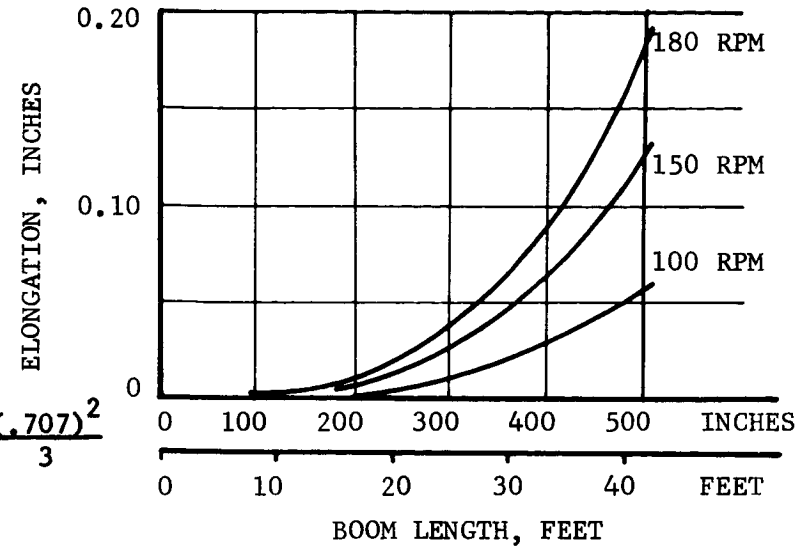

EXAMPLE

$\gamma = 0.285$ lb/in^3 (steel)

$E = 30 \times 10^6$ lb/in^2

$\phi = 45^\circ$, $a = 0$

$$\delta_{max} = \frac{0.285}{386}\left(\frac{2\pi}{60}\right)^2 N^2 \ell^3 \frac{1}{30\times10^6}\frac{(.707)^2}{3}$$

$$\delta_{max} = .00045\left(\frac{N}{100}\right)^2\left(\frac{\ell}{100}\right)^3$$

1.2.2 Bending Stresses and Lateral Deflections

The load component normal to the boom will produce moment and shear force stress resultants as sketched below. These resultants may be found from

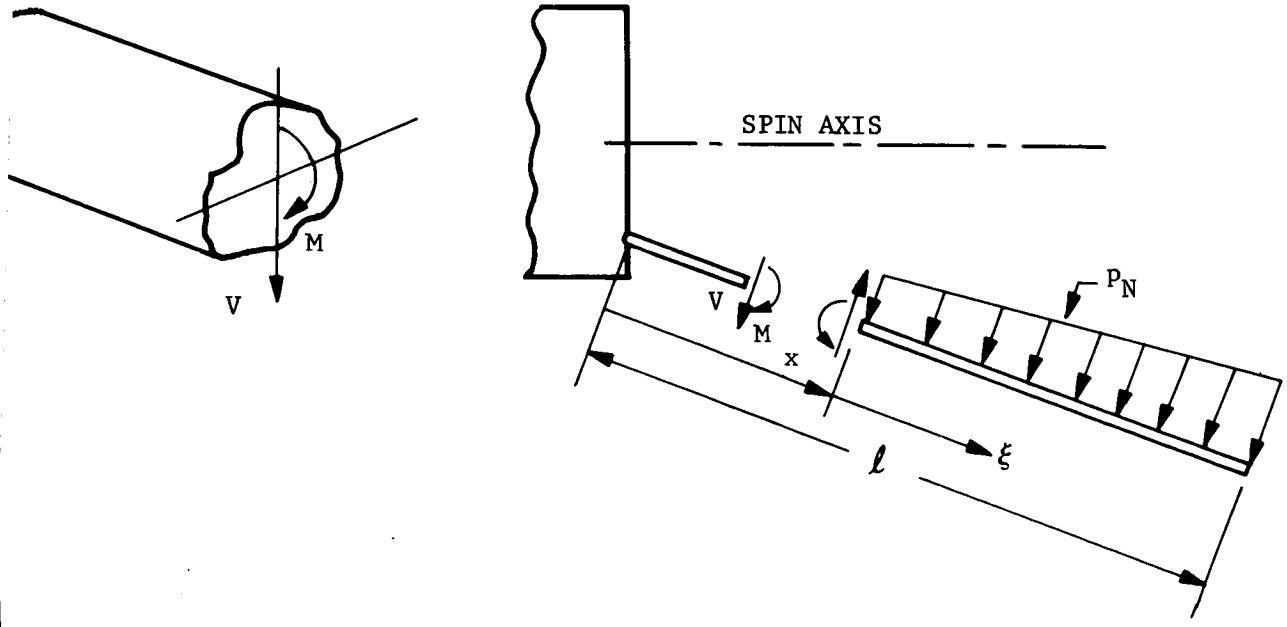

equilibrium with the result

$$M = \int_x^\ell \xi\, p_N\, d\xi = \frac{\gamma A}{386}\omega^2 \cos\phi \int_x^\ell (a + \xi \sin\phi)\xi\, d\xi$$

$$M = \frac{\gamma A}{386}\omega^2 \cos\phi \left[a\,\frac{\ell^2 - x^2}{2} + \frac{\ell^3 - x^3}{3}\sin\phi\right] \tag{8}$$

$$V = \int_x^\ell p_N\, d\xi = \frac{\gamma A}{386}\omega^2 \cos\phi \int_x^\ell (a + \xi \sin\phi)\, d\xi$$

$$V = \frac{\gamma A}{386}\omega^2 \cos\phi \left[a\,(\ell - x) + \frac{\ell^2 - x^2}{2}\sin\phi\right] \tag{9}$$

At the base of the antenna, where these are maximum, we have

$$M_{max} = \frac{\gamma A}{386}\omega^2 \ell^3 \cos\phi \left[\frac{a}{2\ell} + \frac{\sin\phi}{3}\right] \tag{10}$$

$$V_{max} = \frac{\gamma A}{386}\omega^2 \ell^2 \cos\phi \left[\frac{a}{\ell} + \frac{\sin\phi}{2}\right] \tag{11}$$

We consider two cases for a circular tube with a slit:

<u>Case 1</u> The slit is in the plane of the load.

<u>Case 2</u> The slit is perpendicular to the plane of the load.

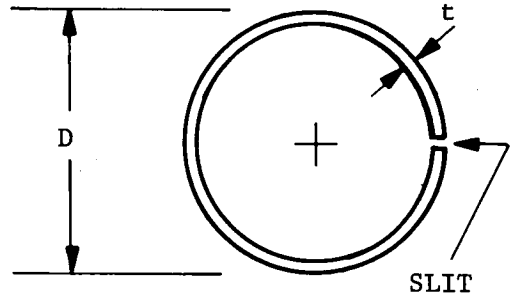

$$A = \pi Dt \qquad I = \frac{\pi}{8} D^3 t$$

<u>Case 1</u> <u>Slit in the Plane of Loading</u>

In this case the loading occurs in a plane of symmetry for the section, hence the moment and shear resultant act at the centroid of the section as sketched on the right. The slit is shown on the outside, but may be on the inside with the same results.

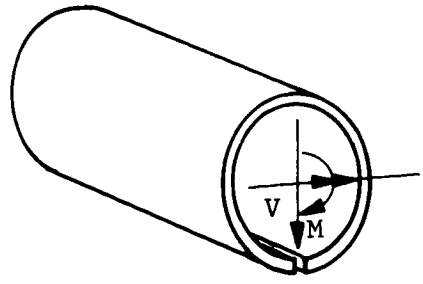

he bending moment results from axial tresses, σ, as sketched on the right. he stress is a maximum at the base of he antenna and at the outer most points rom the neutral axis. We have

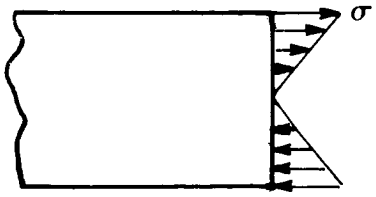

$$\sigma_{max} = \frac{M_{max}\,(D/2)}{I} = \frac{(D/2)}{\frac{\pi}{8} D^3 t} \frac{\gamma(\pi D t)}{386} \omega^2 \ell^3 \cos\phi \left[\frac{a}{2\ell} + \frac{\sin\phi}{3}\right]$$

$$\sigma_{max} = \frac{4\gamma\,\omega^2\ell^3}{386\,D} \cos\phi \left[\frac{a}{2\ell} + \frac{\sin\phi}{3}\right] \qquad (12)$$

OTE: Independent of the tube thickness t.

XAMPLE

$\gamma = 0.285$ lb/in^3(steel)

$\phi = 45^o$, a = 0, D = 1"

$$\sigma_{max} = \frac{0.285}{386}\left(\frac{2\pi}{60}\right)^2 N^2 \ell^3 (.707)^2 \frac{4}{3}$$

$$\sigma_{max} = 54{,}000 \left(\frac{N}{100}\right)^2 \left(\frac{\ell}{100}\right)^3$$

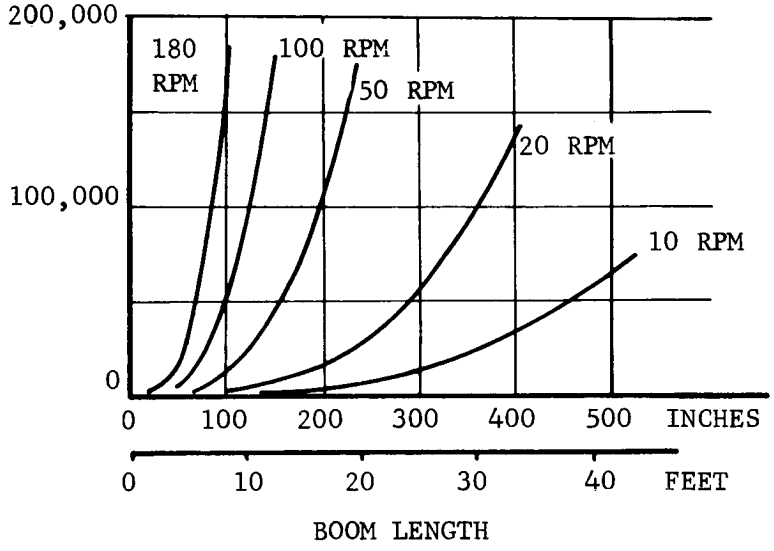

he shear force results from shear tresses as sketched on the right. he stress is a maximum at the base f the antenna and at the netrual axis.

e have

$$\tau_{max} = \frac{2V_{max}}{A} = \frac{2\gamma}{386} \omega^2 \ell^2 \cos\phi \left[\frac{a}{\ell} + \frac{\sin\phi}{2}\right] \qquad (13)$$

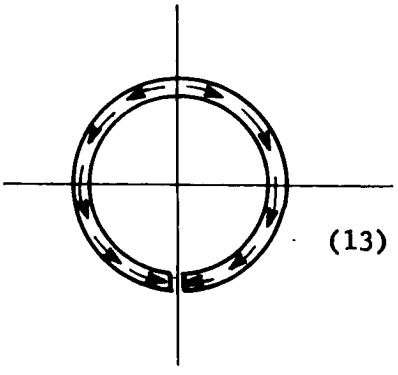

OTE: Independent of cross section dimensions.

EXAMPLE

$\gamma = 0.285$ lb/in^3 (steel)

$\phi = 45^o$, $a = 0$

$$\tau_{max} = \frac{0.285}{386}\left(\frac{2\pi}{60}\right)^2 N^2 \ell^2 (.707)^2$$

$$\tau_{max} = 405\left(\frac{N}{100}\right)^2\left(\frac{\ell}{100}\right)^2$$

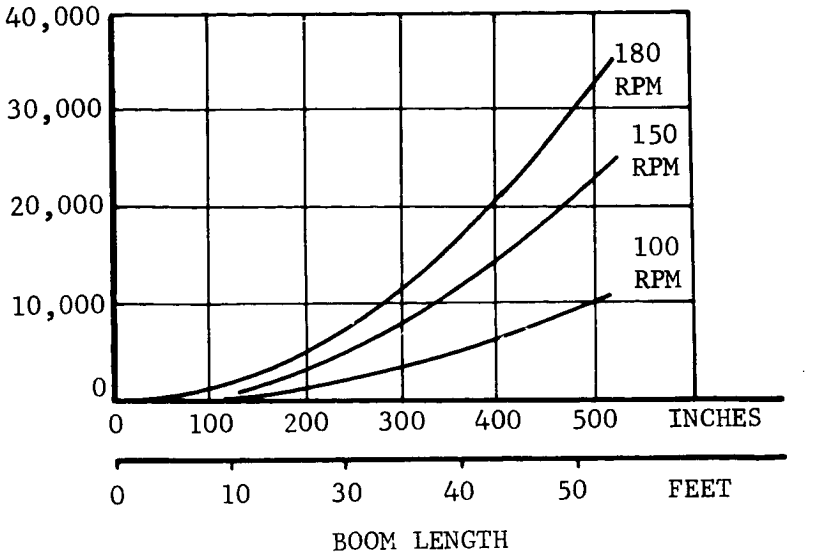

The bending deflection, y, is obtained from the equation

$$\frac{d^2y}{dx^2} = \frac{M}{EI} = \frac{\gamma(\pi Dt)}{386\ E\ \frac{\pi}{8} D^3 t}\omega^2 \cos\phi\left[a\frac{\ell^2 - x^2}{2} + \frac{\ell^3 - x^3}{3}\sin\phi\right]$$

Integrating and noting the boundary conditions $\frac{dy}{dx} = 0$ and $y = 0$ at $x = 0$, we obtain

$$y = \frac{8\gamma\omega^2}{386\ E\ D^2}\cos\phi\left[\frac{a}{2}\left(\frac{\ell^2 x^2}{2} - \frac{x^4}{12}\right) + \frac{\sin\phi}{3}\left(\frac{\ell^3 x^2}{2} - \frac{x^5}{20}\right)\right] \qquad (14)$$

The maximum deflection, at the outer end of the antenna $x = \ell$, is

$$y_{max} = \frac{8\gamma\omega^2}{386\ E\ D^2}\ell^5 \cos\phi\left[\frac{5a}{24\ell} + \frac{3}{20}\sin\phi\right] \qquad (15)$$

NOTE: Independent of tube thickness.

EXAMPLE

$$\left.\begin{aligned}\gamma &= 0.285\ \text{lb/in}^3 \\ E &= 30 \times 10^6\ \text{lb/in}^2\end{aligned}\right\}\ \text{(steel)}$$

$$\phi = 45^\circ,\ a = 0,\ D = 1"$$

$$y_{max} = \frac{0.285}{386}\left(\frac{2\pi}{60}\right)^2 \frac{N^2 \ell^5}{30 \times 10^6}\,(.707)^2\,\frac{6}{5}$$

$$y_{max} = 16.2\left(\frac{N}{100}\right)^2\left(\frac{\ell}{100}\right)^5$$

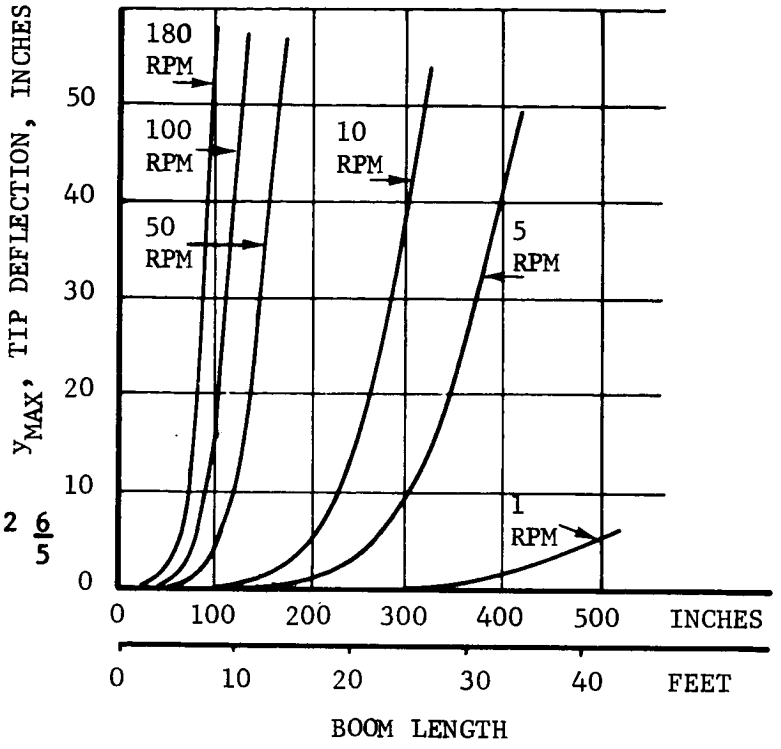

For Case 1, the loading occurs in a plane of symmetry of the cross section, hence there will be no twisting or torsional stresses.

End of Case 1

Case 2 Slit Perpendicular to the Plane of Loading

For Case 2 the loading occurs in a plane that is not a plane of symmetry for the cross section. In this case the shear resultant, V, must act at

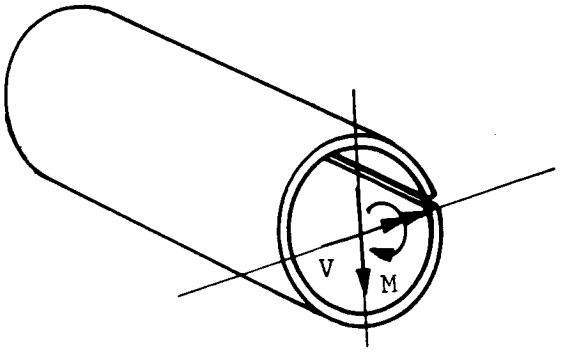

the "shear center" of the cross section in order to have pure bending without twisting. However, the centrifugal loading provides a shear resultant which acts at the centroid of the section. Transferring the shear resultant to the

shear center, we introduce a torque T = Ve, which will produce torsional shear stresses and twisting of the beam.

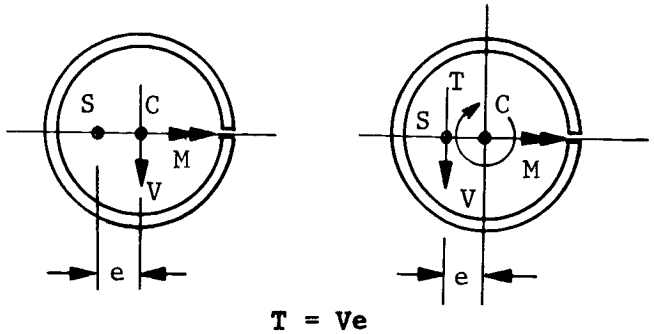

T = Ve

C represents centroid position
S represents shear center

For Case 2, the axial stresses and elongations are unchanged and remain as given by Equations (2) through (7). The bending moment and shear force expressions are unchanged and remain as given by Equations (8) through (11). The torque resultant, T, is obtained easily as

$$T = Ve = \frac{\gamma Ae}{386}\omega^2 \cos\phi \left[a(\ell - x) + \frac{\ell^2 - x^2}{2}\sin\phi\right]. \qquad (16)$$

At the base of the antenna T will be maximum and we have

$$T_{max} = V_{max}\, e = \frac{\gamma Ae}{386}\omega^2\ell^2 \cos\phi \left[\frac{a}{\ell} + \frac{\sin\phi}{2}\right] \qquad (17)$$

The bending stresses and lateral deflections [Equations (12), (14) and (15)] remain unchanged, but we must develop new equations for the shear stresses and torsional deflections.

The bending shear stresses may be found from equilibrium of a small portion of the beam as shown below.

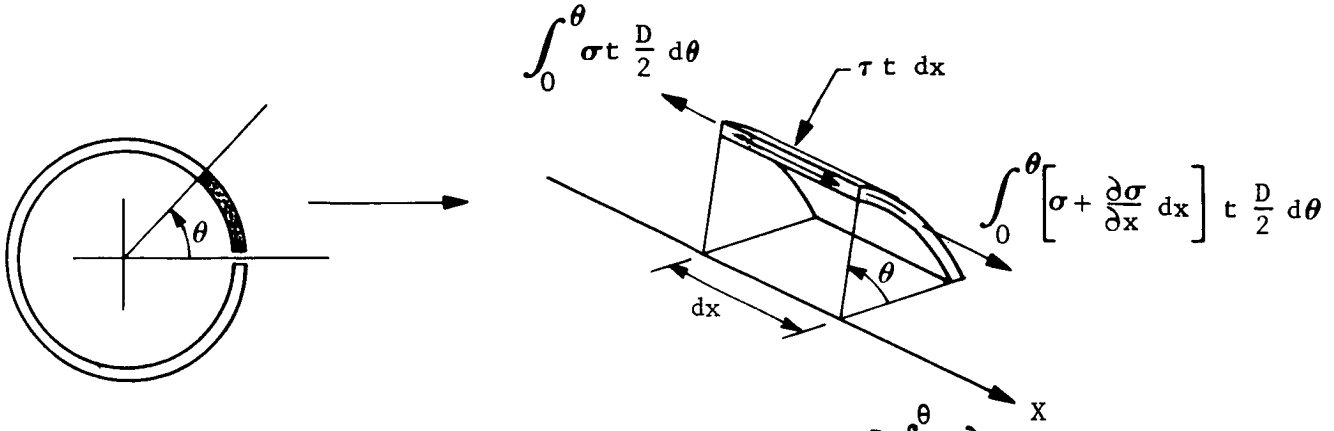

From Force Equilibrium in the x-direction: $\tau = -\frac{D}{2}\int_0^\theta \frac{\partial \sigma}{\partial x} d\theta$

The bending stress, σ, is given by

$$\sigma = \frac{M\left(\frac{D}{2}\right)}{I} \sin\theta$$

Hence

$$\tau = -\frac{(D/2)^2}{I} \frac{dM}{dx} \int_0^\theta \sin\theta\, d\theta$$

Integrating and noting $\frac{dM}{dx} = -V$, we have

$$\tau = \left(\frac{D}{2}\right)^2 \frac{V}{I} (1 - \cos\theta)$$

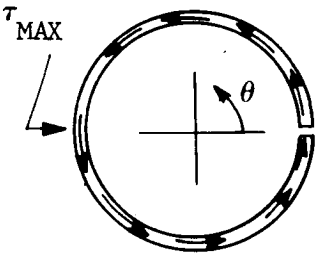

This distribution is sketched to the right. It is a maximum for $V = V_{max}$, [Equation (11)] and $\theta = 180^\circ$, in which case we have

$$\tau_{max} = \frac{4\gamma}{386} \omega^2 \ell^2 \cos\phi \left[\frac{a}{\ell} + \frac{\sin\phi}{2}\right] \qquad (18)$$

which is twice as large as the corresponding shear stress for Case 1 [Equation (13)].

The distance to the "shear center" may now be found by observing that

$$Ve = \int_0^{2\pi} \tau\, t \left(\frac{D}{2}\right)^2 d\theta$$

$$Ve = \left(\frac{D}{2}\right)^4 t \frac{V}{I} \int_0^{2\pi} (1 - \cos\theta)\, d\theta$$

$$e = \frac{D^4 t}{16 \frac{\pi}{8} D^3 t} 2\pi$$

$$e = D$$

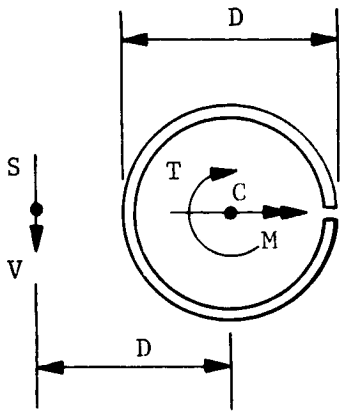

Now the torque resultant is

$$T = \frac{\gamma A D}{386} \omega^2 \cos\phi \left[a(\ell - x) + \frac{\ell^2 - x^2}{2} \sin\phi\right]$$

The torsional shear stress is given by[1]

$$\tau = \frac{T(3\pi D + 1.8\, t)}{4\pi^2 D^2 t^2}$$

and is distributed as shown on the right. The torsional rotation is given by[1]

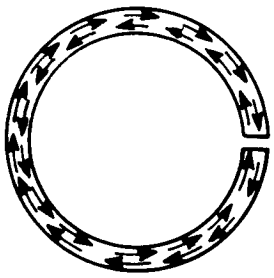

$$\psi = \int_0^x \frac{3T}{\pi D t^3} dx$$

$$\psi = \frac{3\gamma(\pi D t) D}{386\, \pi D t^3} \omega^2 \cos\phi \left[a\left(\ell x - \frac{x^2}{2}\right) + \left(\frac{\ell^2 x}{2} - \frac{x^3}{6}\right) \sin\phi\right]$$

[1] Roark, Formulas for Stress and Strain, McGraw-Hill Book Company, Inc., 1954, Table IX-12.

At $x = \ell$,

$$\psi_{max} = \frac{3\gamma D}{386\ t^2}\ \omega^2 \ell^3\ \cos\phi \left[\frac{a}{2\ell} + \frac{\sin\phi}{3} \right]$$

The torsional stress and deflection formulas are valid only for small displacements and neglect the effects of end constraint. Because the boom is very flexible in torsion, a large deflection torsional theory is needed. This is not developed since the results so far suggest that the DeHavilland boom approach is not promising.

End of Case 2

1.2.3 Discussion

a. The results indicate very large bending stresses and deflections and, although not fully developed, very large torsional stresses and rotations, in the boom lengths of 10 to 40 feet. The stresses and deflections are too large by several orders of magnitude. It is concluded that the thin-walled DeHavilland booms do not appear feasible for this application.

b. As expected, the longitudinal stresses and deflections are small compared to the bending and torsional stresses and deflections.

c. The theory and results presented here are based upon assumptions of linear, small displacement theory. The results are inaccurate for increasingly larger displacements. However, the results do indicate trends and may be used as gross measures for feasibility. For accurate results, improved theories must be used, especially for torsion, which include the following effects:

1. The effect of structural deflections upon load. The load will increase as the boom deflects outwardly.

2. The coupling between axial forces and bending moments. This is the consideration of the familiar P_y bending moment term.

3. The effect of axial stresses to support torque loads under large rotations.

4. The effect of cross section distortion under load. This effect is of particular importance for very thin tube walls.

d. It is expected that the mode of failure for the boom under the centrifugal loading will be local buckling, or crippling of the thin tube wall. Crippling stresses vary depending upon the type of material and the ratio D/t. Crippling stresses are not accurately predicted analytically; the designer must rely upon empirical data, which is scarce, or, preferably, perform structural tests on sample tubes to establish design criteria. For the DeHavilland booms D/t may vary from 100 to 500 which is quite high. For such high ratios, crippling stresses will tend to be low, say 50,000 psi at best. From the curve on the first example of Case 1, a stress level of 50,000 psi will restrict the spin rate to 10 to 20 rpm for boom lengths of 10 to 40 feet. This spin rate is much lower than presently envisioned (150 to 180 rpm).

e. The deflection limitations are not well defined presently, but assuming a limitation of a few inched, the graph in the third example of Case 1 suggests that the spin rate must be 1 to 10 rpm for 10 to 40 foot booms. Again, this spin rate is much longer than presently envisioned.

f. The numerical results given here were based upon a steel boom of uniform thickness. The results were relatively independent of the cross section dimensions. Examination of the equations for stresses and deflections suggests the following changes to make the booms more attractive:

1. Use a stiffer, lighter material. Beryllium, with $\gamma = 0.067$ lb/in^3 and $E = 43 \times 10^6$ lb/in^2, may be the best choice. It will provide an advantage of $\frac{.285}{.067} \cdot \frac{43}{30} = 6.1$.

2. A decrease in the spin rate, ω, is mandatory if the booms are to be used. The spin rate is established from attitude stability criteria where the product $I_{spin}\,\omega$ must be larger than a specified value. It may be worthwhile examining the feasibility of increasing I_{spin} in order to decrease ω. (I_{spin} is the moment of inertia about the satellite spin axis.)

3. It may be profitable to use a boom with a tapering wall-thickness. This will decrease the load, but will also decrease the material available to carry the stresses and provide stiffness. It may be that the net result is improved performance. At least this should be examined.

1.3 STRESSES AND DEFLECTIONS OF CANTILEVERED RECTANGULAR HONEYCOMB BOOM ANTENNAS

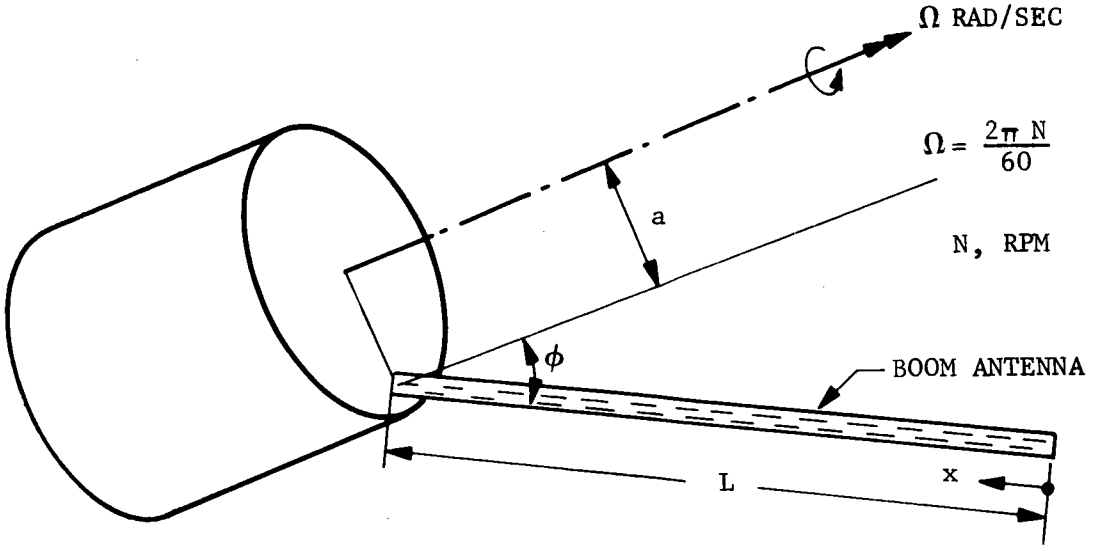

The antenna will experience centrifugal forces due to the spacecraft spin rate Ω Rad/Sec.

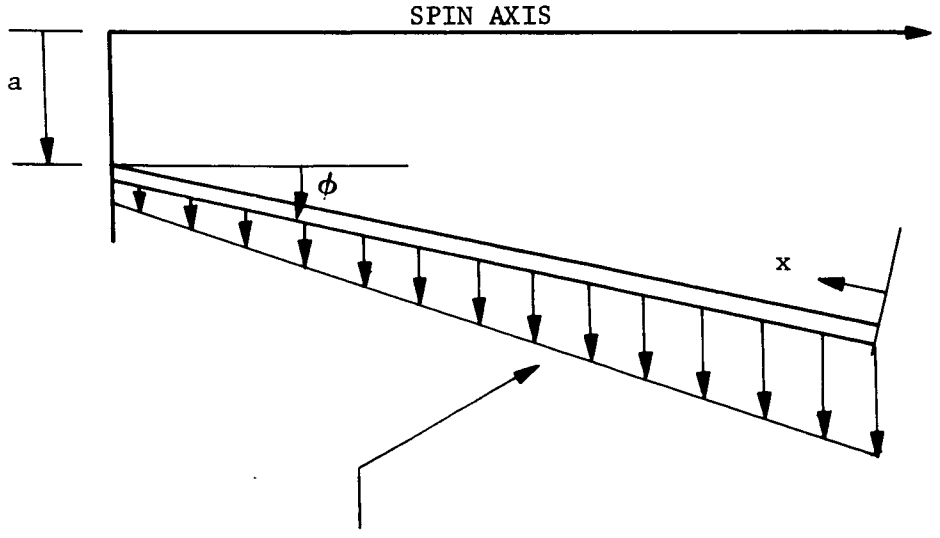

$$p = \rho \left[a + (L-x) \sin\phi \right] \Omega^2$$

ρ is mass per unit length of antenna

$\rho = \frac{\gamma A}{386}$ γ = Specific weight of material, LB/IN^3

A = Area of cross section, IN^2

As in Section 1.2, the loading is separated into a component parallel to the antenna axis $p_P = p \sin \phi$, which will produce axial stresses and elongation, and a component normal to the antenna axis, $\rho_N = \cos \phi$ which will produce bending stresses and lateral deflections.

1.3.1 Stresses and Deflections Due to Lateral Loading on Constant Section Beam

As a start we will consider a beam of constant section. The linearly varying lateral load can be separated into a uniformly distributed load, p_{N_1}, and a triangular load, p_{N_2}.

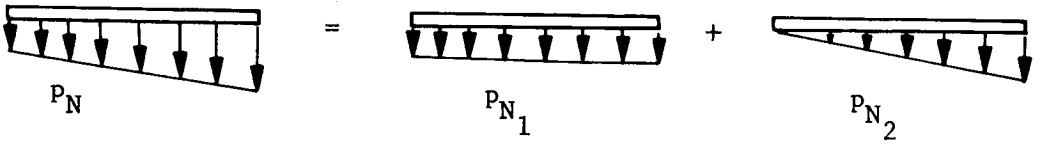

Beam deflections may be found by using the method of virtual work.

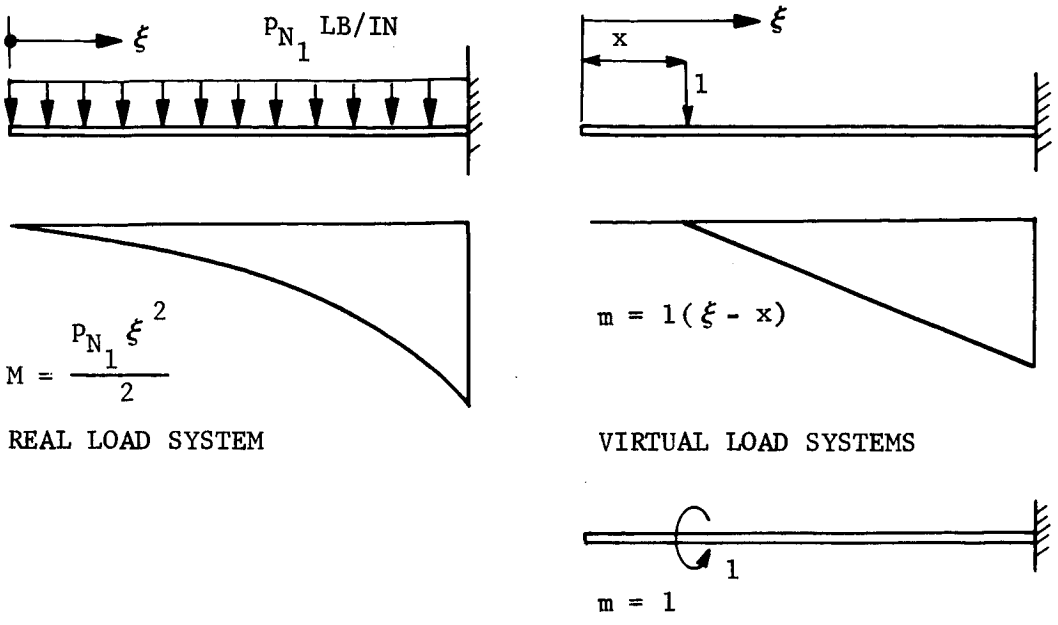

The deflection δ_1 at any point, x, along the length of the beam due to P_{N_1} is

$$\delta_1 = \int_x^L \frac{Mm\, d\xi}{EI}$$

$$\delta_1 = \frac{1}{EI} \int_x^L \frac{P_{N_1} \xi^2}{2} (\xi - x) d\xi$$

$$\delta_1 = \frac{P_{N_1}}{2EI} \int_x^L (\xi^3 - \xi^2 x) d\xi = \frac{P_{N_1}}{2EI} \left[\frac{\xi^4}{4} - \frac{x\xi^3}{3} \right]_x^L$$

E = Youngs Modulus
I = Moment of Inertia
L = Length

$$\delta_1 = \frac{p_{N_1}}{24\ EI}\left[x^4 - 4L^3x + 3L^4\right] \tag{20}$$

The rotation, θ_1, at any point, x, due to p_{N_1} is

$$\theta_1 = \frac{1}{EI}\int_x^L \frac{p_{N_1}\,\xi^2}{2}(1)d\,\xi = \frac{p_{N_1}}{2EI}\int_x^L \xi^2\,d\,\xi$$

$$\theta_1 = \frac{p_{N_1}}{6EI}\left[L^3 - x^3\right] \tag{21}$$

From Eq. (19) it is evident that

$$p_{N_1} = \rho\ a\ \Omega^2\ \cos\phi \tag{22}$$

$$p_{N_2} = \rho(L - x)\Omega^2\ \sin\phi\ \cos\phi \tag{23}$$

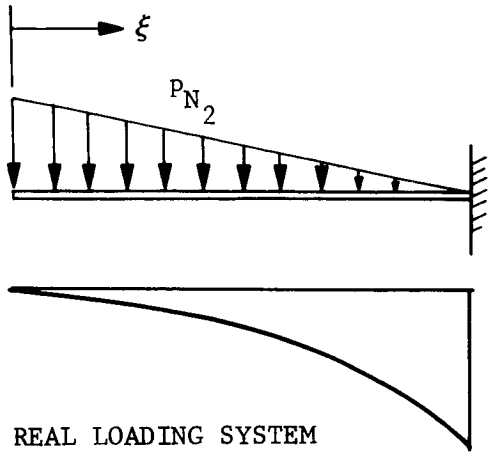

REAL LOADING SYSTEM

The triangular load, p_{N_2}, as shown is

$$p_{N_2} = C(L - \xi)$$

where C is a constant

$$C = \rho \Omega^2 \sin \phi \cos \phi$$

The moment M is

$$M = \frac{C(L - \xi)\xi^2}{2} + \frac{C \xi^3}{3}$$

Check:

$$M\big|_{\xi=0} = 0 \; ; \qquad M\big|_{\xi=L} = \frac{CL^3}{3}$$

The deflection δ_2 at any point x due to p_{N_2} is

$$\delta_2 = \frac{C}{EI} \int_x^L (\xi - x) \left(\frac{L\xi^2 - \xi^3}{2} + \frac{\xi^3}{3} \right) d\xi$$

$$\delta_2 = \frac{C}{EI} \int_x^L \left(\frac{L\xi^3 - \xi^4}{2} + \frac{\xi^4}{3} - \frac{Lx\xi^2 + x\xi^3}{2} - \frac{x\xi^3}{3} \right) d\xi$$

$$\delta_2 = \frac{C}{EI} \left[\frac{L\xi^4}{8} - \frac{\xi^5}{30} - \frac{xL\xi^3}{6} + \frac{x\xi^4}{24} \right]_x^L$$

$$\delta_2 = \frac{\rho\Omega^2 \sin \phi \cos \phi}{120EI} \left[11L^5 - 15L^4 x + 5Lx^4 - x^5 \right] \tag{24}$$

The rotation at any point x due to p_{N_2} is

$$\theta_2 = \frac{C}{EI} \int_x^L \left(\frac{L\xi^2 - \xi^3}{2} + \frac{\xi^3}{3} \right) d\xi = \frac{C}{EI} \left[\frac{L\xi^3}{6} - \frac{\xi^4}{8} + \frac{\xi^4}{12} \right]_x^L$$

$$\theta_2 = \frac{\rho\Omega^2 \sin \phi \cos \phi}{24\, EI} \left[3L^4 - 4Lx^3 + x^4 \right] \tag{25}$$

Finally, of course, the total deflections and rotations due to the lateral load is obtained by superposition.

$$\delta = \delta_1 + \delta_2$$

$$\theta = \theta_1 + \theta_2$$

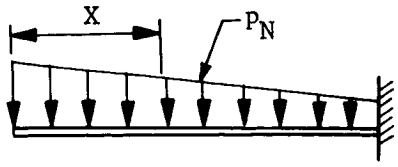

The bending moment at any section x is

$$M = \frac{\rho a \cos\phi\, \Omega^2 x^2}{2} + \frac{\rho \sin\phi \cos\phi\, \Omega^2}{6} (3Lx^2 - x^3) \qquad (26)$$

The shear is

$$V = \rho\, \Omega^2 \cos\phi\, (ax + Lx \sin\phi - \frac{x^2}{2} \sin\phi) \qquad (27)$$

Stresses are given by standard beam formulas

$$\sigma = \frac{Mc}{I} \; ; \quad v = \frac{VQ}{Ib}$$

1.3.2 Stresses and Elongation Due to Longitudinal Loading on Constant Section Beam

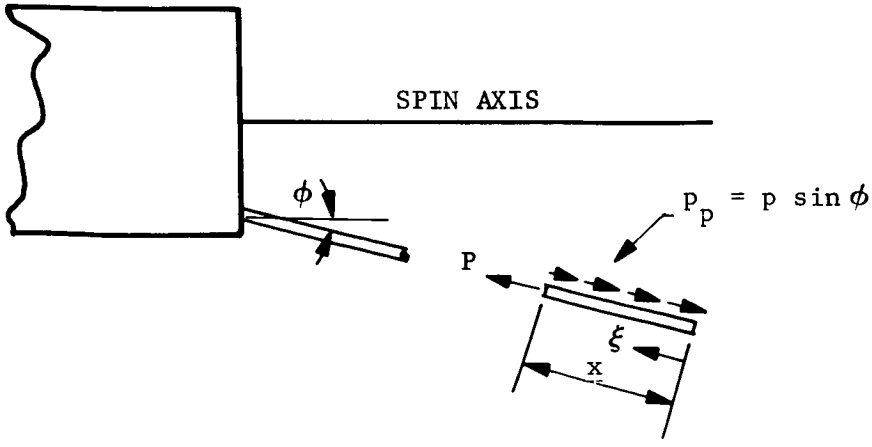

The equations for stress and elongation due to longitudinal loading were developed in Section 1.2. These equations will be rewritten here because of the change in reference of ξ and x.

$$P = \int_0^x p \sin\phi \, d\xi = \int_0^x \rho \left(a \sin\phi + (L - \xi) \sin^2\phi \right) \Omega^2 d\xi$$

$$P = \rho\Omega^2 \left[a\xi \sin\phi + L\xi \sin^2\phi - \frac{\xi^2}{2} \sin^2\phi \right]_0^x$$

$$P = \rho\Omega^2 \left[ax \sin\phi + x \left(L - \frac{x}{2} \right) \sin^2\phi \right] \tag{28}$$

The axial stresses are given by $\frac{P}{A}$ where A is the cross sectional area. In the case of a honeycomb beam, A is the facing area.

$$\sigma = \frac{\rho\Omega^2}{A} \left[ax \sin\phi + \left(L - \frac{x}{2} \right) \sin^2\phi \right] \tag{29}$$

The axial elongation is given by

$$\delta = \int_x^L \frac{\sigma}{E} d\xi = \frac{\rho\Omega^2}{AE} \int_x^L \left(a\xi \sin\phi + \xi \left(L - \frac{\xi}{2} \right) \sin^2\phi \right) d\xi$$

$$\delta = \frac{\rho\Omega^2}{AE} \left[a \frac{\xi^2}{2} \sin\phi + \left(\frac{L\xi^2}{2} - \frac{\xi^3}{6} \right) \sin^2\phi \right]_x^L$$

$$\delta = \frac{\rho\Omega^2}{AE} \left[\frac{a}{2} (L^2 - x^2) \sin\phi + \frac{1}{6} (2L^3 - 3Lx^2 + x^3) \sin^2\phi \right] \tag{30}$$

The maximum deflection occurs at the free end, (x = 0), and is

$$\delta_{max} = \frac{\rho\Omega^2}{AE} \left(\frac{aL^2}{2} \sin\phi + \frac{L^3}{3} \sin^2\phi \right) \tag{31}$$

1.3.3 Deflections Due to Lateral Loading on a Tapered Beam

We now move on to consider a tapered cantilever beam under lateral loading similar to that investigated in Section 1.3.1. The large end of the tapered beam will logically be placed at the fixed end. In the analysis the tapered beam can be treated as a series of beam elements of increasing size.

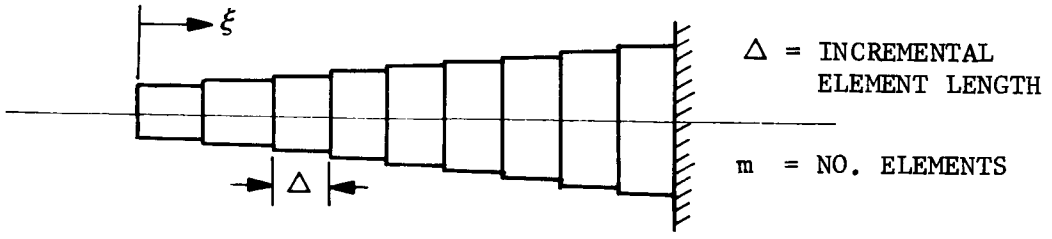

The deflection is obtained by summing the contribution due to each element

$$\delta_1 = \frac{a\Omega^2 \cos\phi}{24\,E} \sum_{i=1}^{m} \frac{\rho_i}{I_i} \left[3\xi^4 - 4x\xi^3 \right]_{\xi_i}^{(\xi_i + \Delta)} \tag{32}$$

$$\theta_1 = \frac{a\Omega^2 \cos\phi}{6E} \sum_{i=1}^{m} \frac{\rho_i}{I_i} \left[\xi^3 \right]_{\xi_i}^{(\xi_i + \Delta)} \tag{33}$$

$$\delta_2 = \frac{\Omega^2 \sin\phi \cos\phi}{120\,E} \sum_{i=1}^{m} \frac{\rho_i}{I_i} \left[-4\xi^5 + 15L\xi^4 - 20xL\xi^3 + 5x\xi^4 \right]_{\xi_i}^{(\xi_i + \Delta)} \tag{34}$$

$$\theta_2 = \frac{\Omega^2 \sin\phi \cos\phi}{24\,E} \sum_{i=1}^{m} \frac{\rho_i}{I_i} \left[4L\xi^3 - \xi^4 \right]_{\xi_i}^{(\xi_i + \Delta)} \tag{35}$$

NOTE: The equations in this section assumes a linear mass distribution. This may or may not be true in the practical case depending on how the beam is designed. However, in the configuration now under consideration, the lateral loading is almost linearly varying.

Upon closer examination of Equations (32), (33), (34), and (35) one sees that the deflections and rotations are dependent on the ratio of density to moment of inertia for each element and some function of the beam length.

Hence

$$(\delta,\theta) = f_1(\xi,L) \sum_{i=1}^{m} \frac{\rho_i}{I_i} \tag{36}$$

To get a feel for how deflections and rotations are influenced by the taper consider a honeycomb beam of width b, height h, and skin thickness t.

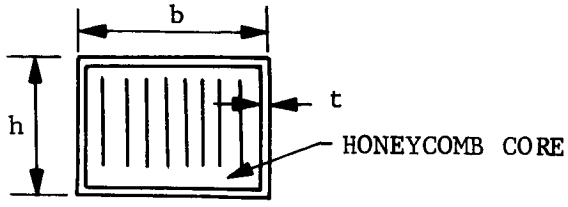

For such a section the mass per unit length, ρ, is

$$\rho = \rho_{skin} + \rho_{core}$$

$$\rho = \gamma_{skin}(h + b)2t + \gamma_{core}bh \tag{37}$$

If $\rho_{core} \ll \rho_{skin}$ and $b \approx h$ and if t is constant along the length of the beam, we can say

$$\rho = f_2(h) \tag{38}$$

where f_2 is some function. The moment of inertia of the section is given by

$$I = \frac{2th^3}{12} + \frac{bth^2}{2} \tag{39}$$

Again for $b \approx h$, and constant t along the beam length

$$I = f_3(h^3) \tag{40}$$

Using Equations (36), (37), and (40) one can deduce from this approximation that beam deflections and rotations vary as $1/h^2$.

$$(\delta,\theta) = f_1(\xi,L)\ g_1\left(\frac{1}{h^2}\right) \tag{41}$$

g_1 is another function.

Let us take a closer look at functions $f_1(\xi,L)$ and $g_1(1/h^2)$ in Eq. (41). Consider for the moment, only the deflection δ_1 due to lateral load p_{N_1}. Consider in particular, only the contribution to δ_1 of the j-th element of the beam. Thus, if the limits are substituted into Eq. (32) choosing Δ small,

$$\delta_1(j) = \frac{a\Omega^2\cos\phi}{24\ E}\ \frac{\rho_j}{I_j}\left[3(j+\Delta)^4 - 3j^4 - 4x(j+\Delta)^3 - 4xj^3\right].$$

At the free end of the cantilever $x = 0$, and

$$\delta_1(j)\big|_{x=0} = \frac{a\Omega^2\cos\phi}{24\ E}\ \frac{\rho_j}{I_j}\ 3\left[(j+\Delta)^4 - j^4\right]$$

Expanding into binominal series

$$(j+\Delta)^4 - j^4 = \cancel{\Delta^4}^{0} + 4\cancel{\Delta^3}^{0}j + 6\cancel{\Delta^2}^{0}j^2 + 4\Delta j^3 \cong 4\Delta j^3$$

Substituting this into Eq. (41) we find δ_1 at the free end due to the j-th element a function of j^3/h^2.

$$\delta_1(j)\big|_{x=0} = g\left(\frac{j^3}{h^2}\right)$$

Hence for optimum distribution of material in the beam to minimize deflection at the tip the depth of the beam h should increase as $\xi^{3/2}$. Obviously this would lead to a beam which is deeper than it is long. We could continue and develop a similar expression for δ_2, but at this point we will not pursue the optimum beam any further because:

a. A "beam" of such proportiona no longer can be treated by beam theory.

b. Such a structure would be impractical for our application.

We will pursue a practical tapered beam with reasonable proportions.

1.3.4 Stresses and Elongation Due to Longitudinal Loading on Tapered Beam

$$P = \Omega^2 \sum_{i=1}^{n} \rho_i \left[a\xi \sin\phi + \left(L\xi - \frac{\xi^2}{2}\right)\sin^2\phi\right]_{\xi_i}^{(\xi_i + \Delta)} \tag{42}$$

$$\sigma = \Omega^2 \sum_{i=1}^{n} \frac{\rho_i}{A_i} \left[a\xi \sin\phi + \left(L\xi - \frac{\xi^2}{2}\right)\sin^2\phi\right]_{\xi_i}^{(\xi_i + \Delta)} \tag{43}$$

where n = number of elements between section x and the free end

m = total number of elements

$$\delta = \frac{\Omega^2}{E} \sum_{i=n}^{m} \frac{\Delta_i}{A_i} \sum_{i=1}^{n} \rho_i \left[a\xi \sin\phi + \left(L\xi - \frac{\xi^2}{2}\right)\sin^2\phi\right]_{\xi_i}^{(\xi_i + \Delta)} \tag{44}$$

1.3.5 Investigation of Preliminary Design with Constant Cross Section

As a first try at a cantilever boom antenna we chose a honeycomb beam of constant cross section as shown in the sketch. This will serve as a check on the equations derived in Sections 1.3 to 1.3.4 and will also indicate whether reasonable stresses and deflections are possible with a structure of this type for our particular application.

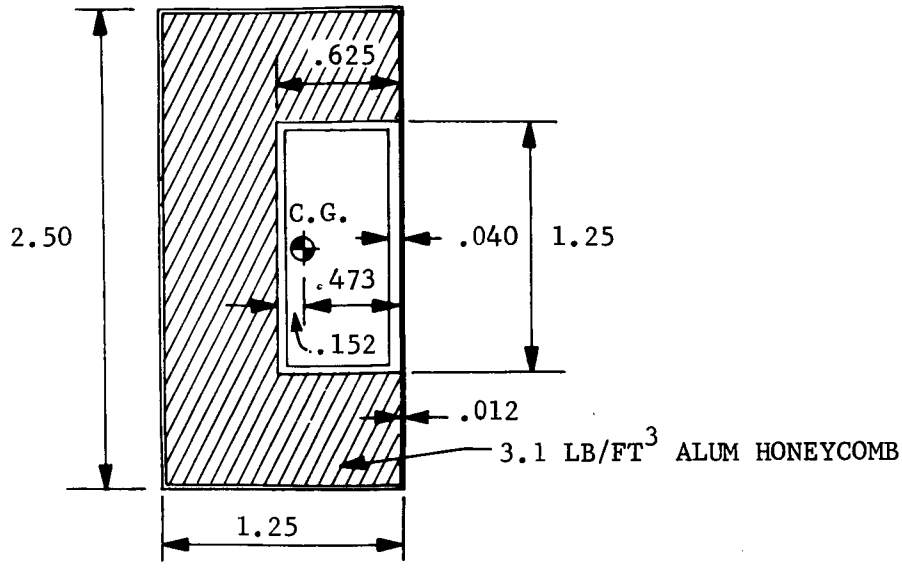

Calculation of center of gravity

$$C.G. = \frac{-.625(1.25)(\frac{3}{1728})(1)(.312) + 2(.625)(.040)(.10)(.312) + (1.35)(.040)(.10)(.625)}{.0287}$$

$$C.G. = \frac{.004262}{.02807} = .152" \text{ measured from center line.}$$

Calculation of section properties:

$$I = .024(1.25)(1.25)^2 + .080(.625)(.625)^2 + \frac{.024(2.5)^3}{12} + \frac{.080(1.25)^3}{12}$$

$$I = .1107 \text{ in}^4$$

$$Z = \frac{.1107}{.125} = .0886 \text{ in}^3$$

$$A_{skin} = .024(1.25 + 2.50) + .080(.625 + 1.25) = .240 \text{ in}^2$$

$$A_{core} = 2.5(1.25) - .625(1.25) = 2.344 \text{ in}^2$$

$$w = .1(.240) + \frac{3}{1728}(2.344) = .02807 \text{ lb/in}$$

$$\rho = \frac{w}{386} \text{ lb-sec}^2$$

The lateral deflection is given by Equations (20 and (24).

$$\delta = \frac{\rho a \Omega^2 \cos \phi}{24 EI}(x^4 - 4L^3x + 3L^4) + \frac{\rho \Omega^2 \sin \phi \cos \phi}{120 EI}(11L^5 - 15L^4x + 5Lx^4 - x^5)$$

Assume $\phi = 45^o$; a = 15" and let $E = 10^7$

$$\delta = \frac{.02807(15)(.707)\Omega^2}{386(24)(10^7)(.1107)}(x^4 - 4L^3x + 3L^4)$$

$$+ \frac{.02807(.50)\Omega^2}{386(120)(10^7)(.1107)}(11L^5 - 15L^4x + 5Lx^4 - x^5)$$

$$\delta = .2902 \times 10^{-10}\Omega^2 (x^4 - 4L^3x + 3L^4)$$

$$+ .2737 \times 10^{-12}\Omega^2(11L^5 - 15L^4x + 5Lx^4 - x^5) \qquad (45)$$

The maximum lateral deflection occurs at x = 0, and is

$$\delta_{max} = (.8706 \times 10^{-10}L^4 + .03011 \times 10^{-10} L^5)\ \Omega^2 \qquad (46)$$

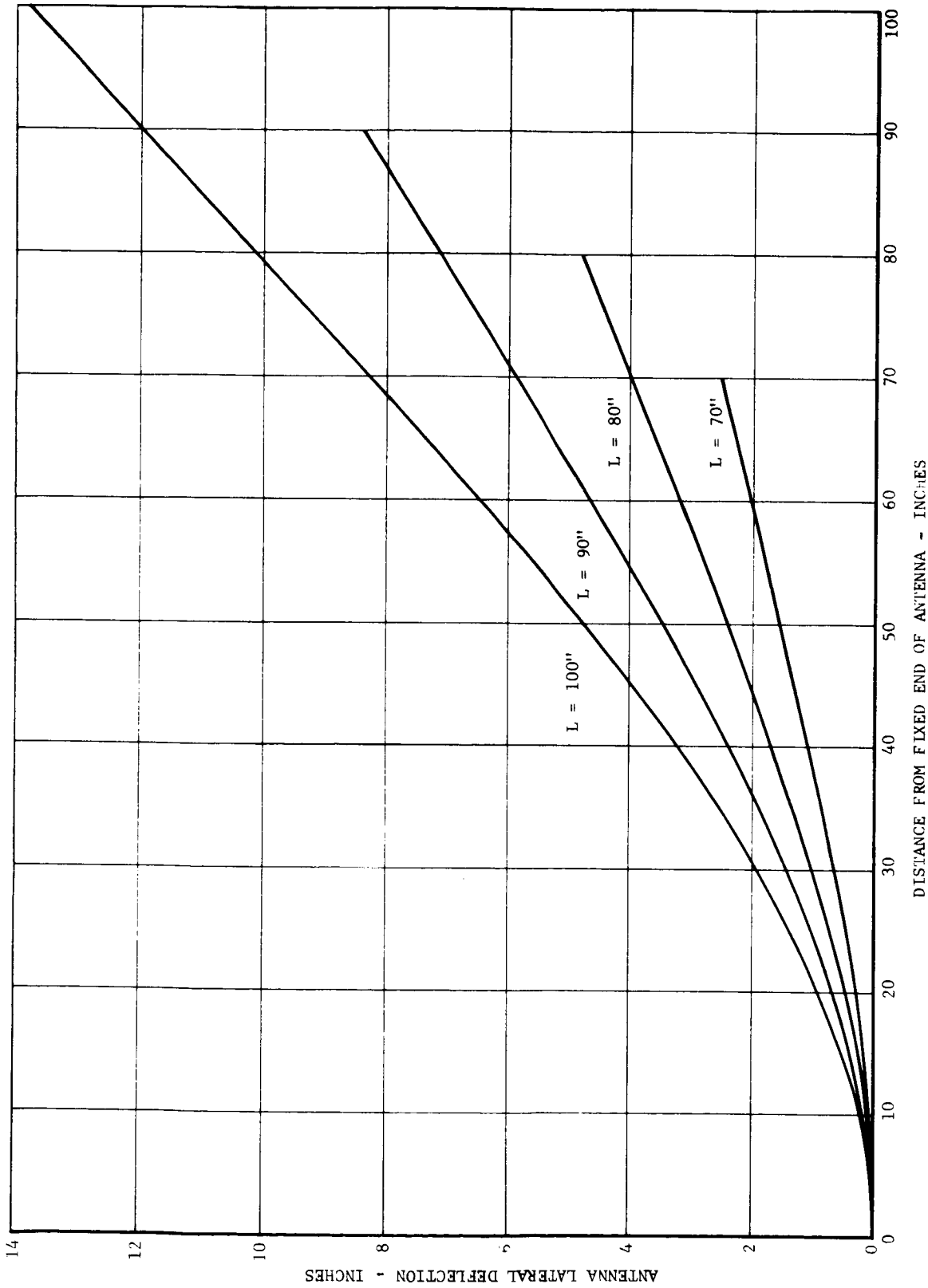

Figure 1-1 Antenna Lateral Deflection at Spin Rate Ω = 180 rpm

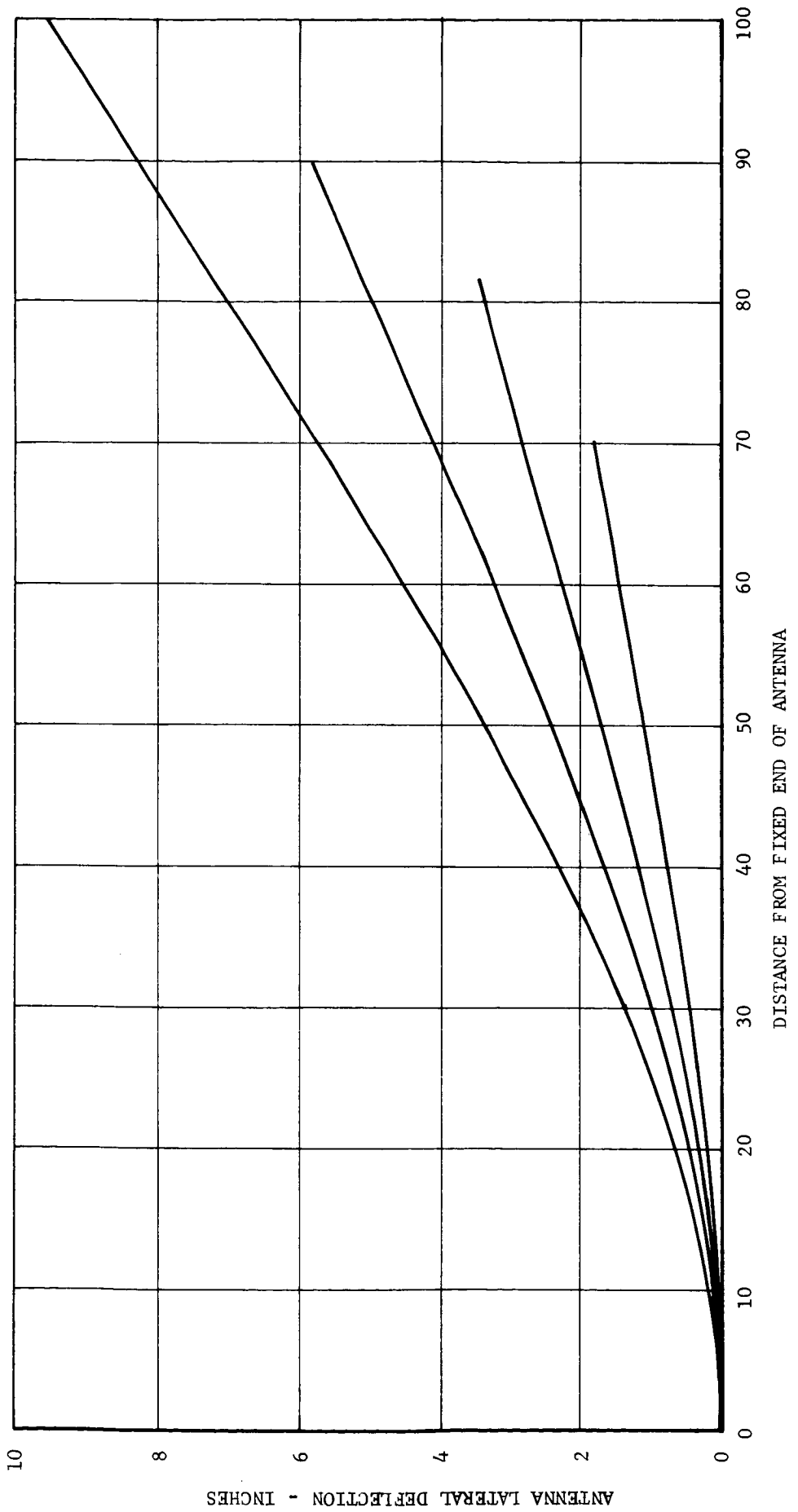

Figure 1-2 Antenna Lateral Deflection At Spin Rate Ω = 150 rpm

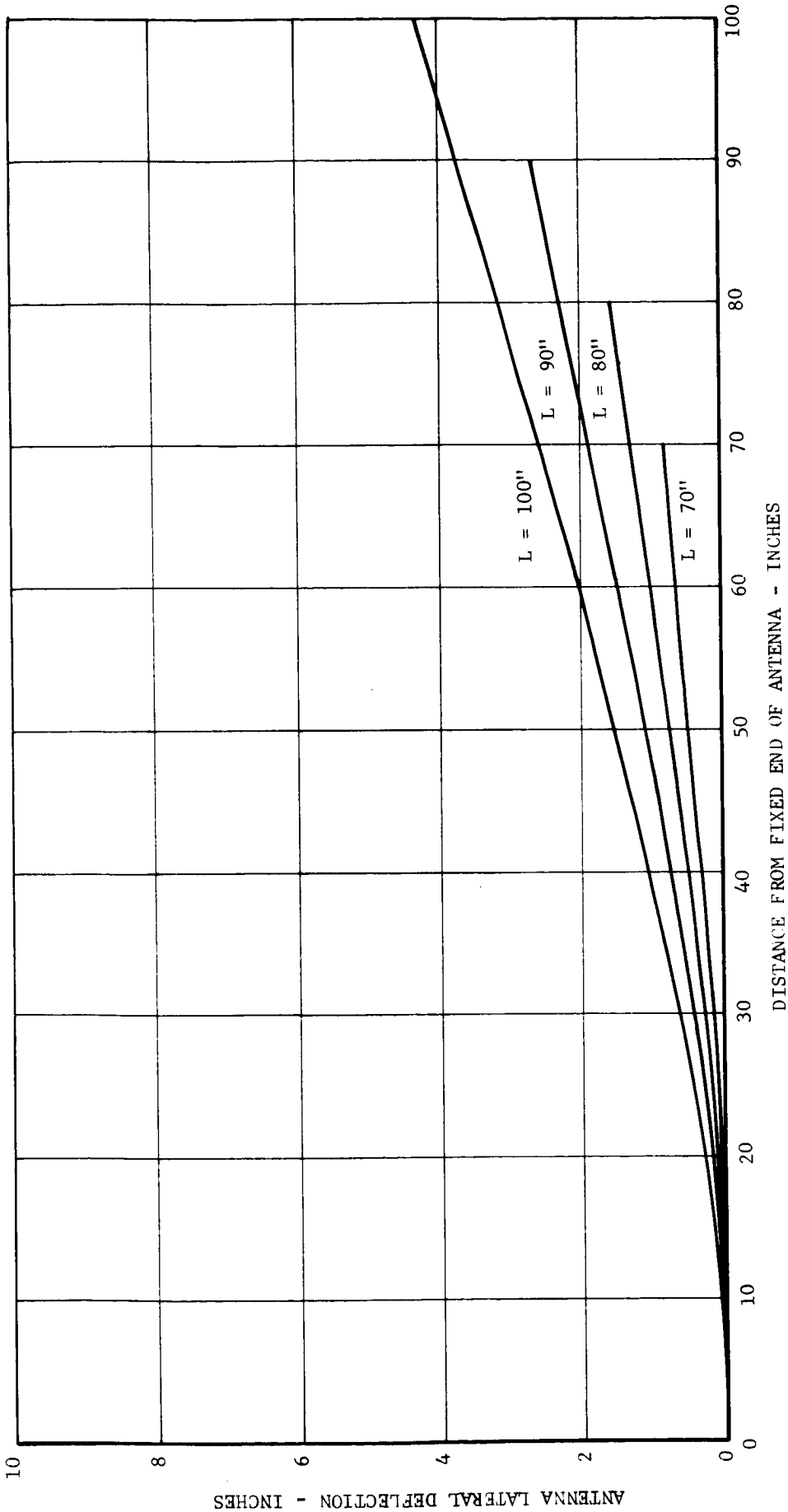

Figure 1-3 Antenna Lateral Deflection at Spin Rate Ω = 100 rpm

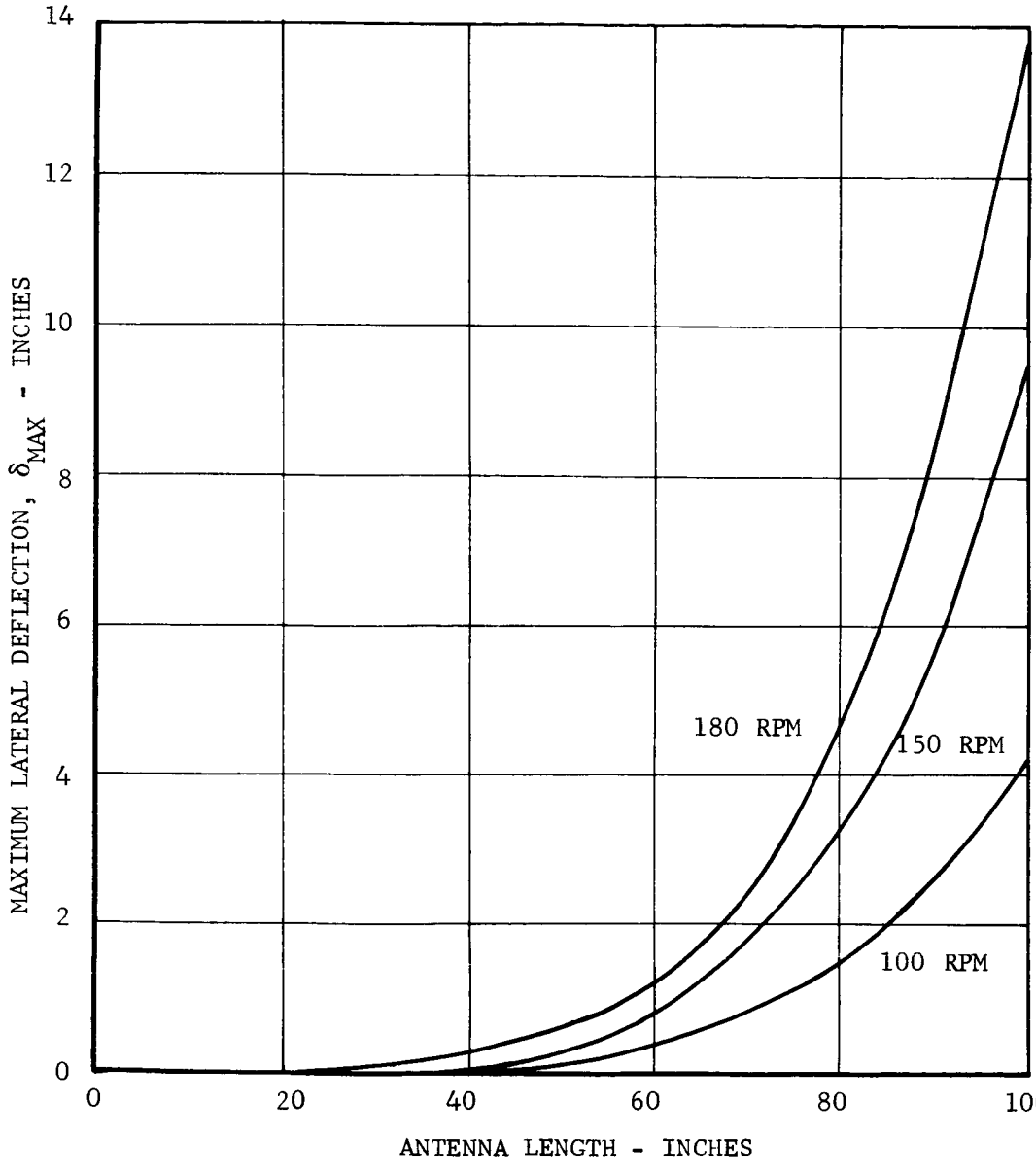

Figure 1-4 Maximum Lateral Deflection for Various Antenna Lengths and Spin Rates

The maximum bending stress occurs at the fixed end and is

$$\sigma_{max} = \frac{\rho \cos \phi \, L^2 \Omega^2}{Z} \left(\frac{a}{2} + \frac{L}{3} \sin \phi \right)$$

$$\sigma_{max} = \frac{.02807(.707)L^2\Omega^2}{386(.0886)} \left(\frac{15}{2} + \frac{L}{3} (.707) \right)$$

The stress is shown in Figure 1-5 for various antenna lengths and spin rates.

The curves in Figure 1-5 shows that bending stresses are rather high. In addition, axial stresses will be superimposed. To get an idea of an upper bound we will calculate the axial stresses at three spin rates for an antenna length of 100 inches.

$$\sigma_{max} = \frac{\rho \Omega^2}{A} \sin \phi \; (aL + \frac{L^2}{2} \sin \phi)$$

For a = 15; L = 100

$$\sigma_{max} = \frac{.02087 \; \Omega^2}{386(.240)} (.707)(1500 + 5000(.707))$$

$$\sigma_{max} = 0.8019 \; \Omega^2$$

For 100 rpm: σ_{max} = 87.9 psi

For 150 rpm: σ_{max} = 197.8 psi

For 180 rpm: σ_{max} = 284.9 psi

It is apparent that axial stresses are small compared to bending stresses. Although bending stresses are high they can be reduced by making the cross section deeper or wider.

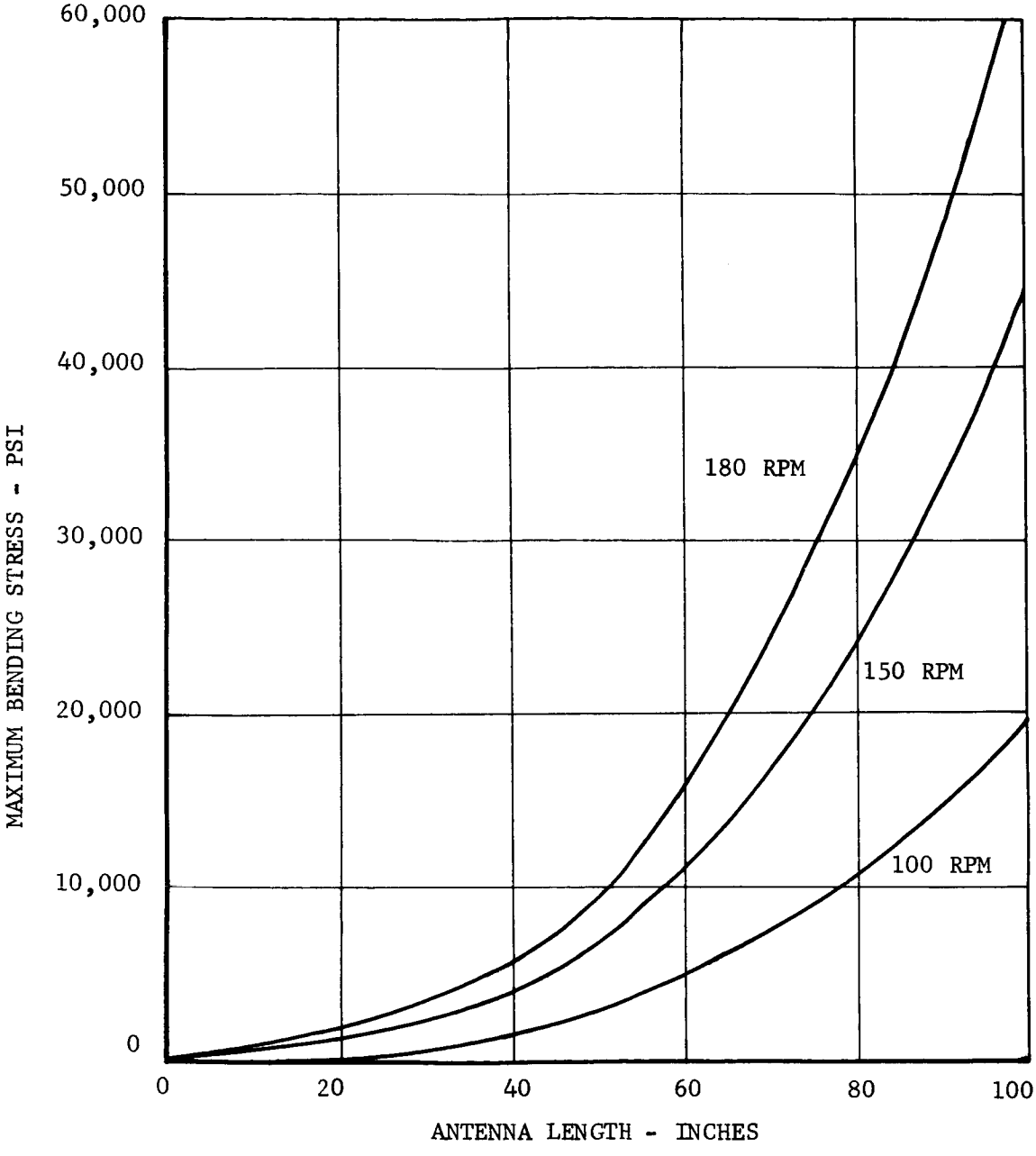

Figure 1-5 Bending Stress Versus Antenna Length

In general, shear stresses in honeycomb sandwich beams are normally carried by the core. However, because of the odd shape of the cross section under consideration we should take a closer look at shear stresses.

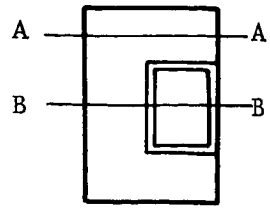

We know that the shear stress, τ, is given by

$$\tau = G\gamma$$

where

G = shear modulus

γ = shear strain

Hence the shear force is

$$F = G \gamma A$$

If a unit shear strain is applied to the cross section the shear forces in the core and facing are an indication of the relative shear stiffnesses of the two components. Representative values of shear modulus for 3.1 lb/ft^3 core of 5052 or 5056 aluminum are shown below.

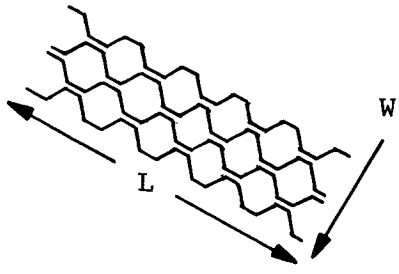

	Typical	Minimum
L Direction	41,800 psi	32,000
W Direction	22,000	16,000

For an average value of shear modulus choose G_c = 28,000 psi

Section A-A For unit slice dx

$$F_{facing} = G_F\gamma\ A_F = 3.85 \times 10^6(1)(.024 \times 1) = .0924 \times 10^6 \text{ lb/in}$$

$$F_{core} = G_C\gamma\ A_C = 28{,}000(1)(1.25 \times 1) = .0350 \times 10^6 \text{ lb/in}$$

Section B-B For unit slice dx

Assume all facing shear stress is carried by outer skins.

$$F_{facing} = 3.85 \times 10^6(1)(.052 \times 1) = .2002 \times 10^6 \text{ lb/in}$$

$$F_{core} = 28{,}000(1)(.625 \times 1) = .0175 \times 10^6 \text{ lb/in}$$

The above calculations assume a uniform distirbution of shear stress within the facing and core. Actually there will be some warping of the cross section thereby causing some deviation from uniformity. This actual distribution cannot be predicted by elementry beam theory. However it is apparent in Section B-B that all the shear is carried in the facing. In Section A-A approximately 75 percent of the shear is carried in the facing. For these preliminary calculations we will assume that all shear is carried by the facings and that the core serves only to support the facings.

The maximum shear force is

$$V_{max} = \rho\Omega^2 \cos\phi\left(aL + \frac{L^2}{2}\sin\phi\right)$$

For 180 rpm, Ω = 18.85 rad/sec, and L = 100"

$$V_{max} = \frac{(.02087)(18.85)^2(.707)}{386}(1500 + 5000(.707))$$

$$V_{max} = 68.387 \text{ lb}$$

As an approximation of the maximum bending shear stress we can assume that all the shear force is carried in the side facings. This should be an upper bound number

$$\tau_{approx} = \frac{V}{2ht_f} = \frac{68,387}{2(2.5)(.012)} = 1140 \text{ psi}$$

The shear stresses will be examined in more detail below.

In the following paragraphs the shear distribution in the facings and the shear center will be determined.[2] Shown below is the assumed shear flow directions for the cut-back section.

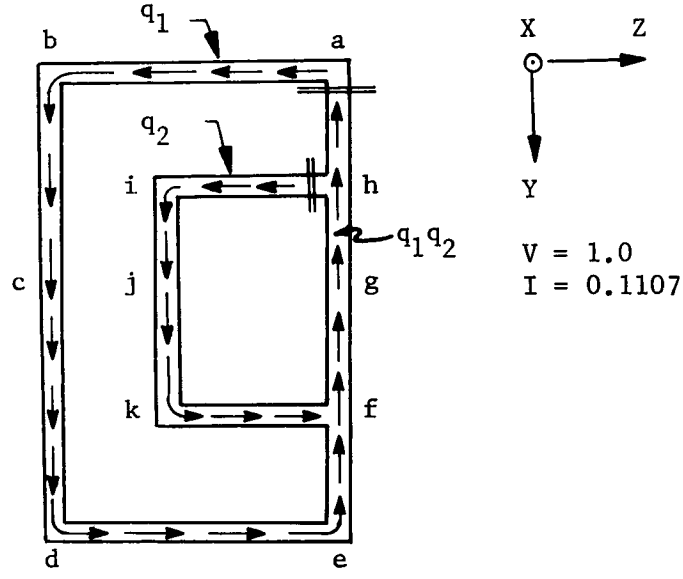

$$q_x = \frac{V_Y}{I_Z} \sum Z\ A = \frac{1.0}{0.1107} \sum ZA$$

$$q = 9.0334 \sum ZA$$

[2] Bruhn, E.F., "Analysis and Design of Flight Vehicle Structures," Tri-State Offset Co., Cincinnati, Ohio.

Starting at point a,

$q_b = 9.0334(1.25)(1.25 \times .012) = .1694$ lb/in

$q_c = .1694 + 9.0334(.625)(1.25 \times .012) = .2541$ lb/in

$q_a = .2541 + 9.0334(-.625)(1.25 \times .012) = .1694$ lb/in

$q_e = .1694 + 9.0334(-1.25)(1.25 \times .012) = 0$

$q_f = 0 + 9.0334(-.9375)(.625 \times .012) = -.0635$ lb/in

Starting at point h,

$q_i = 9.0334(.625)(.625 \times .040) = .1411$

$q_j = .1411 + 9.0334(.3125)(.625 \times .040) = .2117$ lb/in

$q_k = .2117 + 9.0334(-.3125)(.625 + .040) = .1411$ lb/in

$q_f = .1411 + 9.0334(-.625)(.625 \times .040) = 0$

$q_g = -.0635 + 9.0334(-.3125)(.625 \times .052) = -.1552$

$q_h = -.1552 + 9.0334(.3125)(.625 \times .052 = -.0635$

$q_a = -.0635 + 9.0334(.9375)(.625 \times .012) = 0$

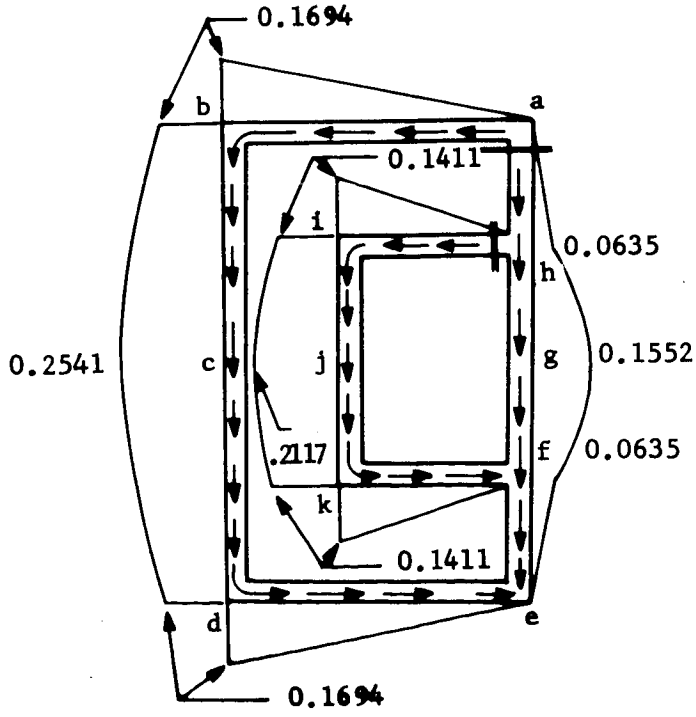

Cut-back Shear Flow Pattern

This cut-back shear flow pattern is obtained by assuming zero shear flow at points a and h so that the problem is reduced or cut-back to one that is statically determinate. We must now determine the two redundant shear flows and superimpose them on the shear flow above.

The equation for angular twist per unit length, θ, is

$$2\,AG\,\theta = \sum q\,\frac{L}{t}$$

A = enclosed area
G = shear modulus
L = length of shear flow data
t = thickness

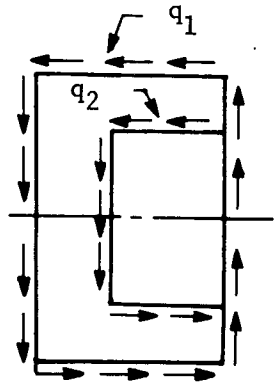

$$A_1 = 2.50 \times 1.25 = 3.125$$

$$A_2 = 1.25 \times .625 = 0.78125$$

$$2A_1G\theta_1 = \left[\frac{.1694}{2}\left(\frac{1.25}{.012}\right) + .1694\left(\frac{1.25}{.012}\right) + \frac{2x.0847}{3}\left(\frac{1.25}{.012}\right) - \frac{.0635}{2}\left(\frac{.625}{.012}\right) - .0635\left(\frac{.625}{.012}\right) - \frac{2x.0917}{3}\left(\frac{.625}{.052}\right)\right] 2 + q_1\left(\frac{6.25}{.012}\right) + (q_1 + q_2)\left(\frac{1.25}{.052}\right)$$

$$2A_1G\theta_1 = 53.3114 + 544.8718\,q_1 + 24.0385\,q_2 \qquad (47)$$

$$2A_2G\theta_2 = \left[\frac{.1411}{2}\left(\frac{.625}{9040}\right) + .1411\left(\frac{.625}{.040}\right) - .0635\left(\frac{.625}{.052}\right) - \frac{2x.091}{3}\left(\frac{.625}{.052}\right)\right]2 + q_2\left(\frac{2.50}{.040}\right) + (q_1 + q_2)\left(\frac{1.25}{.052}\right)$$

$$2A_2G\theta_2 = 1.8098 + 24.038\,q_1 + 86.538\,q_2 \qquad (48)$$

If the load is applied through the shear center, θ is zero and hence Equations (47) and (48) reduce to

$$544.8718\ q_1 + 24.0385\ q_2 = -53.3114 \qquad (49)$$

$$24.038\ q_1 + 86.538\ q_2 = -1.8098 \qquad (50)$$

Solving Equations (49) and (50),

$$q_1 = -.0981 \text{ lb/in}$$

$$q_2 = .006342 \text{ lb/in}$$

Check: $24.038(-.09812) + 86.538(.006342) = -1.8058$

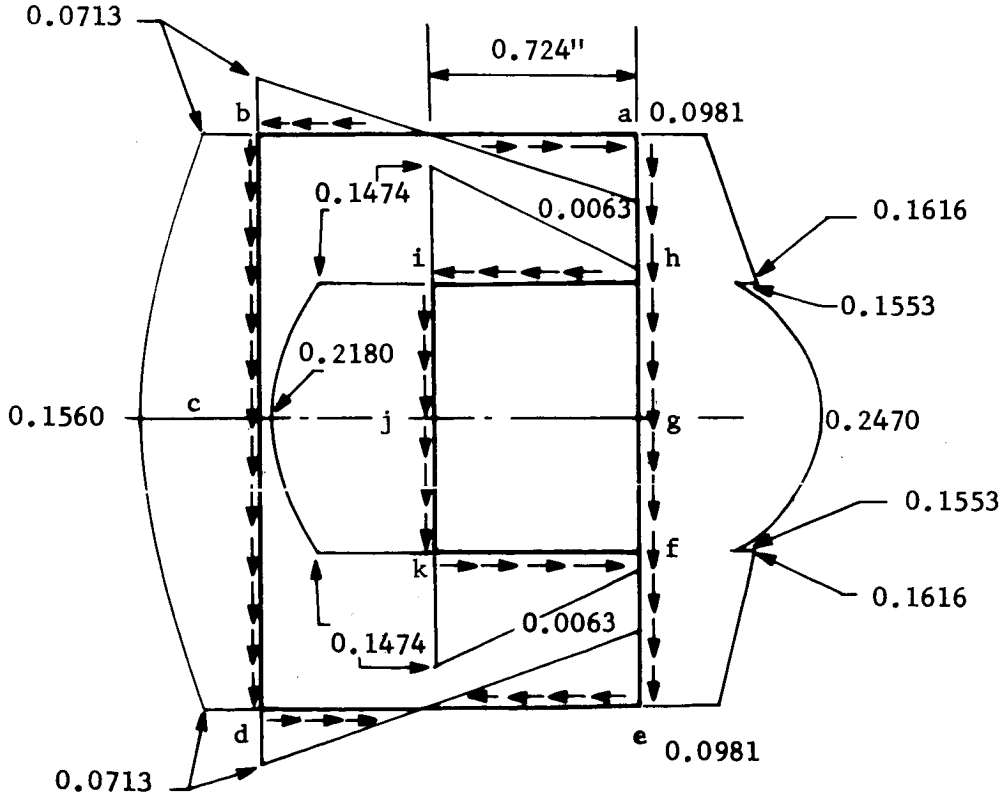

Actual Shear Flow Pattern

Check: ΣV

$$.0713(2.50) + .0847(\tfrac{2}{3})(2.50) + .1474(1.25) + .0706(\tfrac{2}{3})(1.25)$$
$$+ .0981(1.25) + .0635(\tfrac{1}{2})(1.25) + .1553(1.25)$$
$$+ .0917(\tfrac{2}{3})(1.25) = .9954 \approx 1.0$$

The exact shear stress distribution has now been established for a unit shear force. From Page 37 the maximum shear force for an antenna of 100 inch spinning at 180 rpm is $V_{max} = 68.387$ lb.

Hence, the maximum shear stress is

$$\tau_h = \frac{.1616(68.387)}{.012} = 920.9 \text{ psi} \longleftarrow \text{max}$$

$$\tau_g = \frac{.2470(68.387)}{.052} = 324.8 \text{ psi}$$

$$\tau_j = \frac{.2180(68.387)}{.040} = 372.7 \text{ psi}$$

The moment of the shear flows about an arbitrary point must be balanced by the moment of the externally applied point g,

$$2(.1474)(\tfrac{1}{2})(.625)(.625) + (.1843 + .0688)(.625) - 2(.0981)(\tfrac{1}{2})(.724)(1.25)$$
$$+ 2(.0713)(\tfrac{1}{2})(.526)(1.25) + .1783(1.25)$$
$$+(.1412)(1.25) = e'$$

$$e' = .5670"$$

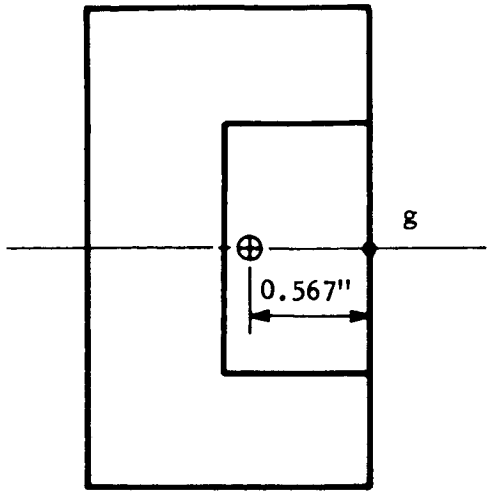

Shear Center Location

From Page 27, C. G. is located at .473" from point g. Hence, inertial loads on the antenna would be applied at an offset of (.567 - .473) or approximately .10 inches. This offset causes torsional stresses and deflections.

We will now determine the torsional stiffness of this section. Recall Equations (47) and (48) which are rewritten below.

$$2G\theta_1 = 17.0596 + 174.359\ q_1 + 7.6932\ q_2 \qquad (51)$$

$$2G\theta_2 = 2.3163 + 30.766\ q_1 + 110.761\ q_2 \qquad (52)$$

But $\theta_1 = \theta_2$. Equating and solving,

$$q_2 = \frac{14.7433 + 143.593\ q_1}{103.069}$$

Substituting into Eq. (51) yields

$$7.70 \times 10^6\ \theta = 18.160 + 185.077\ q_1$$

For a unit rotation

$$q_1 = 0.41604 \times 10^5$$

Now substitute into the torque equation

$$T = 2A_1q_1 + 2A_2q_2$$

$$T = 2(3.125)(.4160 \times 10^5) + 2(.7813)\left(\frac{14.7433 + 143.593(.3150 \times 10^5)}{103.069}\right)$$

$$T = 0.3505 \times 10^6 \text{ lb-in/rad/in} \qquad \text{Torsional stiffness}$$

As a rough check consider a simple rectangular section as shown

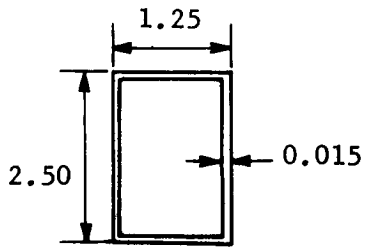

$$K = \frac{2t^2(a-t)^2(b-t)^2}{at + bt - 2t^2} \cong \frac{2t\,a^2b^2}{a+b}$$

$$= \frac{2(.015)(1.25)^2(2.50)^2}{3.75} = .07812$$

$$T = KG\theta = .07812(3.85 \times 10^6)(1) = .3008 \times 10^6$$

To get an idea of the magnitude of the torsional rotations, consider an upper bound torque of

$$T_{U.B.} = V_{max}\, e$$

$$T_{U.B.} = 68.387(.10) = 6.8387 \text{ lb-in}$$

If this torque is applied at the tip,

$$\Theta = \frac{TL}{KG} = \frac{6.8387(100)}{.3505 \times 10^6}$$

$$\Theta = .001954 \text{ rad} = .112^\circ$$

Hence, torsional distortions of the antenna are small compared to bending deflections. We will not derive the exact torsional equations.

1.4 STRESSES AND DEFLECTIONS OF GUYED RECTANGULAR HONEYCOMB BOOM ANTENNAS

In this section we will investigat boom antennas which are fixed at one end, free at the other, and supported at intermediate points by guy wires. As a start, we will consider a beam guyed by a single cable which is rigid compared to the beam. Hence the problem reduces to one of a propped beam.

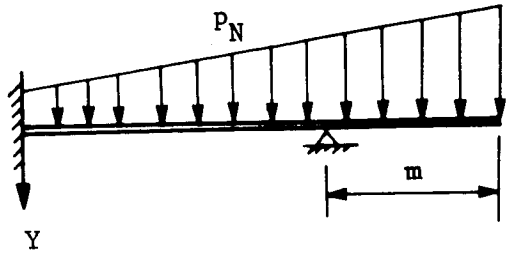

We can solve this problem by superimposing upon the results obtained in Section 1.3, those deflections and stresses due to a concentrated reaction R.

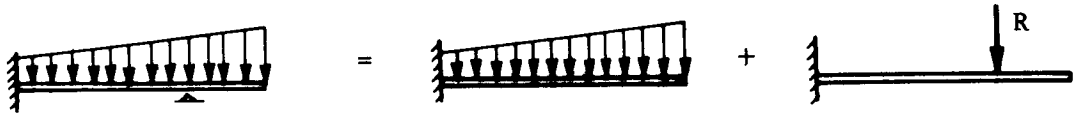

Consider the cantilevered beam loaded with reaction R.

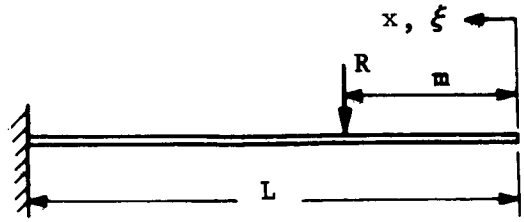

For $0 \le x \le m$:

$$\delta = \frac{1}{EI}\int_m^L R(\xi - m)(\xi - x)d\xi = \frac{R}{EI}\left[\frac{\xi^3}{3} - \frac{m\xi^2}{2} - \frac{x\xi^2}{2} + mx\xi\right]_m^L$$

$$\delta = \frac{R}{EI}\left[\frac{L^3}{3} - \frac{m^3}{3} - \frac{mL^2}{2} + \frac{m^3}{2} - \frac{xL^2}{2} + \frac{xm^2}{2} + mxL - m^2x\right]$$

$$\delta = \frac{R}{EI}\left[\frac{L^3}{3} - \frac{mL^2}{2} - \frac{xL^2}{2} + mxL - \frac{mx^2}{2} + \frac{m^3}{6}\right] \qquad (53)$$

$$\theta = \frac{1}{EI}\int_m^L R(\xi - m)d\xi = \frac{R}{EI}\left[\frac{\xi^2}{2} - m\xi\right]_m^L$$

$$\theta = \frac{R}{EI}\left[\frac{L^2}{2} - mL + \frac{m^2}{2}\right] \qquad (54)$$

For $m \le x \le L$:

$$\delta = \frac{1}{EI}\int_x^L R(\xi - m)(\xi - x)d\xi = \frac{R}{EI}\left[\frac{\xi^3}{3} - \frac{m\xi^2}{2} - \frac{x\xi^2}{2} + mx\xi\right]_x^L$$

$$\delta = \frac{R}{EI}\left[\frac{L^3}{3} - \frac{mL^2}{2} - \frac{xL^2}{2} + mxL - \frac{mx^2}{2} + \frac{x^3}{6}\right] \qquad (55)$$

$$\theta = \frac{R}{EI}\left[\frac{L^2}{2} - mL + mx - \frac{x^2}{2}\right] \qquad (56)$$

Superimposing results from Section 1.3.1, the deflections and rotations for the propped beam are:

For $0 \le x \le m$:

$$\delta = \frac{\rho a\Omega^2 \cos\phi}{24\,EI}(x^4 - 4L^3x + 3L^4) + \frac{\rho\Omega^2 \sin\phi\cos\phi}{120\,EI}(11L^5 - 15L^4x + 5Lx^4 - x^5)$$

$$+ \frac{R}{6EI}(2L^3 - 3mL^2 - 3xL^2 + 6mxL - 3mx^2 + m^3) \qquad (57)$$

$$\theta = \frac{\rho a\Omega^2 \cos\phi}{6\,EI}(L^3 - x^3) + \frac{\rho\Omega^2 \sin\phi\cos\phi}{24\,EI}(3L^4 - 4Lx^3 + x^4)$$

$$+ \frac{R}{2EI}(L^2 - 2mL + m^2) \qquad (58)$$

For $m \le x \le L$:

$$\delta = \frac{\rho a\Omega^2 \cos\phi}{24\,EI}(x^4 - 4L^3x + 3L^4) + \frac{\rho\Omega^2 \sin\phi\cos\phi}{120\,EI}(11L^5 - 15L^4x + 5Lx^4 - x^5)$$

$$+ \frac{R}{6EI}(2L^3 - 3mL^2 - 3xL^2 + 6mxL - 3mx^2 + x^3) \qquad (59)$$

$$\theta = \frac{\rho a\Omega^2 \cos\phi}{6\,EI}(L^3 - x^3) + \frac{\rho\Omega^2 \sin\phi\cos\phi}{24\,EI}(3L^4 - 4Lx^3 + x^4)$$

$$+ \frac{R}{2EI}(L^2 - 2mL + 2mx - x^2) \qquad (60)$$

The redundant R is obtained by requiring $\delta = 0$ at $x = m$ in either of Equations (57) or (61)

$$\delta\big|_{x=m} = \frac{\rho a\Omega^2 \cos\phi}{24\,EI}(m^4 - 4L^3m + 3L^4) + \frac{\rho\Omega^2 \sin\phi\cos\phi}{120\,EI}(11L^5 - 15L^4m + 5Lm^4 - m^5)$$

$$+ \frac{R}{6EI}(2L^3 - 6mL^2 + 6m^2L - 2m^3) \overset{\text{set}}{=} 0 \qquad (61)$$

$$R = -\frac{\rho a\Omega^2 \cos\phi}{8}\left(\frac{m^4 - 4L^3m + 3L^4}{L^3 - 3mL^2 + 3m^2L - m^3}\right)$$

$$-\frac{\rho\Omega^2 \sin\phi\cos\phi}{40\,EI}\left(\frac{11L^5 - 15L^4m + 5Lm^4 - m^5}{L^3 - 3mL^2 + 3m^2L - m^3}\right) \qquad (62)$$

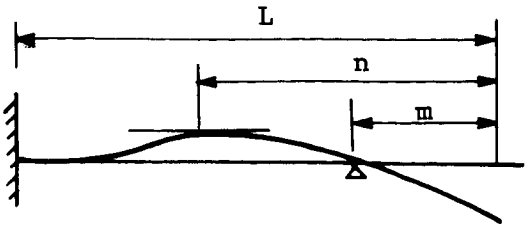

Deflected shape of propped beam

We now have sufficient equations to determine the optimum distance m to minimize the deflections in the antenna. If we desired we could effect a solution by trial and error as follows:

a. Choose a distance m and determine redundant R from Eq. (62).
b. Determine distance n from Eq. (60) such that $\theta = 0$ and $n \neq L$.
c. Solve for deflection δ_n at n from Eq. (59).
d. Solve for deflection δ_o at $x = 0$ from Eq. (57).
e. Compare δ_n and δ_o and pick a new m to adjust deflections so that they are equal.
f. Repeat cycle.

In this fashion we could place the rigid guy wire to provide the least deflection. However, these equations are somewhat unwieldy. Hence we will solve this problem with the aid of a structural analysis program on the digital computer in Section 1.4.1.

1.4.1 Computer Solution for Optimum Placement of Single Guywire

In Section 1.4 a method was outlined for determining the optimum placement of a prop by hand computation. With our present capability in automated analysis, this problem was easily solved on the digital computer. Four lengths of propped antennas were investigated (100 inch, 90 inch, 80 inch, and 70 inch). The computer models were made so that each antenna was composed of a number of two-inch elements as shown below. For convenience the origin of x has been moved to the fixed end.

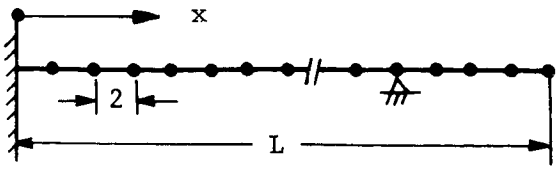

Computer Model

Each antenna was analyzed for the centrifugal loading with the prop at several locations along the length of the antenna. The resulting deflected shapes are shown in Figures 1-6, 1-7, 1-8, and 1-9. Observe that the deflected shapes are quite sensitive to location of the prop. In order to determine the optimum placement of the prop for each antenna length, Figure 1-10 was plotted. In this figure, the absolute maximum tip deflections and interior span deflections are shown as a function of prop location. Hence the intersection of the two deflection curves would indicate the optimum location of the prop for minimum deflections. Note that in all four cases the optimum prop location was very close to 75 percent of the total length. Deflections are two orders of magnitude smaller than those of the cantilevered antenna; all deflections are less than .10 inch.

1.4.2 Computer Model "B" of Propped Antenna

In Section 1.4.1 the optimum prop location was presented for several lengths of antennas. However, the results in that form was inconvient for J. Patmore to use. In this section we will revise our structural model (B) so that the joints in the model coincide with the center of the slots in the antenna. Model "B" will have 98 elements of 0.97866 inch each to make up a total length of 95.909 inches. Choosing the optimum prop distance of ~ 75 percent of the length, the prop is placed at x = 72.421 inches.

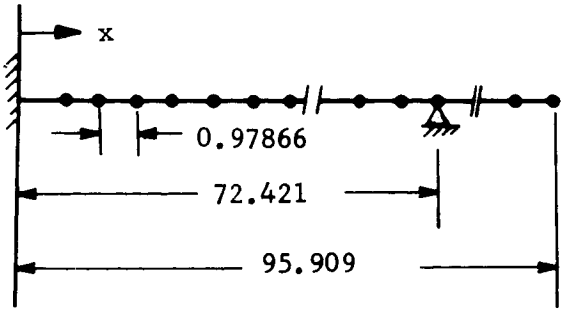

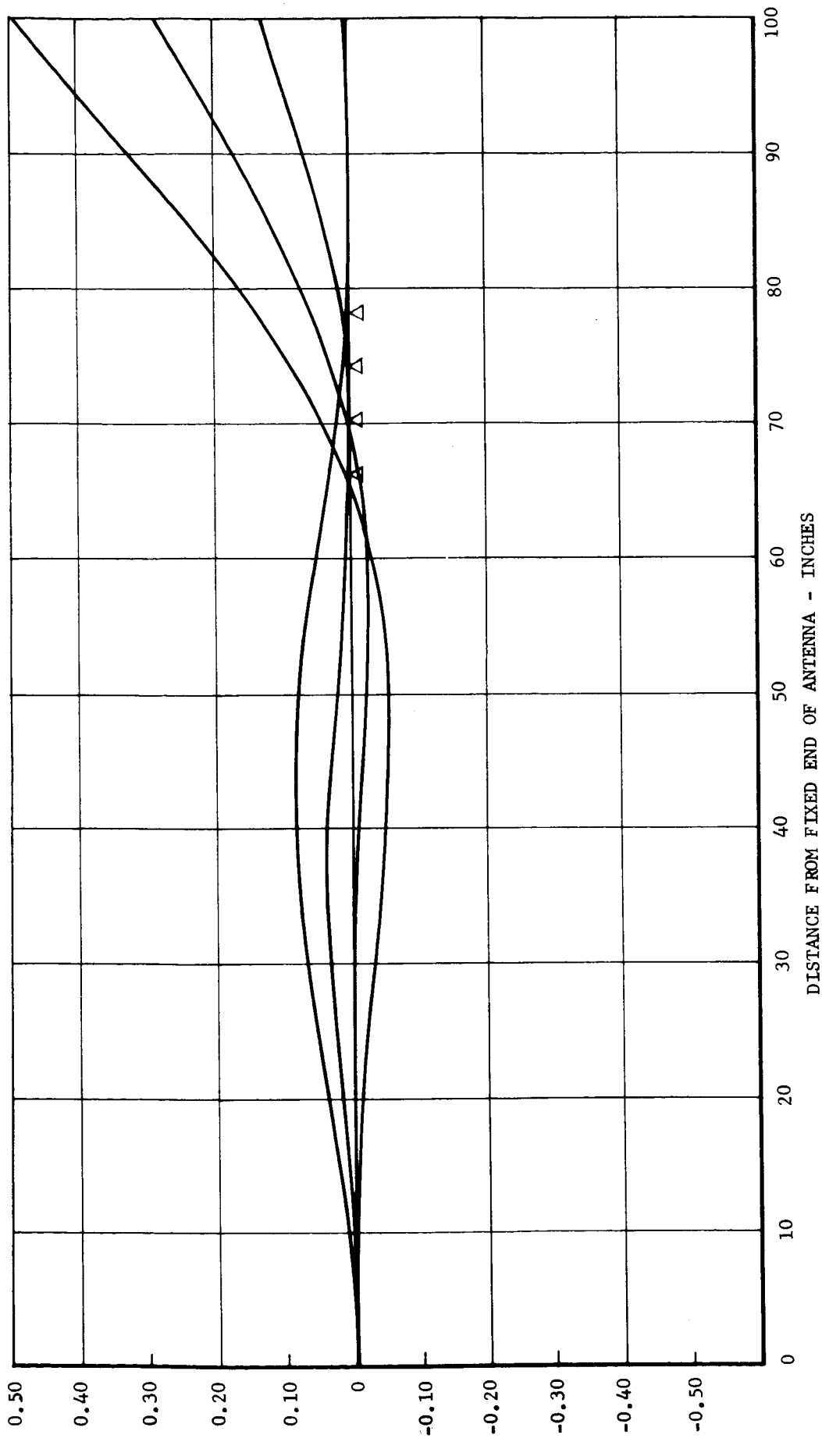

Figure 1-6 Deflected Shape for 100" Antennas Propped at 66, 70, 74, 78 Inches, Spin Rate Ω = 180 rpm

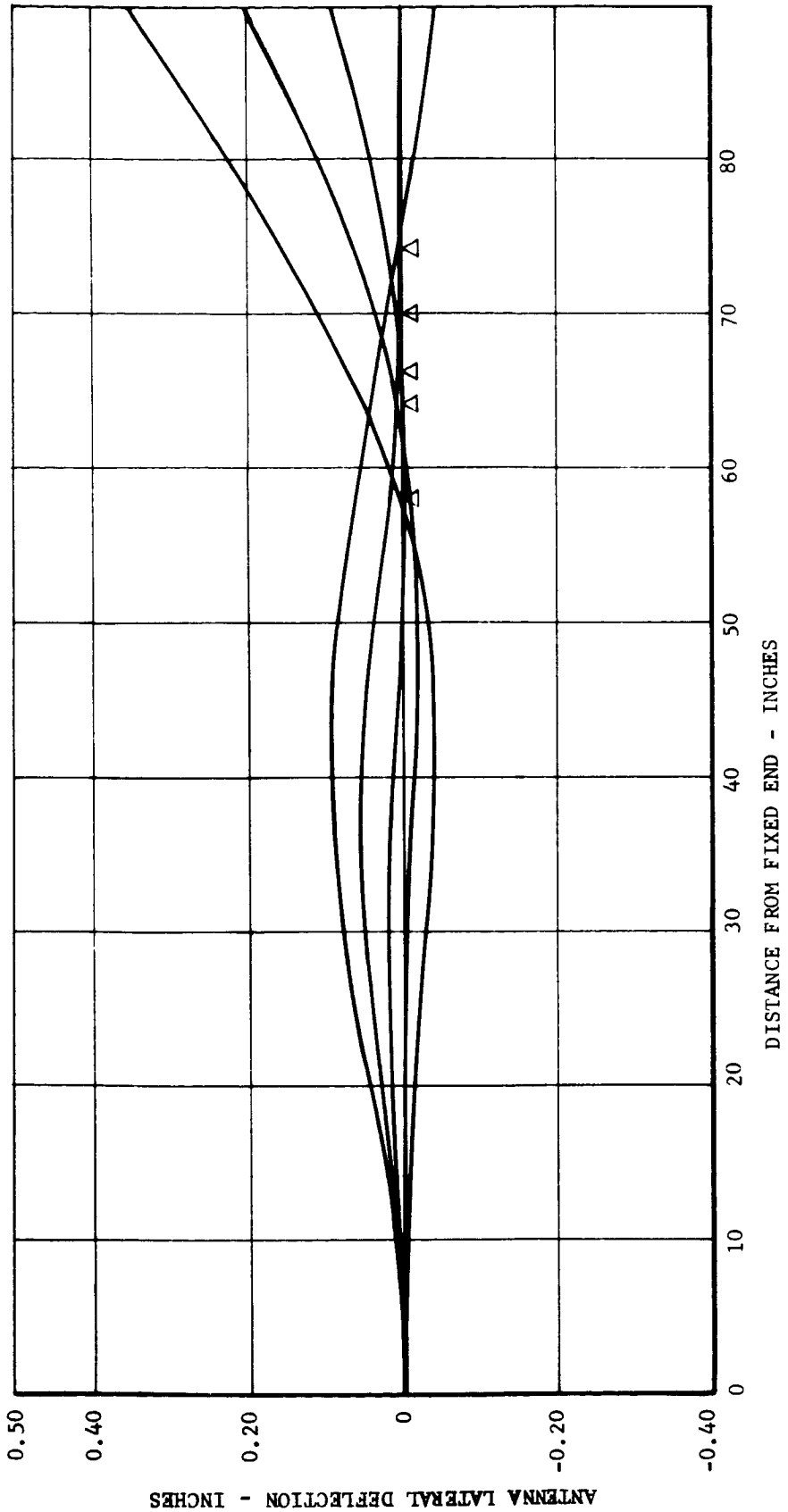

Figure 1-7 Deflected Shape for 90" Antennas Propped at 58, 62, 66, 70, 74 Inches, Spin Rate Ω = 180 rpm

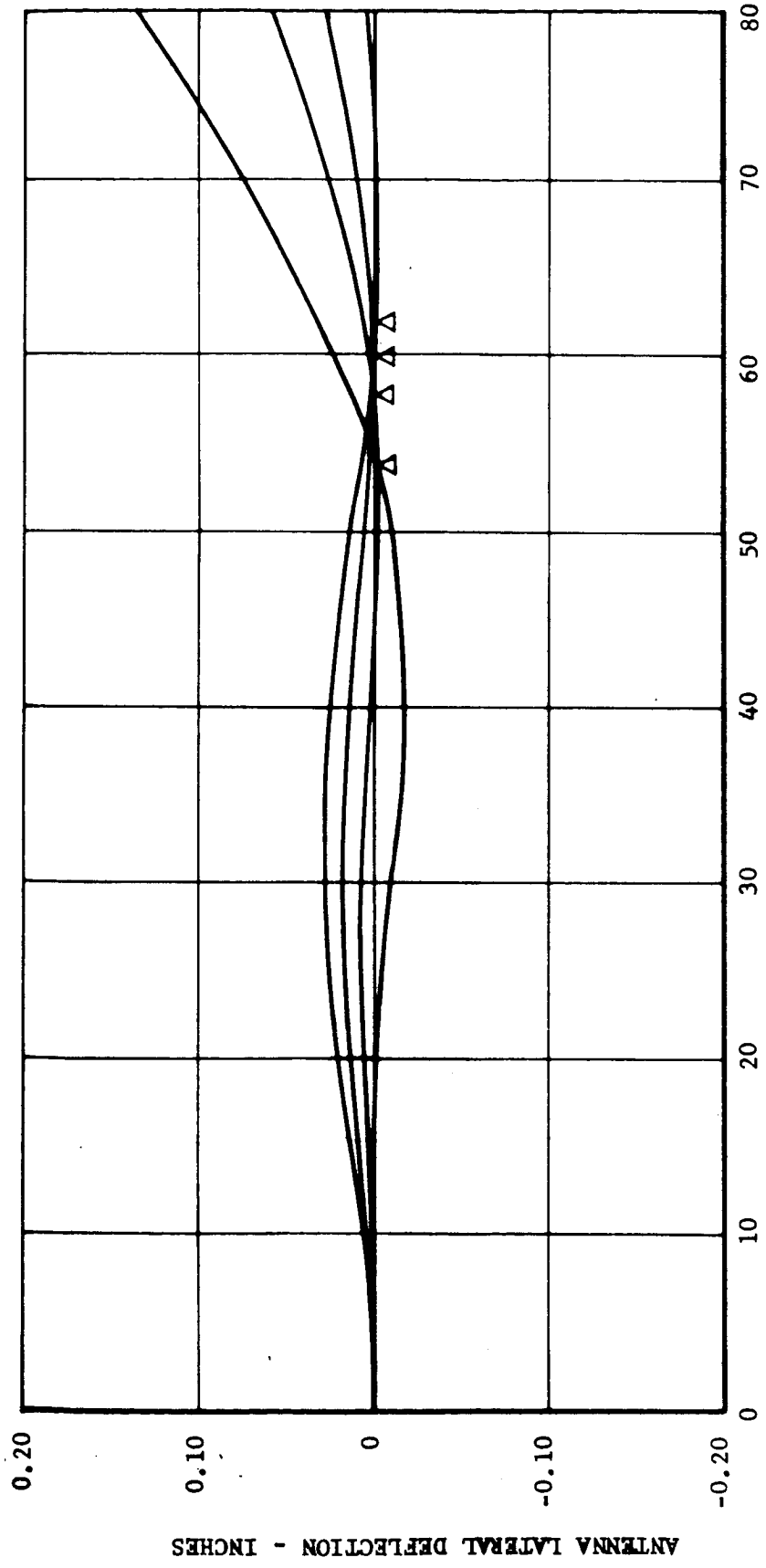

Figure 1-8 Deflected Shape for 80" Antennas Propped at 54, 58, 60, 62 Inches, Spin Rate Ω = 180 rpm

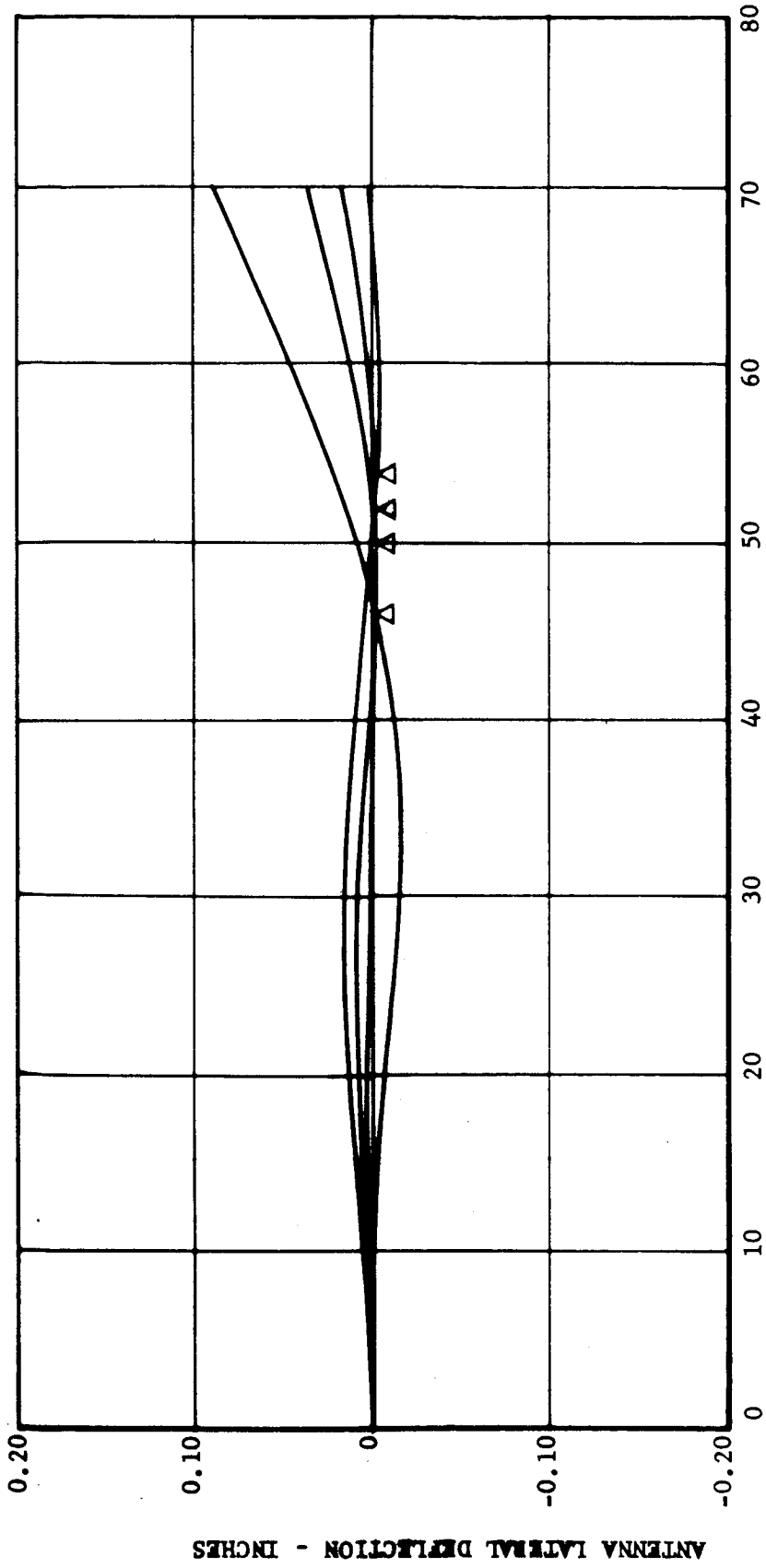

Figure 1-9 Deflected Shape for 70" Antennas Propped at 46, 50, 52, 54 Inches, Spin Rate Ω = 180 rpm

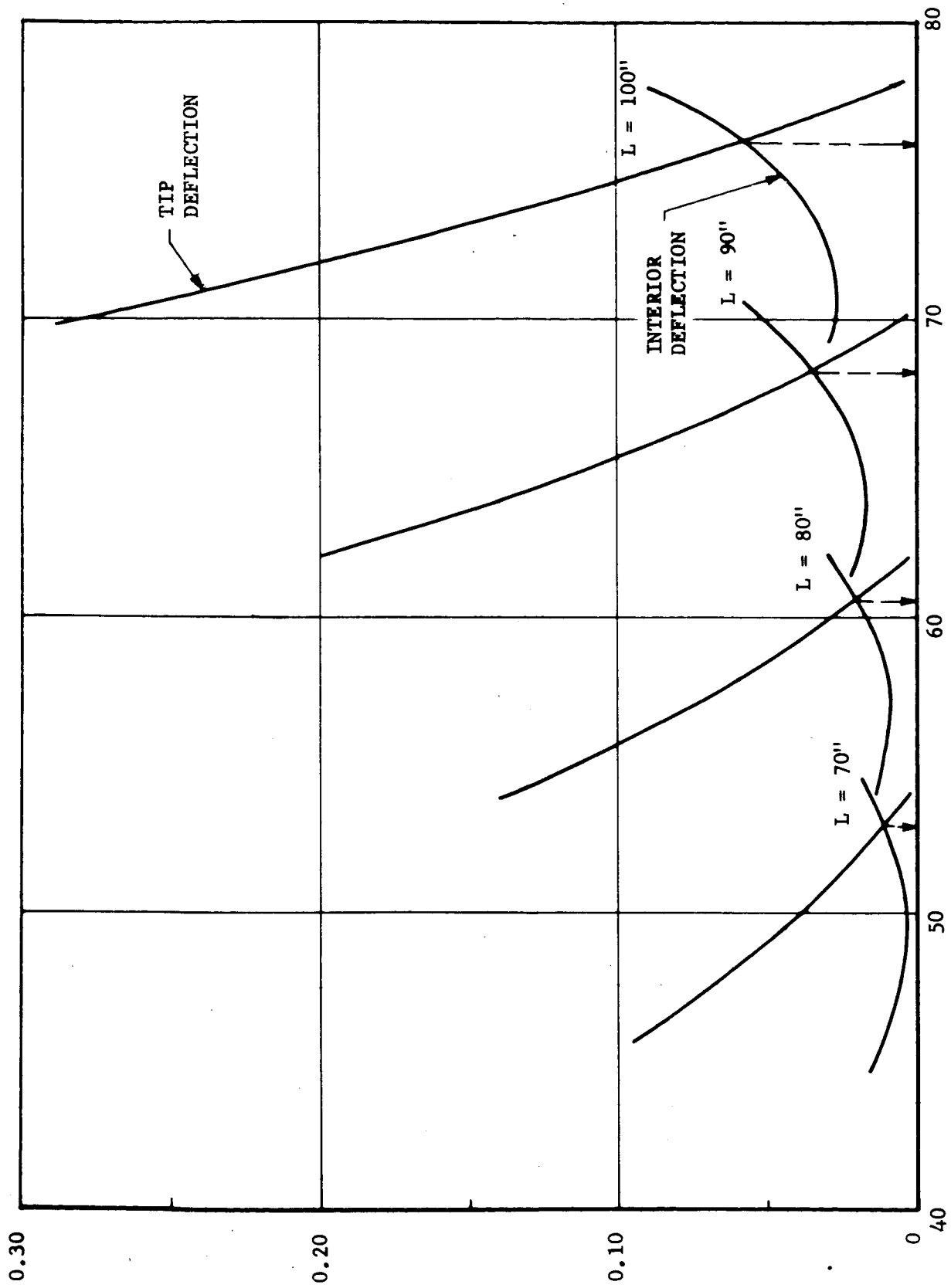

Figure 1-10 Optimum Prop Locations for Minimum Deflections, Spin Rate Ω = 180 rpm

The resulting deflected shape, moment and shear diagrams for a spin rate of 100 rpm are shown in Figures 1-11, 1-12, and 1-13. Maximum bending and shear stresses calculated were

$$\delta_{max} = 13,861 \text{ psi}$$

$$\tau_{max} = 135 \text{ psi}$$

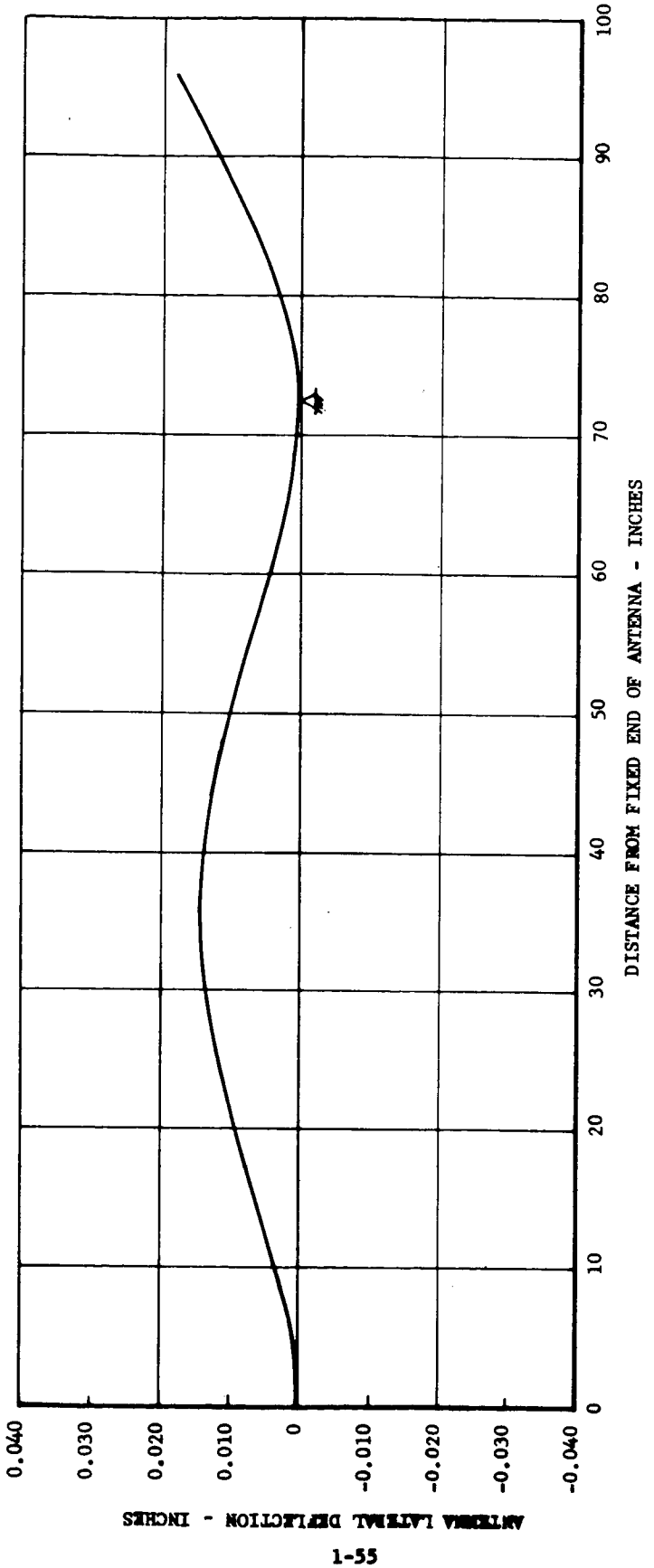

Figure 1-11 Deflected Shape for 95.909" Antenna Propped at x = 72.421 Inches, Spin Rate Ω = 100 rpm

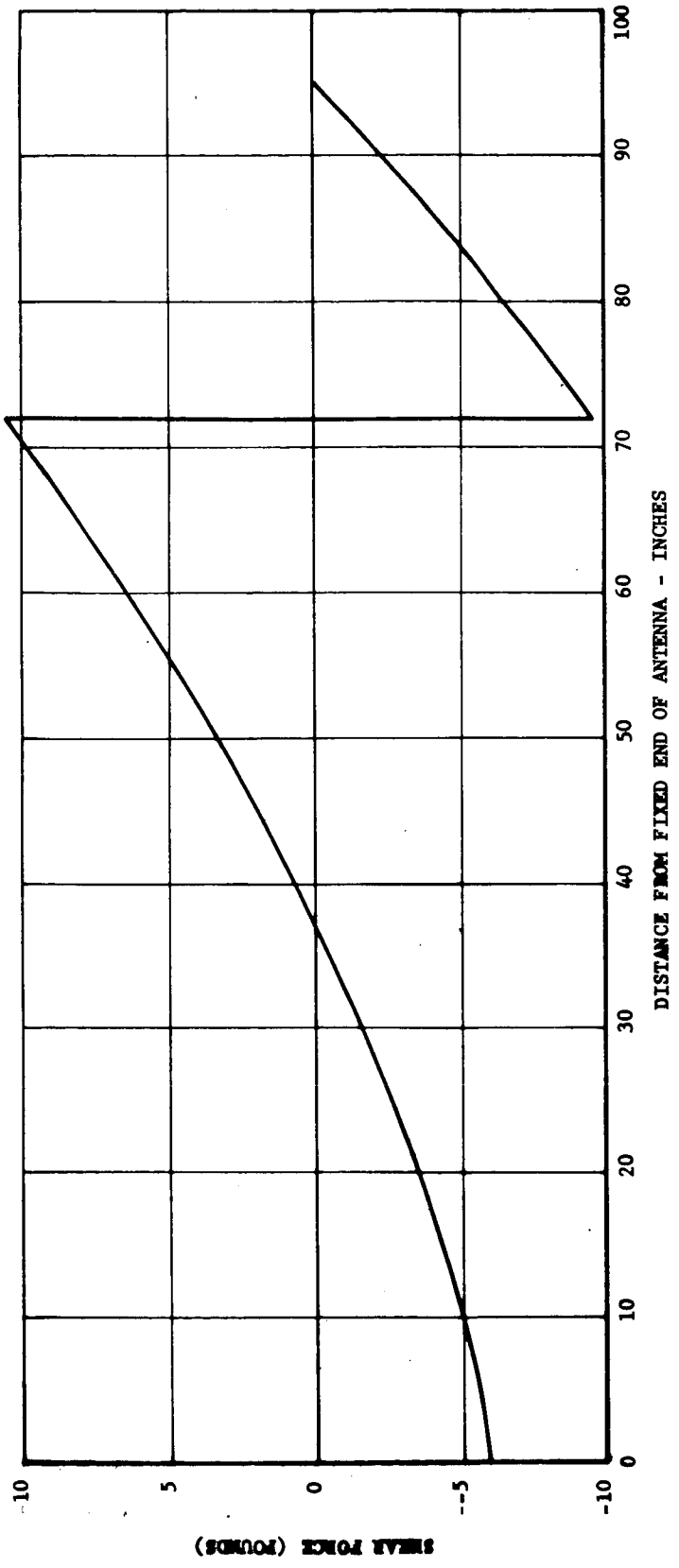

Figure 1-12 Shear Diagram for 95.909" Antenna Propped at x = 72.421 Inches, Spin Rate Ω = 100 rpm

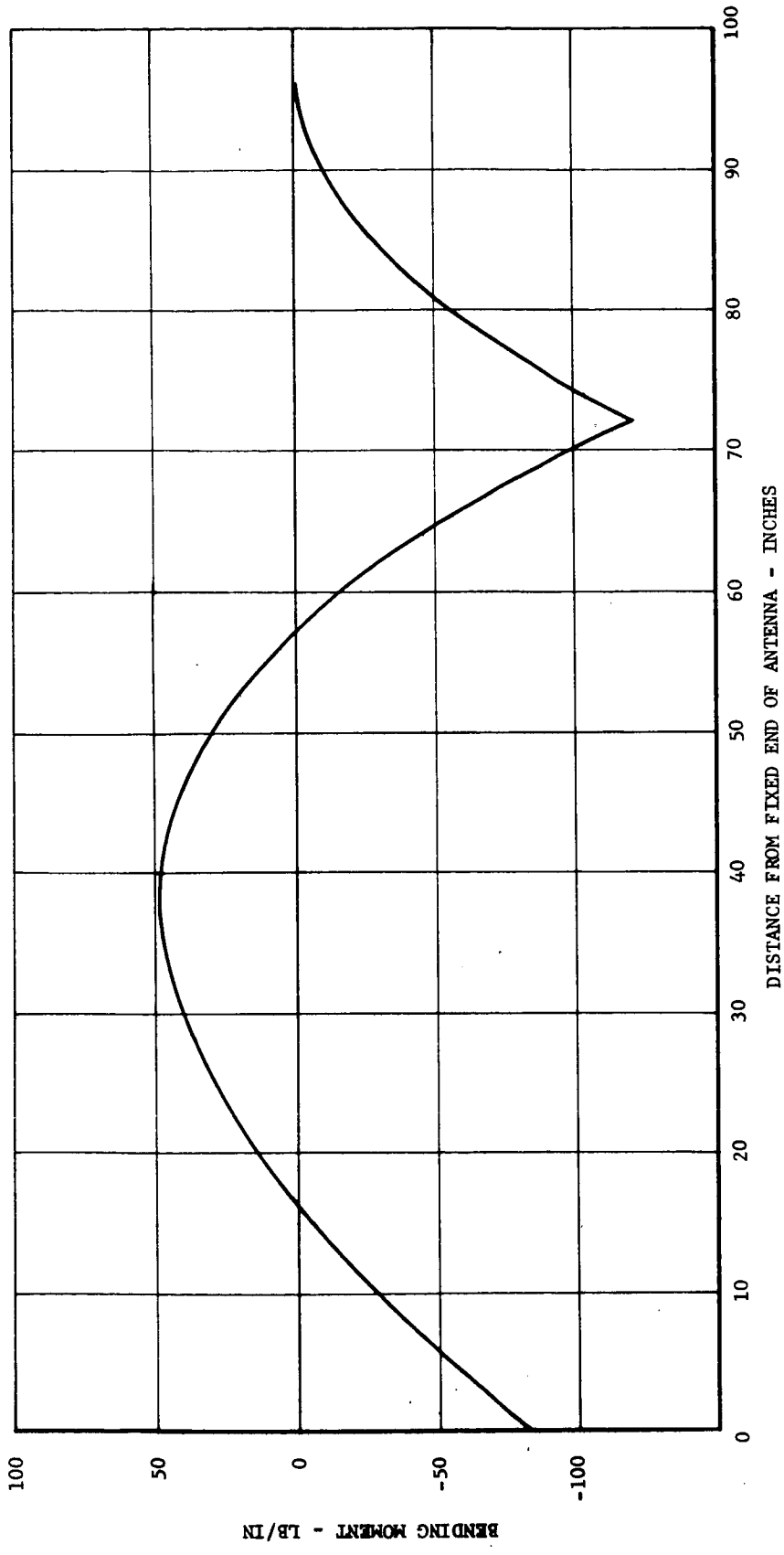

Figure 1-13 Moment Diagram for 95.909" Antenna Propped at x = 72.421 Inches, Spin Rate Ω = 100 rpm

SECTION 2
ANTENNA ELECTRICAL ANALYSIS

2.1 INTRODUCTION

The Navigation Satellite concept requires an antenna which will produce a fan beam with a very narrow beamwidth in one plane and a beamwidth in the plane of the fan broad enough to give complete coverage over the surface of the earth. Location accuracy is directly related to the narrow beamwidth.

It is well known that the beamwidth in a given plane is inversely proportional to the antenna aperture size in wavelengths in that plane. For a given specified beamwidth a compromise must be made between frequency of operation and practical physical dimensions. The upper limit of the latter is dictated by the specific dynamics of the system or satellite. Furthermore, the antenna must be such that it can be collapsed into a relatively small package and unfurled or extended.

The simplest type of antenna which is capable of meeting all the requirements is the array antenna. The planar wavelength dimensions of the array determine its beamwidths. The radiating elements of microwave arrays are generally excited in cascade from a single transmission line because of the restrictions placed on element spacing by the desired radiation pattern. The spacing must not be more than 0.7 of the wavelength in the transmission line if a single major beam is desired. A broadside beam, that is one truly normal to the array, is acquired by forcing the phase difference between adjacent elements to zero. This is the case for a resonant array for which the element spacing is one-half guide wavelength and a short circuit one-quarter guide wavelength from the last element. At half guide wavelength spacings, the phase difference between adjacent elements is made zero by a physical phase reversal. Any desired amplitude distribution may be assigned to the array by appropriate selection of the radiating slot conductances. A uniform amplitude distribution yields the narrowest beamwidth, the greatest gain, and the steepest slope off the peak of the main beam and is therefore the distribution which is most advantageous for application to the Navigation Satellite Antenna. However, the side lobe level is also the highest, but offers no problems to the detection scheme proposed.

Resonant arrays may be constructed on any of the transmission lines commonly used for propagation of microwave energy. The limitations for a given line are determined by the conductive wall losses for the length and frequency required to achieve a given beamwidth, and the manner of radiating the energy in phase at half wave length spacings. In order to meet these conditions in coaxial lines requires dipole radiators and frequencies lower than about 4 GHz. The array then becomes more complex, longer and heavier. The simplest type of radiator is a resonant slot which is positioned on the line such that it cuts across the current lines which flow on the conductor walls. The slot may be positioned such that it presents a pure conductance of any desired value to the incident energy. Radiating slots on rectangular wave guides is a subject which has been given considerable attention. The design equations are well founded and proven and can be found in most of the antenna literature.

This study is principally concerned with problem areas which may be forseen to arise from the **Navigation Satellite application and to investigate extendable wave guide arrays.**

2.2 CIRCULAR WAVEGUIDES

Circular wave guide arrays lend themselves readily to applications where 360 degree coverage is required for in this case circular symmetry of the wave guide is maintained. However, if hemispherical or smaller angular coverage is required to achieve greater directivity the radiating elements are positioned such that circular symmetry is lost. This is important because the plane of incident polarization for the lowest TE_{11} mode of propagation cannot be insured to be in a unique plane. Any change in cross section, bending or warping of the guide, or any discontinuity which lies in a plane other than that of the incident polarization may cause coupling to and excite the orthogonal TE_{11} mode. The first order TM_{01} mode which excites only longitudinal currents as in coaxial lines could be used more effectively to excite the slots except that without a TE_{11} mode suppresser there is always the possibility that the TE_{11} mode may be excited.

The DeHavilland boom as an unfurable circular wave guide slotted array is not readily acceptable for a Navigation Satellite application. The open seam of the guide when extended will most likely experience some twisting which will cause radiation when the seam and plane of incident polarization are misaligned. It has been found that off axis displaced longitudinal slots cause coupling to the orthogonal mode which in turn excites the radiating slot with a different phase and amplitude. The investigations of longitudinal off axis displaced shunt slots on a circular waveguide are reported in Appendix A.

The DeHavilland structure might be adaptable if it could be made to latch about a ridge which would be inserted into the guide. The ridge would have the two fold purpose of insuring that the seam and incident polarization vector will not be misaligned. There are obvious problems of latching the closing seam edges to the ridge and of extending the ridge itself.

2.3 RECTANGULAR AND ELLIPTICAL WAVEGUIDES

Elliptical wave guides make up the general category of which circular guides are a special case. Eccentricities of greater than zero split the degenerate modes of a circular guide into even and odd modes, the odd TE_{11} mode being dominant. The greater the eccentricity the greater the separation between cut-off wave lengths of the even and odd dominant modes The field distributions approximate that of rectangular wave guides and therefore, slot radiators should perform in a like manner. Elliptical wave guides have the low loss feature characteristic of circular wave guides in their favor. However, considerable experimenting would have to be done to develop design curves for resonant slots of arbitrary conductance or at least to demonstrate similarities or dissimilarities to the existing design curves for rectangular wave guide slots. Elliptical wave guides are not then to be dismissed as a possible transmission line on which to build a resonant slotted array.

Subsequent discussions and analysis will, however, be confined to rectangular wave guides because of their popularity and familiarity.

Appendix B describes an experiment on a long, 110 wave length, short circuited section of rectangular waveguide which was subjected to various degrees of constant curvature bending in both E and H planes. Measurement of the change in null position of the standing wave pattern was made to determine the change in phase velocity with bending. The experiment was performed to investigate the tolerable upper limit on bending of a structurally unsupported rectangular wave guide and to determine the phase change per unit of length vs radius of curvature.

It was found that for E plane bending the velocity of propagation was decreased. The opposite effect occurred for H plane bending but at a much lower rate. In either case the effect was negligible in comparison to equivalent effects caused by practical construction tolerances.

2.4 EXTENDABLE WAVEGUIDE ARRAYS

Several means of extending long wave guide arrays and their associated inherent electrical problem areas and possible solutions are presented.

Any discontinuities in a wave guide resulting from an abrupt change in the cross section, as in the case of telescoping sections, or a misalignment of the mating of two identical guides, as in the case of a hinged joint, will introduce an equivalent shunt or series impedance or combination of both at the junction. The resultant impedance discontinuity, because of its associated complex reflection and transmission coefficients, will set up a different standing wave pattern on either side of the junction than that for which the radiating slots were designed. The resultant constant phase surface will no longer be parallel to the array as required for a normal broadside beam.

The best means for eliminating the effect of the discontinuity is to resonate it with its conjugate reactance at the plane of the discontinuity, if such a unique plane and conjugate exist. An alternate matching method is to place an identical equivalent reactance in the guide a quarter of

the guide wave length from the plane of the discontinuity to be "tuned out". In either case, the phase shift through the discontinuity will be unchanged.

For extendable arrays made up of either hinged sections or telescoping sections an electrical choke joint will most likely be required to provide electrical continuity and prevent radiation at the joint. The joint would further maintain proper alignment of the sections. The complete design would have to be determined empirically and could take the form of the standard choke flanges for rectangular wave guides.

The design of telescoping guides is discussed in the following paragraphs.

The design is based upon matching the impedances of the two guide cross-sections at the design frequency. Assuming rectangular wave guide and single mode propagation only the guide impedance is, in general, given by

$$z_o = \frac{2\frac{b}{a}\eta}{\sqrt{1-\left(\frac{\lambda_o}{2a}\right)^2}} \qquad (1)$$

where a and b are the inside wide and narrow dimensions of the guide respectively, η is the free space impedance = 120 π ohms and λ_o is the free space wave length.

The outer large guide will be numbered 1, and the inside telescoping guide Numbered 2. Then if

$$Z_1 = Z_2$$

$$\frac{2\left(\frac{b}{a}\right)_1\eta}{\sqrt{1-\left(\frac{\lambda_o}{2a_1}\right)^2}} = \frac{2\left(\frac{b}{a}\right)_2\eta}{\sqrt{1-\left(\frac{\lambda_o}{2a_2}\right)^2}}$$

$$\frac{\left(\frac{b}{a}\right)_1^2}{\left(\frac{b}{a}\right)_2^2} = \frac{1-\left(\frac{\lambda_o}{2a_1}\right)^2}{1-\left(\frac{\lambda_o}{2a_2}\right)^2}$$

$$\left(\frac{b_2}{b_1}\right)^2 = \frac{\left(2a_2\right)^2 - \lambda_o^2}{\left(2a_1\right)^2 - \lambda_o^2} \qquad (2)$$

a_1 and b_1, the dimensions of the larger outer guide, are known and a_2 is designed to be somewhat smaller than $(a_1 - 2t_{a2})$ where t_{a2} is the wall thickness of the narrow sides of guide 2 as shown in Figure 2-1.

The value of b_2 is found from Equation (2). The wall thickness plus tolerance between guides, t_{b2}, is found from

$$t_{b2} = \frac{b_1 - b_2}{2} \qquad (3)$$

The choke section is designed such that a short circuit exists between the guides at the plane of the junction. Two typical junctions might appear as in Figure 2-2. The dielectric sleeve provides a good mechanical surface for sliding and makes the choke section more effective electrically. Some type of mechanism must obviously be included to stop and hold the guide at the correct position.

The radiating elements either side of the junction where the change in cross section occurs should not be closer than one-half of the respective guide wave length in order that the higher order modes excited by the junction be attenuated sufficiently. The spacing from the junction of the first and last elements of adjoining sections should be multiples of the corresponding half guide wave lengths, and positioned with respect to the longitudinal center line such that the phase difference is zero.

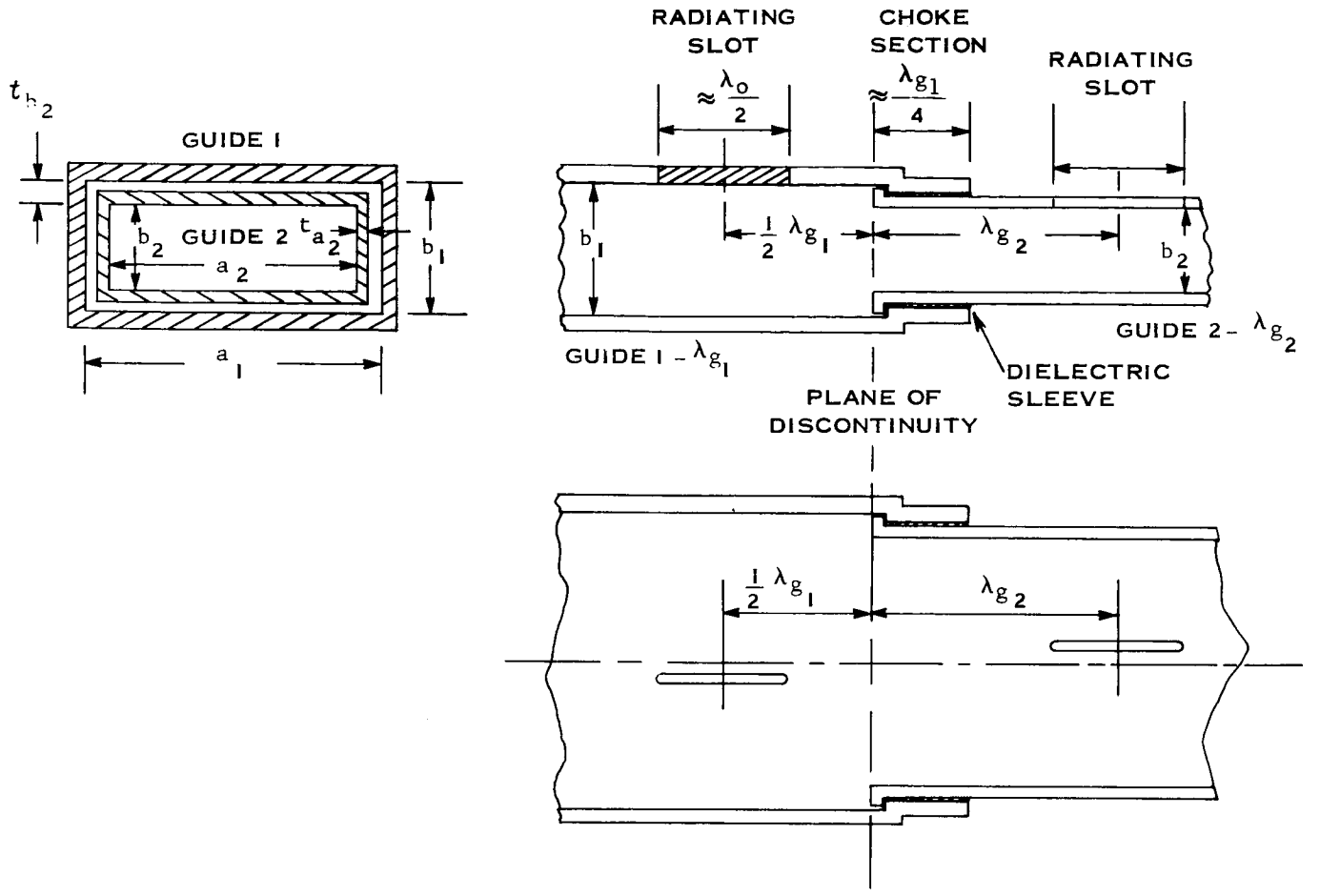

Figure 2-1 Telescoping Guide Cross-Sections

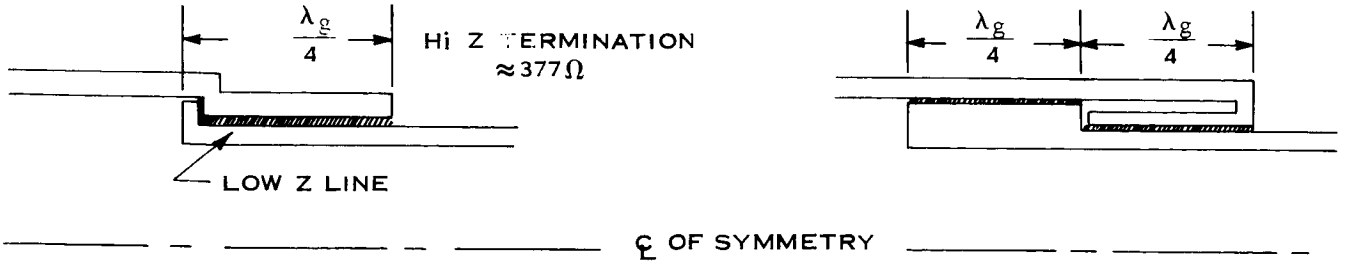

Figure 2-2 Choke Joint Cross-Section

If both sections have the same number of elements n, the radiation patterns of each section will be nearly identical regardless of the small different physical element spacings on each array. The resultant pattern is dependent upon the spacing between arrays and differs only slightly from that of a single long array of the same total number of elements, namely, 2n. If the spacing is made less than 25 percent of the length of either array section, the first side lobe will not exceed the -13 db level with respect to the main beam, and the first zero position is reduced by about 20 percent from that of an array of 2n elements.

However, the radiating energy from the smaller telescoping guide suffers a phase lag with respect to the radiation from the larger guide on account of the step in the narrow dimension. If the step is 0.05 inches, a wall thickness, and the frequency is 8.0 GHz or $\lambda_o = 1.475"$, the phase lag is found as follows:

$$\Delta B = 2\pi \frac{\Delta}{\lambda_o}$$

$$= 360 \frac{.050}{1.475} = 12.2^o = .0678\ \pi \text{ radians.}$$

This will result in a beam shift from the normal by an amount given by

$$\alpha \approx \frac{\Delta B}{2\pi \frac{\rho}{\lambda}} \quad \text{radians}$$

where ρ is the separation between the phase centers of the sources. Each section may be considered a source with its phase center located at its corresponding geometric center. If each section contains 50 elements, then $\frac{\rho}{\lambda}$ is nearly 50, and

$$\alpha \approx \frac{.0678\ \pi}{2\pi \times 50} = 0.678 \text{ mrad}$$

$$\alpha \approx 0.041^{\circ}$$

This beam shift from the normal may be eliminated by making the telescoping antenna symmetrical about its extended geometric center, such that there are smaller telescoping sections either side of the larger enveloping section. Such an arrangement is shown in the sketch of Figure 2-3. For the system shown, the beam shift to the left of the extended array center is equal to the beam shift to the right and the resultant is a somewhat broader normal beam. The deflection of the array as a result of the spinning satellite and the array angle to the spin axis may be controlled by extending the telescoping sections into a channel with a cross section of the honey-comb structure. This structure itself may be hinged at convenient locations to fold into a package only slightly longer than one third of the overall length of the array.

An alternate method of achieving a normal beam is to feed the array at its geometric center. Such a feeding arrangement shown in Figure 2-4 uses a short slot 3 db hybrid coupler and is less frequency sensitive than a single long end-fed array. The system can be considered as two end fed colinear arrays. The separation between the first elements of the two arrays is a very small fraction of the length of either array so that the beamwidth is broadened only slightly. Reflections from the two arrays cancel at the input and add in phase at the terminated port.

2.5 ARRAYS OF ARRAYS

The radiation pattern in the Fraunhofer or far field region for a general space array is an extension of the two element development as follows.

Consider two identically space oriented radiating elements which are described by similar space radiation factors $F_1(\gamma, \eta)$, and $F_2(\gamma, \eta)$.

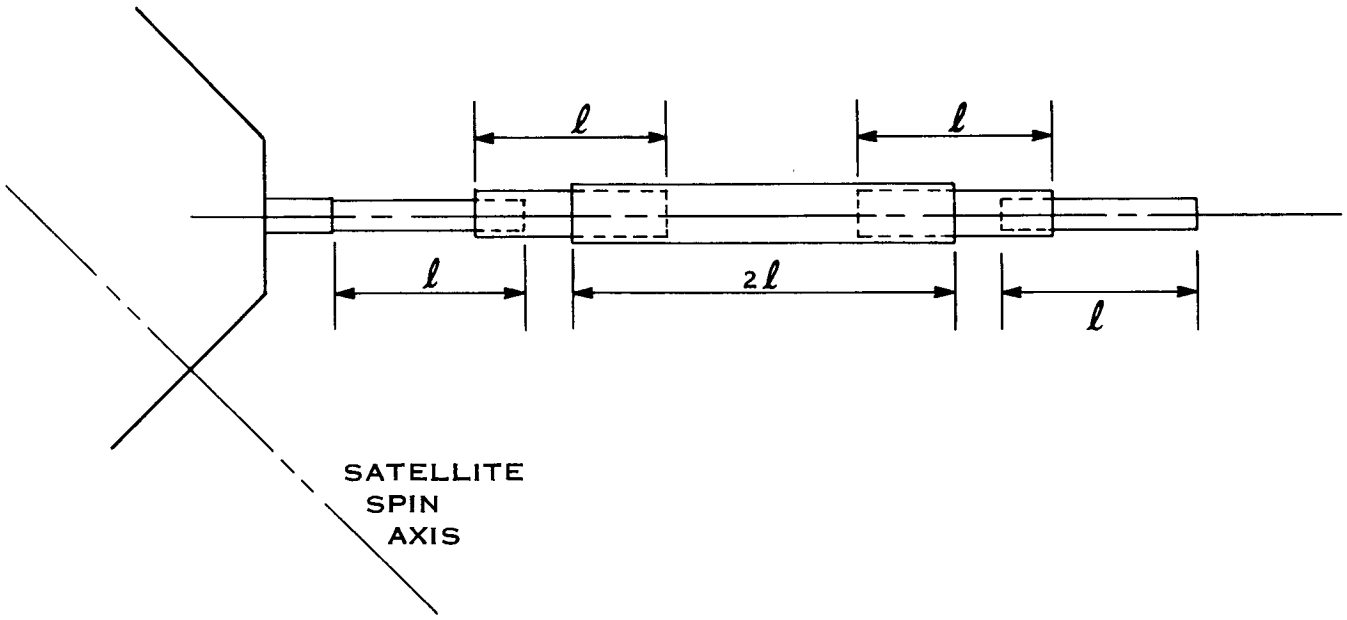

Figure 2-3 Telescoping Array.

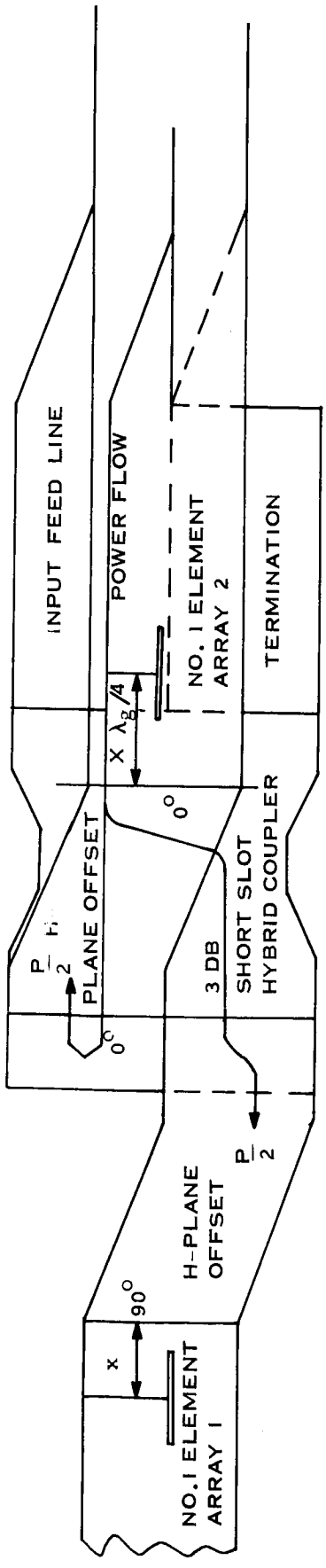

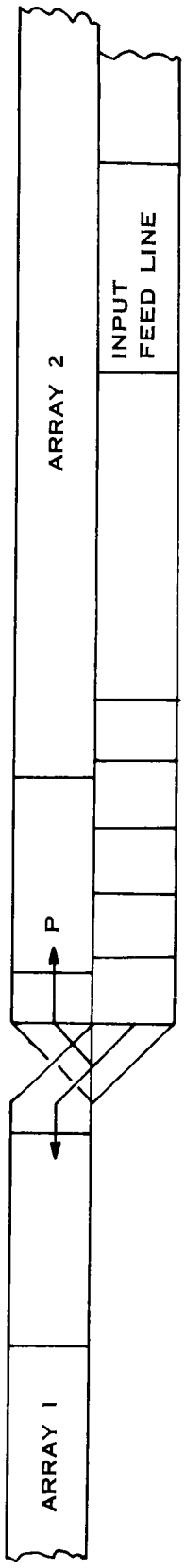

Figure 2-4 Center Feed Schematic

If the origin is taken as the midpoint of the line connecting the two sources, then at the given spatial position shown in Figure 2-5, source 1 has a phase lead and source 2 an equivalent phase lag given by $\left(\frac{\bar{d}}{2}\right) \cdot (\bar{a}_r)$. In general source 2 may have a phase Ψ different from source 1. At point P then the total field is given by

$$E_p(\gamma, \eta) = F_1(\gamma, \eta) e^{j \frac{2\pi}{\lambda}\left(\frac{\bar{d}}{2} \cdot \bar{a}_r\right)} + F_2(\gamma, \eta)\, e^{-j\left(\frac{2\pi}{\lambda}\frac{\bar{d}}{2} \cdot \bar{a}_r - \Psi\right)} \tag{4a}$$

$$= e^{j\frac{\Psi}{2}}\left[F_1(\gamma, \eta)\, e^{+j\left(k\frac{\bar{d}}{2} \cdot \bar{a}_r - \frac{\Psi}{2}\right)} + F_2(\gamma, \eta)\, e^{-j\left(k\frac{\bar{d}}{2} \cdot \bar{a}_r - \frac{\Psi}{2}\right)}\right] \tag{4b}$$

$F_1(\gamma, \eta)$ and $F_2(\gamma, \eta)$ may describe single or multiple arrays of elements oriented in any manner whatsoever with respect to the given coordinates, and with a phase reference at the points 1 and 2.

If source 1 is taken as the origin Equation (4) becomes

$$E_p(\gamma, \eta) = F_1(\gamma, \eta) + F_2(\gamma, \eta)\, e^{j(k\,\bar{d}\cdot\bar{a}_r + \Psi)} \tag{5a}$$

$$= e^{j(k\bar{d}\cdot\bar{a}_r + \Psi)1/2}\left[F_1(\gamma, \eta)\, e^{-j\,1/2\,(k\bar{d}\cdot\bar{a}_r + \Psi)} + F_2(\gamma, \eta)\, e^{j1/2\,(k\bar{d}\cdot\bar{a}_r + \Psi)}\right] \tag{5b}$$

If there are n sources having the same pattern factor $F(\gamma, \eta)$ and different only in amplitude, A, and phase Ψ, the first of Equations (5a) becomes:

$$E_p(\gamma, \eta)_n = F(\gamma, \eta) \sum_{i=1}^{n} A_i\, e^{j(\Psi i + ik\,\bar{d} \cdot \bar{a}_r)} \tag{6}$$

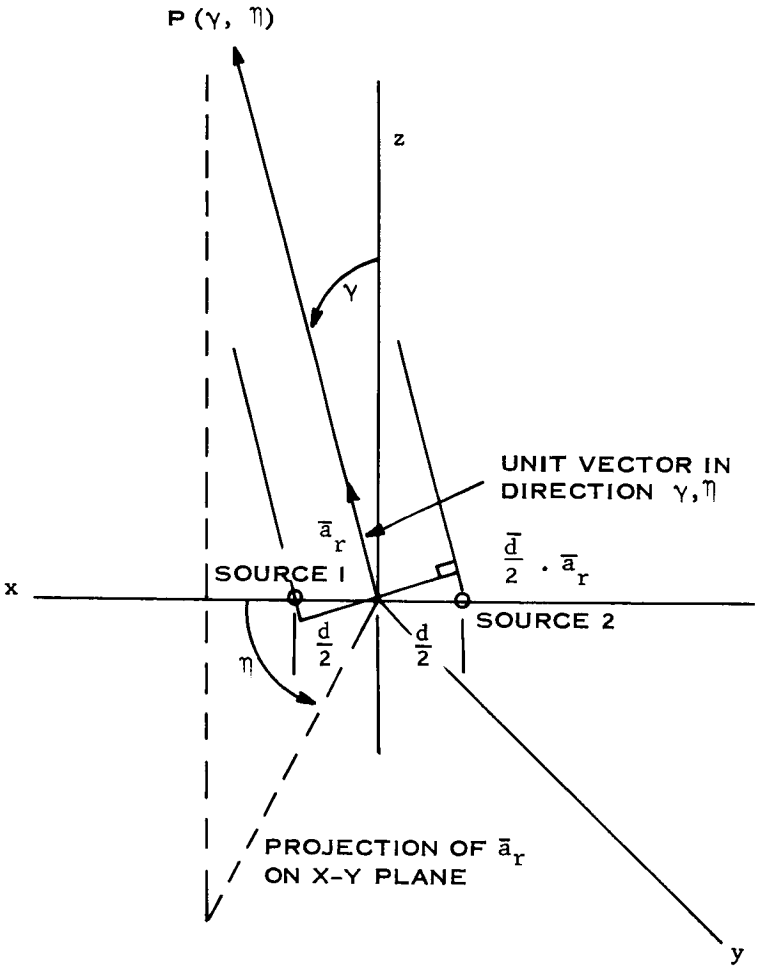

Figure 2-5 Linear Array Coordinates

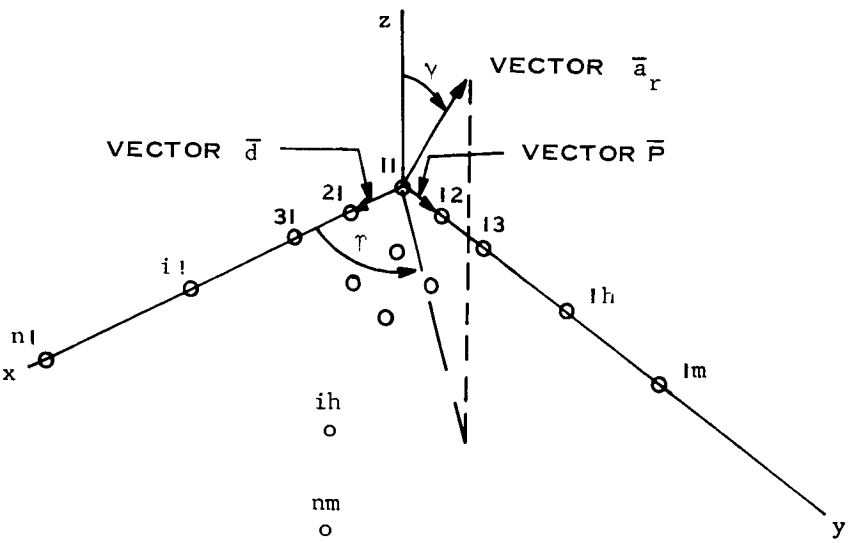

Figure 2-6 Planar Array Coordinates

Equations (5) and (6) can then be incorporated to consider m number of similar parallel arrays of elements spaced p apart as shown in Figure 2-6. Then

$$E_p\ (\gamma,\ \eta)_{nm} = F\ (\gamma,\ \eta) \sum_{i=1}^{n} \sum_{k=1}^{m} A_{ih}\ e^{j\ (\psi_{ih} + ki\bar{d}\cdot\bar{a}_r + k\ (h-1)\ \bar{p}\cdot\bar{a}_r)} \quad (7)$$

where $\bar{d}$ and $\bar{p}$ are vectors which in general make any angle to the x and y axes respectively, that is, the locus of the i elements may describe any curve in a plane or in space.

Equation (6) can be readily summed if the amplitude A_i of all the elements are made equal, and there is a linear phase progression from element to element along the x axis. The result is

$$E_p\ (\gamma,\ \eta) = F\ (\gamma,\ \eta)\ \frac{\sin n\ \omega}{n \sin \omega}\ e^{j\ \frac{n-1}{2}\ \omega} \quad (8)$$

where

$$\omega = \psi + \frac{2\pi}{\lambda}\ (\bar{d}_x \cdot \bar{a}_r)\ .$$

If the phase is referred to the center point of the array equation (8) becomes

$$E_p\ (\gamma,\ \eta) = F\ (\gamma,\ \eta)\ \frac{\sin n\ \omega}{n \sin \omega} \quad (9)$$

It can be shown that if the separation between end elements of two identical colinear arrays is equal to the length of one array, the beamwidth of the main beam is equal to that for an array of nearly four times the length of one array; however, the first sidelobe is only four db down. If the separation is 25 percent of the length of one array, the height of the highest side lobe does not

increase above the -13 db level with respect to the main lobe. The beamwidth is reduced by about 15 percent with respect to that for an array with twice the number of elements of either array, that is, when the separation between the end elements of the two equal length arrays is zero. Obviously, there is no advantage for a given length of a single array to omit a certain number of the center elements to obtain a narrower beam for then each section contains less than half the total number of elements of the original array. A given angular beamwidth and side lobe level achievable with a single array of n elements and length nd can also be achieved by two identical colinear in phase arrays of 0.4 n elements with a separation between first elements of 0.1 nd. For example, a 100 inch array can be replaced by two 40 inch arrays if the separation between ends is 10 inches. Or, conversely, if the separation must be at least 40 inches, each array length must be 160 inches and would be equivalent to a 400 inch array. There is, therefore, a compromise to be made between overall length, separation, frequency, beamwidth and tolerable side lobe level.

If now the identical in-phase-arrays are restriced to be only parallel, it can be shown using Equations (9) and (4) that the radiation pattern factor is described by the following:

$$E_p(\gamma, \eta) = F(\gamma, \eta) \cos\left(\frac{2\pi}{\lambda}\bar{p} \cdot \bar{a}_r\right) \cos\left(\frac{2\pi}{\lambda}\bar{r} \cdot \bar{a}_r\right) \frac{\sin\left(n\frac{\pi\bar{d}}{\lambda} \cdot \bar{a}_r\right)}{n \sin\left(\frac{\pi\bar{d}}{\lambda} \cdot \bar{a}_r\right)} e^{j\eta} \tag{10}$$

If the phase reference is at the center of the system, then

$$\eta = \frac{2\pi}{\lambda}\left(\bar{r} \cdot \bar{a}_r + \bar{p} \cdot \bar{a}_r\right)$$

Figure 2-7 illustrates the system.

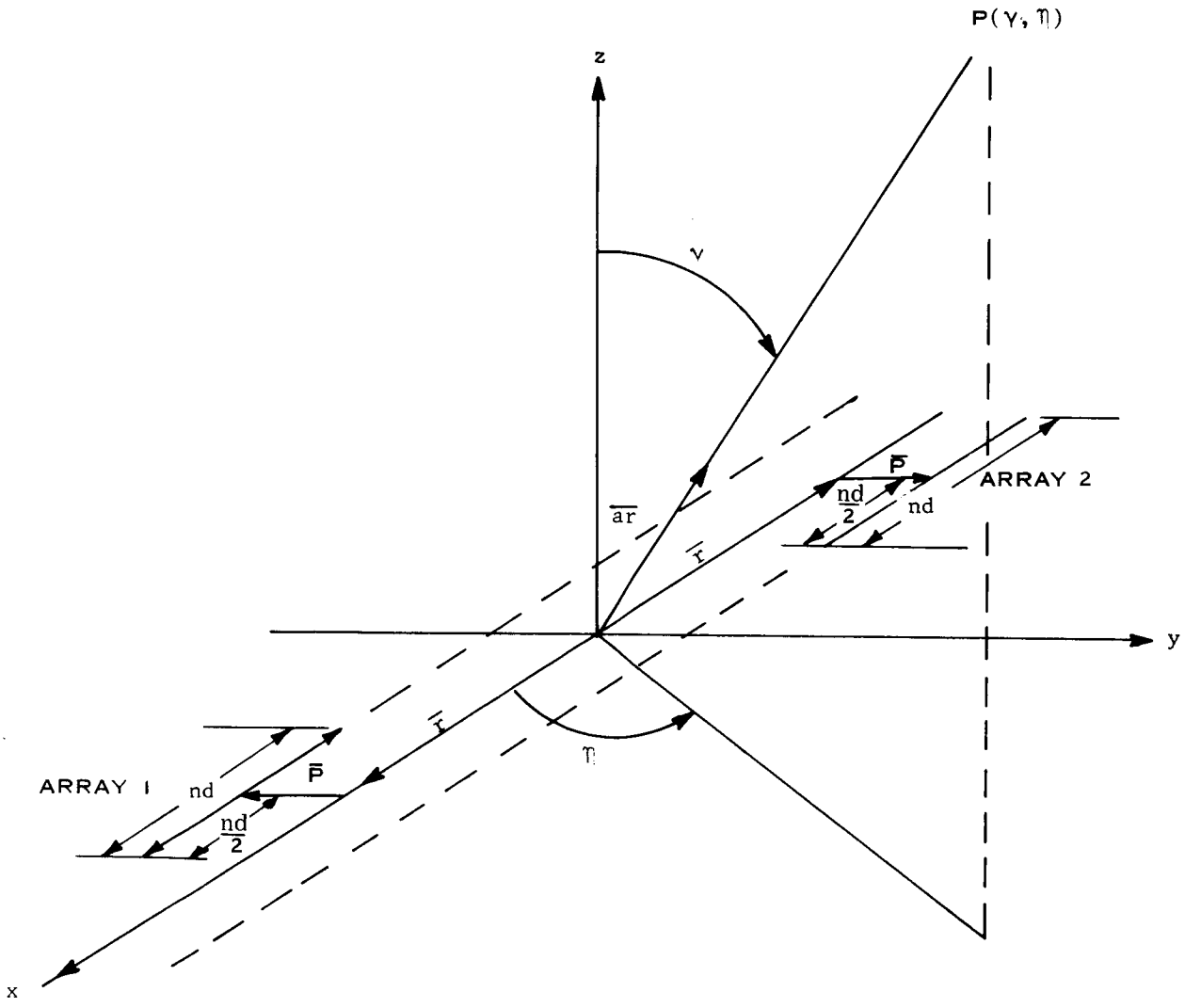

Figure 2-7 Planar Array of Arrays

If now we consider the separation in the y direction, $\bar{p}$, and the pattern in the z-y plane, $\bar{r} \cdot \bar{a}_r = 0$, $\bar{d} \cdot \bar{a}_r = 0$ and

$$E_p\left(\gamma, \frac{\pi}{2}\right) = F\left(\gamma, \frac{\pi}{2}\right) \cos\left(\frac{2\pi}{\lambda} p \sin\gamma\right)$$

The optimum spacing is $2p = \frac{\lambda}{2}$ for then a single maximum occurs at $\gamma = 0$ providing $F\left(\pi, \frac{\pi}{2}\right) = 0$. As the separation 2p becomes larger in integral numbers of half wave lengths, there occur equal numbers of auxiliary major lobes on both sides of the broadside main beam. For odd integers, t, there occur $\left(\frac{t-1}{2}\right)$ maxima either side of the normal beam to $\gamma = 90^\circ$ at positions given by

$$\sin\gamma = \frac{2}{t}\left(1, 2, 3, \text{---}, \frac{t-1}{2}\right), \; t \text{ odd}$$

For even integers or integral numbers of wave lengths, m, there occur m maxima either side of the main beam to $\theta = 90^\circ$ at positions given by

$$\sin\gamma = \frac{1}{m}(1, 2, 3, \text{---} \; m)$$

For either case there is always a major lobe or beam at $\gamma = 0^\circ$.

2.6 FAN BEAM ANALYSIS

Section 3.3 describes in more detail the programming of the computer to analyze the distortion of a fan beam generated by a long resonant array which has been deflected according to a predetermined analytical expression.

The general problem statement is as follows: determine the locus of points defining the simulated detected peak of the fan beam for conical cuts about the satellite spin axis for the satellite-antenna configuration shown in Figure 2-8. Determine the deviation of these points from the linear in order to arrive at a tolerable length and deflection of array to meet the required location accuracy.

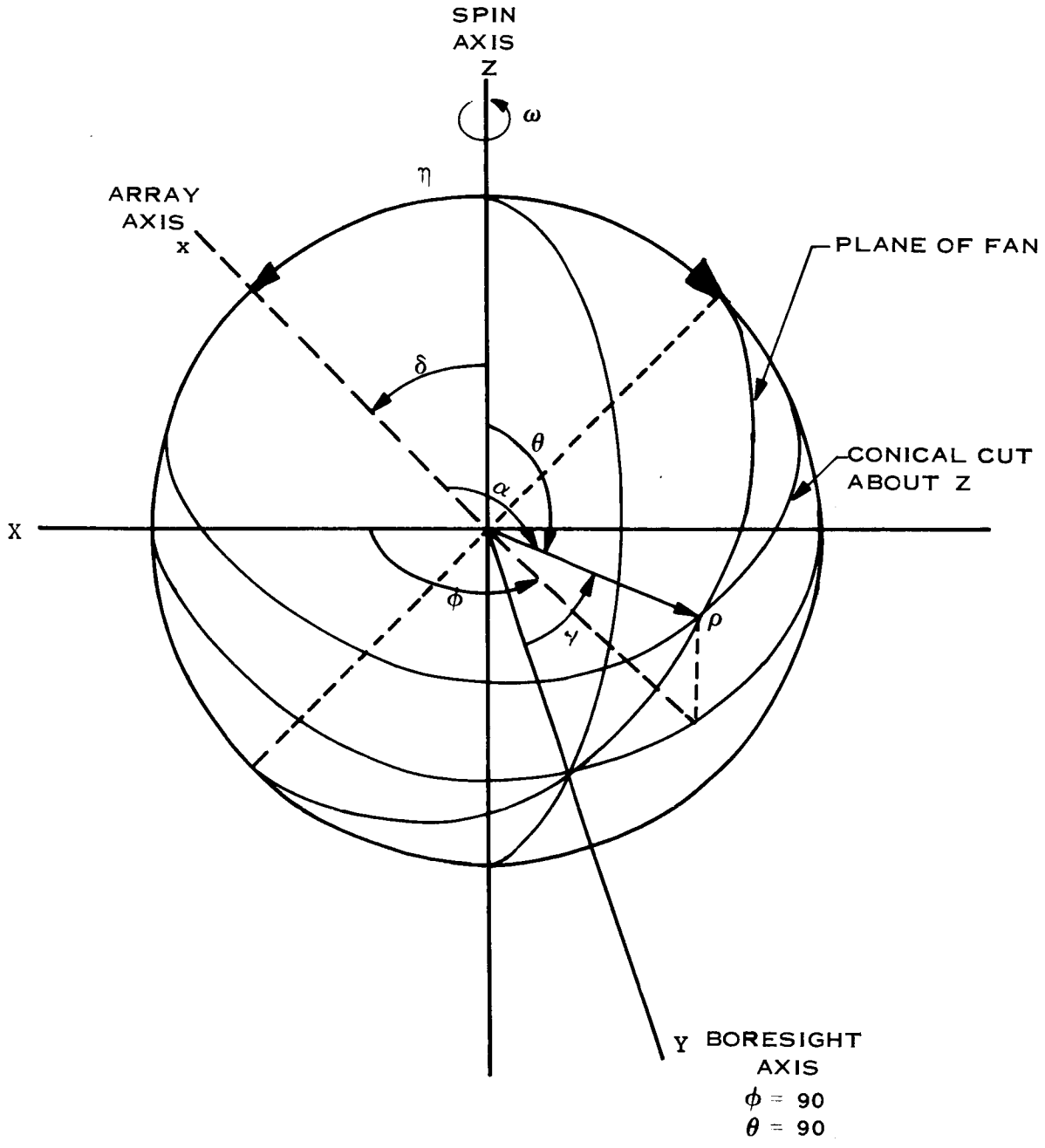

Figure 2-8 Computation Coordinate System

The array axis will be oriented at an angle δ to the satellite spin axis. The deflection of the array may be in general defined by parametric expressions of x, the undeflected array axis, in both y and z planes. The element spacing must be kept constant. The analysis will assume no variations in element amplitudes or phases while the array is deflected and the frequency does not change from resonance. An option will be available to change the amplitudes and phases of the elements of the array. The element radiation pattern will be that of a narrow rectangular resonant shunt slot in the broadside of a rectangular wave guide.

The radiation pattern will be computed from the following expression (Reference Section 2.5, Equation (7)):

$$E(\theta,\phi) = F(\theta,\phi) \sum_{i=1}^{n} \sum_{h=1}^{m} A_{ih} e^{j(\Psi_{ih} + k\bar{id} \cdot \bar{a}_r + k(h-1)\,\bar{p} \cdot \bar{ar})} \qquad (11)$$

where $F(\theta,\phi)$ is the element radiation pattern factor

k is the propagation constant $= 2\pi/\lambda_g$

λ_g is the guide wave length

$\bar{id}$ is the vector to the i th element

$(h-1)\bar{p}$ is the vector to the (h-1) th array

n is the number of elements of each array

m is the number of parallel arrays.

For the cases to be analyzed, the frequency of operation has been chosen to be 8.000 GHz; the wave guide size WR112, and the number of parallel arrays, 1. All Ai's are equal and all Ψ i's are zero. $F(\theta,\phi)$ is given by

$$F(\theta,\phi) = [T]\, F(\eta,\gamma)$$

where

$$F(\eta,\gamma) = 1/2\ (1 + e \cos \gamma)\ \frac{\cos\left(\frac{\pi}{2} \sin\gamma\right)}{\cos^2\gamma} \qquad (12)$$

is the assumed radiation pattern of the slot radiators referenced to the coordinate system coinciding with the array axis.

[T] is the transformation factor relating the coordinates of the array, η, γ to those of the satellite, θ, ϕ (reference Figure 2-8).

2.7 A MEASUREMENT-VERIFICATION SCHEME

2.7.1 Introduction

A measurement scheme is described which could be used to check the computed beam distortions resulting from a bent array. The accuracy obtainable from such measurements which involves the determination of the position of the peak of the fan beam is estimated to be .05 db in amplitude and .06° in position.

The measurement of distortions in beam shape, asymmetries in side lobe levels and null depths are not meaningful unless the asymmetries are of much greater magnitude than the effects of measurement errors. The source of the largest measurement error of a carefully designed antenna range is the phase difference between the center of an aperture and the outermost edge which is caused by the finite separation between source and test sites. Secondary errors are introduced as a result of reflections of the source. The computed patterns for the 100 element array deflected in accordance with the 100 rpm spin rate curve do not show asymmetries of sufficient magnitude to ignore the effects of measurement errors.

The measurable quantity is the angular deviation, $\Delta\phi$, between the peak of the beam of the deflected array and that of the undeflected array. Reference is made again to Figure 2-8. For a given θ, ϕ is varied until the peak of the beam is located. Figure 2-9 is a plot of the computed angular positions of the peak of the beam for 100 element array, 100 inches long, which has spin rates of 0, 100, and 180 rpm corresponding to various degrees of array deflection. The points are plotted against θ and ϕ which explains the curvature. The projection of the peak onto the Z-X plane would plot very nearly as a straight line and is indeed so for $\omega = 0$.

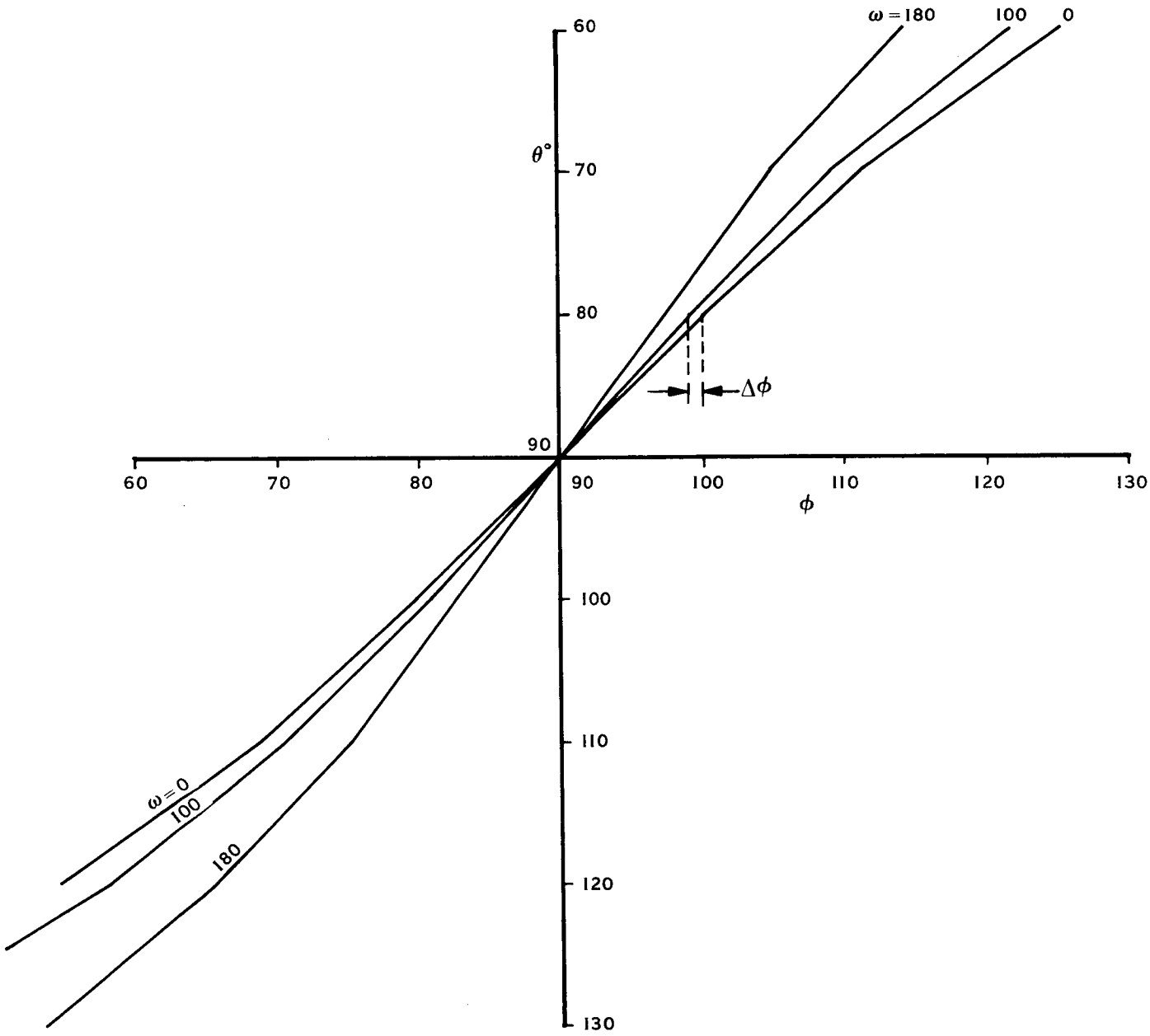

Figure 2-9 θ, ϕ Angular Positions of Peak of Fan Beam Undeflected (ω=0) and Deflected Arrays (ω=100, 180 rpm)

2.7.2 Technical Plan

By using the WDL rooftop track-mounted dual-axis tower and the 350-foot range patterns may be obtained for direct comparison to those calculated by the computer.

Referring to Figure 2-10, the undeflected array axis would be oriented at an angle of 45° to the horizontal rotation axis of the tower. The base or input end of the array would be rigidly supported at this angle and fixed to the horizontal rotary section of the tower. An auxilary rigid member would be attached to the horizontal rotary section orthogonal to the horizontal axis and parallel to the plane of the radiating slots. This member would be used to support the tension lines which would deflect the guide in a direction away from the horizontal spin axis. Shown also in Figure 2-10 are diagrams of the measurement and computer oriented coordinate systems. The two systems are seen to be identical by a simple rotation of the axes of either.

Conical cuts about the spin axis for any given angle, θ, from the spin axis are obtained by taking cuts about the horizontal axis for a given angle θ about the vertical axis. The angles may be read directly from either the servo indicator or the chart paper to an accuracy of $.06^{\circ}$. However, a measurement error of 0.2 db in determination of the peak can result in a position error of 0.3°. By using a linear potentiometer in the recording equipment an accuracy of .01 in power ratio may be achieved. This is equivalent to .045 db which would still result in a position error of 0.15°.

The procedure would be as follows: first locate the angular positions of the main axis of the beam called the boresight position to which all subsequent positions will be referred. Then for a given angle, θ, about the vertical axis the new position, ϕ, of the peak of the fan is determined by rotating the array about the horizontal axis. The procedure is repeated for different θ angles.

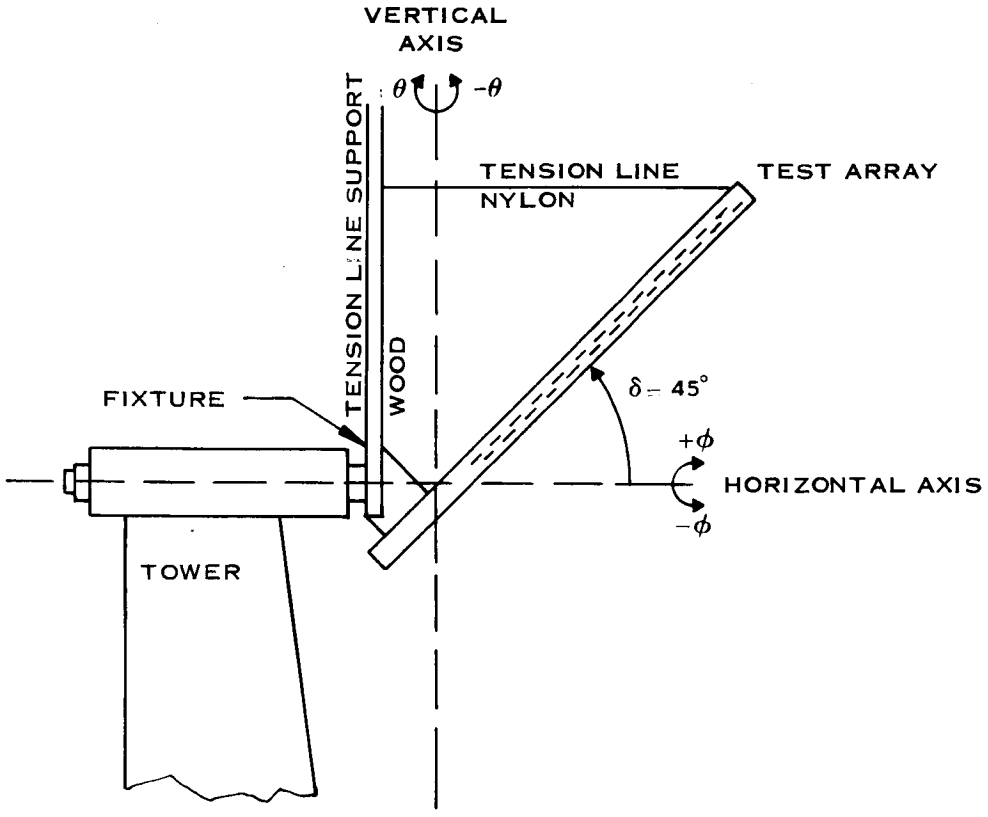

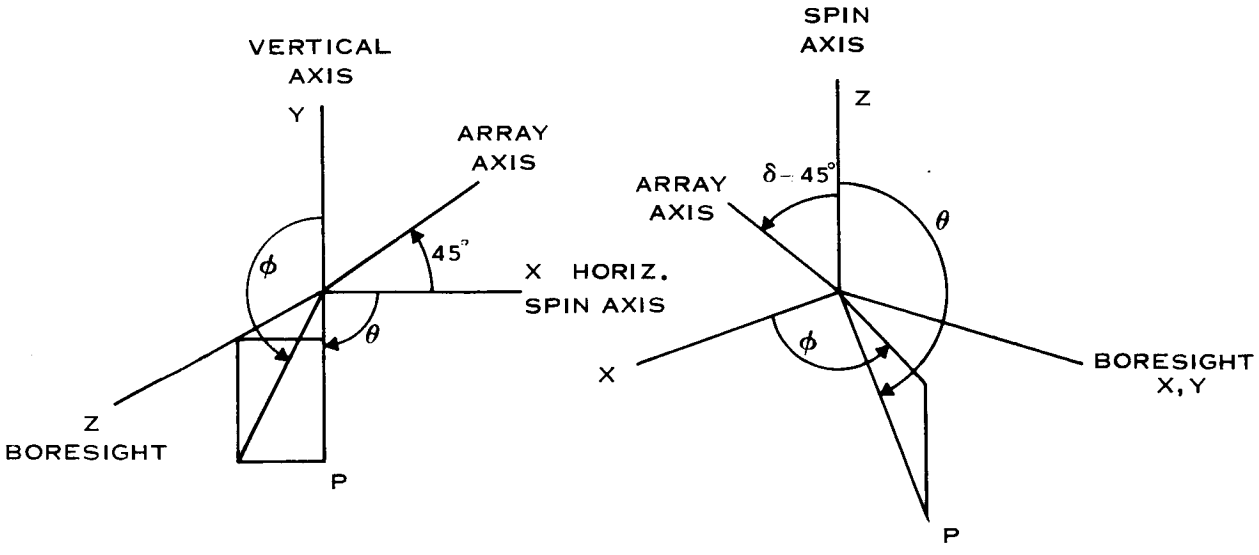

Measurement Coordinates **Computation Coordinates**

Figure 2-10 Boresight View From Source

This would be done first for the undeflected array and then for the deflected array, using the same θ angle in each case. The angle $\Delta\phi$ for a given θ is obtained directly from the pattern recordings.

2.7.3 Deflection Curve and Array Design

A laboratory experiment was performed on a section of waveguide to investigate a practical deflection curve which could be simulated on the range. The waveguide had the same electrical characteristics as the model given the computer and was deflected in the H plane. The results of the experiment was an analytical expression for a realizable deflection curve for a prescribed length based upon the design of the multi-element shunt-slot resonant array.

The deflection curve for a cantilever beam loaded by a force Q at the unsupported end is given by

$$y = \frac{Qx^2}{6EI}(3\ell - x) \qquad (13)$$

where y is the deflection at a position x along the axis of the undeflected beam. The load Q is applied at the end of the beam of length ℓ. I is the moment of inertia about the neutral axis and E is the modulus of elasticity of the material of the beam.

For aluminum alloys: $E = 8.95 \times 10^5$ psi

For the waveguide of O.D 1.250" x 0.625" and 0.064" wall thickness:

$$I = \frac{BA^3 - ba^3}{12} \text{ in}^4$$

where the capital letters refer to the outer dimensions and the lower case letters to the inner dimensions. A and B are respectively the broad and narrow dimensions. The deflection is in a plane parallel to the broad dimension, that is, in the H plane of the waveguide. Then

$$I = .043 \text{ in}^4$$

For Q = 30 lbs and ℓ = 40 inches the deflection y at x = ℓ is

$$y = \frac{Q\ell^3}{3EI} = 1.665 \text{ inches}$$

The following table shows the comparison between the calculated and measured deflection of the waveguide for a vertical load of 30 lbs applied at a distance of 40 inches from the rigidly supported end.

x (inches)	y $\left[= 1.300 \times 10^{-5} x^2 (120-x)\right]$ inches	Measured Deflection (inches)
10	0.143	.172
20	0.520	.525
30	1.052	1.050
40	1.665	1.653

2.7.4 Array Design for Pattern Computation

For $f_o = 8 \times 10^9$ cps., $\lambda_o = 1.4750$ inches. In waveguide size: 1.25 x 0.625 O. D. x 0.064 wall thickness.

$$\frac{\lambda_{g/2}}{\lambda_o} = \frac{d}{\lambda_o} = 0.6635$$

The element spacing d is then

$$d = 0.9787 \text{ inches}$$

For n = 40,

and the position of the first element at x = 6.00" the length of the guide will be

$$l = (n - 1)\, d + 6.00"$$
$$= 44.168"$$

The deflection curve is then given by

$$y = 1.300 \times 10^{-5}\, x^2\, (132.504 - x) \qquad (14)$$

The voltage amplitude associated with each slot is

$$E_i = \frac{1}{n} = \frac{1}{40}$$

$$E_i = .025$$

The phase of each slot is

$$\Psi_i = 0$$

2.7.5 Results of Pattern Computation

Figure 2-11 contains voltage plots of the computed patterns for the deflected and undeflected arrays for angles of 80, 70, 60 and 50 degrees. Figure 2-12 is a plot of the projection of the peak of the fan beam on the X-Z plane; see Figure 2-8. The X coordinate is proportional to sin θ sin (ϕ - 90) and the z coordinate is proportional to cos θ. Figure 2-12 shows that the plane of the fan makes an angle of 45° to the Y-Z plane for the undeflected array as expected. When the array is deflected according to the manner previously described the projection of the peak of the fan beam on the X-Z plane still describes a straight line. The plane of the fan now makes an angle of about 41.5° to the Y-Z plane.

For comparison the projection on the X-Z plane of the peak of the fan beam produced by the 100 element array spinning at 100 rpm is also shown in Figure 2-12. The straight line shown is only the linear portion of the true projection. The deviations from this line are reported in a subsequent section.

Figure 2-13 shows the deflection curves for the 40 element array and for the 100 element array "spinning at 100 rpm".

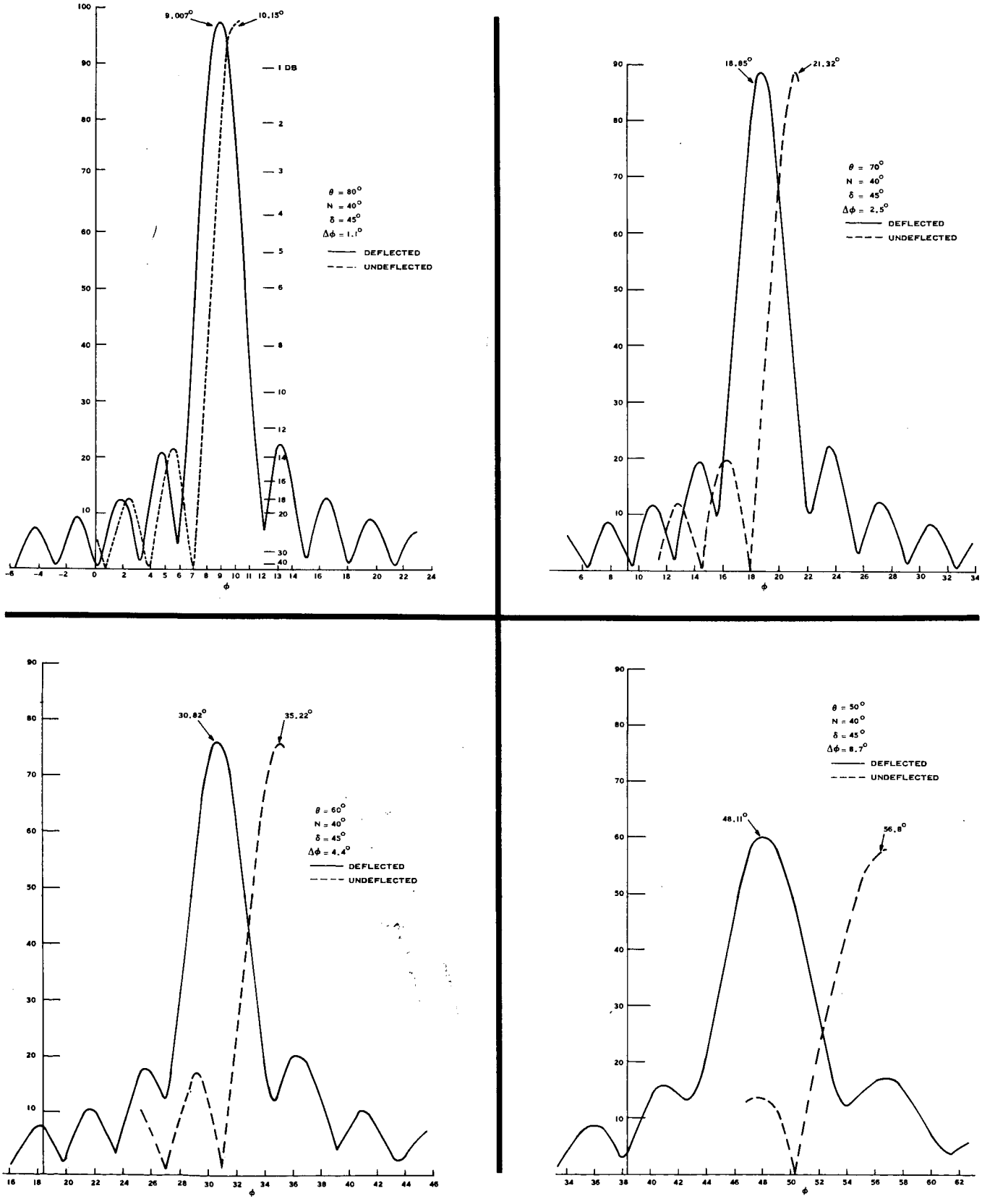

Figure 2-11 Computed Voltage Patterns for Deflected and Undeflected Arrays

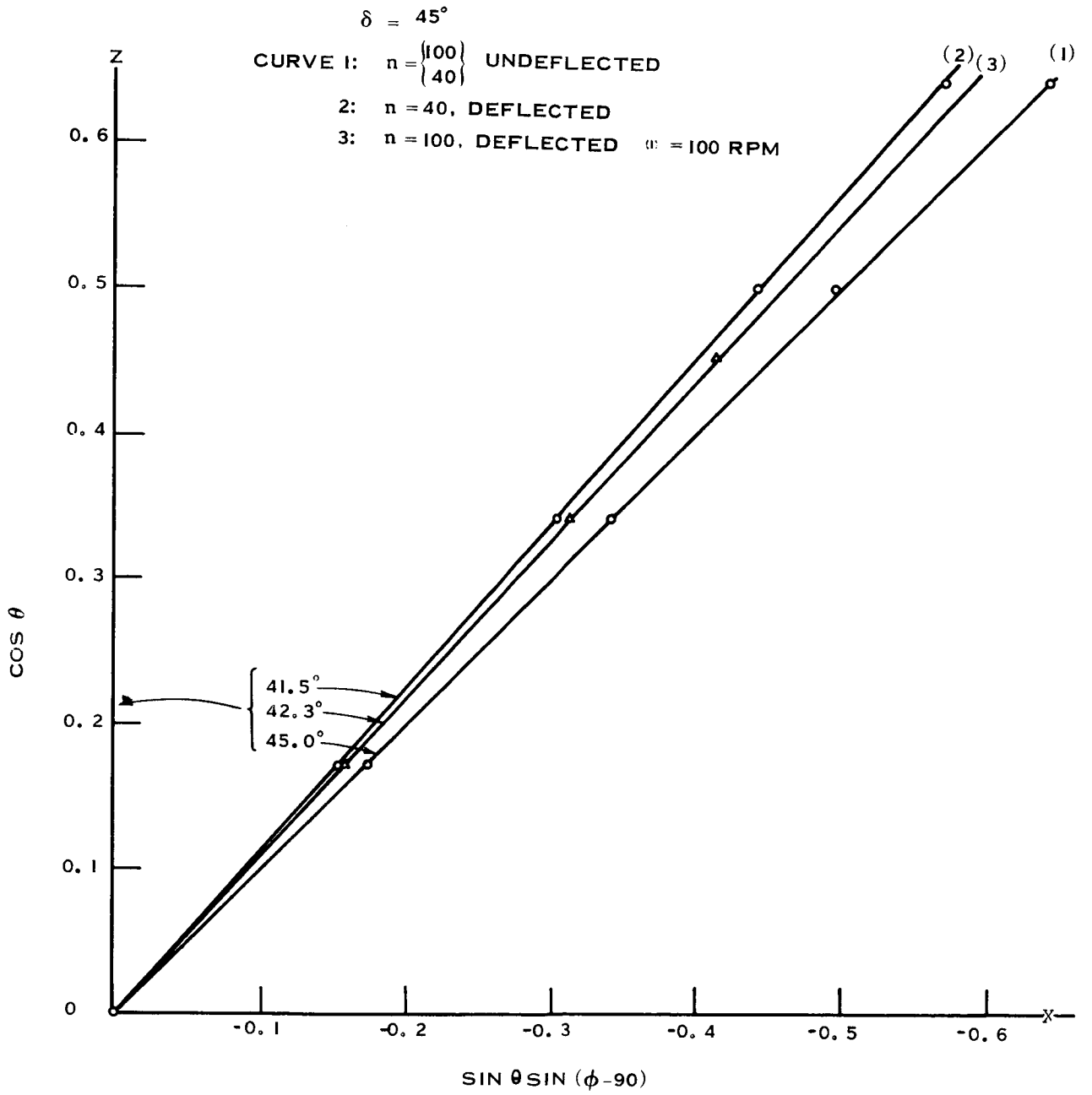

Figure 2-12 Projection of Peak of Fan Beam on X-Z Plane

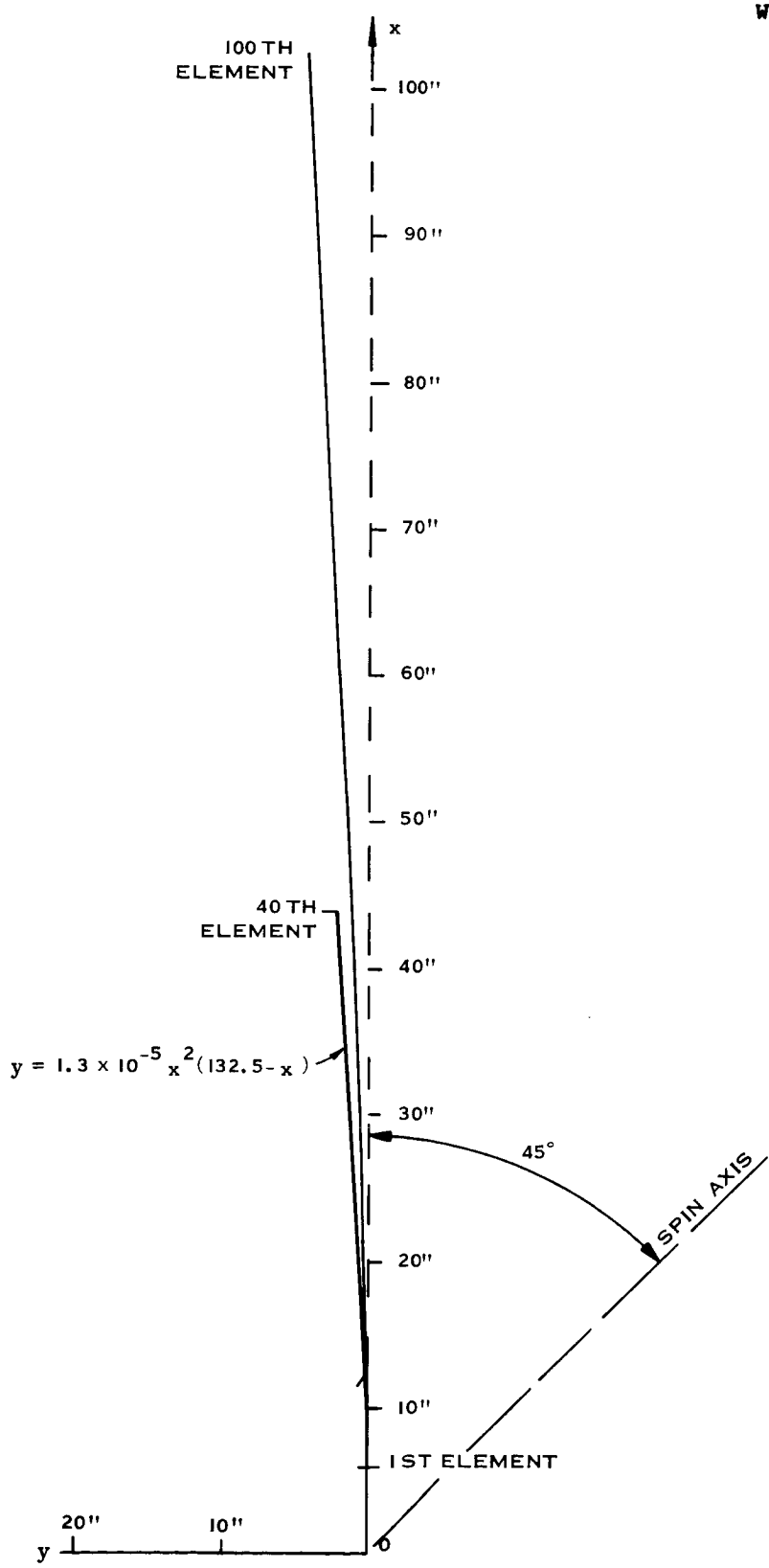

Figure 2-13 Deflection Curve for 100-Element Array (ω=100 rpm) and 40-Element Array

2.7.6 Array Design for Fabrication

In order to eliminate the accumulation of tolerance errors in the positioning of each slot radiator of a resonant array, the longitudinal positions are referrenced to the number 1 slot. A tolerance of ± 0.001" is placed on the position such that between any slot and the first the maximum phase error will be only ± 0.18°, and between any two slots, twice this.

Figure 2-14 is a fabrication sketch of the array. Table 2-1 gives the position of each slot along the axis of the array with respect to the first slot.

2.7.7 Range Geometry and Measurement Errors

The range geometry is as shown in Figure 2-15. The separation introduces only a 17° phase error between the center and the outermost edge of a 4 foot long array. This phase error results in a measurement error of about 0.5 db in side lobe level and negligible errors in gain or beamwidth. However, nulls are filled in and the first null will appear only about -22 db in depth for an undeflected array.

If the patterns are limited to -15° in ϕ defined in Figure 2-10 the amount of reduction of the reflected energy will be greater than 20 db as a result of the directivity of the test antenna.

If the source antenna has a total 3 db beamwidth in the vertical plane of about 12° the amount of reduction of the reflected energy is also greater than 20 db.

The total reduction of reflected energy over the direct energy is then greater than 40 db over the restricted range of ϕ. The measurement error introduced by the reflected energy is then less than 0.1 db.

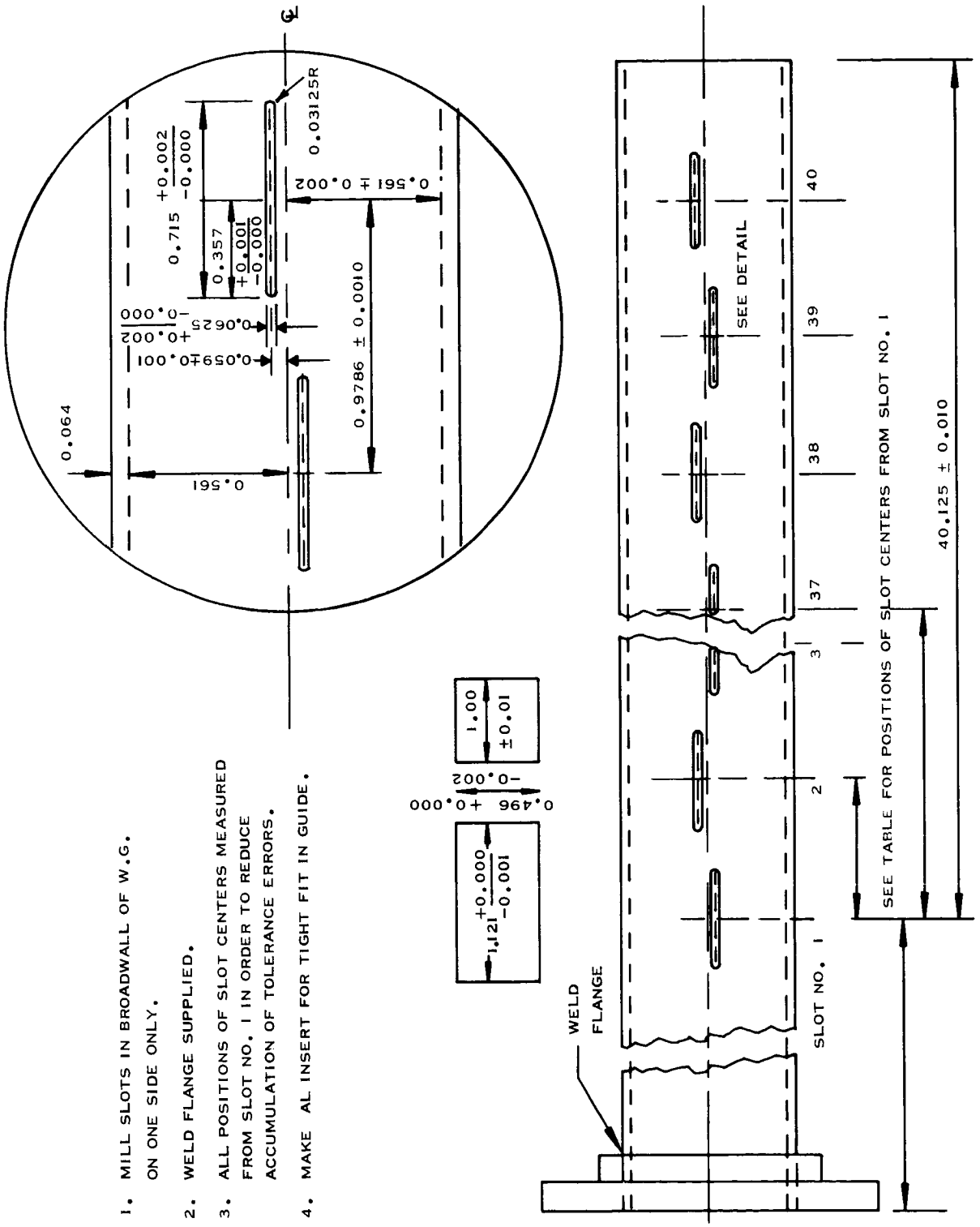

Figure 2-14 Fabrication Sketch-Slotted Waveguide Antenna Array

Table 2-1 Slot Positions (Tolerance: ±.001")

Slot No.	Distance From Slot No. 1	Slot No.	Distance From Slot No. 1
1	0.000	21	19.573
2	0.979	22	20.552
3	1.957	23	21.531
4	2.936	24	22.509
5	3.915	25	23.488
6	4.893	26	24.467
7	5.872	27	25.445
8	6.851	28	26.424
9	7.829	29	27.403
10	8.808	30	28.381
11	9.787	31	29.360
12	10.765	32	30.339
13	11.744	33	31.317
14	12.723	34	32.296
15	13.701	35	33.275
16	14.680	36	34.253
17	15.659	37	35.232
18	16.637	38	36.211
19	17.616	39	37.189
20	18.595	40	38.168

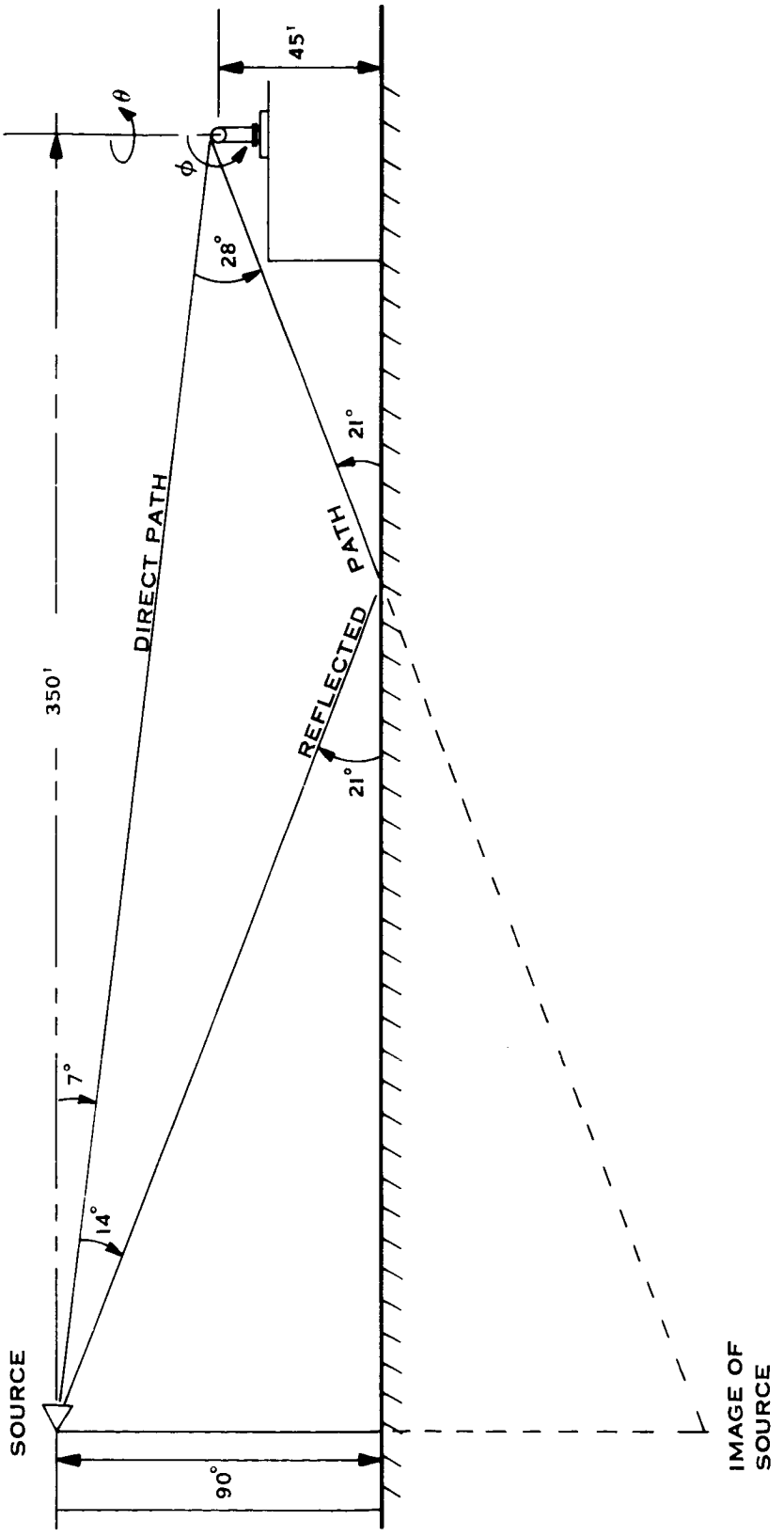

Figure 2-15 Antenna Range Geometry

SECTION 3

COMPUTER SIMULATION

3.1 INTRODUCTION

An antenna mounted on a spinning satellite will, in general, be deformed by the centrifugal force. This deformation may be expected to produce a corresponding deformation of the antenna's radiation pattern. A digital computer program was written to investigate and evaluate this effect. The program allows for the variation of a large number of parameters, such as antenna length, number of slots, spin rate, and mounting angle, δ. The program considers either guyed or unguyed cantilever antennas.

3.2 THEORETICAL DEVELOPMENT

3.2.1 Antenna Deflection

The antenna radiation pattern is a vector function of the slot positions. To determine these positions we solve the familiar differential equation for small deflections of uniform elastic beams, i.e.,

$$\frac{d^2y}{dx^2} = \frac{M}{EI}$$

where M is the bending moment, E is Young's modulus, I is the moment of inertia of the cross section of the beam about a horizontal line passing through the centroid of the section and lying in the plane of the cross section. The x-axis is along the undeflected antenna and the y-axis is normal to the x-axis and in the plane of the deflection with positive sense away from the spin axis. See Figure 3-1.

To determine M(x) we use the relations

$$\frac{d^2M}{dx^2} = p(x)$$

where p(x) is the loading function. Let ρ be the mass per unit length, ω the spin rate and δ the mounting angle, then the loading normal to the antenna is given by

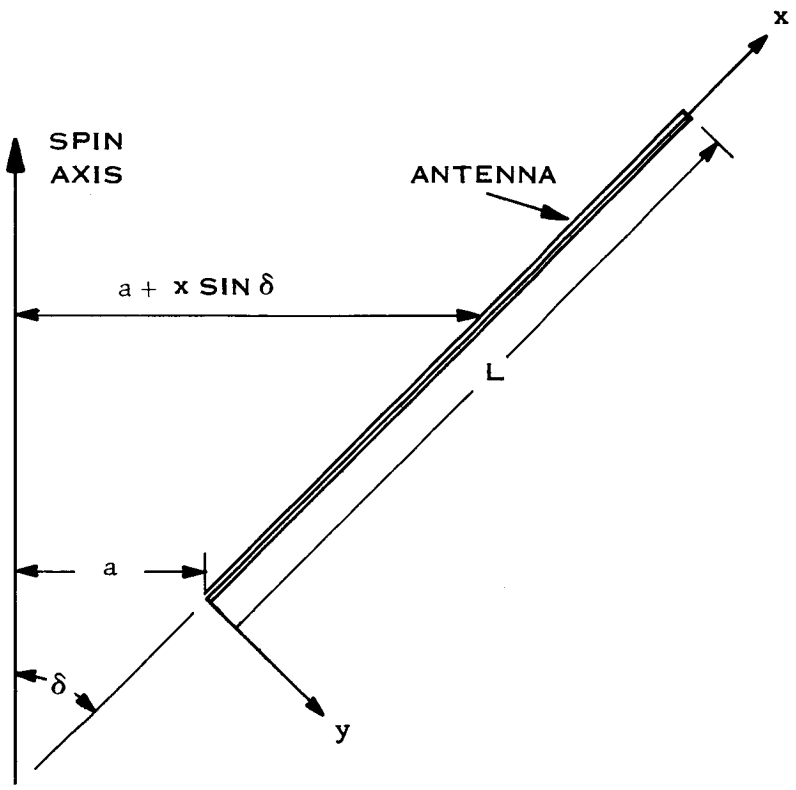

Figure 3-1 Position of Antenna Relative To Spin Axis

$$p(x) = \rho\omega^2(a + x \sin\delta) \cos\delta$$

3.2.2 Cantilever Antenna

For the simple cantilever antenna these two differential equations, along with the boundary conditions

$$y(0) = 0 \qquad M(L) = 0$$

$$y'(0) = 0 \qquad M'(L) = 0$$

yield the result:

$$y(x) = \frac{\rho\omega^2 \cos\delta}{24\,EI} x^2 \left[\frac{\sin\delta}{5} x^3 + ax^2 - 2L(2a + L \sin\delta)\, x + 2L^2(3a + 2L \sin\delta \right] \tag{15}$$

$$y'(x) = \frac{\rho\omega^2 \cos\delta}{24\,EI} x \left[\sin\delta\, x^3 + 4ax^2 - 6L(2a + \sin\delta) + 4L^2(3a + 2L \sin\delta \right]$$

However what we need to compute the radiation pattern is the position of the ith slot as a function of i. Since adjacent slots are separated by a constant distance Δs, which we may assume to be unchanged by small deflections, we may write

$$\Delta s = \sqrt{1 + \left(\frac{\Delta y_i}{\Delta x_i} \right)^2}\ \Delta x_i \tag{16}$$

where $\Delta x_i = x_i - x_{i-1}$ and $\Delta y_i = y(x_i) - y(x_{i-1})$. From the mean value theorem for derivatives we know that

$$y'(\xi_i) = \frac{y(x_i) - y(x_{i-1})}{x_i - x_{i-1}}$$

for some ξ such that $x_{i-1} \le \xi_i \le x_i$. Substituting $y'(\xi_i) = (\Delta y_i / \Delta x_i)$ and solving Equation (16) for Δx_i we obtain

$$\Delta x_i = \frac{\Delta s}{\sqrt{1 + y'(\xi_i)^2}} \tag{17}$$

Then, given an initial value of x, say x_0, we can solve for x_i and y_i from the recursion relations

$$\begin{aligned} x_i &= x_{i-1} + \Delta x_i \\ y_i &= y_{i-1} + y'(\xi_i)\Delta x_i \end{aligned} \tag{18}$$

provided ξ_i is known. In practice $\xi_i = x_{i-1} + 1/2\ \Delta x_{i-1}$ is found to give sufficiently good results.

3.2.3 Guyed Antenna

The guyed configuration is more complex but a closed form solution can still be obtained by solving the differential equations separately for two sections of the antenna. Let a guy wire be attached to the antenna at x = b, and let $y_I(x)$ be the solution on the interval $(0 \le x \le b)$ and $y_{II}(x)$ be the solution on the interval $(b \le x \le L)$. The boundary conditions may then be stated as

$$y_I(0) = 0 \qquad y_I(b) = y_{II}(b) = 0 \qquad y_{II}''(L) = 0$$

$$y_I'(0) = 0 \qquad y_I'(b) = y_{II}'(b) \qquad y_{II}'''(L) = 0$$

$$y_I''(b) = y_{II}''(b)$$

These conditions lead to eight linear equations in the eight unknown constants of integration.

After considerable amount of algebraic manipulation the following results are obtained:

$$y_I(x) = Cx^2 \left[\frac{1}{2} \sin\delta\, x^3 + \frac{1}{4} H_{11}\, x^2 + \frac{1}{3} H_{12}\, x + \frac{1}{2} H_{13} \right]$$

$$y'_\ell(x) = C \left[\sin\delta\, x^4 + H_{\ell 1}\, x^3 + H_{\ell 2}\, x^2 + H_{\ell 3}\, x + H_{\ell 4} \right]$$

where

ℓ = I or II

$$C = \frac{\rho\omega^2 \cos\delta}{24\, EI}$$

$$D = \frac{b^2}{10}(5a + b \sin\delta)$$

$$E = bL(2a + L \sin\delta)$$

$$F = L^2(3a + 2L \sin\delta)$$

$$H_{11} = 4a$$

$$H_{12} = 3(D - 3E + F)/b$$

$$H_{13} = -6(D + E - F/3)$$

$$H_{14} = 0$$

$$H_{21} = 4a$$

$$H_{22} = -6E/b$$

$$H_{23} = 4F$$

$$H_{24} = -3b(D - E + F)$$

3.2.4 Antenna Pattern Equations

Let the antenna lie in x y plane. We define a vector $\bar{r}_i$ from the origin 0 to the ith slot. Also let $\hat{e}$ be a unit vector directed toward an observer in the far field. The unit vector $\hat{e}$ may be expressed in terms of the parametric angles η,γ as

$$\hat{e}(\gamma,\eta) = \begin{pmatrix} \cos\eta \sin\gamma \\ \sin\eta \sin\gamma \\ \cos\gamma \end{pmatrix}$$

See Figure 3-2.

The resultant field is then given by

$$E(\hat{e}) = f(\hat{e}) \sum_{i=1}^{n} E_i \exp j\left[\psi_i + 2\pi(\bar{r}_i \cdot \hat{e})/\lambda\right] \tag{20}$$

where n is the number of slots, $f(\hat{e}) = f(\gamma)$ is a factor describing the pattern of a single slot (assumed to be the same for all slots), E_i is the amplitude and ψ_i the phase (relative to slot 1) of the ith slot, and λ is the free space wavelength. The pattern factor $f(\hat{e})$ is given by

$$f(\hat{e}) = f(\gamma) = \frac{1}{2}(1 + \cos\gamma) \frac{\cos\left(\frac{\pi\ell}{\lambda}\sin\gamma\right)}{1 - \left(\frac{2\ell}{\lambda}\sin\gamma\right)^2} \tag{21}$$

where ℓ is the slot length. The nominal slot length is $\ell = \lambda/2$. Making this substitution, $f(\gamma)$ simplifies to

$$f(\gamma) = \frac{(1 + \cos\gamma)\cos\left(\frac{\pi}{2}\sin\gamma\right)}{2\cos^2\gamma}$$

3.2.5 Co-ordinate Transformation

Let δ be the angle between the spin axis and the undeflected antenna. We can define another co-ordinate system (XYZ) having the satellite spin axis as its Z axis, with Y = z, and with X completing the orthogonal-right-handed triad. See Figure 3-3.

The transformation $T(\delta)$ from the XYZ co-ordinate system is given by

$$T(\delta) = \begin{pmatrix} \sin\delta & 0 & \cos\delta \\ \cos\delta & 0 & -\sin\delta \\ 0 & 1 & 0 \end{pmatrix} \tag{22}$$

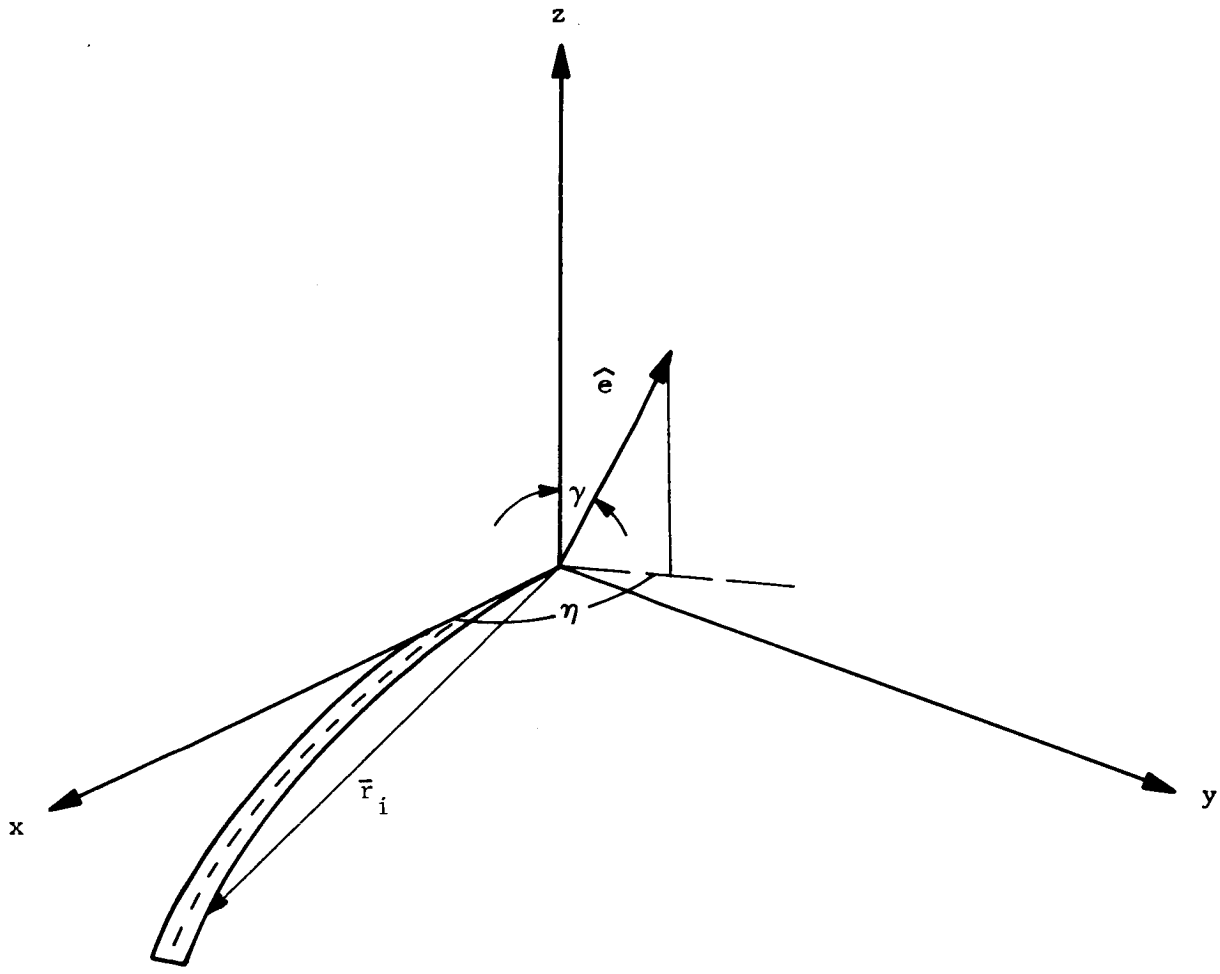

Figure 3-2 Antenna Coordinate System

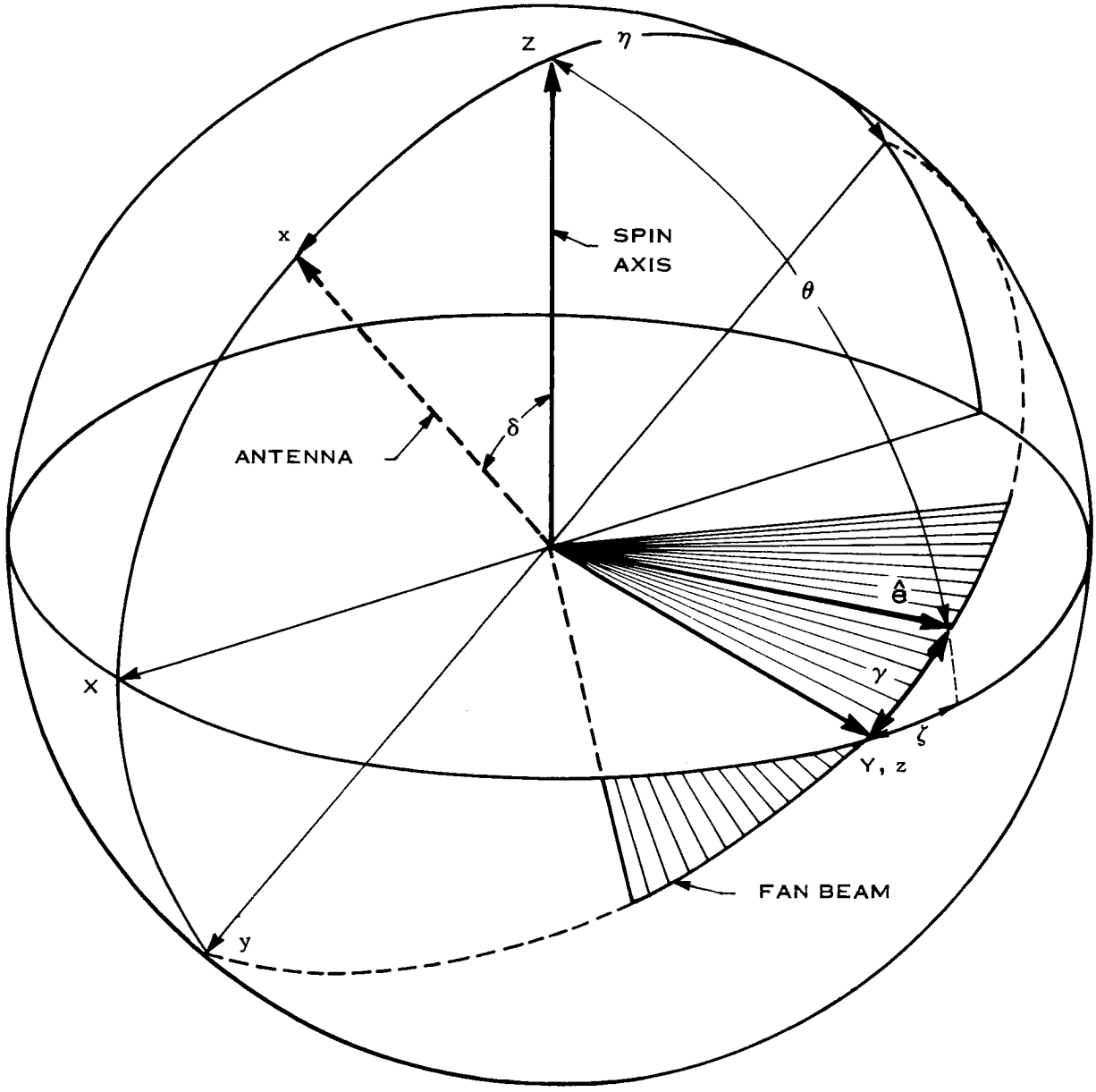

Figure 3-3 System Geometric Relationships

In the XYZ system the unit vector $\hat{e}$ directed toward an observer is given by

$$\hat{e}(\theta,\varphi) = \begin{pmatrix} \cos\varphi & \sin\theta \\ \sin\varphi & \sin\theta \\ & \cos\theta \end{pmatrix}$$

where θ is the angle between $\hat{e}$ and the spin axis, and φ is the angle from the X-axis to the projection of $\hat{e}$ on the XY-plane. It is convenient to define another angle, ζ, also measured in the XY-plane, by the equation $\zeta = \varphi - \pi/2$. See Figure 3-3 for illustration of these angles.

3.2.6 Beam Maximum

In the XYZ system rotation about the spin axis is measured by φ, while θ remains constant. Thus to evaluate the beam as it would appear to an observer, a value of θ is selected and then φ is varied over the range of interest in the neighborhood of maximum field strength E_{max}. Thus for a given value of θ and φ we have

$$\hat{e}(\gamma,\eta) = T(\delta)\ \hat{e}(\theta,\varphi) \qquad (23)$$

It can be shown that for an ideal undeflected antenna the fan beam lies in the yz-plane with absolute maximum in the z direction. Thus E is maximized with respect to η when $\eta = -\pi/2$ and the absolute maximum, E_{max}, occurs at $\gamma = 0$. By expanding the transformation equation above we obtain the relations

$$\cos\eta \sin\gamma = \cos\varphi \sin\theta \sin\delta + \cos\theta \cos\delta$$

$$\sin\eta \sin\gamma = \cos\varphi \sin\theta \cos\delta - \cos\theta \sin\delta$$

$$\cos\gamma = \sin\varphi \sin\theta$$

Thus, for an ideal beam, the maximizing value of φ is given by

$$\varphi = \cos^{-1}(-\cot \delta \cot \theta).$$

3.2.7 Beam Deflection

When the antenna undergoes a small deflection in the xy-plane the maxima will, in general, no longer occur at $\eta = -\pi/2$. However the beam may remain substantially planar, in which case the maxima will occur at η = const. If a maximum occurs at (θ,φ), the corresponding value of η is given by

$$\eta = \tan^{-1}\left(\frac{\cos\varphi \sin\theta \cos\delta - \cos\theta \sin\delta}{\cos\varphi \sin\theta \sin\delta + \cos\theta \cos\delta}\right)$$

If $\Delta\eta/\Delta\theta$ is small over the range of θ it is useful to determine a mean value of η, η' which then may be regarded as defining a reference plane which closely approximates the almost planar beam. This reference plane can be thought of as an ideal planar beam generated by an antenna mounted at an angle $\delta' = \delta + \left(\eta' + \frac{\pi}{2}\right)$ which will be referred to as the effective mounting angle. Using this ideal planar beam as a model we have

$$\varphi' = \cos^{-1}(-\cot \delta' \cot \theta)$$

and the residual is given by

$$\Delta\varphi(\theta) = \varphi' - \varphi$$

where

$$\eta' = \frac{1}{K}\sum_{i=1}^{K} \eta(\theta_o - i\,\Delta\theta)$$

3.3. SIMULATION

3.3.1 Program Description

The philosophy in writing this computer program was to make it as general and versatile as possible within the scope of the study. Most separable functions are written as subroutines to allow modular interchange and easy modification. The entire program is written in FORTRAN IV and is thus usable on any machine with a FORTRAN IV compiler. However, a user's manual is not as yet available.

The general flow of the program is illustrated in Figure 3-4. The data consists of a set of physical parameters and a set of program control parameters. The physical parameters considered are listed below.

ω	satellite spin rate
E	Young's modulus for antenna material
I	antenna moment of inertia
W	antenna weight/length
L	antenna length
a	radial distance of antenna mount from spin axis
x_o	distance from antenna base to first slot center
s	slot spacing
λ	free space wavelength
nx	number of slots/row
ny	number of rows
δ	acute angle between antenna and spin axis
θ_o	initial value of θ
$\Delta\theta$	step size in θ
$\Delta\varphi$	step size in φ
E_t	detection threshold value of E

(The following parameters apply only to antenna pair.)

x_m	separation in x direction
n_a	number of slots in "A" antenna
n_b	number of slots on "B" antenna

The main control parameters are TAB, XTOL, YTOL, FKEY, PLOT, and PHS.

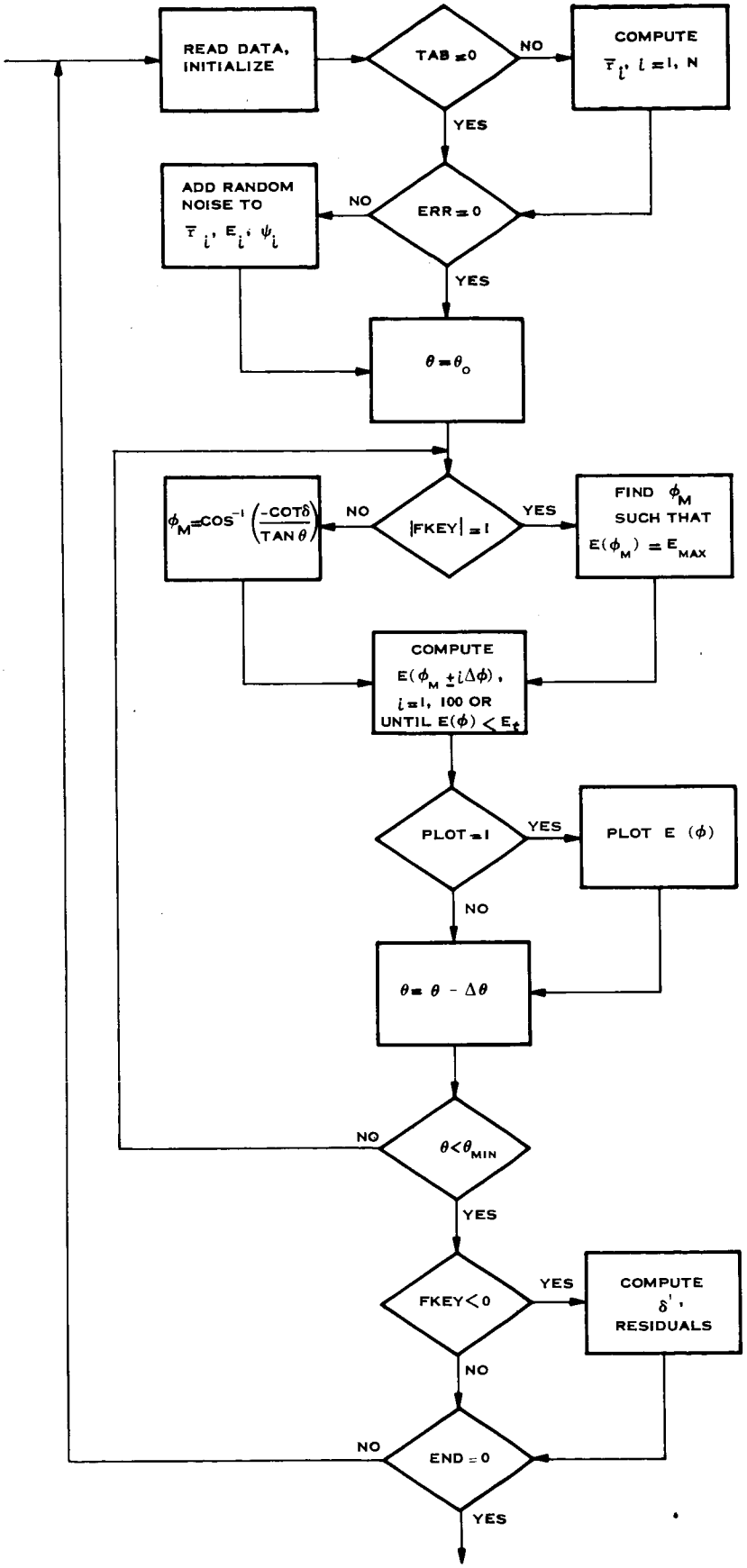

Figure 3-4 Flow Chart of Beam Analysis Program

The TAB options are as follows:

(1) TAB = 0, do not compute new $\bar{r}_i$;
(2) TAB = 1, compute $\bar{r}_i$ with simple cantilever formula;
(3) TAB = 2, compute $\bar{r}_i$ with guyed cantilever formula;
(4) TAB = 3, compute $\bar{r}_i$ with a special subroutine.

At present there are three special subroutines which may be used under option (4);

(1) The values of $\bar{r}_i$ and ψ_i, are read in as data;
(2) The values of $\bar{r}_i$ are computed for an antenna with a single discreet applied force;
(3) The values of $\bar{r}_i$, E_i, and ψ_i are set up for an antenna pair.

The XTOL and YTOL options allow the simulation of random variation of each slots x or y co-ordinate within specified tolerances. The errors may be considered simultaneously or independently. The effect of these errors on phase and amplitude is also considered. A uniformly distributed set of pseudo random numbers on the unit interval is obtained using a recursion generator which may be formally represented as $R_i = g(R_{i-1})$ where $R_1 = g(1)$. A uniformly distributed set is used rather than a normally distributed set, on the hypothesis that the uniform distribution will tend to show "worst case" behavior whereas a normally distributed set would tend to demonstrate the "most probable case." No attempt was made to prove this hypothesis.

If XTOL $\neq$ 0, then

$$\left.\begin{aligned} \Delta x_i &= (2R_i - 1)\,(\mathrm{XTOL}) \\ x_i &= x_i + \Delta x_i \\ \psi_i &= \frac{2\pi}{\lambda_g}\,\Delta x_i \end{aligned}\right\} \quad i = 1,n$$

If YTOL $\neq$ 0, then

$$\left.\begin{aligned} \Delta y_i &= (2R_i - 1)\ (\text{YTOL}) \\ y_i &= y_i + \Delta y_i \\ F_{Ai} &= F_{Ai} + 5\ \Delta y_i \end{aligned}\right\} \quad i = 1,n$$

The parameter FKEY serves in two capacities. First if |FKEY| = 1, the value of φ, φ_M, which maximizes E (for a specified value of θ) is determined numerically. If |FKEY| $\neq$ 1, then the theoretical value for an undeflected beam crossed normally is used, i.e., $\varphi_M = \cos^{-1}(-\cot \delta \cos \theta)$. Secondly, if FKEY is negative, the effective mounting angle $\bar{\delta}$ and residual values of $\Delta\varphi$ are determined.

The parameter PLOT (as one might suspect) controls the plotting option. If PLOT = 0, the set of values $E(\varphi)$, θ = constant is processed for plotting on the Philco-Calcomp plotter.

The parameter PHS is meaningful only when the antenna pair option is used. If PHS = 0, the two antennas are driven in phase, otherwise they are driven 180^o out of phase.

3.3.2. Simulated Antenna Pattern

First consider an ideal fan beam generated by an undeflected antenna. Figure 3-5 shows a broad dimension view of the beam and Figure 3-6 shows an "edge" view of the beam, displaying normal (90^o) cross-section for several values of θ. Figure 3-7 is a contour plot of the field. Lines of constant field strength are plotted as functions of θ and ξ. Some care must be exercised in deriving information from this figure since it resembles a mercator projection, and thus has certain inherent distortions, (i.e., Greenland appears to be as large as South America).

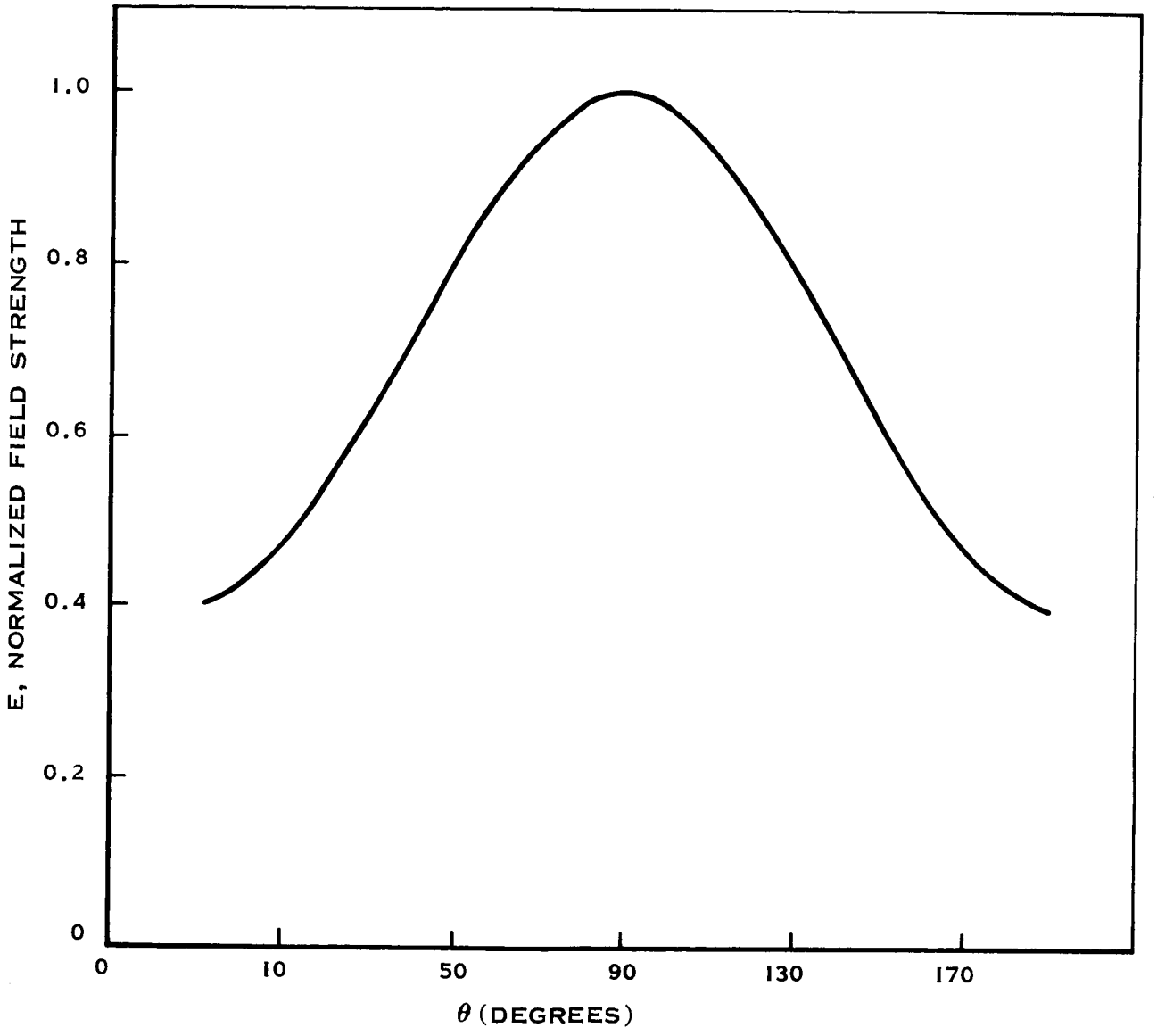

Figure 3-5 Broad Dimension View (δ=90°) of Undeflected Fan Beam

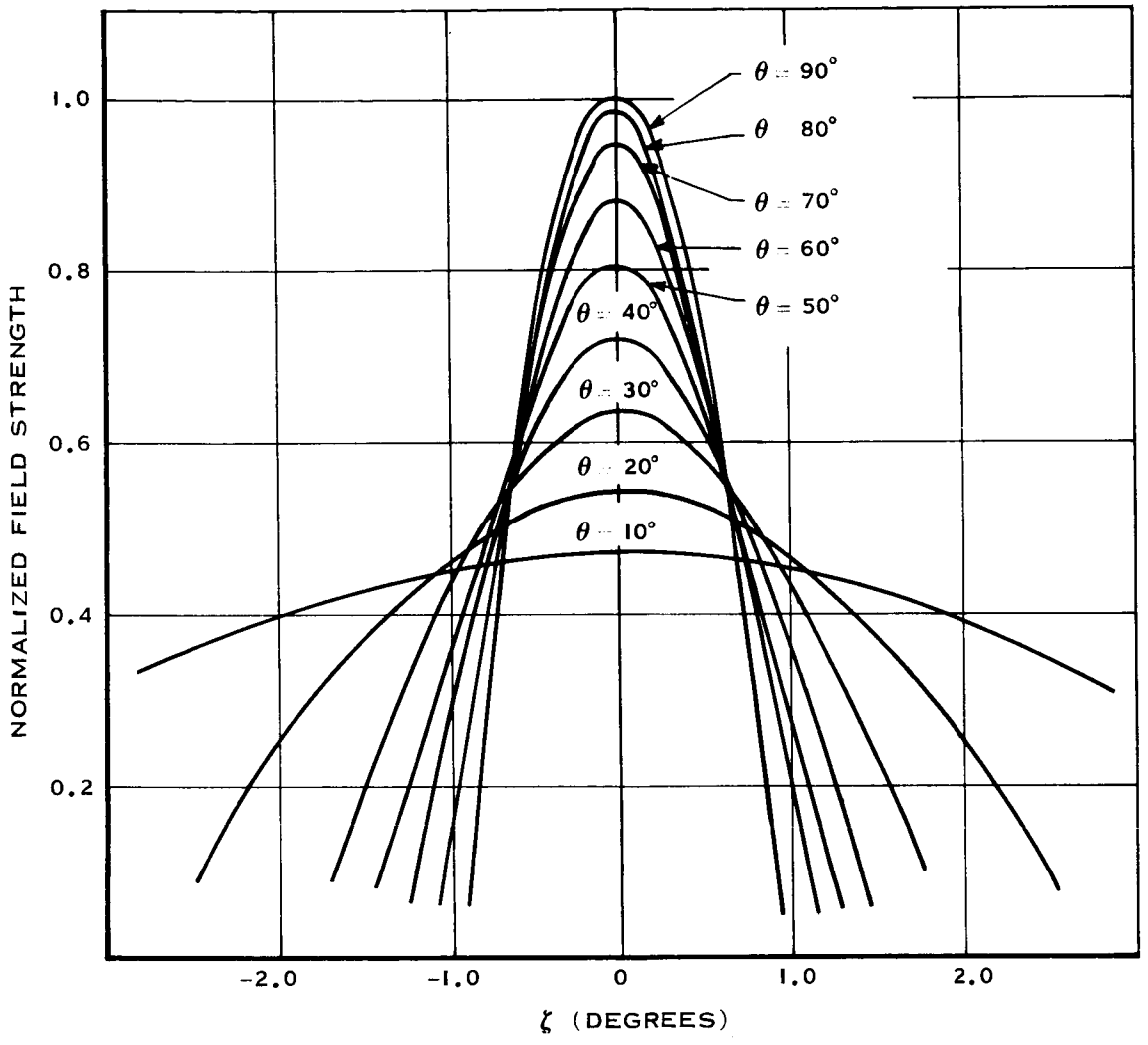

Figure 3-6 Edge View of An Ideal Fan Beam

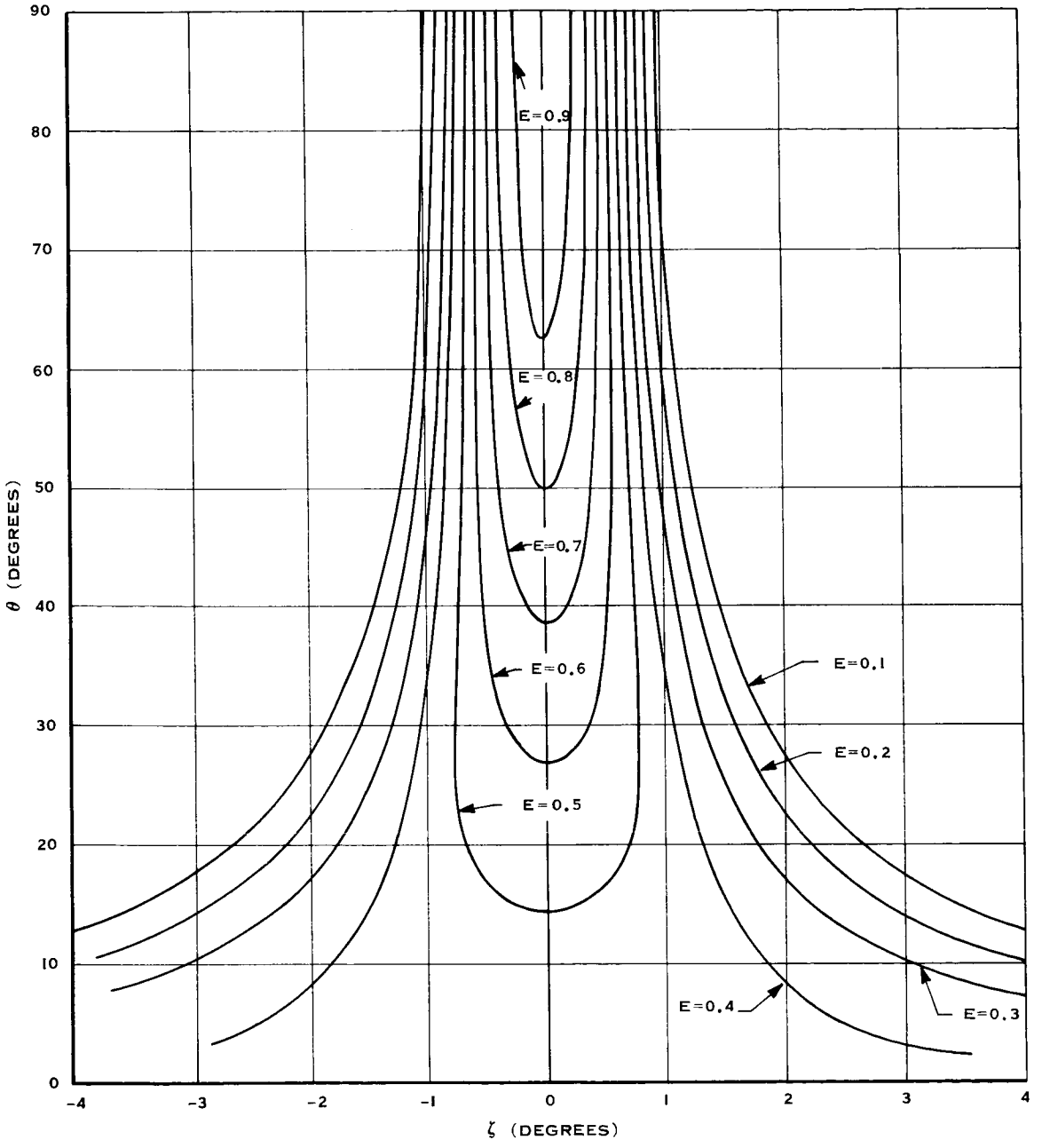

Figure 3-7 Contour Plot of Fan Beam

Some definitions will be useful at this point.

(1) Geometric Maximum. The geometric maxima of an ideal fan beam occurs at $\eta = -\pi/2$, i.e., $\frac{\max}{\eta} E(\gamma,\eta) = E(\gamma, -\pi/2)$. More intuitively it is simply the center of a symmetric beam.

(2) Cross-Section Maximum. A cross-section maximum is defined to be $\frac{\max}{\varphi} E(\varphi,\theta)$. The surprising (possibly) thing about cross-section maxima is that they do not in general coincide with geometric maxima for other than normal cross-sections ($\delta = \pi/2$). This result is due to the fact that $E(\gamma, -\pi/2)$ decreases montonically as γ increases, and to the finite width of the fan beam. See Figures 3-8, 3-9 and 3-10.

(3) Mean Threshold (or Detector) Maximum. First we define φ_{in} as the minimum value of φ such that $E(\theta,\varphi) \geq E_t$ and φ_{out} as the minimum value of φ such that $\varphi_{out} \geq \varphi_{in}$ and $E(\theta,\varphi) \leq E_t$, where E_t corresponds to a detector threshold. (In this study $E_t = 0.6\ E_{max}$.) The mean threshold maximum is then defined to be $E(\theta,\varphi_{mean})$ where $\varphi_{mean} = (\varphi_{in} + \varphi_{out})/2$. For the interval ($60^\circ < \theta < 90^\circ$), $\varphi_{mean} < \varphi_{geometric}$, due to the gradual narrowing of the beam at the $E = 0.6\ E_{max}$ level.

Figure 3-11 shows the relative position of geometric maxima, cross-section maxima and mean threshold points for an undeflected fan beam cut diagonally ($\delta = 45^\circ$).

Also note that crossing the beam at an acute angle causes the apparent beam width to increase as θ decreases from $\pi/2$. This effect is due to the fact that the crossing angle, equal to δ at $\theta = \pi/2$, decreases to zero at $\theta = \pi/2 - \delta$. This makes the beam slightly asymmetric as well as increasing the apparent beam width. However, these effects are small in the region of interest ($60^\circ < \theta < 120^\circ$). All the effects mentioned so far have been for an ideal undeflected antenna.

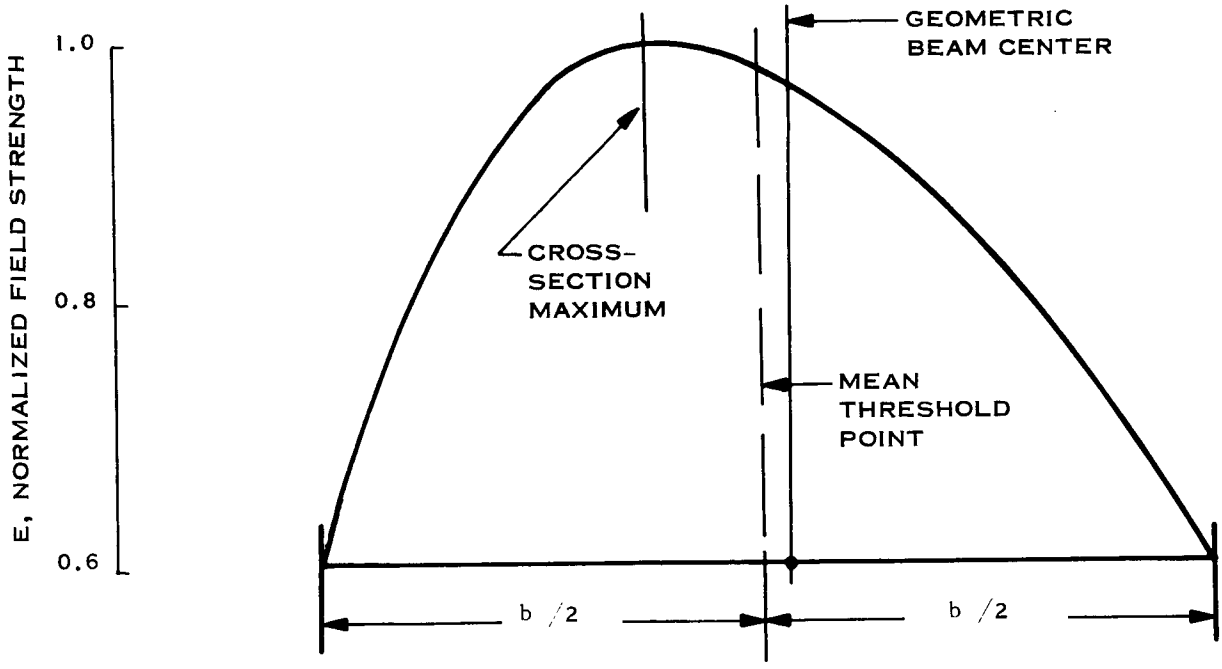

Figure 3-8 Beam Cross Section, Illustrating Defined Terms

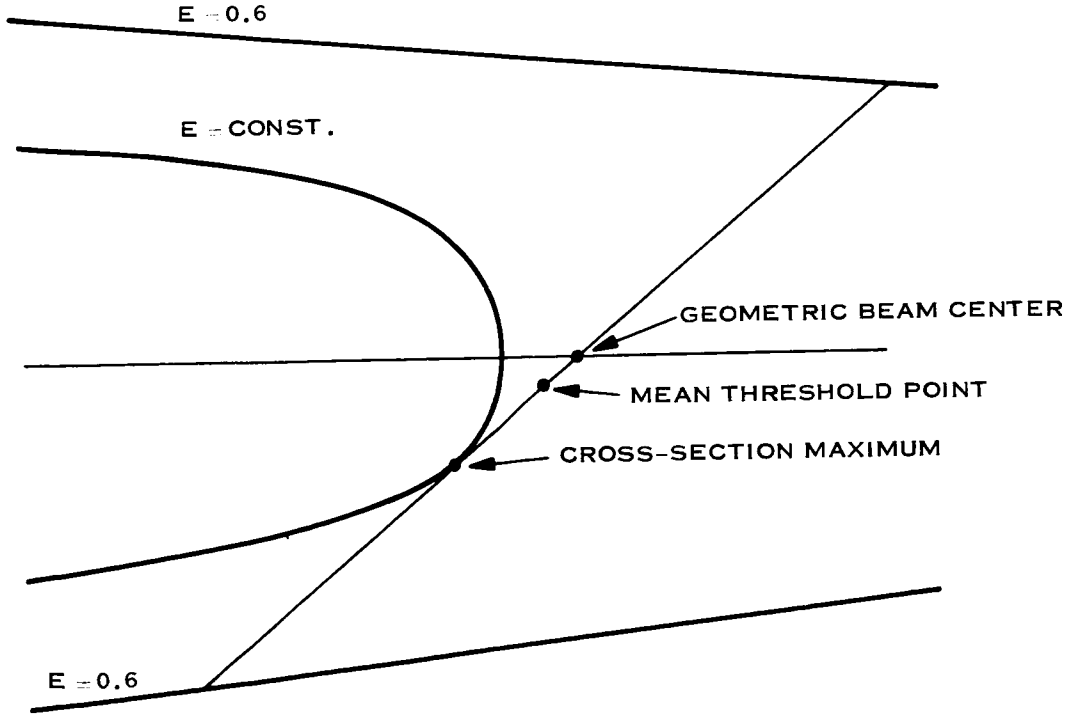

Figure 3-9 "Top" View of Beam, Illustrating Defined Terms

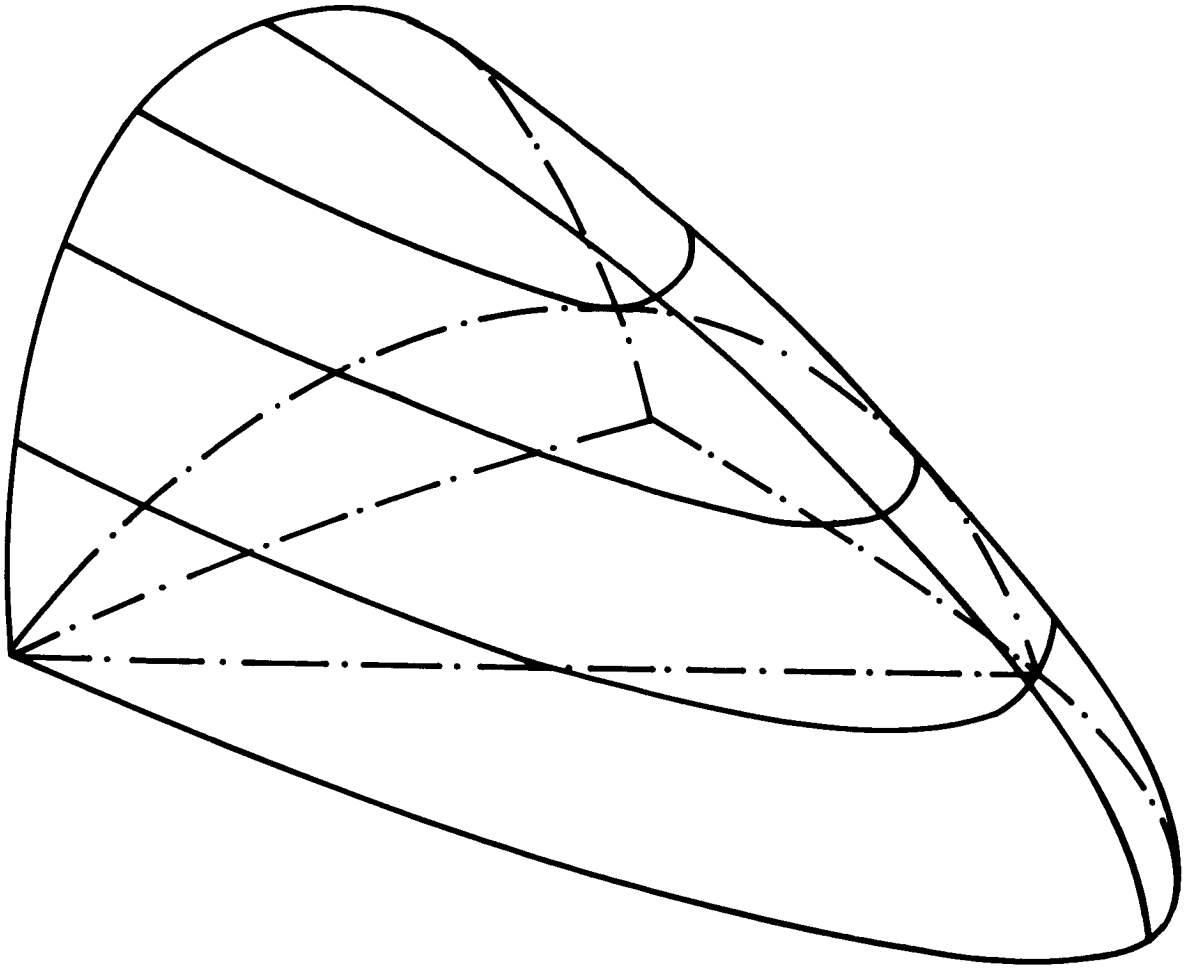

Figure 3-10 Schematic View of A Beam Section

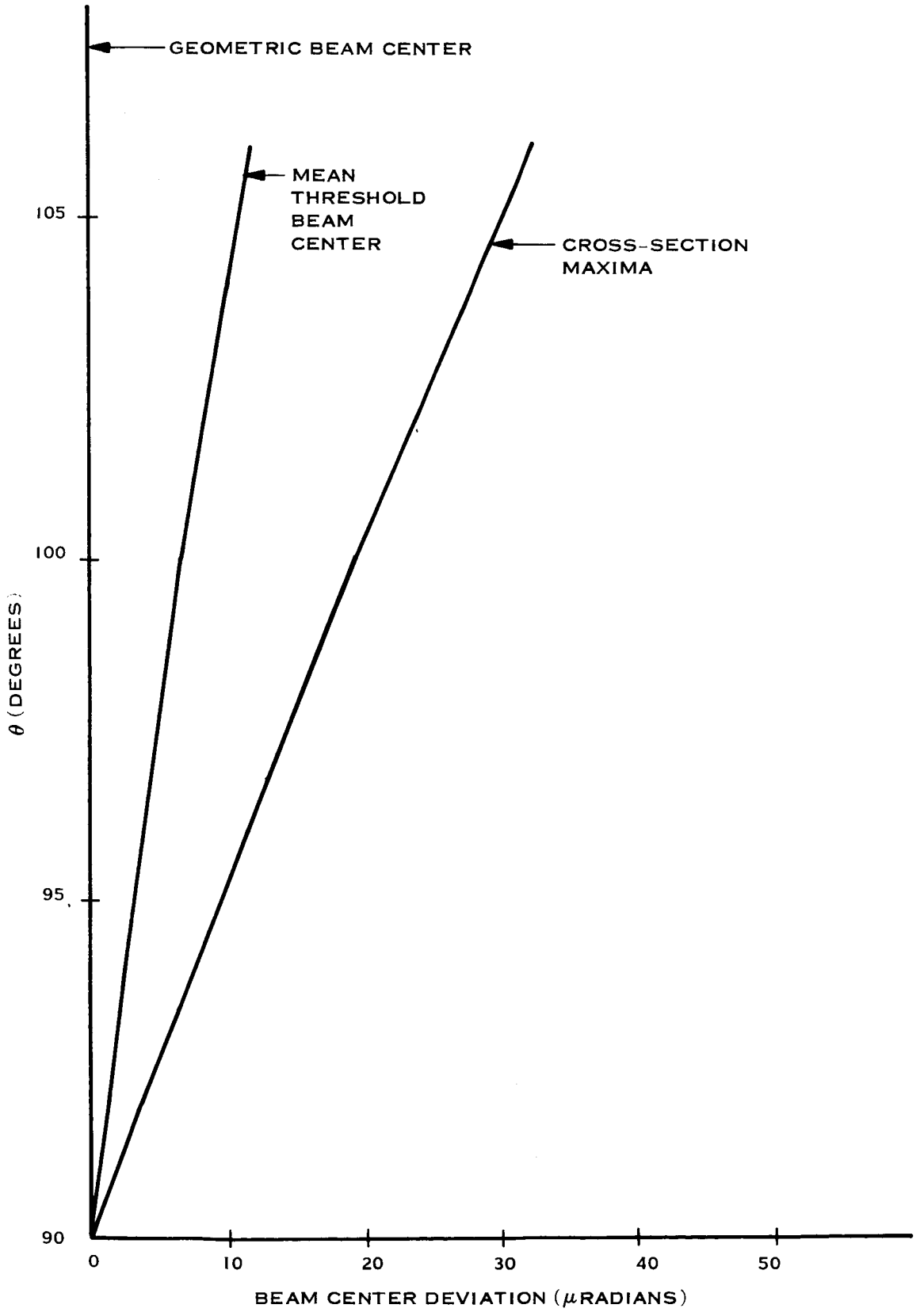

Figure 3-11 Relative Location of Various Beam "Centers" for Undeflected Antenna

3.3.3 Deflected Antenna Effects

Despite the fact that the array is no longer linear after the antenna is deflected, it is found that the fan beam remains very nearly planar. The primary effect is that the beam is turned through about the same angle as the antenna. Thus the pattern generated by a deflected antenna, for deflections of a few degrees, can be closely approximated by a straight antenna lying approximately along the deflected and bent antenna. This is an important conclusion. The degree to which it holds under varying conditions will be discussed later in this report.

The deflected beam is also found to be slightly asymmetric in cross-section. This may be seen in many of the figures included in the Appendix C of this report. It is interesting to note that this asymmetry causes the mean threshold and the cross-section maximum to reverse themselves, i.e., in the deflected case the cross-section maximum is closer to the geometric beam center, contrary to the undeflected case. Deflection also reduces the broad beam beamwidth. See Figure 3-12.

3.3.4 Single Antenna Study

There are so many parameters involved in simulating the antenna pattern that it would be impractical to consider all possible combinations. Instead, all parameters except one were held at a nominal value while that one was allowed to take on several values. The parameters considered in this part of the study were antenna length (and number of radiators), spin rate, antenna mounting angle, as well as guyed and unguyed antennas. The cases considered are tabulated below. The nominal values of the parameters are boxed.

L, antenna length, inches	**83.8**	44.7	64.2	103.4
n, number of radiators	**80**	40	60	100
ω, spin rate, RPS	**2**	1	3	
δ, Mounting angle, degrees	**45**	30	60	
support	**None**	guyed		

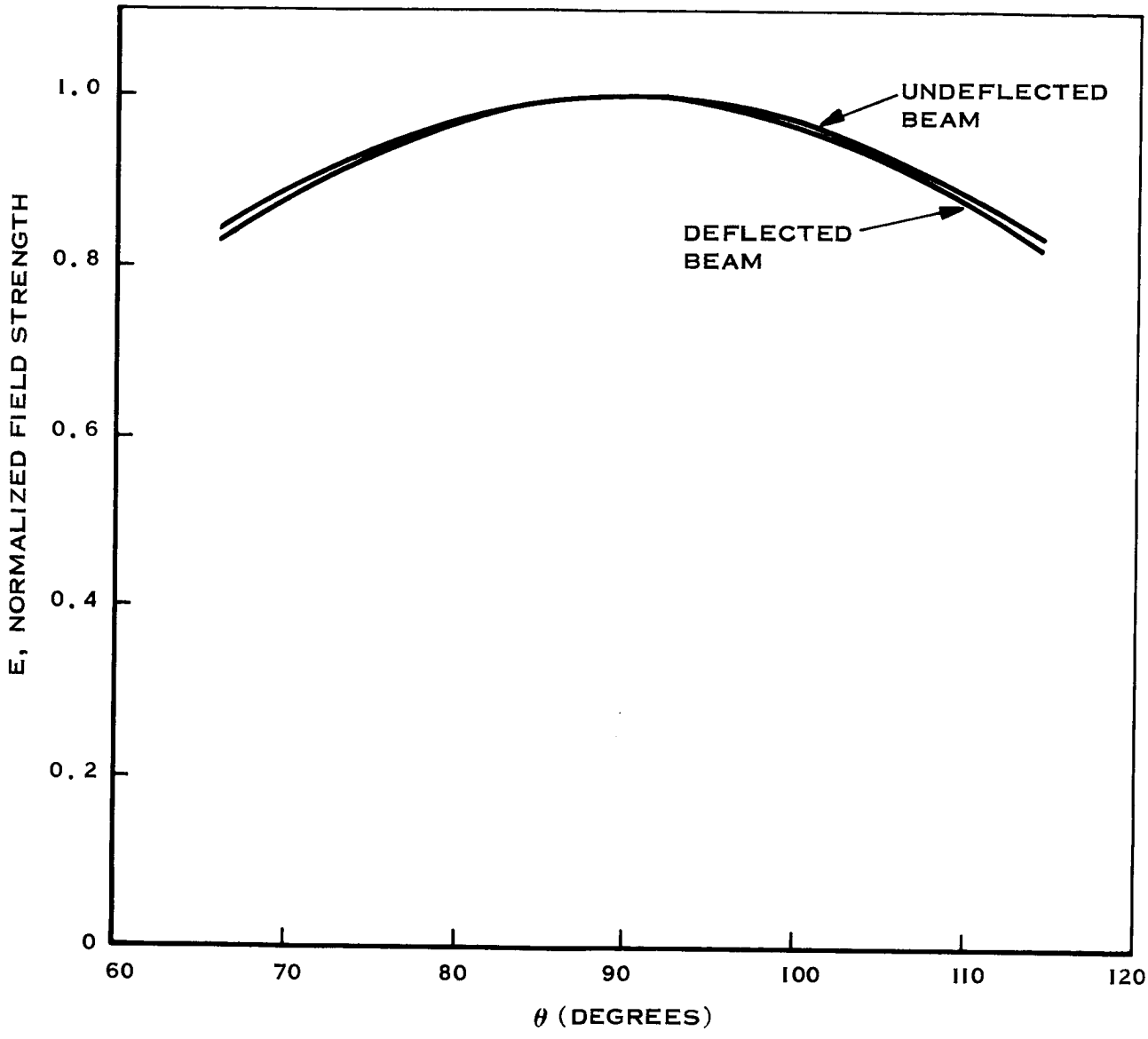

Figure 3-12 Diagonal (δ=45°) View of Broad Beam Profile

The physical deflection of the antenna for the various cases is shown in Figures 3-13, 3-14, 3-15 and 3-16.

The choice of effective mounting angle depends on how "far out" on the beam one is trying to fit it. Thus a minimum value of θ must be specified before the best fit can be determined. The choice of θ_{min} is also related to the satellite altitude, i.e., the higher the satellite the smaller the portion of the beam used. Two values of θ_{min} were used, $\theta_{min} = 81^{\circ}$ corresponding approximately to synchronous altitude, and $\theta_{min} = 66^{\circ}$ corresponding to a 5000 n.mi. orbit.

Figure 3-17 is a plot of the difference, $\Delta\varphi$, between the value of φ computed from the best fit linear approximation and the actual value φ, plotted versus θ. The figure shows $\Delta\varphi(\theta)$ for four values of θ_{min}. Figure 3-18 shows $(|\Delta\varphi_{min}| + \Delta\varphi_{max})/2$ for the combinations of parameters considered and for $\theta_{min} = 81^{\circ}$. Figure 3-19 shows the same data for $\theta_{min} = 66^{\circ}$. Table 3-1 gives a summary of the results. Three beam cross-sections were plotted for each case, at $\theta = 90^{\circ}$, at $\theta = 80^{\circ}$, and at $\theta = 70^{\circ}$. These plots may be found in Appendix C of this report.

Two cases evaluating the effect of random error in slot location were also run. The maximum error allowed in each case was 5/1000 inch. There was no appreciable effect on the pattern, using the simple error model described previously.

3.3.5 Double Antenna Study

All the preceeding concerned itself with a single antenna of N elements all driven in phase. Now we will consider two sets of M and N elements respectively which may be

(1) In or 180° out of phase.
(2) Separated vertically be a distance V.
(3) Separated horizontally (misalligned) by a distance H.

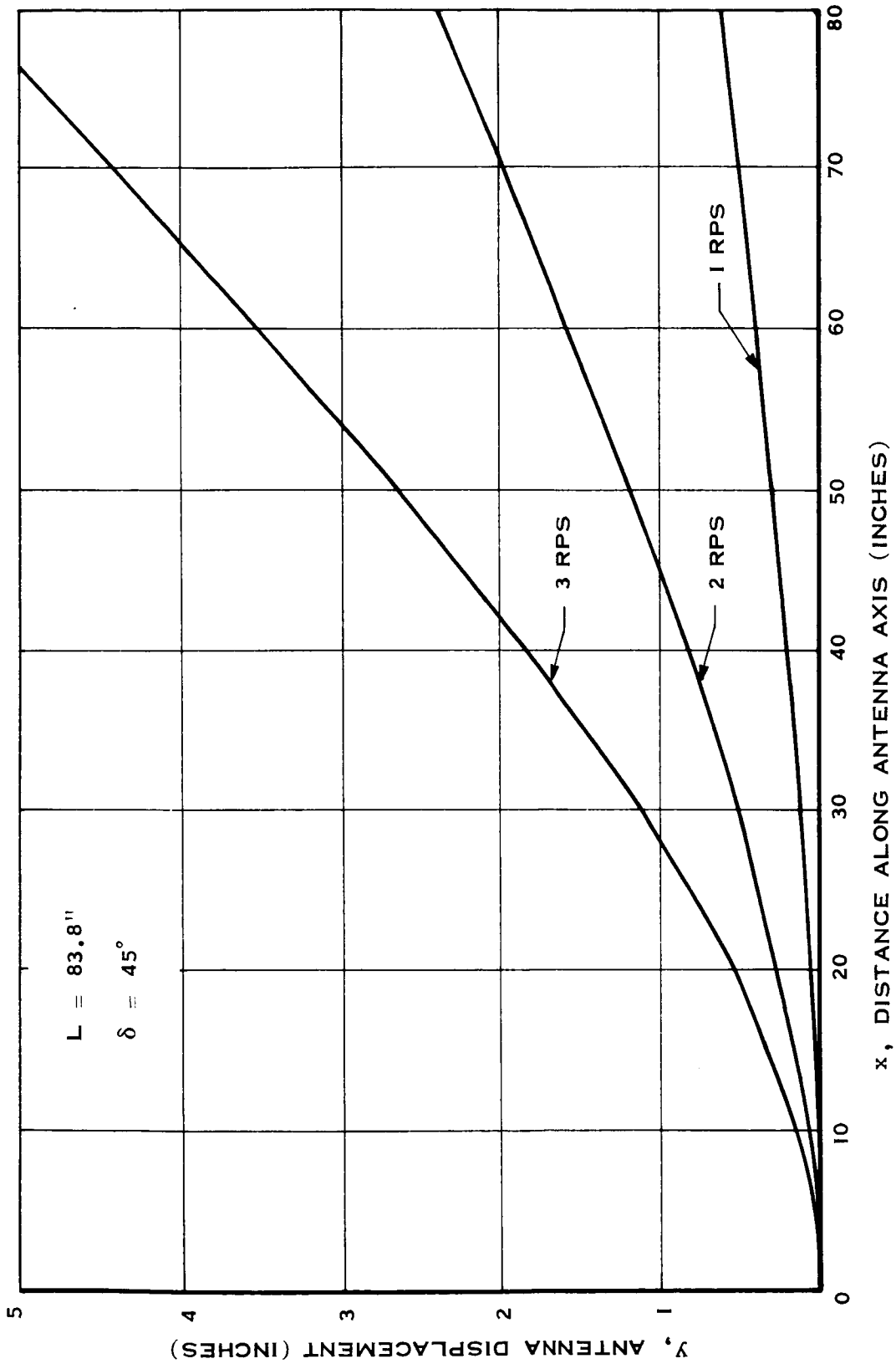

Figure 3-13 Dependence of Antenna Deflection on Spin Rate

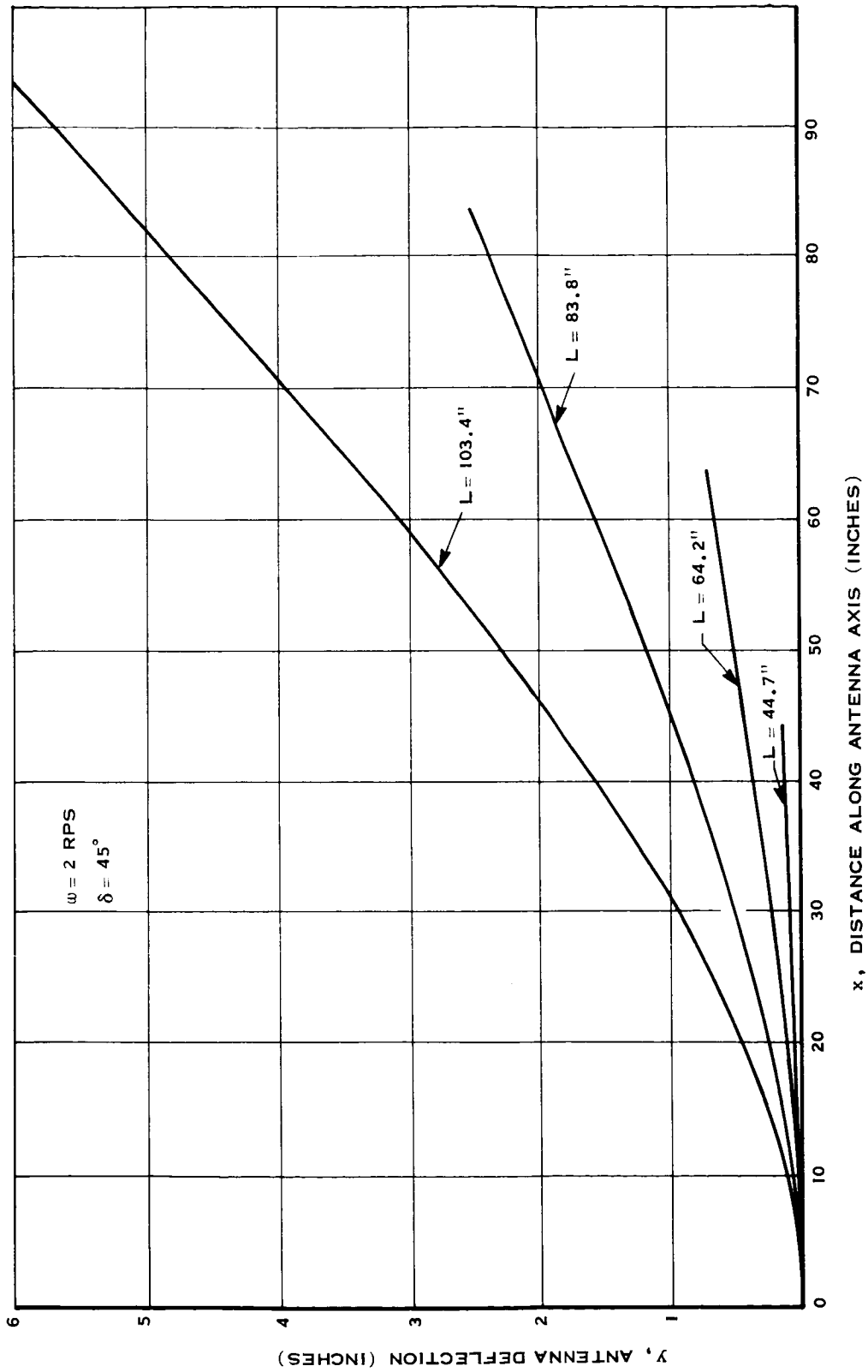

Figure 3-14 Dependence of Antenna Deflection on Antenna Length

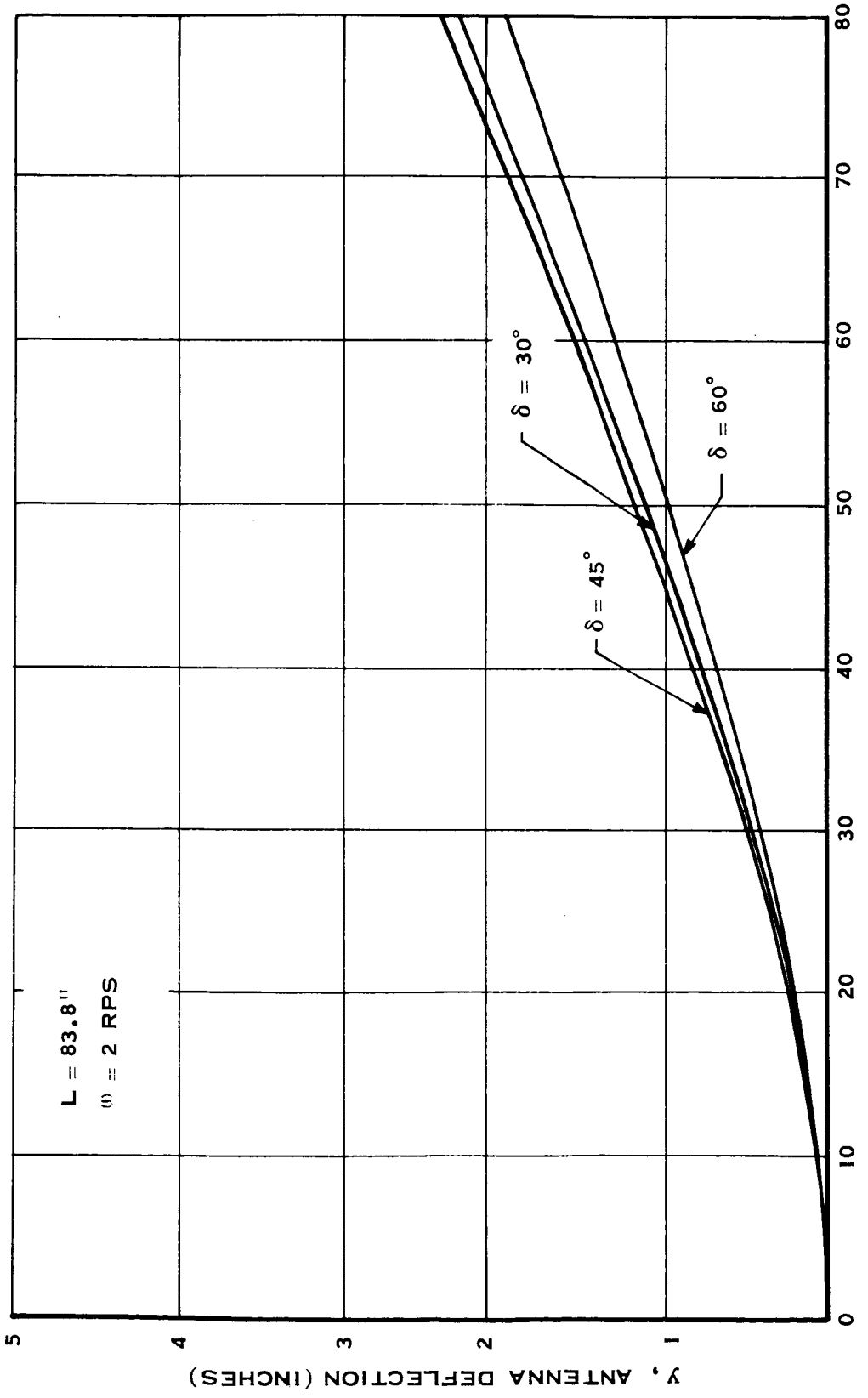

Figure 3-15 Dependence of Antenna Deflection on Mounting Angle

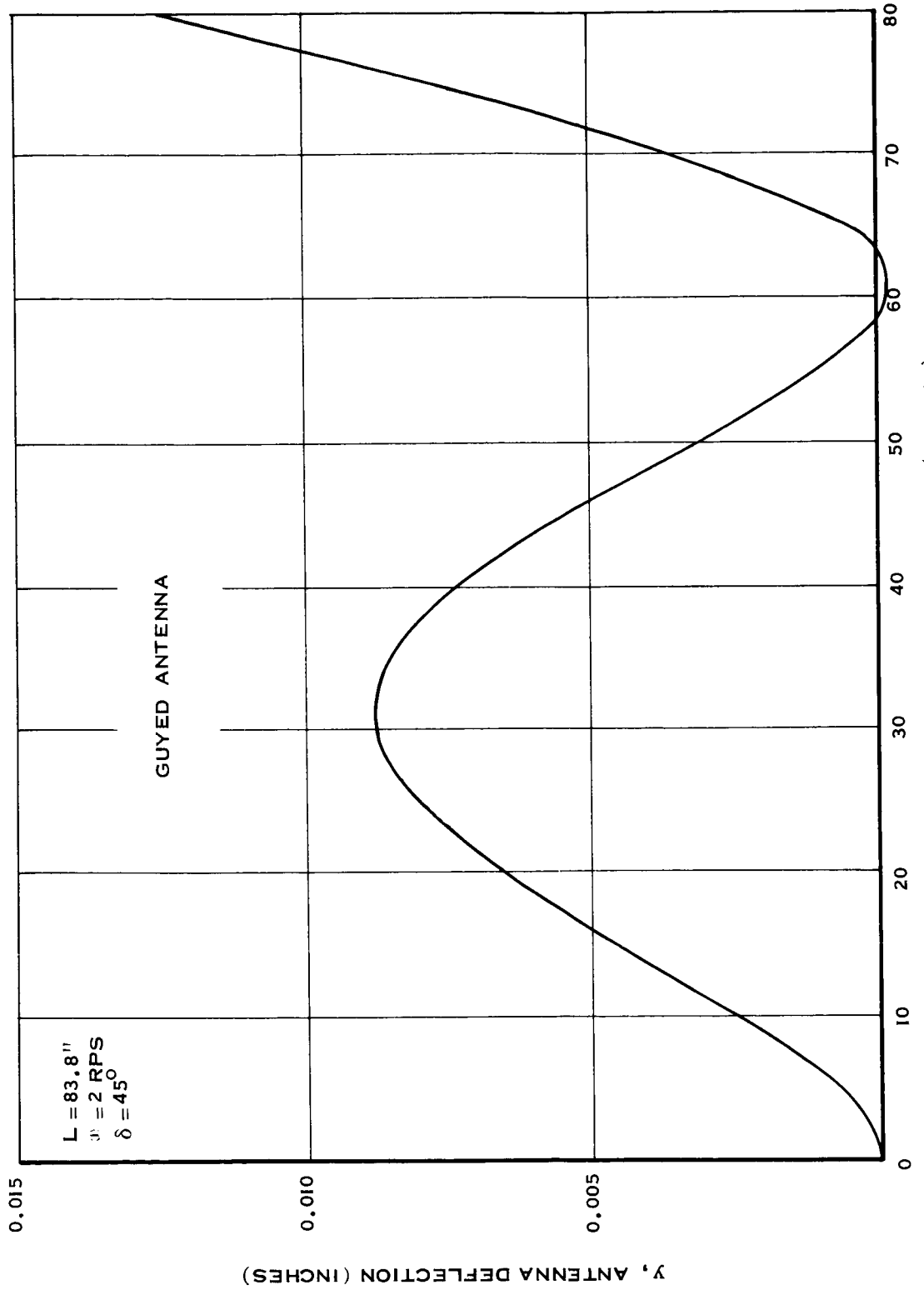

Figure 3-16 Deflection of a Guyed Antenna

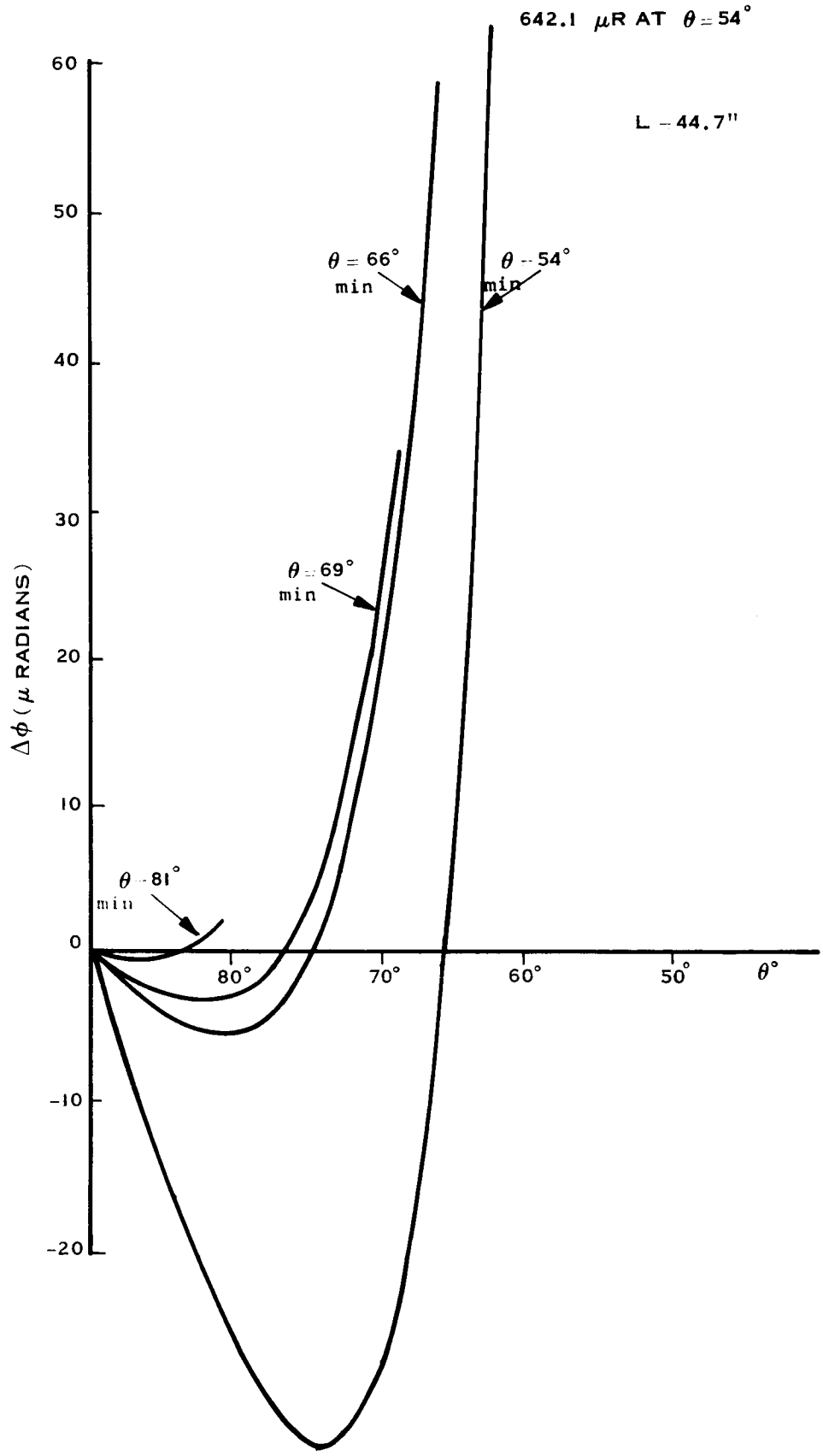

Figure 3-17 Typical Plot Showing Residual Angular Deviations After Best Linear Correction For Particular Minimum θ.

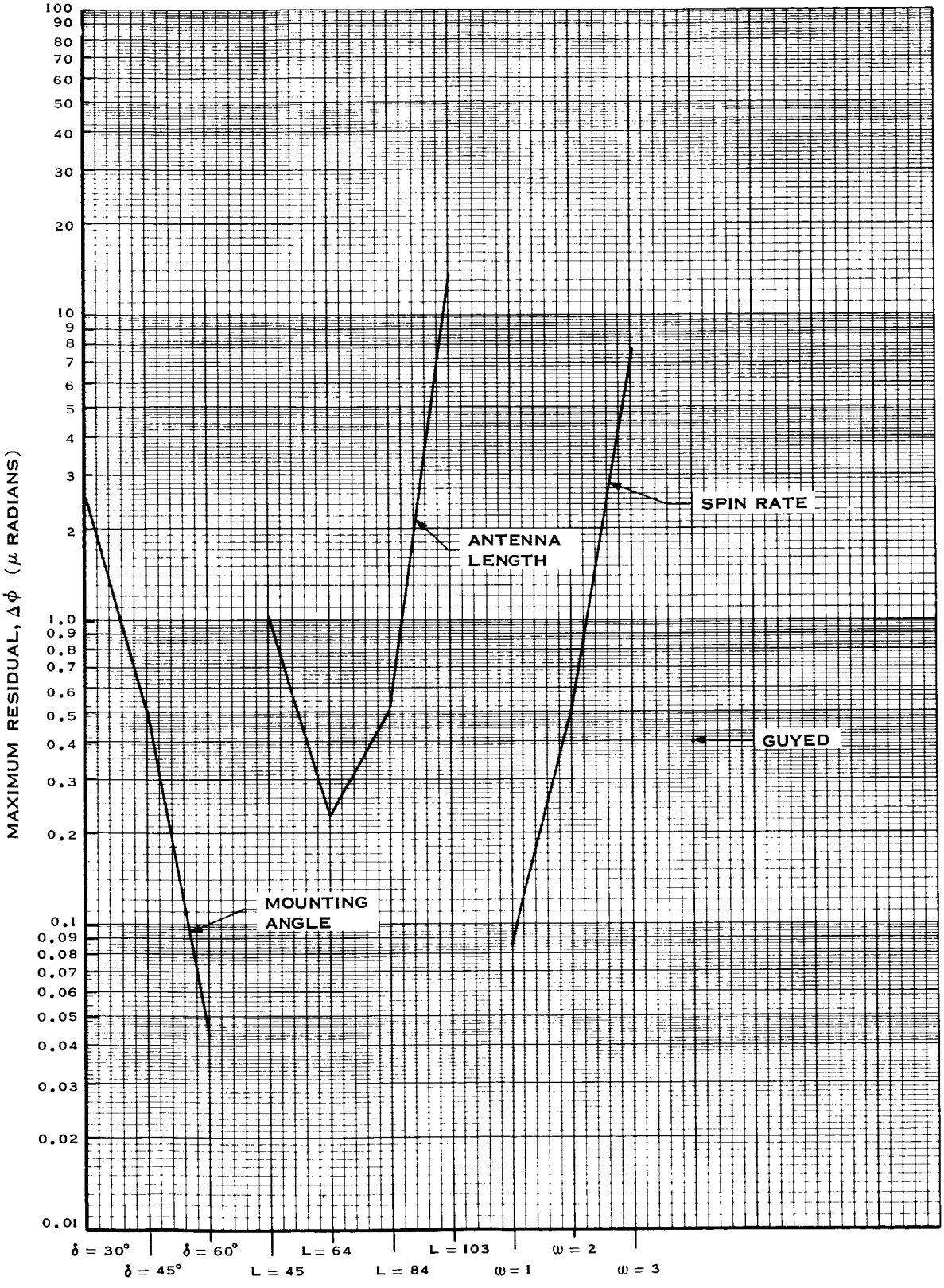

Figure 3-18 Residual In Δφ Due to Beam Non-Planarity Optimized for θ_{Min}=81° (Synchronous Altitude)

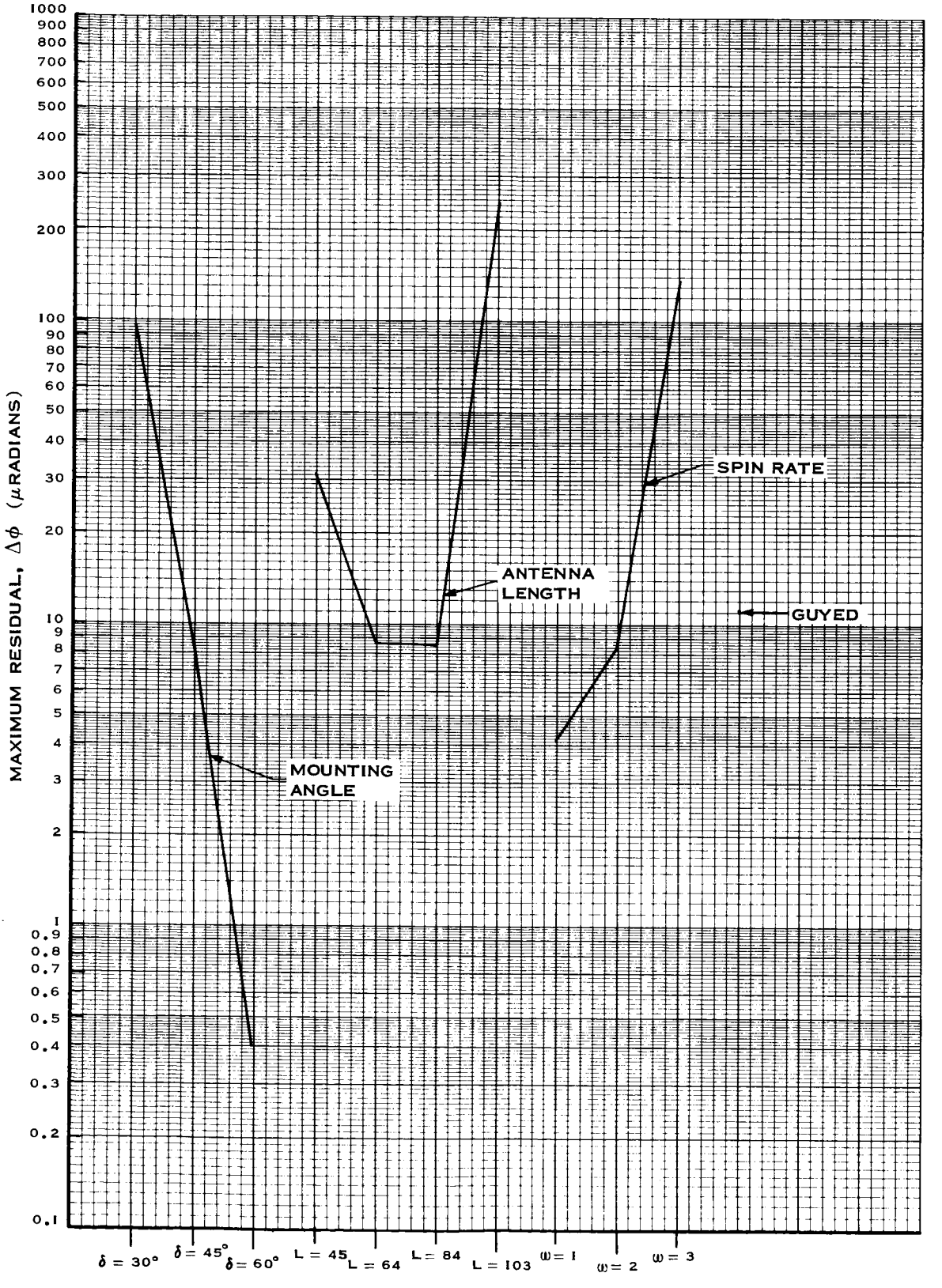

Figure 3-19 Residual in $\Delta\phi$ Due to Beam Non-Planarity Optimized For $\theta_{Min}=66^{\circ}$ (5000 n. mi. Altitude)

Table 3-1 . Summary of Parametric Study

Parameter Varied and Its Value		Maximum Deviation of Spin Angle From Nominal (Linear Approximation) μ radian		Approximate Angle Through Which Beam Turned
		Synchronous Altitude	5000 n.mi. Altitude	
Antenna Mounting Angle	30°	5	200	2°
	45°	1	20	2°
	60°	.1	1	2°
Antenna Length	45"	2	50	.2°
	64"	.5	20	1°
	103"	20	500	4°
Satellite Spin Rate	1 RPS	.2	10	.5°
	2 RPS	1	20	2°
	3 RPS	10	200	4°
Guyed Antenna		1	20	0°

(4) Overlaid in such a way as to form more complicated patterns, such as two radiators, two missing, two radiators, etc.

See Figure 3-20.

Appendix D consists of a number of double antenna pattern cross-sections. On each plot the number of slots m and n, the horizontal and vertical separation of the antennas H and V, the phase $\Psi = 0^{\circ}$ or $\Psi = 180^{\circ}$, and the angle θ as previously defined are given.

It should be noted that $E(\theta,\varphi)$ was evaluated at 201 evenly spaced points to obtain the data for all cross-sections shown. In some cases where the data is varying rapidly, minima and in some instances maxima are obviously missed or are not very well defined. This effect is illustrated to an extreme extent in Figure D-17 where all local maxima should extend to the envelope and all minima should actually be zero.

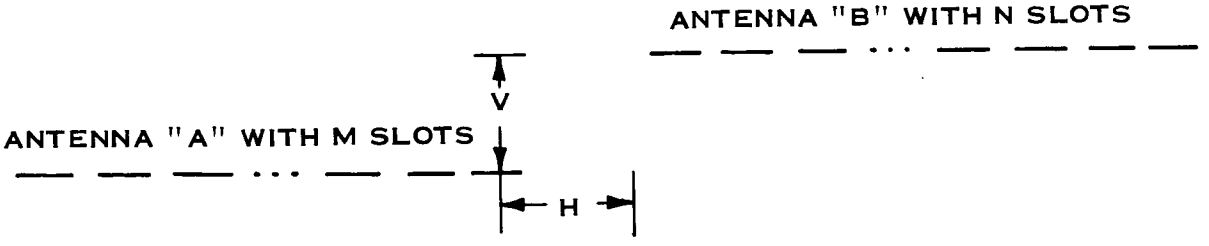

Figure 3-20 Double Antenna Configuration Definition

APPENDIX A

CIRCULAR WAVEGUIDE ARRAY INVESTIGATION

A.1 SUMMARY

This experiment was performed to investigate the feasibility of using a circular waveguide as the transmission line on which to build a very long resonant array. The circular waveguide slotted array was investigated because of the attractiveness of the DeHavilland boom.

The unknown radiation characteristics of an array of relatively small conductance slots in a waveguide can be made known by comparing the radiation patterns against that of a single large conductance slot whose characteristics are known. This is done by phasing the single slot and the array of slots 180 degrees apart and measuring the position and depth of the null in the difference pattern.

The objective of this first experiment was to determine by slotted line techniques the admittance characteristics of a loosely coupled slot for use as a reference.

It was found that for any loosely coupled longitudinal shunt slot in a circular guide the plane of incident polarization was rotated. The reflections from the slot returned also rotated, thus causing the slotted line to radiate. In brief, a circular waveguide with a simple circular cross section cannot maintain a uniform plane of polarization when the propagation is altered by the presence of displaced off-axis shunt slots. Because of the rotation of the plane of polarization, the open slot of a DeHavilland boom would radiate and further interfere with the propagation of energy.

A.2 TECHNICAL PLAN

Figures A-1 through A-5 are Engineering Drawings of the special waveguide slotted line, circular to rectangular guide transition, and circular guide test section containing a number of longitudinal shunt slots.

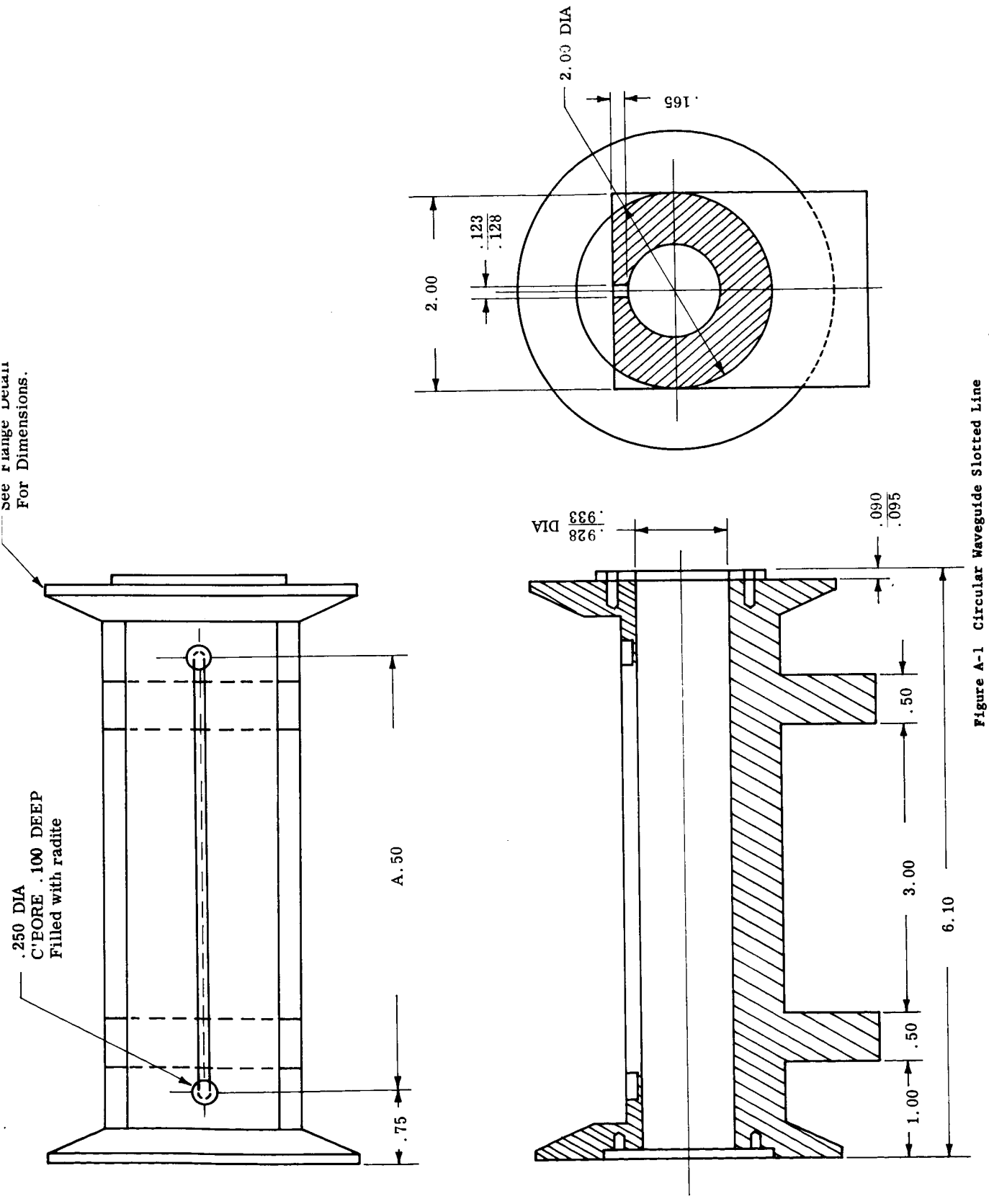

Figure A-1 Circular Waveguide Slotted Line

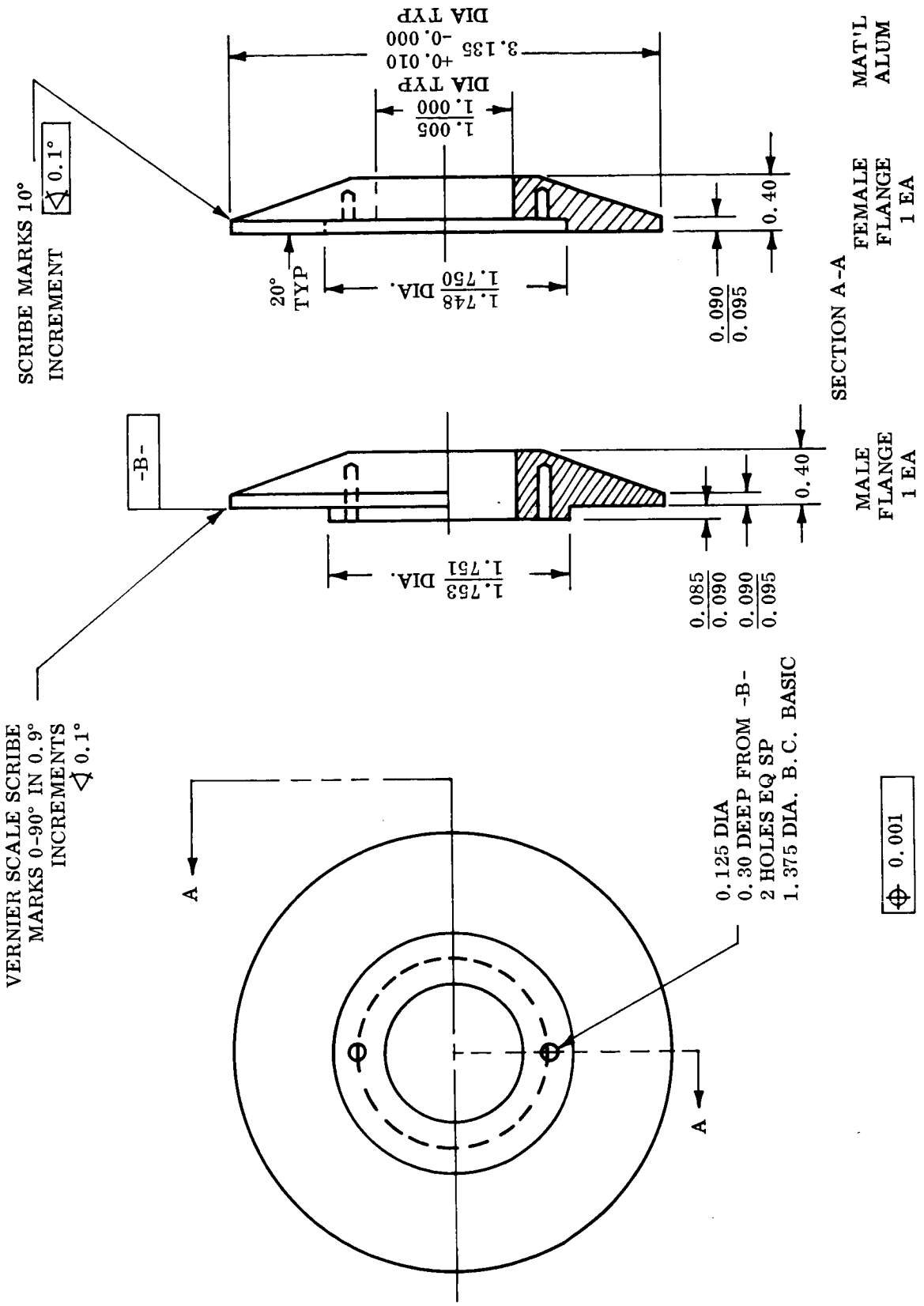

Figure A-2 Flanges

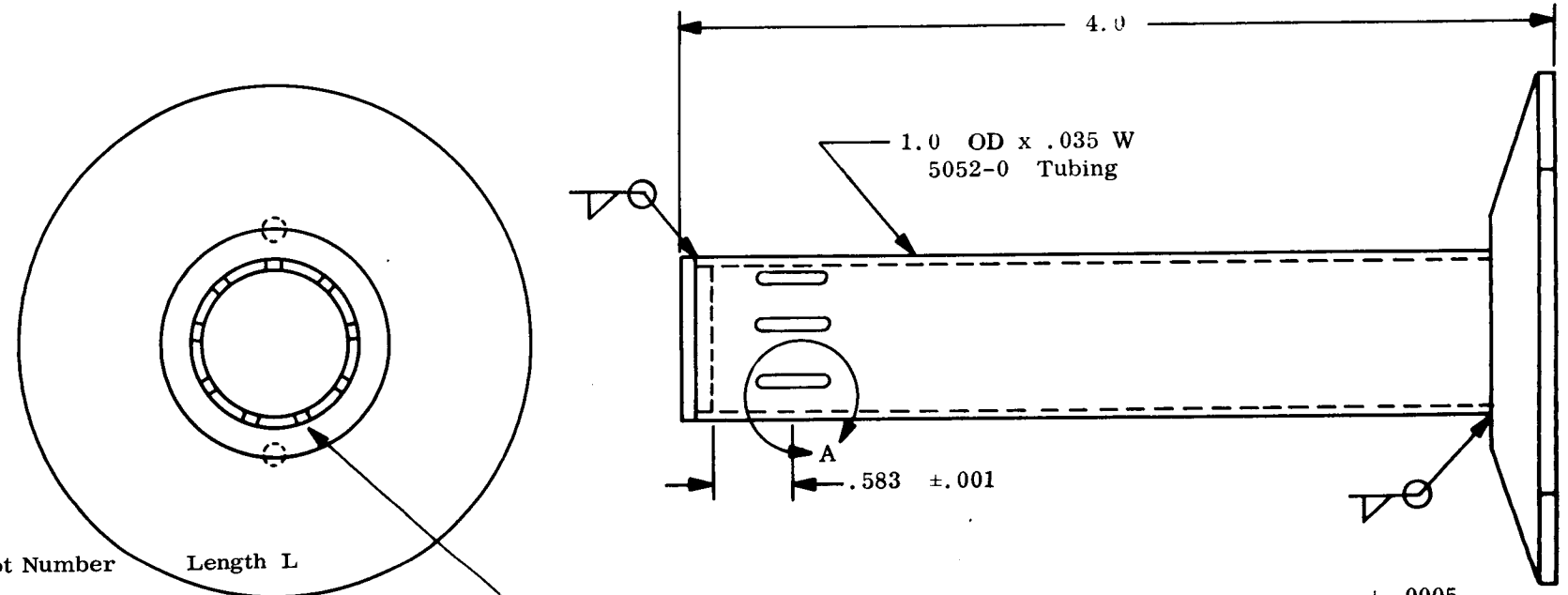

Slot Number	Length L
1	.6301
2	.6314
3	.6327
4	.6340
5	.6354
6	.6406
7	.6458
8	.6498
9	.6520

Figure A-3 Slot Test Section

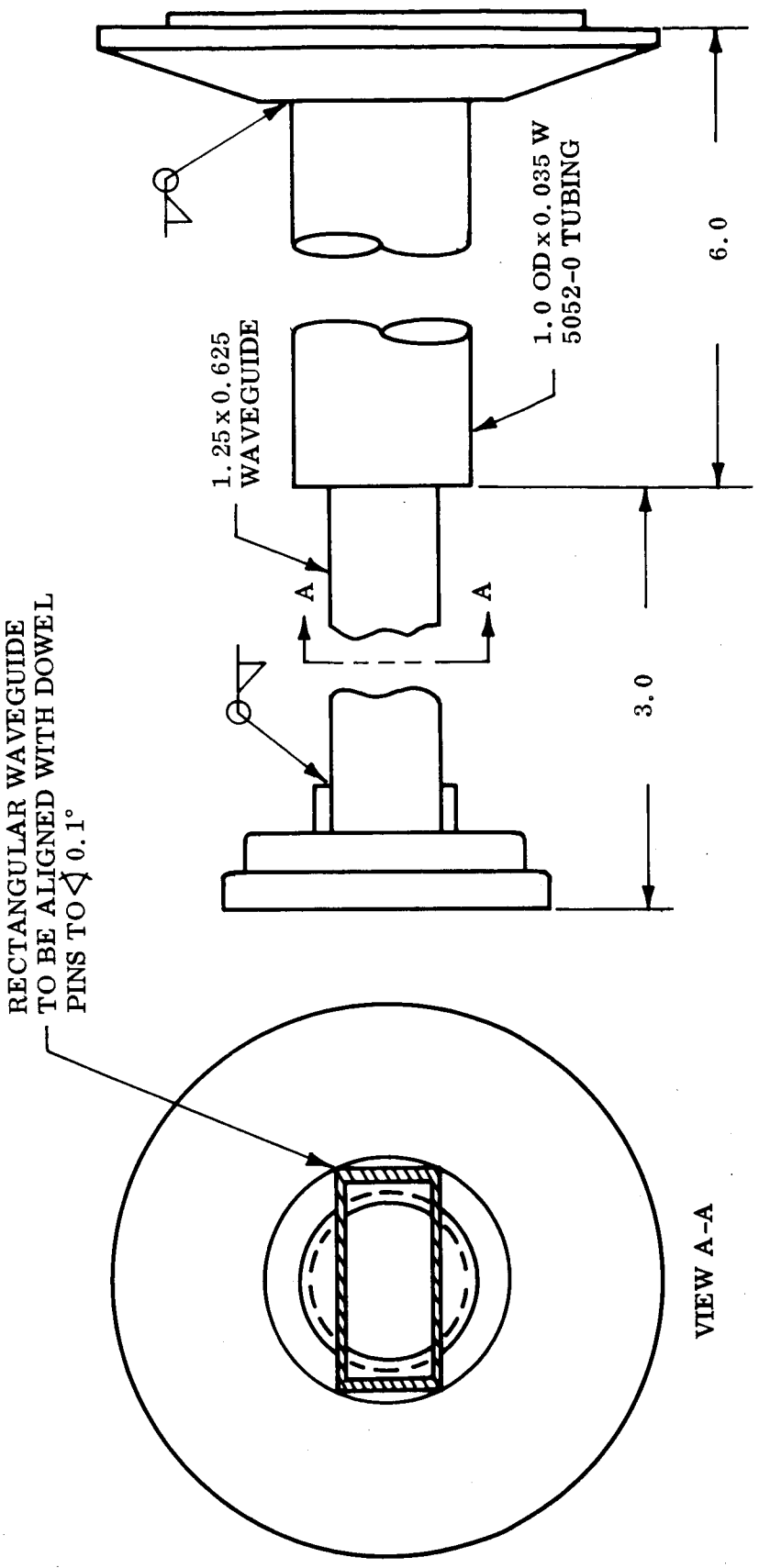

Figure A-4 Rectangular to Circular Transition

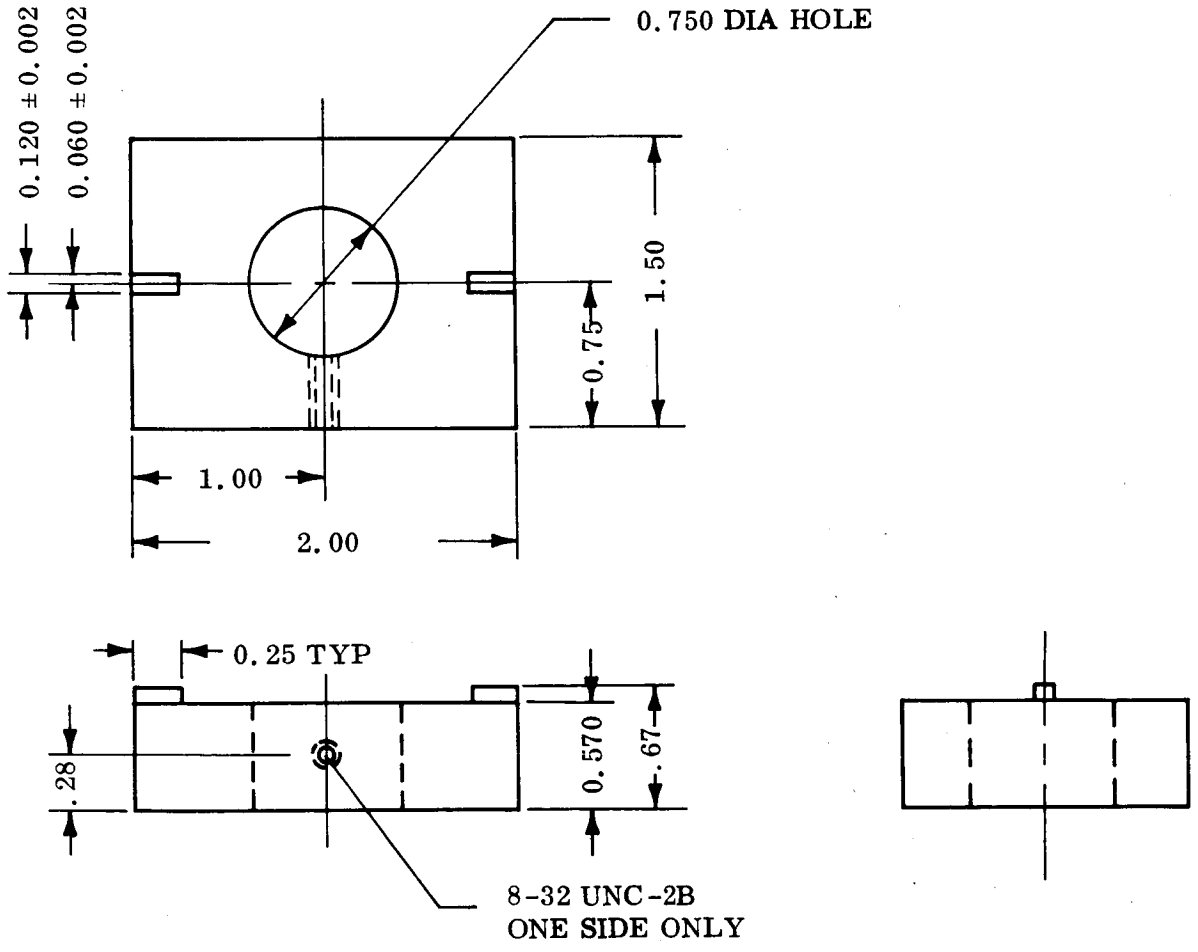

Figure A-5 Probe Carriage

Measurements were made on each slot with all other slots shorted. The VSWR and null shift from a short circuit at the plane of the slot determined the addmittance of the slot. The admittance was determined as a function of the angular displacement of the slot from the plane of the incident polarization. The frequency dependence was also determined. The design resonant frequency was 9.0 GHz.

A.3 TEST RESULTS

The test set-up is shown in Figure A-6.

The test section of guide containing the slots, all of which were shorted except the particular one under test, was rotated about its axis from the vertical angle of 5 degrees. There was no apparent change either in amplitude of the VSWR or position of the null. This VSWR was greater than 40:1, the true null depth was masked by the noise level of the audio amplifier in the indicator. Greater coupling is achieved by a greater angular displacement from the vertical. However, at an angular displacement of 10 degrees, the VSWR became very erratic. An investigation of the radiation fields indicated that the slotted line was radiating. Removing the probe carriage reduced but did not eliminate the radiation, indicating that neither the probe nor its carriage was exciting the slotted line. A short tapered section of resistance card was placed in the load end of the slotted line with the tapered end toward the load. The resistance card was oriented along a diagonal plane orthogonal to the plane of incident polarization, so as to absorb any polarization which might be reflected in all planes except the incident vertical polarization. This eliminated the radiation from the slotted line. The VSWR was now measured to be 3.0:1, but no indication can be made of the power transmitted through the test slot by this measurement. The procedure was repeated for all slots and at the expected resonant frequency 9.00 GHz and minus 100, 200 and 500 MHz. No frequency within this design range was found for any of the slots which did not cause the slotted line to radiate for any angular displacement. The radiation intensity from the test slot did increase as the angular displacement was increased. The radiation intensity was measured always at the same distance along a radial line through the axis of symmetry of the slot.

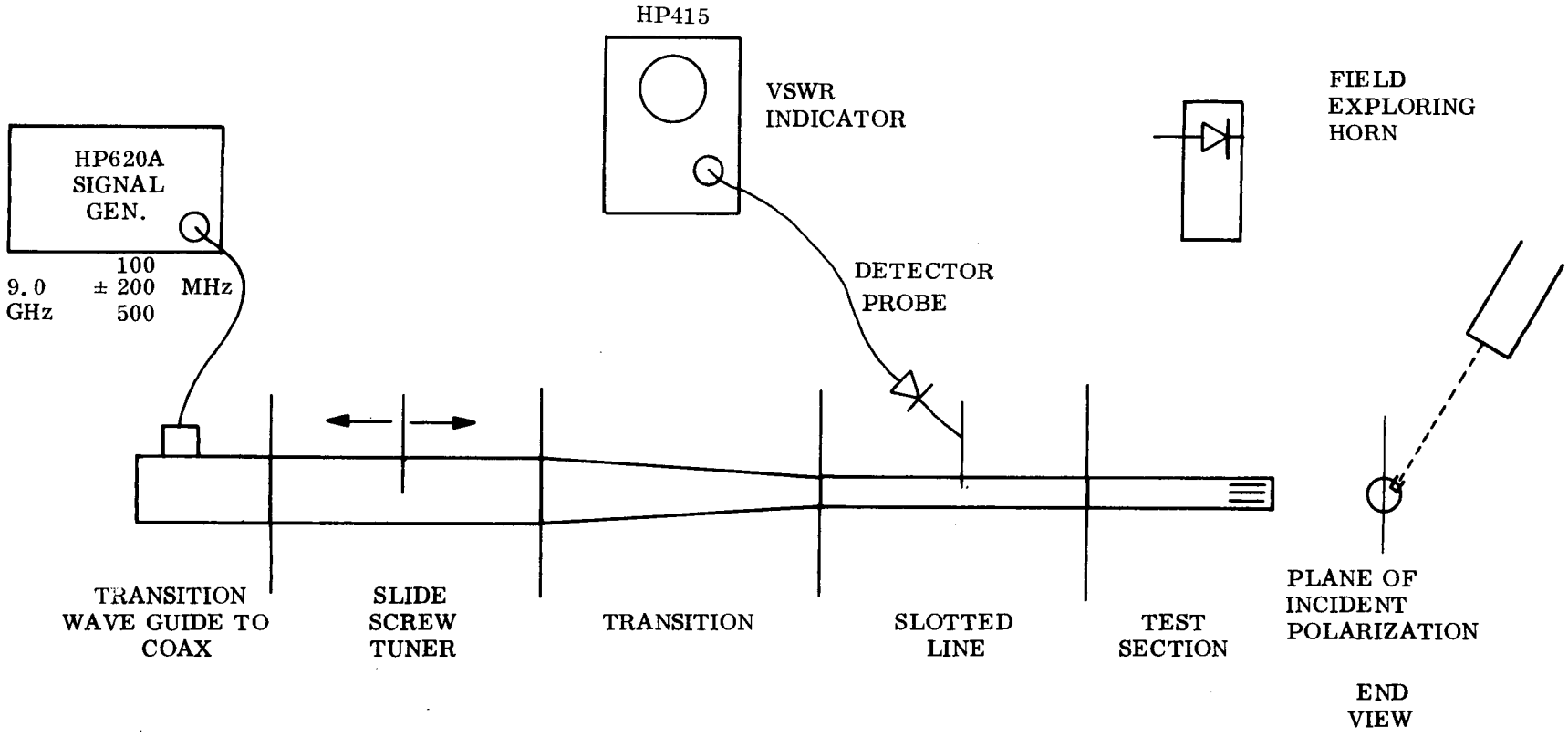

Figure A-6 Circular Waveguide Array Investigation Test Setup

A.4 CONCLUSIONS

Certain disadvantages of using circular waveguide are presented. Because of the circular symmetry of circular guide, it is impossible to obtain electromagnetic propagation characteristics analogous to the simple TE_{10} propagation of rectangular guide. This is due to the fact that for the lowest order of the roots of the cut-off equation (that is, for TE_{11} mode propagation only), there exist two characteristic forms for the same cut-off frequency. In general, the solution of Maxwell's equations for the field distributions in circular waveguide show that for any particular mode of interest which has its unique cut-off wavelength, the expressions can contain either a cosine or sine variation in the cylindrical coordinate ϕ. Both may exist together and, depending upon the relative amplitude and phase relationship, any form of elliptical polarization may result. Consequently, a circular guide involves at least double propagation. Furthermore, any departure of the cross section from exact circular form and symmetry may cause coupling of the two modes of propagation and rotation of the plane of polarization might occur, producing elliptic polarization.

This experiment has pointed out that radiation from longitudinal offset shunt slots in circular guide may cause coupling between the two forms of propagation of the TE_{11} mode, and, unless the waveguide is made structurally rigid, deformation of the cross section will be experienced as the guide is bent or twisted, which also causes coupling of the two modes. Mode purity may be insured by the insertion of a ridge in the plane of polarization desired.

The open seam of the DeHavilland boom would certainly radiate as the polarization plane rotated. This radiation would further interfere with the propagation of energy in the guide, causing additional rotation of the polarization plane and consequent additional misalignment of the resonant slot radiators.

APPENDIX B

EXPERIMENTAL STUDY OF PHASE SHIFT VS. BENDING OF RECTANGULAR WAVEGUIDE

B.1 SUMMARY

It is anticipated that the rectangular waveguide array on the Navigational Satellite will experience large deflections from its static position due to the spinning of the satellite and the angle between the array and the spin axis. The object of this analysis is to determine the effects of bending a rectangular waveguide on the wave propagation factor. It is this factor on which the spacings of the elements of a resonant array are dependent.

The results are normalized to the guide dimensions and wavelength and are applicable for any wall thickness and any radius of curvature between $R = \infty$ and $R = 10$ feet for E-plane bending, and between $R = \infty$ and $R = 25$ feet for H-plane bending. The phase shift for H-plane bending was approximately one-third that for E-plane bending and occurred in the opposite direction. That is, E-plane bending effectively increased the length of the line, whereas H-plane bending effectively reduced the length but only one-third as much for the same radius of curvature. The most severe phase shift in the E-plane was 0.448° per foot occurring for $R = 10$ feet. This corresponds approximately to a phase shift of 0.037° per slot. This same phase shift would be experienced if the slot were displaced from its resonant position by 0.0001 inch.

B.2 TECHNICAL PLAN

In order to obtain meaningful information, the guide will be bent in such a manner as to produce a uniformly distributed phase shift and a constant propagation factor with length. The guide will therefore be formed about three supports to conform to an arc of a circle of constant radius, and the phase length measured with respect to that for the no-bending condition. The effect on the loss with bending will also be measured. Both E-plane and H-plane bending will be investigated.

An expression is derived below which relates the phase shift per unit length to the guide dimensions, the frequency and the radius of curvature of bending. The proportionality factor is experimentally determined. The phase shift is a result of stresses which cause buckling or minor deflections of the narrow dimension b of the rectangular waveguide which effectively increases or decreases the wide dimension a by Δa. This change is caused by a deflection of a thin wall of thickness, t, under stresses causing buckling. As a first order approximation, the deflection is proportional to the square of the ratio of the narrow dimension, b, to the thickness, t. Expressed mathematically:

$$\Delta a = k \left(\frac{b}{t} \right)^2 \qquad \text{(B-1)}$$

where k is a proportionality factor with feet as the dimension, and is a function of the radius of curvature of bending.

The phase shift, $\Delta\emptyset$, per length, L , in a rectangular waveguide due to an incremental change, Δa, in the wide dimension, is found by differentiating the expression for the propagation factor, β, with respect to a.

β for a rectangular waveguide with wide dimension a is given by

$$\beta = \frac{2\pi}{\lambda_o} \left[1 - \left(\frac{\lambda_o}{2a} \right)^2 \right]^{1/2} \qquad \text{(B-2)}$$

β is related to the phase length by the following expression:

$$\beta = \frac{\emptyset}{L} \qquad \text{(B-3)}$$

It follows that

$$\Delta\beta = \frac{\Delta\emptyset}{L}$$

Differentiating Equation (B-2) with respect to a gives for the incremental change in β;

$$\Delta\beta = \pi \left(\frac{\lambda_g}{\lambda_c}\right)\left(\frac{1}{a}\right)^2 \Delta a \qquad \text{(B-5)}$$

Substituting Equations (B-1) and (B-4) into (B-5) results in the following:

$$\frac{\Delta\phi}{L} = \pi k \left(\frac{\lambda_g}{\lambda_c}\right)\left(\frac{b}{a}\right)^2 \left(\frac{1}{t}\right)^2 \qquad \text{(B-6)}$$

The dependence of the proportionality factor k on R, the radius of curvature of bending, is the relationship to be determined by experiment. Assume k is equal to some function of 1/R, in order that k = 0 when R = ∞ (i.e., for an undeflected waveguide); then the phase shift per foot for different waveguides and frequencies and radii of curvature is calculated from the formula:

$$\frac{\Delta\phi}{L} = f\left(\frac{1}{R}\right) \pi \left(\frac{\lambda_g}{\lambda_c}\right)\left(\frac{b}{a}\right)^2 \left(\frac{1}{t}\right)^2 \qquad \text{(B-7)}$$

B.3 TEST CONDITIONS

Due to the availability of test equipment and waveguide stock, the test frequency was chosen at 15.0 GHz. The waveguide was brass RG(91)/u, with inside dimensions 0.622 inch x 0.311 inch, 0.040 inch in wall thickness and 9.33 feet in length. The guide wavelength is calculated to be 1.016 inches. The test waveguide then contains

$$\frac{9.33 \times 12}{1.016} = 110 \text{ guide wavelengths.}$$

The waveguide was shorted at one end and the VSWR at the input was measured. The VSWR was measured for each different radius of curvature, and the one-way loss calculated from the following expression:

$$\text{Loss (1 way) db} = 10 \log_{10}\left(\frac{(\text{VSWR} + 1)}{(\text{VSWR} - 1)}\right)$$

The null position was measured on the slotted line with the aid of a 10 revolution dial indicator for which one revolution corresponds to 0.0100 inch and with divisions every 0.0001 inch.

The constant-radius curvatures were accomplished by forming the guide about supports whose spacings and lengths are given by the expression:

$$x^2 + (y + R)^2 = R^2$$

where x is the distance along the line of the undeflected guide to the support, y is the deflection, and R is the radius of the circle.

B.4 TEST RESULTS

Figure B-1a and B-1b illustrate the experimental arrangement showing the position and lengths of the support about which the waveguide was formed for each of the constant-radius curves.

Table B-1 tabulates the data from the original data sheets.

Figure B-2 is a graphical representation of the data. The ordinate is phase shift per foot of length and the abcissa is the inverse of the radius of curvature.

The VSWR was unchanged from 9.7:1 for all cases of bending. The insertion loss was calculated to be 0.90 db using the equation of Section B.3. The theoretical calculated value is 0.94 db.

B.5 CONCLUSION

The results of the experiment are shown graphically in Figure B-2. This graph shows that $\frac{\Delta\phi}{L}$ is a linear function of $\frac{1}{R}$. It follows then that the proportionality factor k of equation (B-6) also is linearly dependent on $\frac{1}{R}$. Equation (B-7) then becomes

$$\frac{\Delta\phi}{L} = (m)\frac{\pi(\frac{\lambda_g}{\lambda_c})(\frac{b}{a})^2\ (\frac{1}{t})^2}{R} \qquad \text{(B-8)}$$

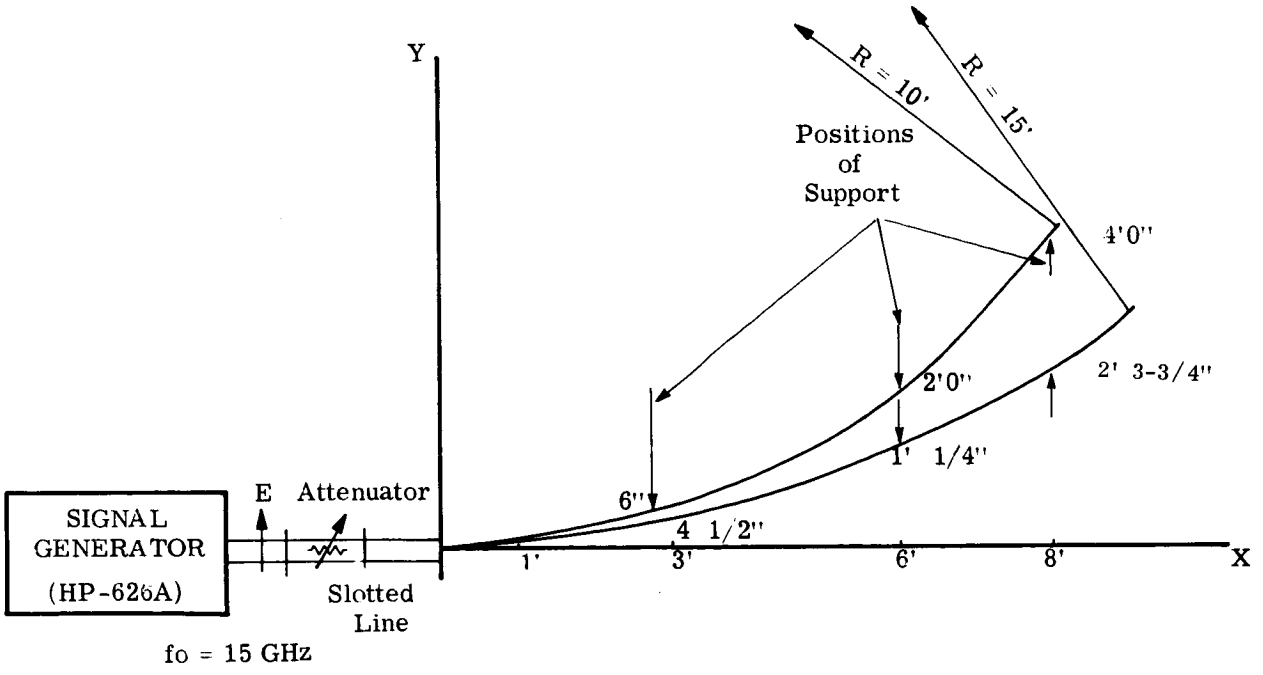

Figure B-1a Bending in E Plane

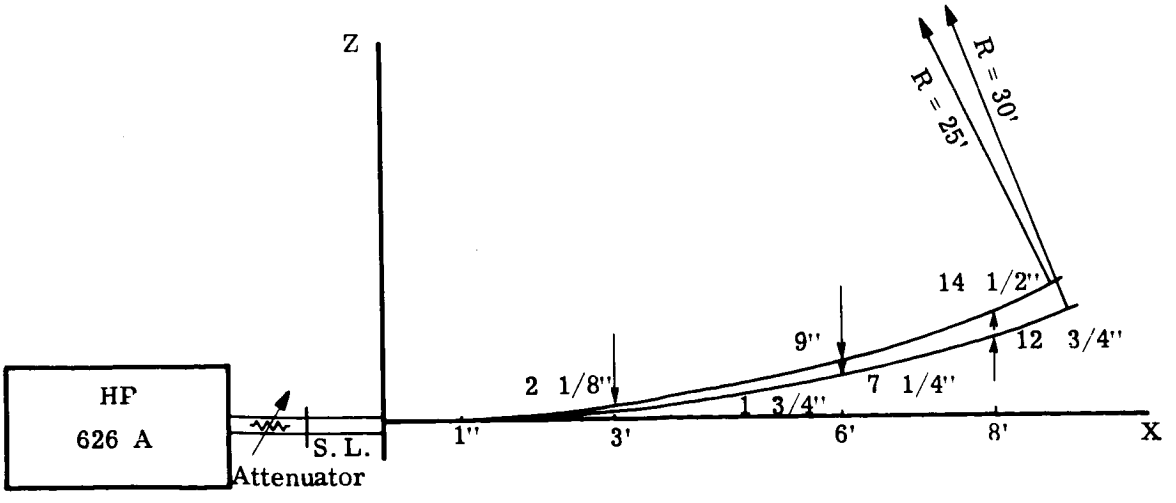

Figure B-1b Bending in H Plane

Table B-1 Data Summary

f_o = 15.0 GC, Waveguide: RG (91) he, Brass: ID: 0.622" x 0.311"

λ_g = 1.023" Wall Thickness: t = 0.040"

L = 0.33 feet

$$\left(\frac{\lambda g}{\lambda_o}\right)\left(\frac{b}{a}\right)^2\left(\frac{1}{t}\right)^2 = \left(\frac{1.023}{1.244}\right)\left(\frac{.311}{.622}\right)^2\left(\frac{1}{.040}\right)^2 = 128.9\ (in^{-2})$$

E Plane

R	$\frac{1}{R}$	$\Delta\phi$	$\frac{\Delta\phi}{L}$
15'	.0667	$+2.50^o$	.268
10'	.100	$+4.18^o$	.448

H Plane

R	$\frac{1}{R}$	$\Delta\phi$	$\frac{\Delta\phi}{L}$
30'	.0333	-0.40^o	.0429
25'	.040	-0.60^o	.0644

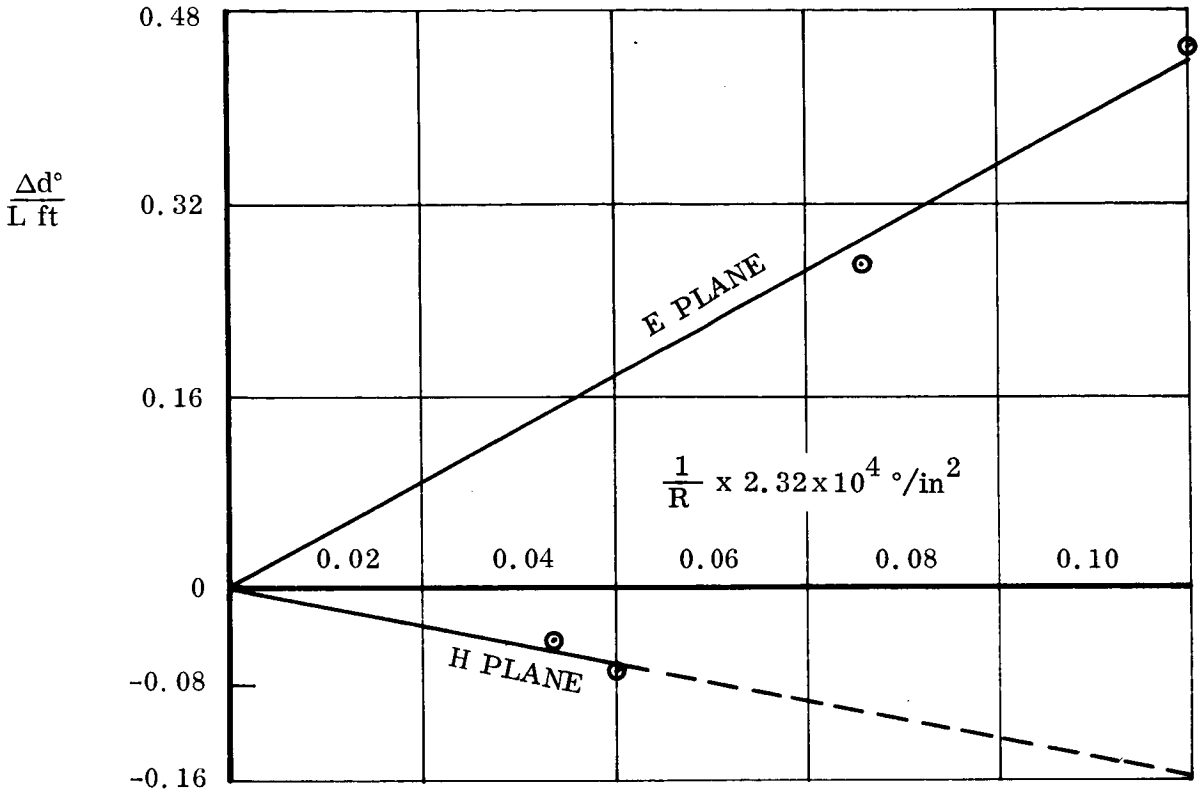

$$\frac{\Delta d}{L} = M \left(\frac{a_g}{a_o}\right) \left(\frac{b}{a}\right)^2 \left(\frac{1}{t}\right)^2 \left(\frac{1}{R}\right)$$

$M_E = 1.93 \times 10^{-4}$ in^2 - E PLANE

$M_H = 0.694 \times 10^{-4}$ in^2 - H PLANE

Figure B-2 Phase Shift Per Foot Vs. 1/R for E and H Plane Bending

where m is a constant with dimensions of inches^2. m is the slope of the line of Figure B-2 if the ordinate of the curve is normalized to the following factor evaluated for the test guide and frequency:

$$\pi \left(\frac{\lambda_g}{\lambda_c}\right)\left(\frac{b}{a}\right)^2 \left(\frac{1}{t}\right)^2 = 2.32 \times 10^4 \ ^{o}/\text{inches}^2$$

For E-plane bending:

$$m = \frac{\frac{\Delta\phi}{L}}{\pi\left(\frac{\lambda_g}{\lambda_c}\right)\left(\frac{b}{a}\right)^2 \left(\frac{1}{t}\right)^2} \qquad (R)$$

$$= \frac{.448^{o}/\text{ft.}}{2.32 \times 10^{4o}/\text{in}^2} \qquad (10 \text{ ft.})$$

$$m = 1.93 \times 10^{-4} \text{ in}^2$$

For H-plane bending:

$$m = \left(\frac{.0644}{2.32 \times 10^4}\right)(25) \text{ in}^2$$

$$m = 6.94 \times 10^{-5} \text{ in}^2$$

The resulting equations are then:

E-plane

$$\frac{\Delta\phi}{L} = (19.3 \times 10^{-5})\ \pi \left(\frac{\lambda_g}{\lambda_c}\right)\left(\frac{b}{a}\right)^2\left(\frac{1}{t}\right)^2\left(\frac{1}{R}\right) \qquad \text{(B-9)}$$

$R > 10$ feet

H-Plane

$$\frac{\Delta\phi}{L} = (6.94 \times 10^{-5})\ \pi \left(\frac{\lambda_g}{\lambda_c}\right)\left(\frac{b}{a}\right)^2 \left(\frac{1}{t}\right)^2 \left(\frac{1}{R}\right) \qquad \text{(B-10)}$$

$R > 25$ feet

These results are useful for rectangular waveguides which have mechanical bending and flexure properties equivalent to the test waveguide and subject to the radius of curvature limits indicated.

The phase shift associated with bending can be explained by a mechanical deformation of the waveguide cross section. For H-plane bending, deformation of the waveguide occurs principally by buckling of the wide dimension instead of the narrow dimension as in the case for E-plane bending. This buckling will result in a change in impedance only, unless the deflecting broad sides reduce the a dimension, which appears to be the case. The resulting phase shift is of such small consequence as to be considered negligible.

APPENDIX C

DEFLECTED ANTENNA PATTERNS

This appendix contains a set of fan beam profiles for each deflected antenna configuration studied. Three cuts of each beam is shown, at $\theta = 90^{\circ}$, 80°, and 70° respectively, where $\theta = 90^{\circ}$ corresponds to the subsatellite point. The cross-sections are not normal to the fan beam but instead correspond to an actual observation for the indicated mounting angle δ. Figures C-1 through C-24 are for a simple cantilever antenna (unguyed), Figures C-25 through C-27 are for an antenna guyed at three-fourths of its length.

The angle, ζ, the abscissa in Figures C-1 through C-27, is defined by the equation $\zeta = \varphi - \pi/2$ and is illustrated in Figure 3-3, page 3-8.

In this appendix the spin rate was designated by Ω although it was referred to as ω throughout most of the text.

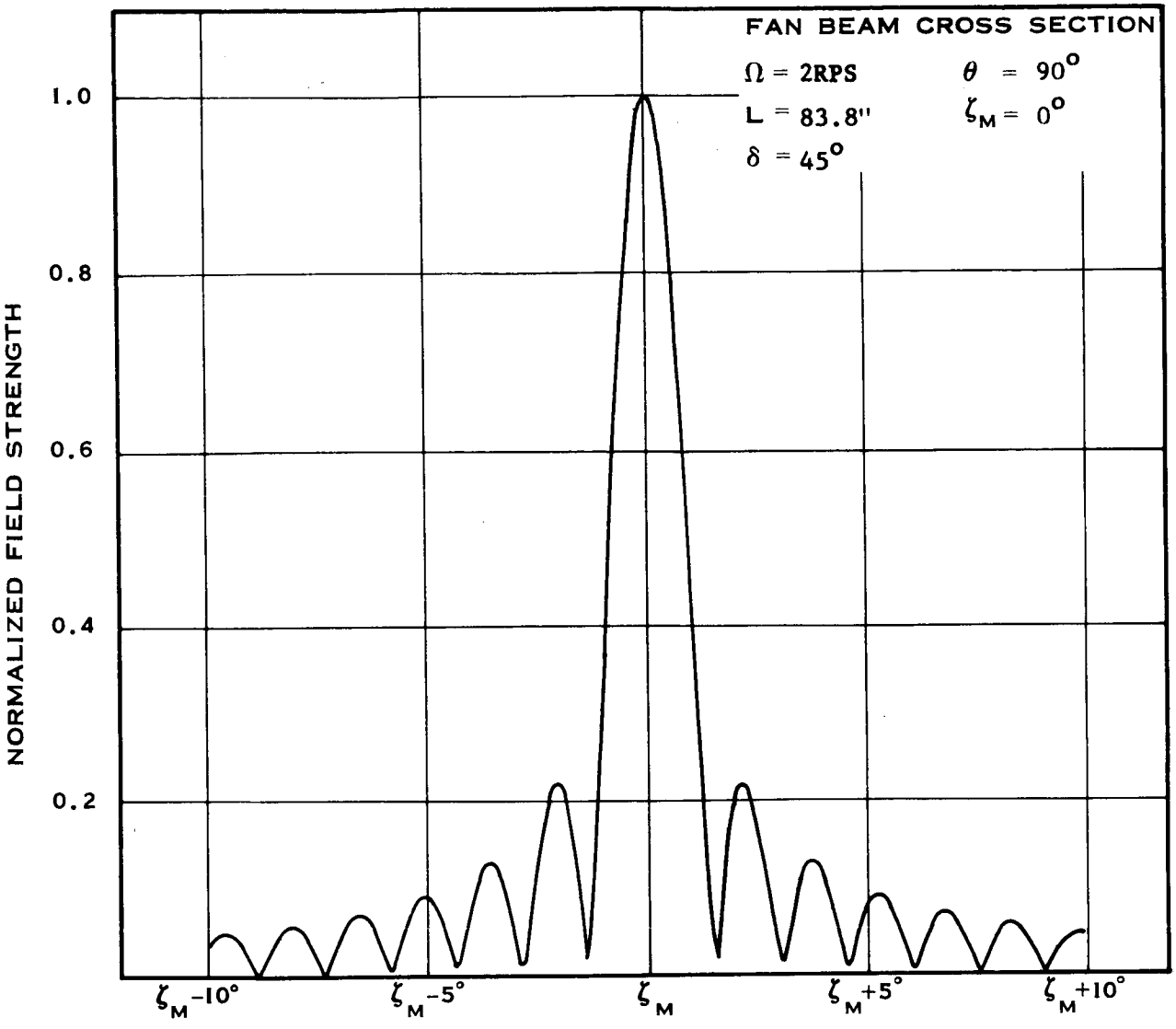

Figure C-1 Unguyed Antenna Pattern

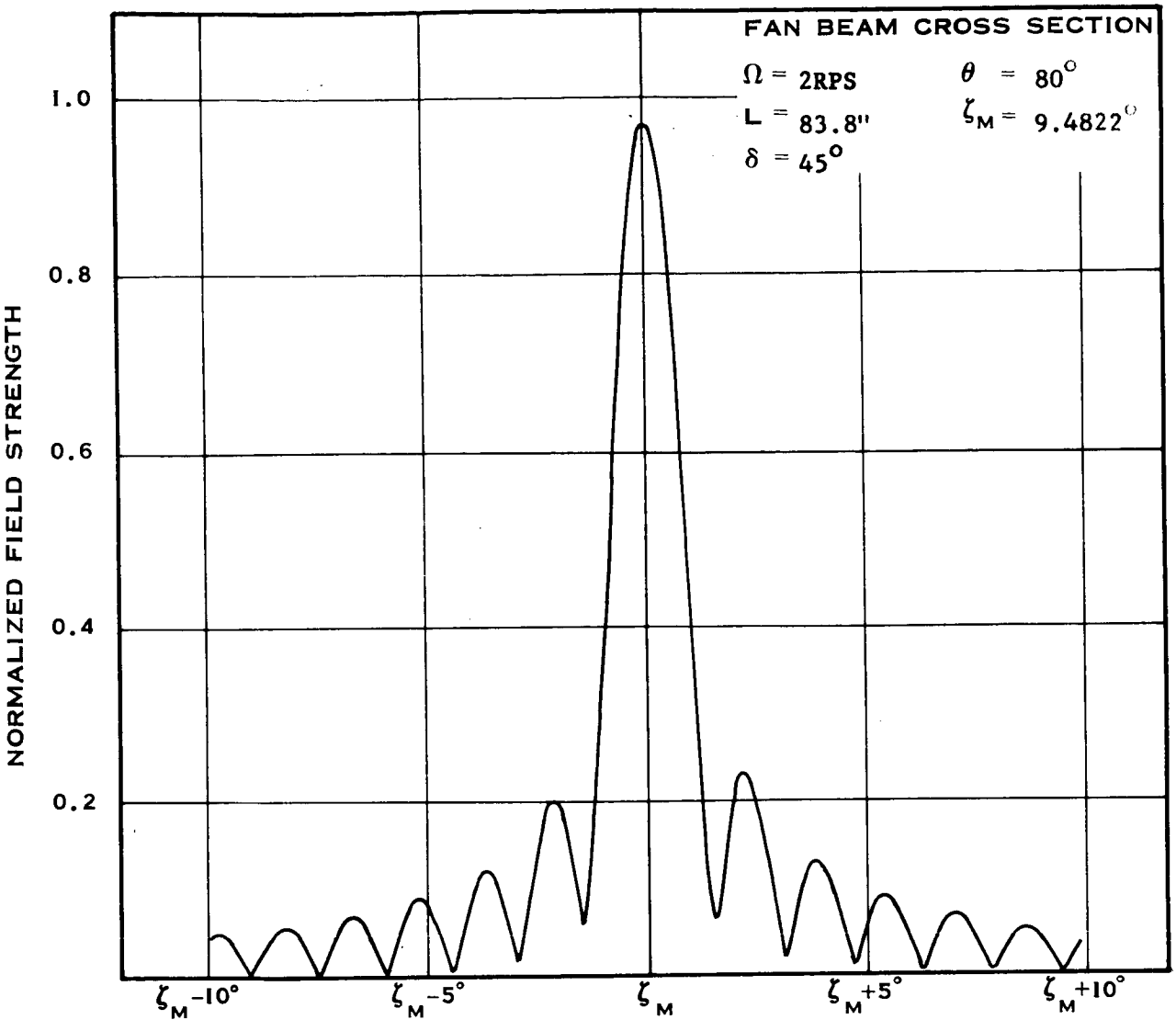

Figure C-2 Unguyed Antenna Pattern

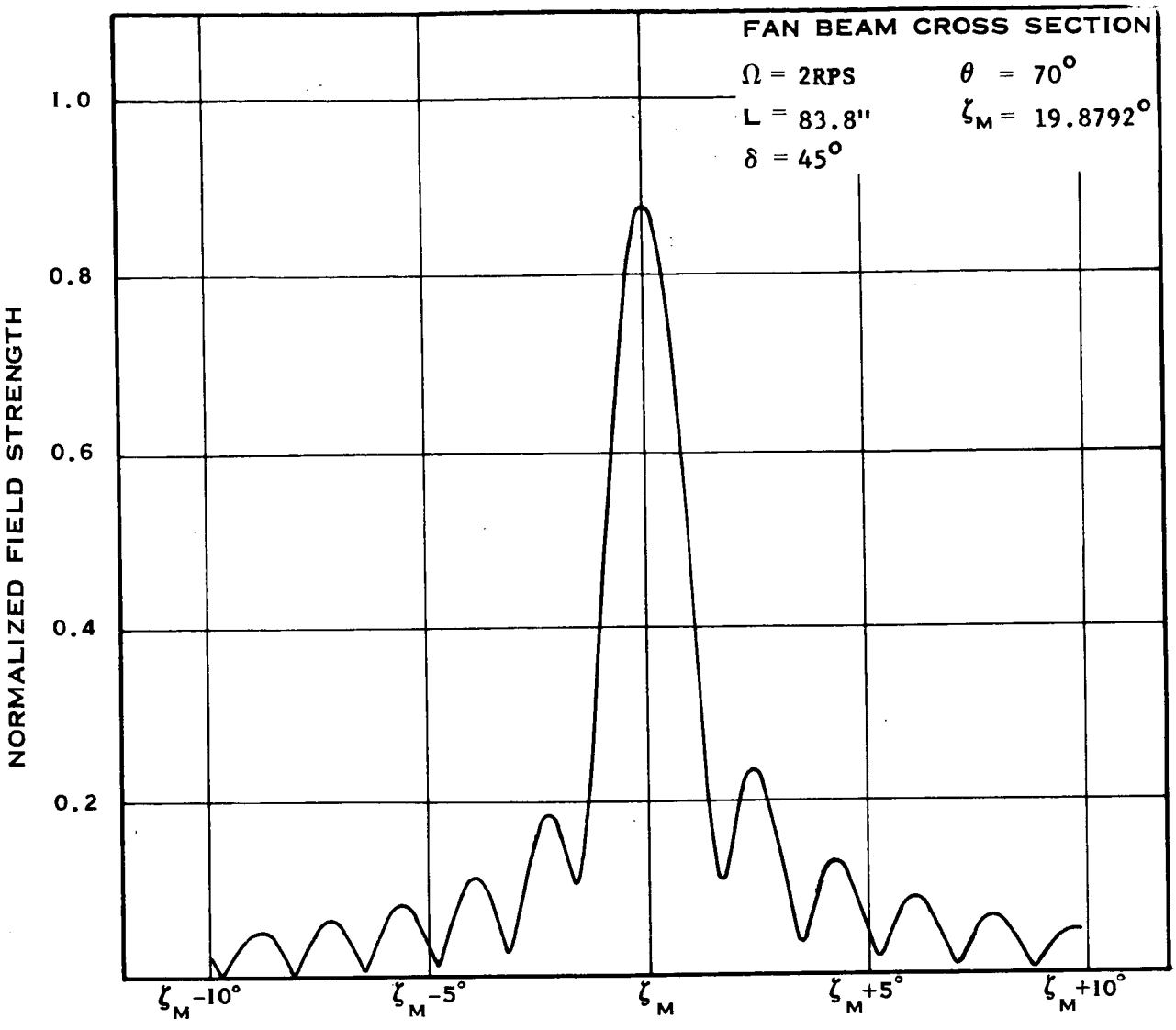

Figure C-3 Unguyed Antenna Pattern

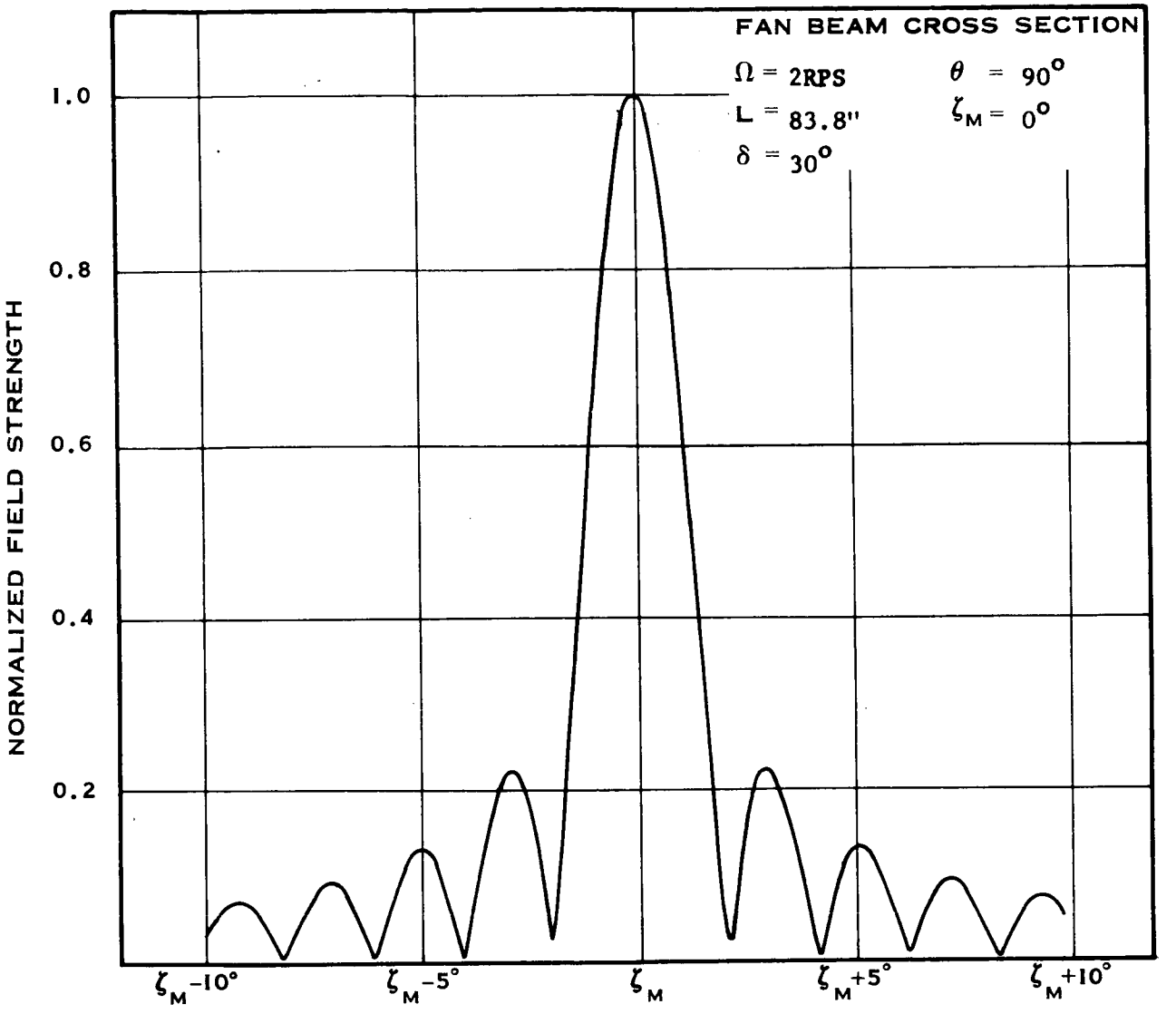

Figure C-4 Unguyed Antenna Pattern

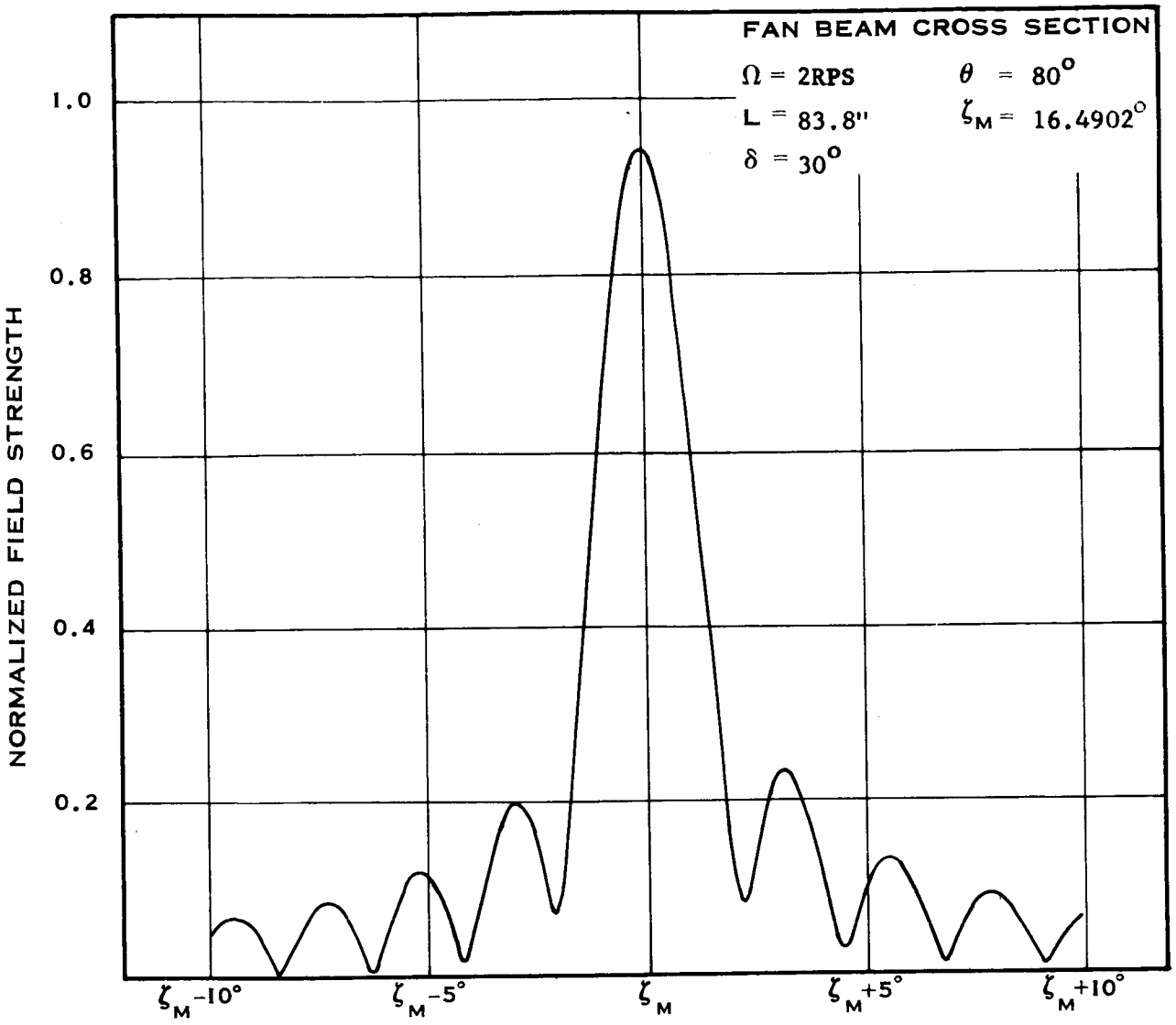

Figure C-5 Unguyed Antenna Pattern

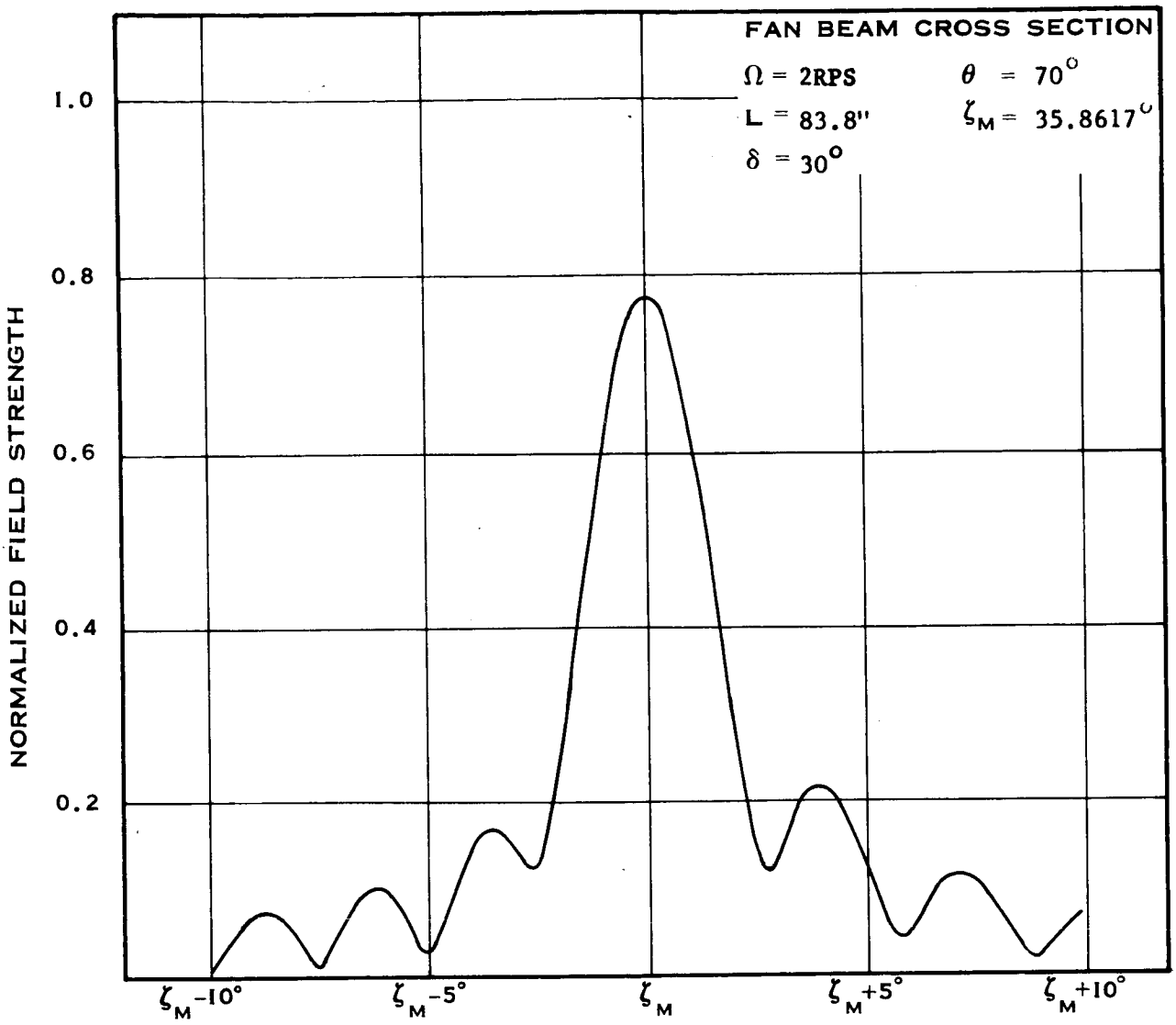

Figure C-6 Unguyed Antenna Pattern

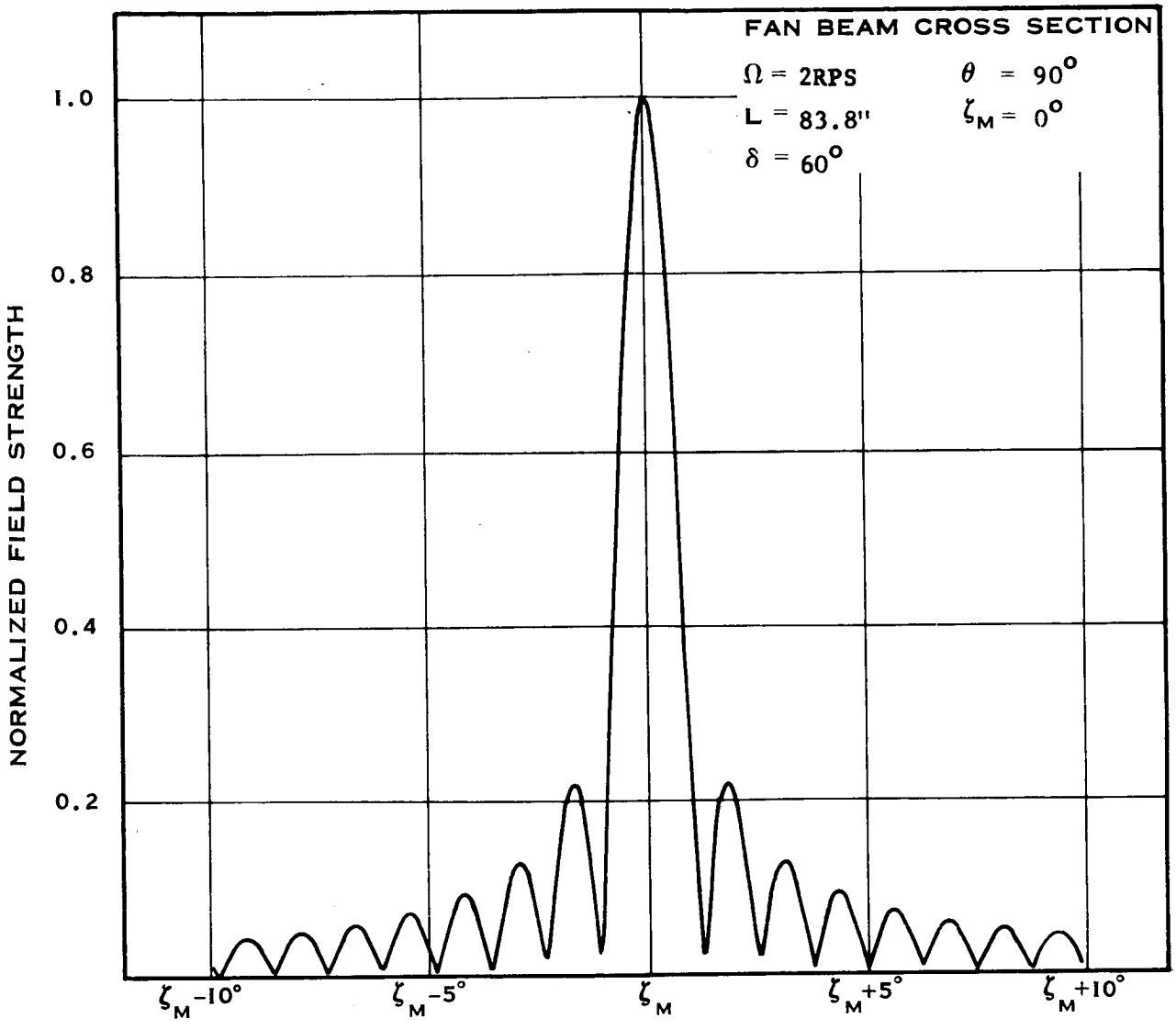

Figure C-7 Unguyed Antenna Pattern

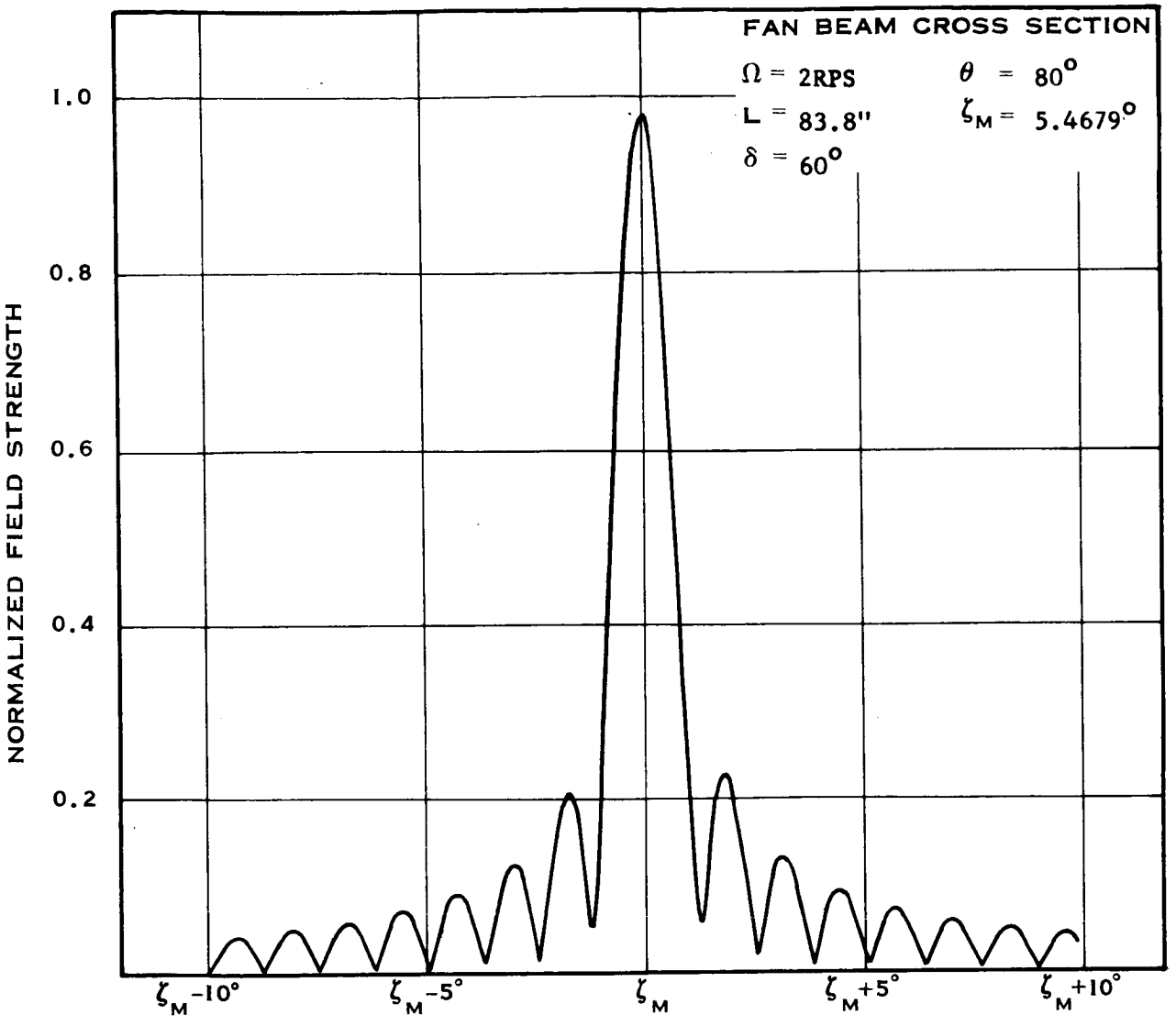

Figure C-8 Unguyed Antenna Pattern

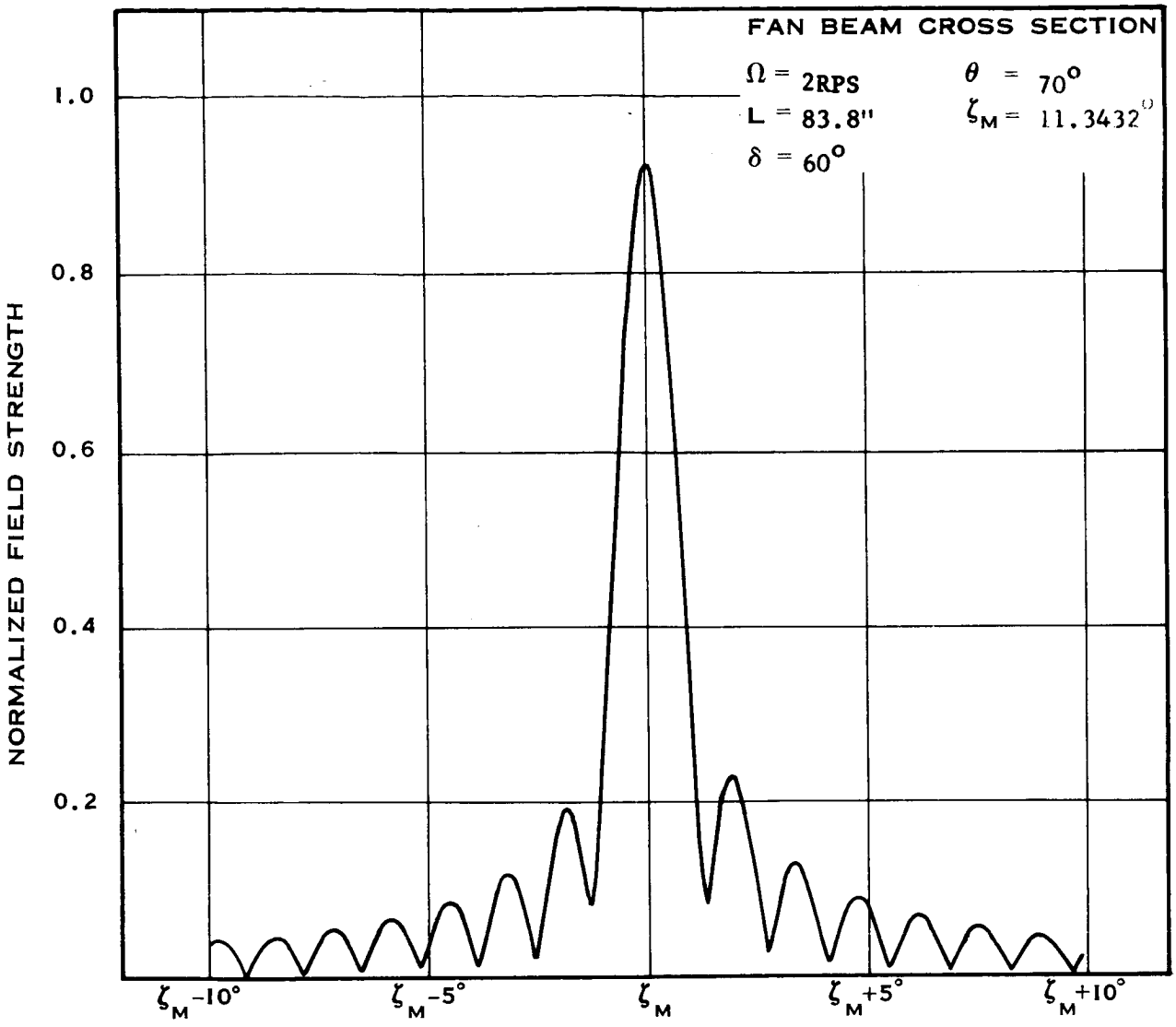

Figure C-9 Unguyed Antenna Pattern

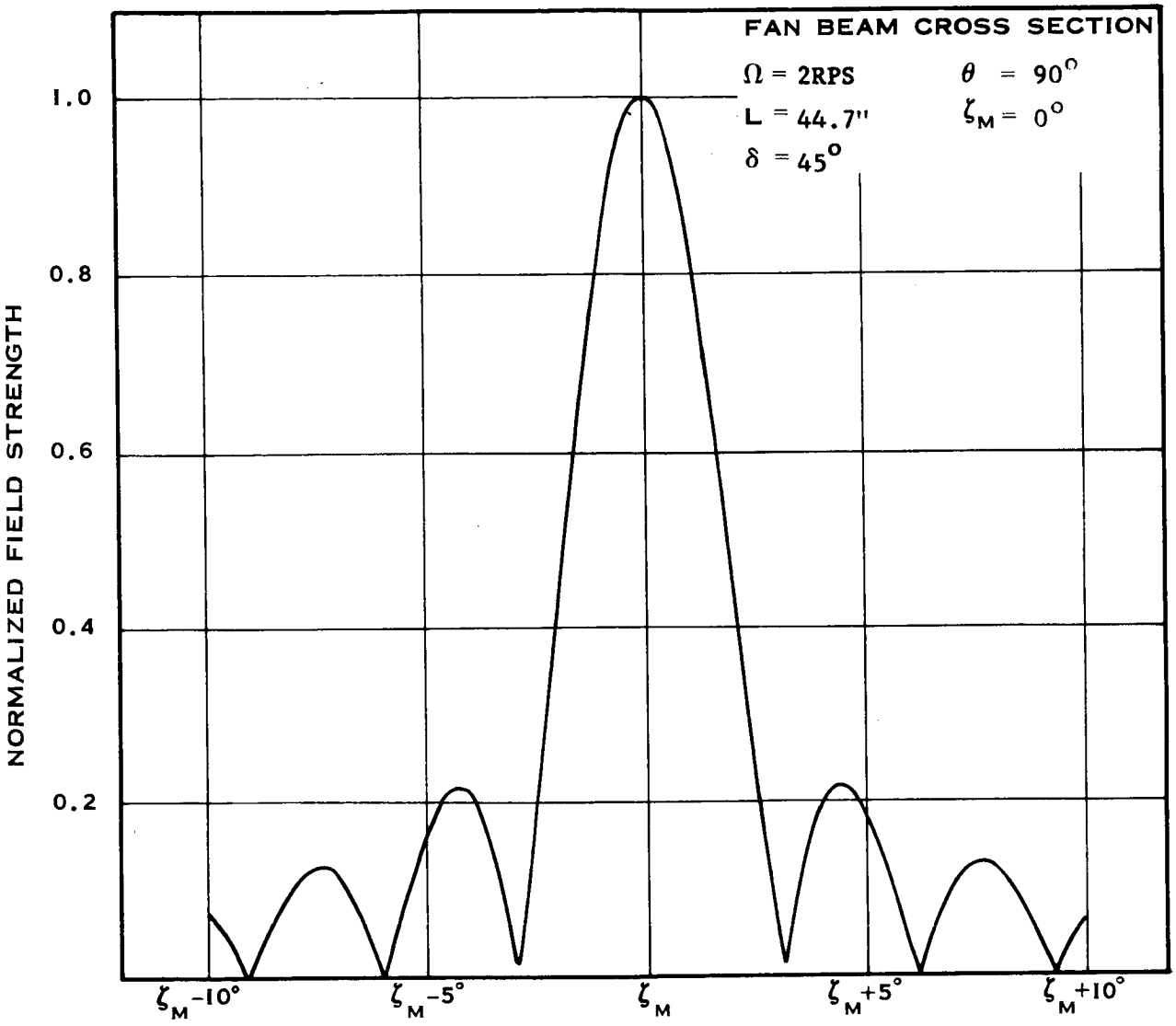

Figure C-10 Unguyed Antenna Pattern

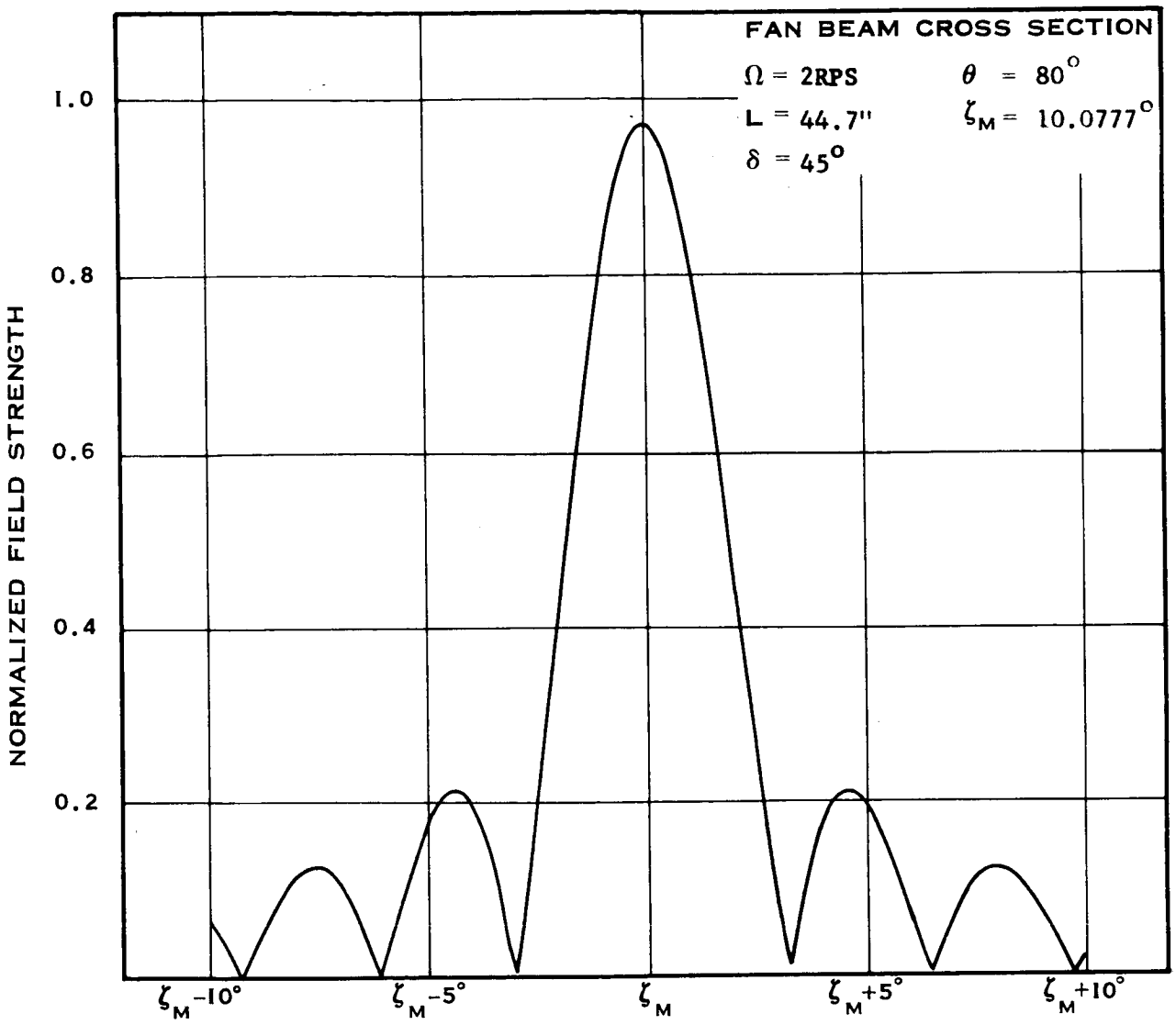

Figure C-11 Unguyed Antenna Pattern

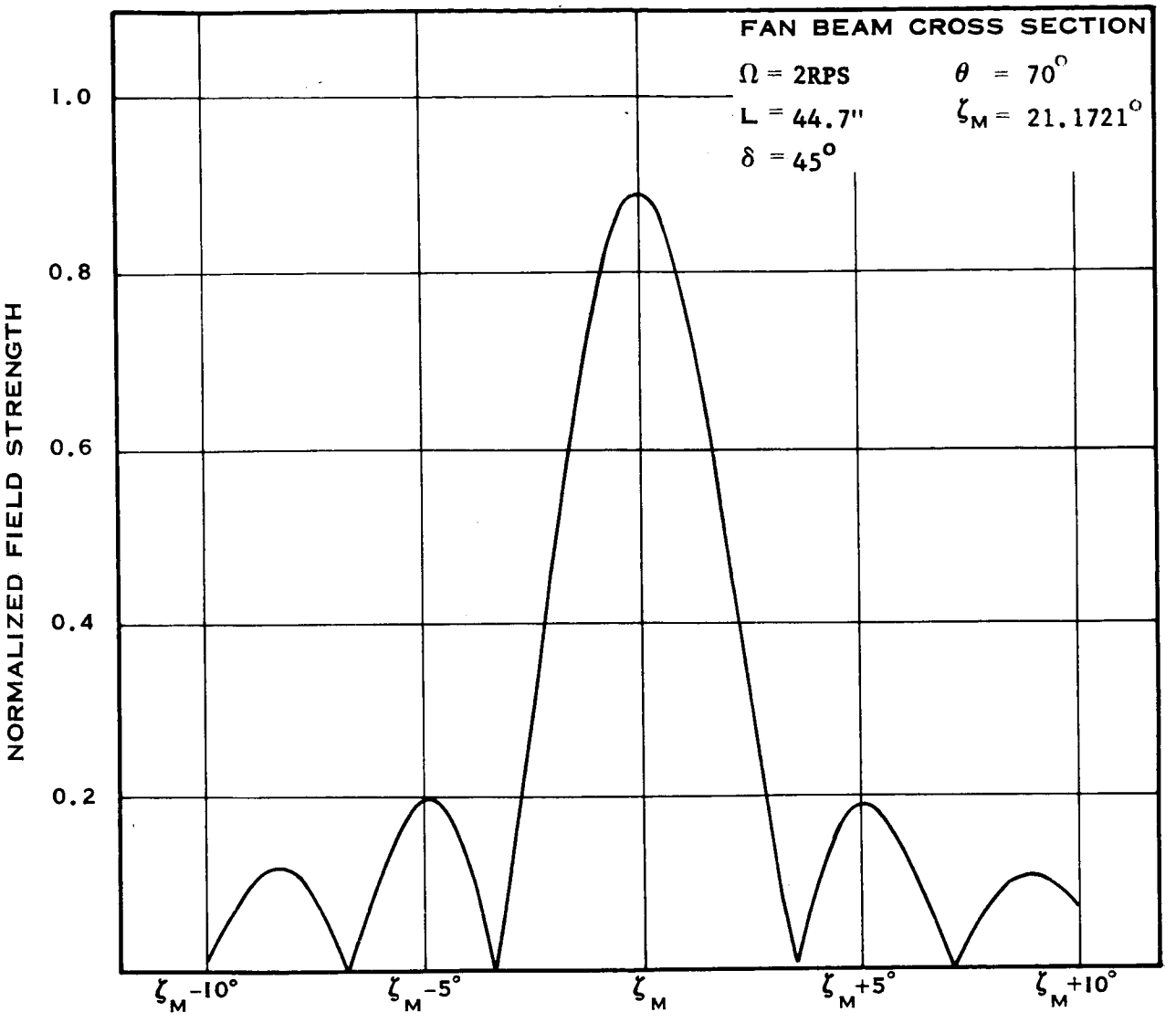

Figure C-12 Unguyed Antenna Pattern

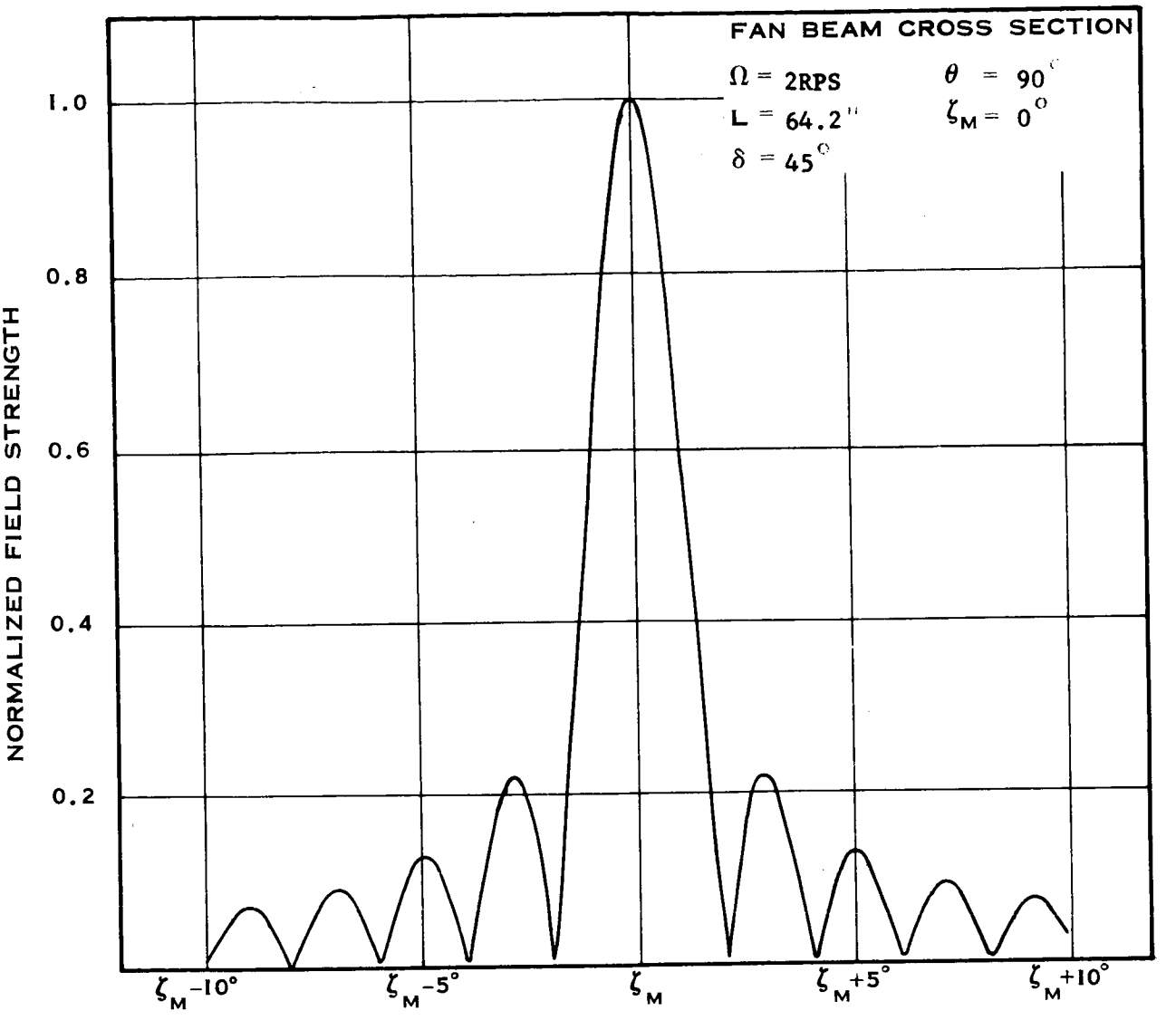

Figure C-13 Unguyed Antenna Pattern

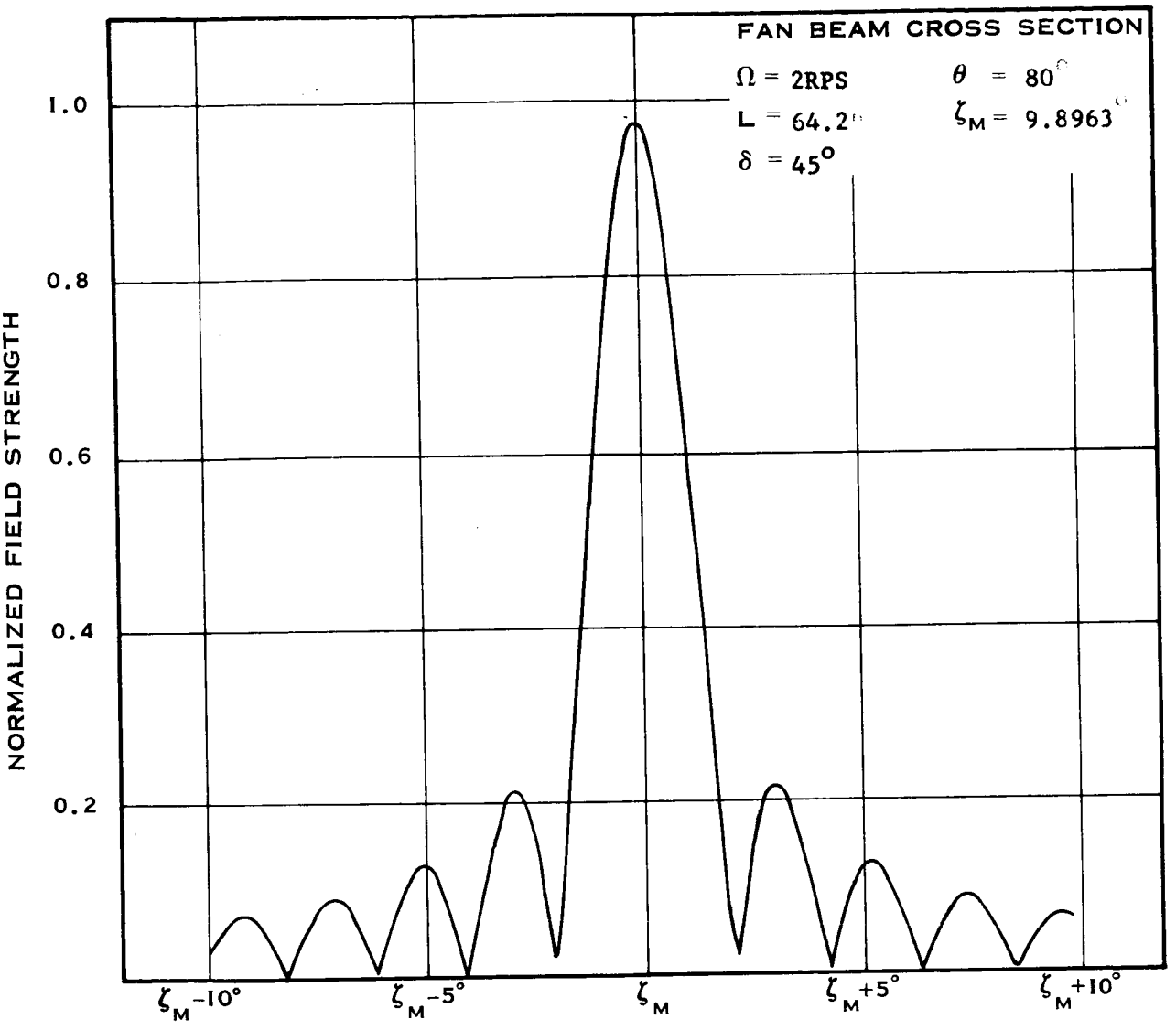

Figure C-14 Unguyed Antenna Pattern

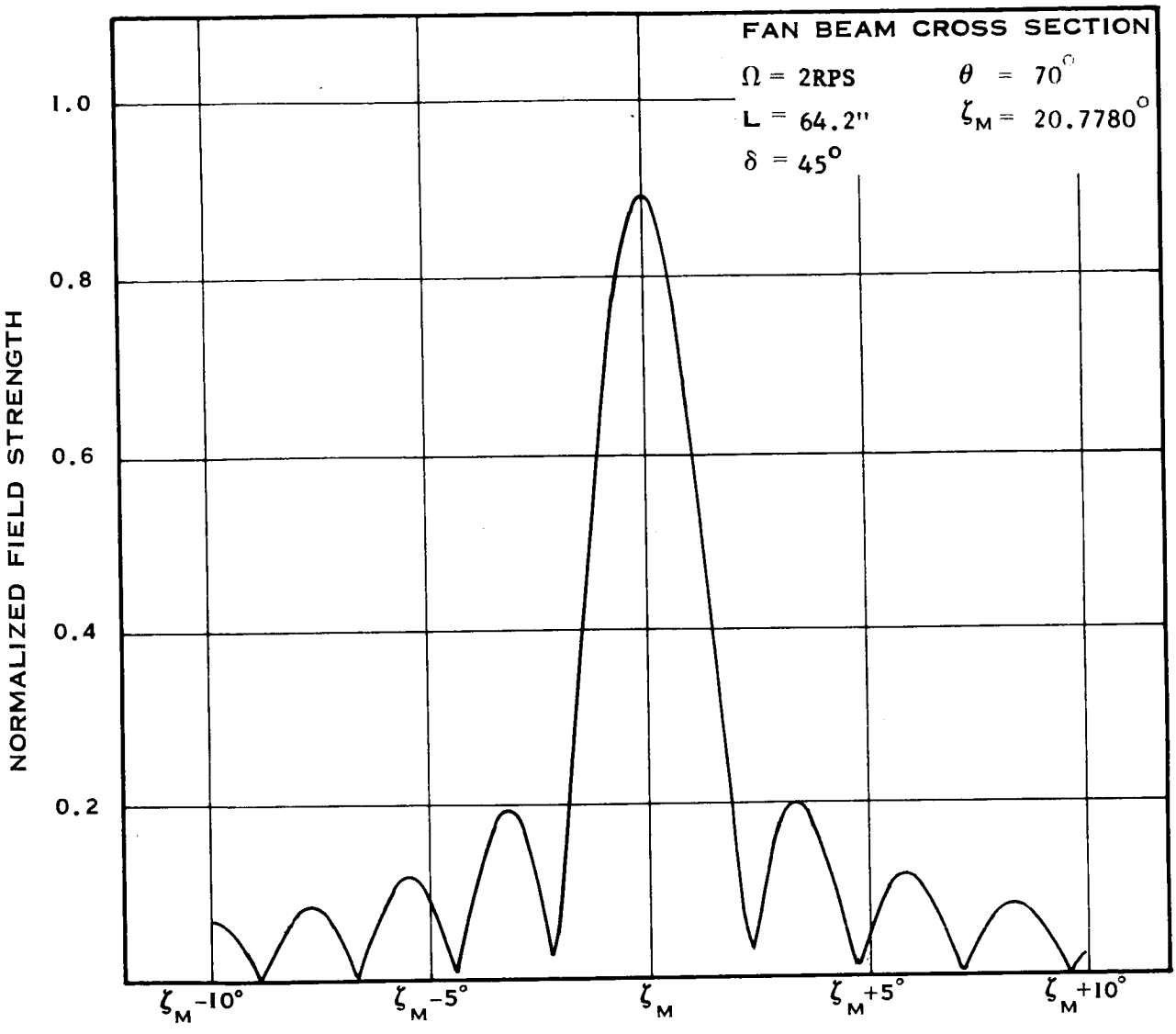

Figure C-15 Unguyed Antenna Pattern

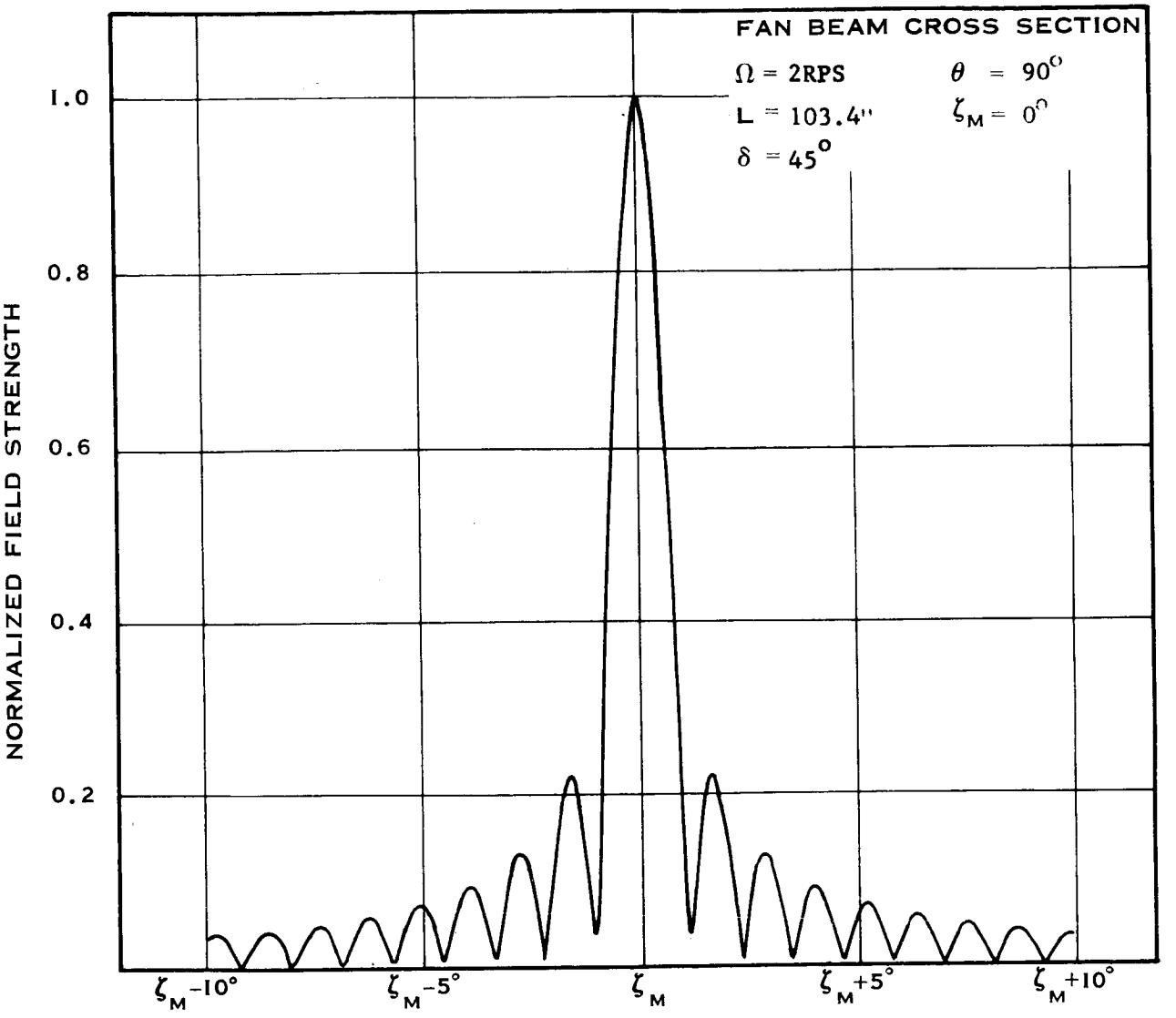

Figure C-16 Unguyed Antenna Pattern

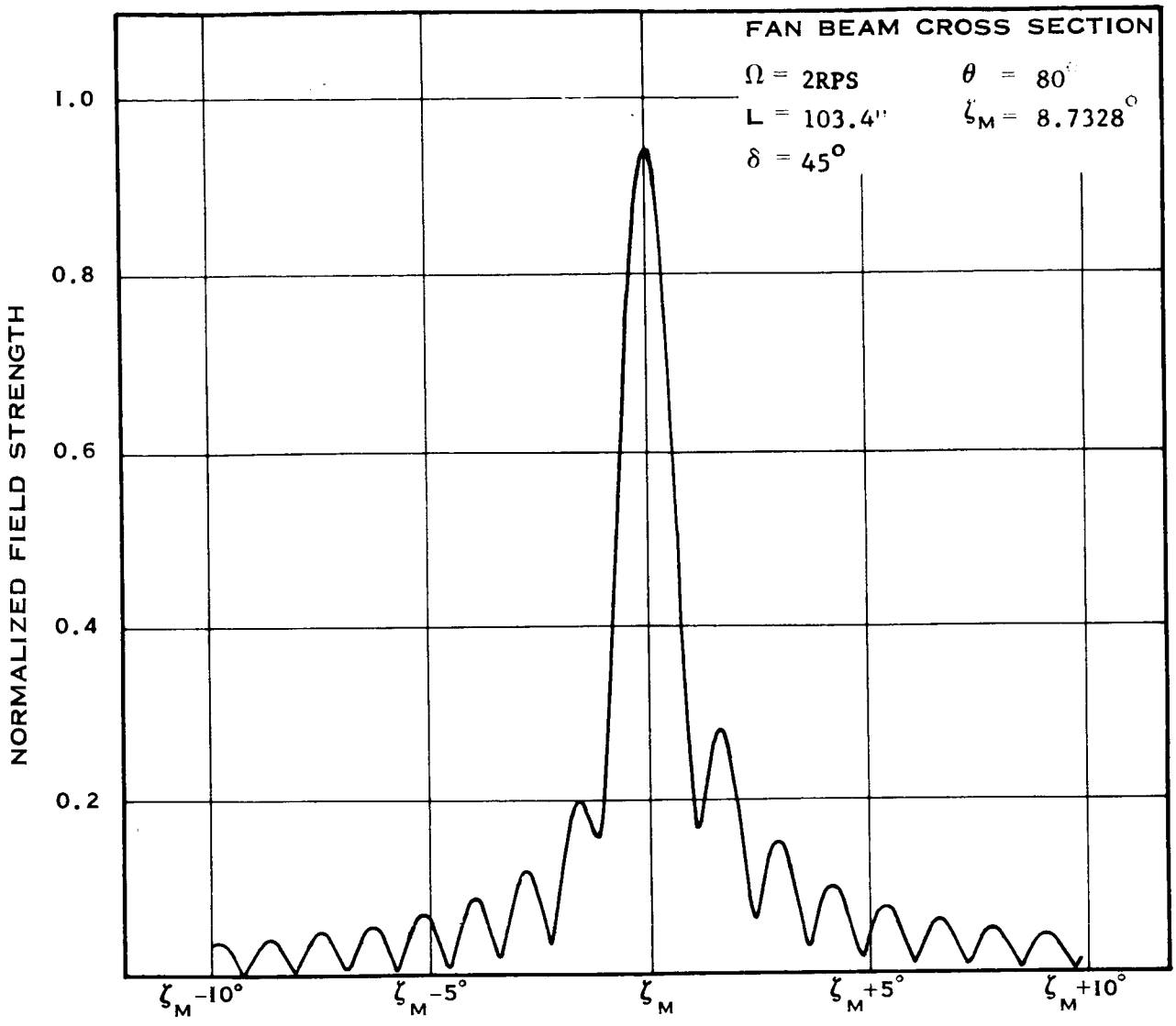

Figure C-17 Unguyed Antenna Pattern

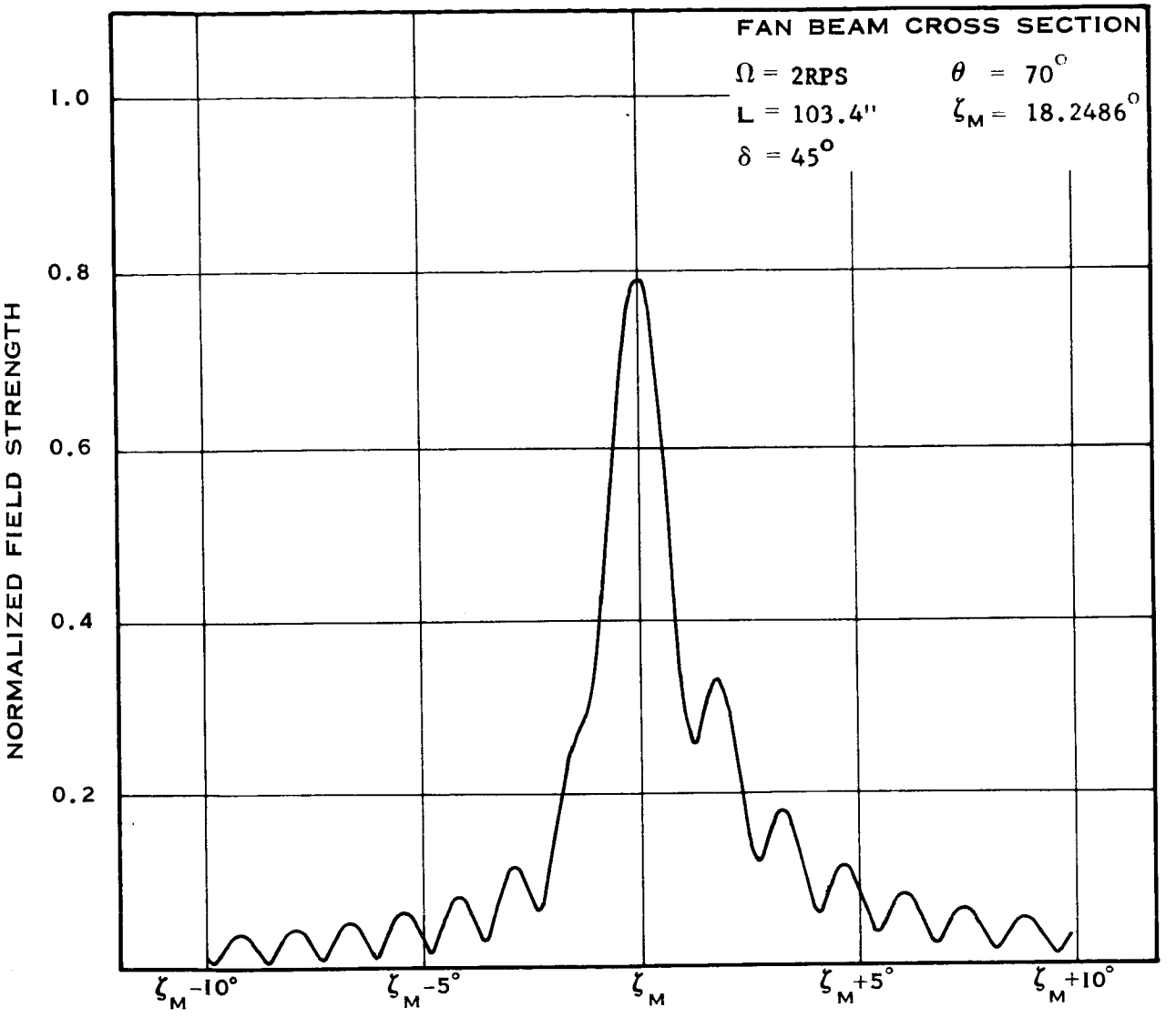

Figure C-18 Unguyed Antenna Pattern

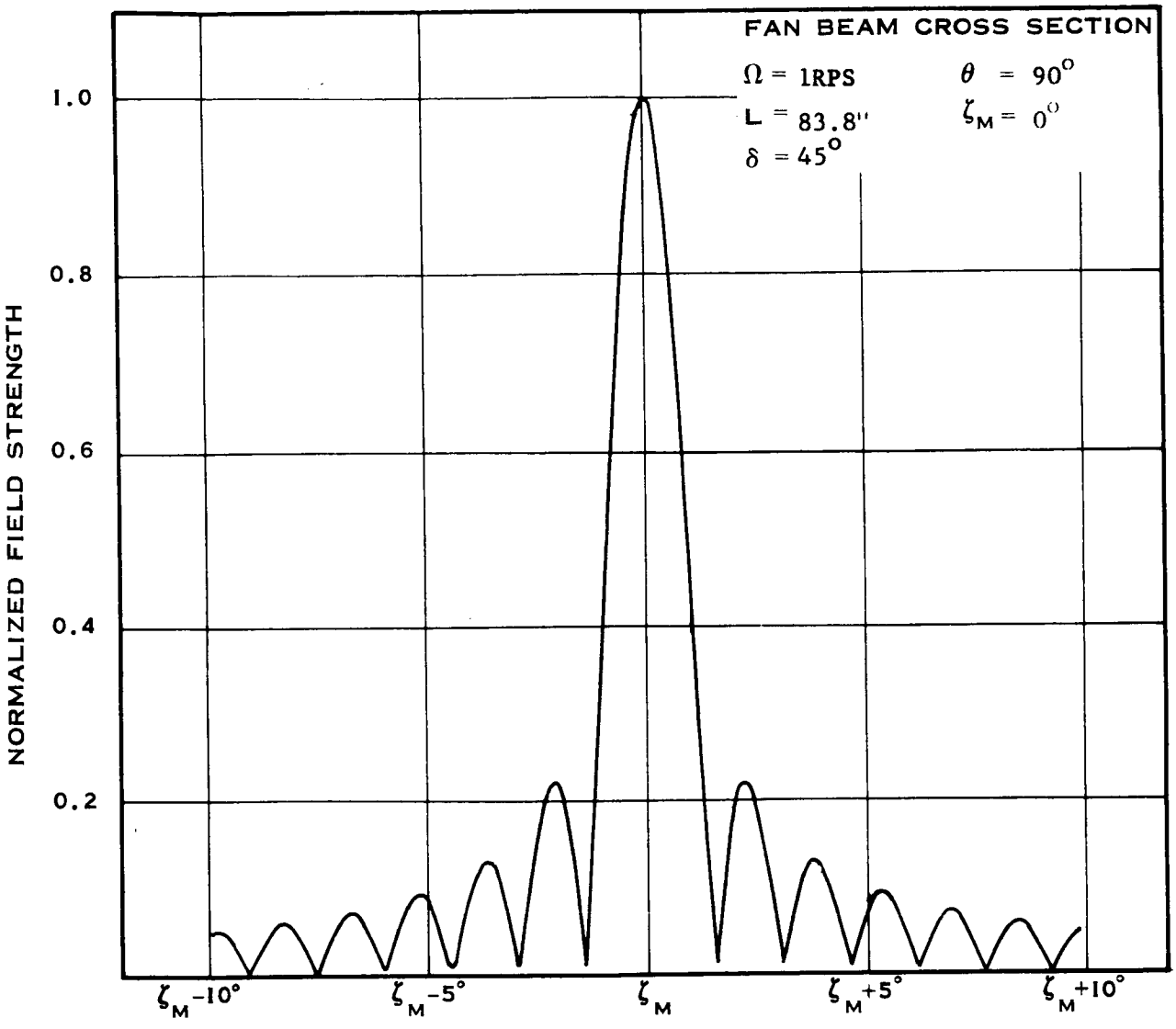

Figure C-19 Unguyed Antenna Pattern

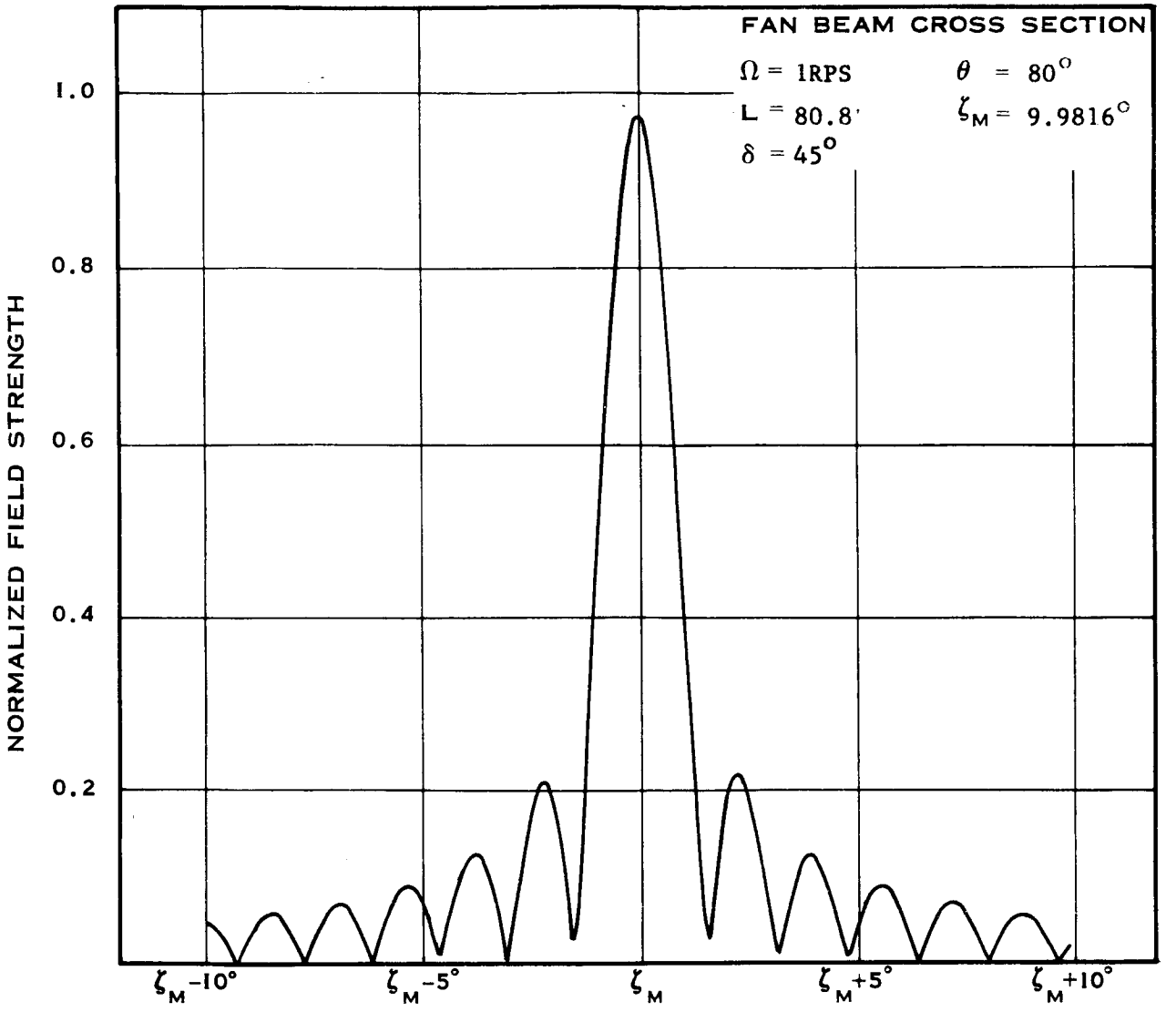

Figure C-20 Unguyed Antenna Pattern

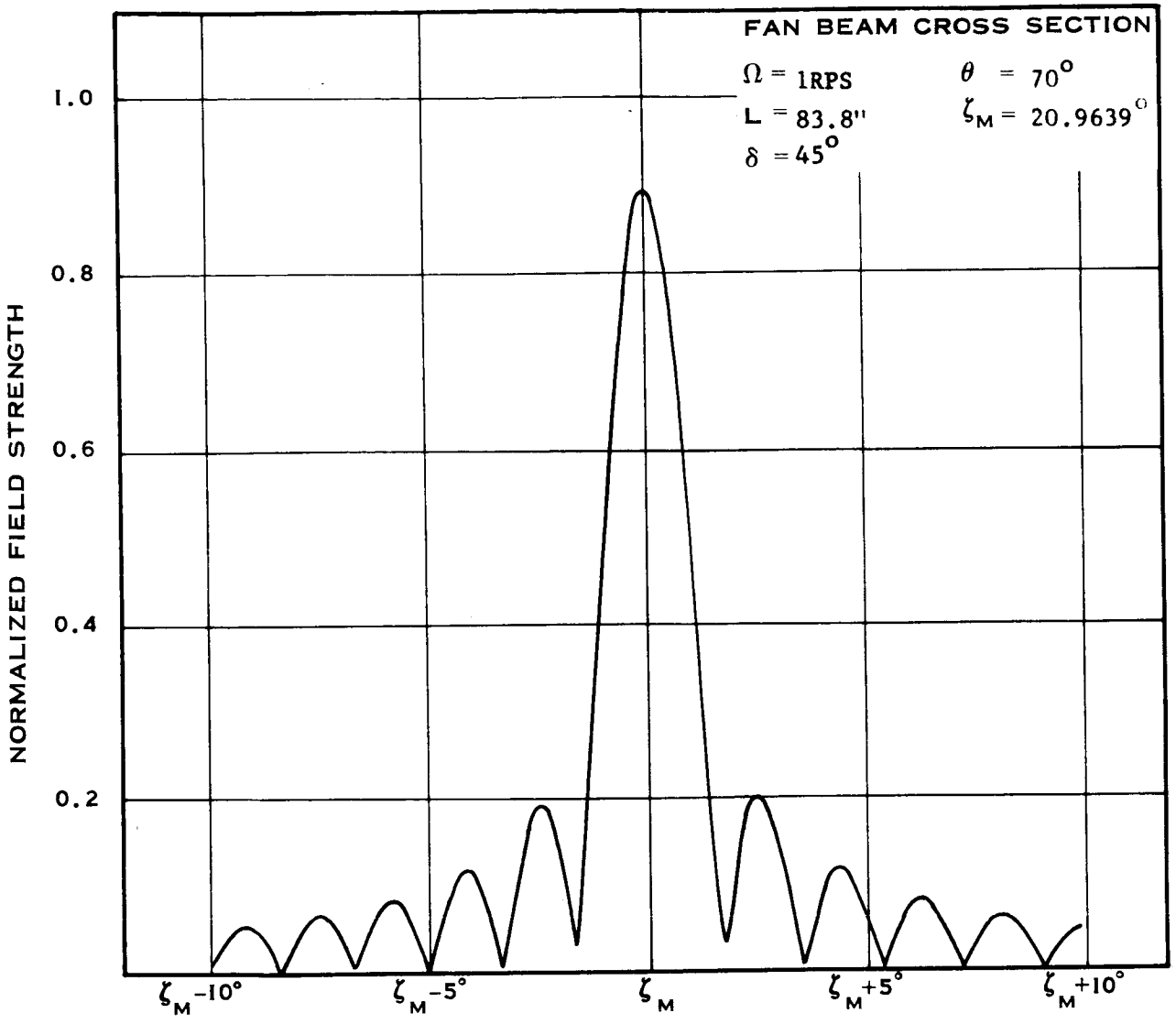

Figure C-21 Unguyed Antenna Pattern

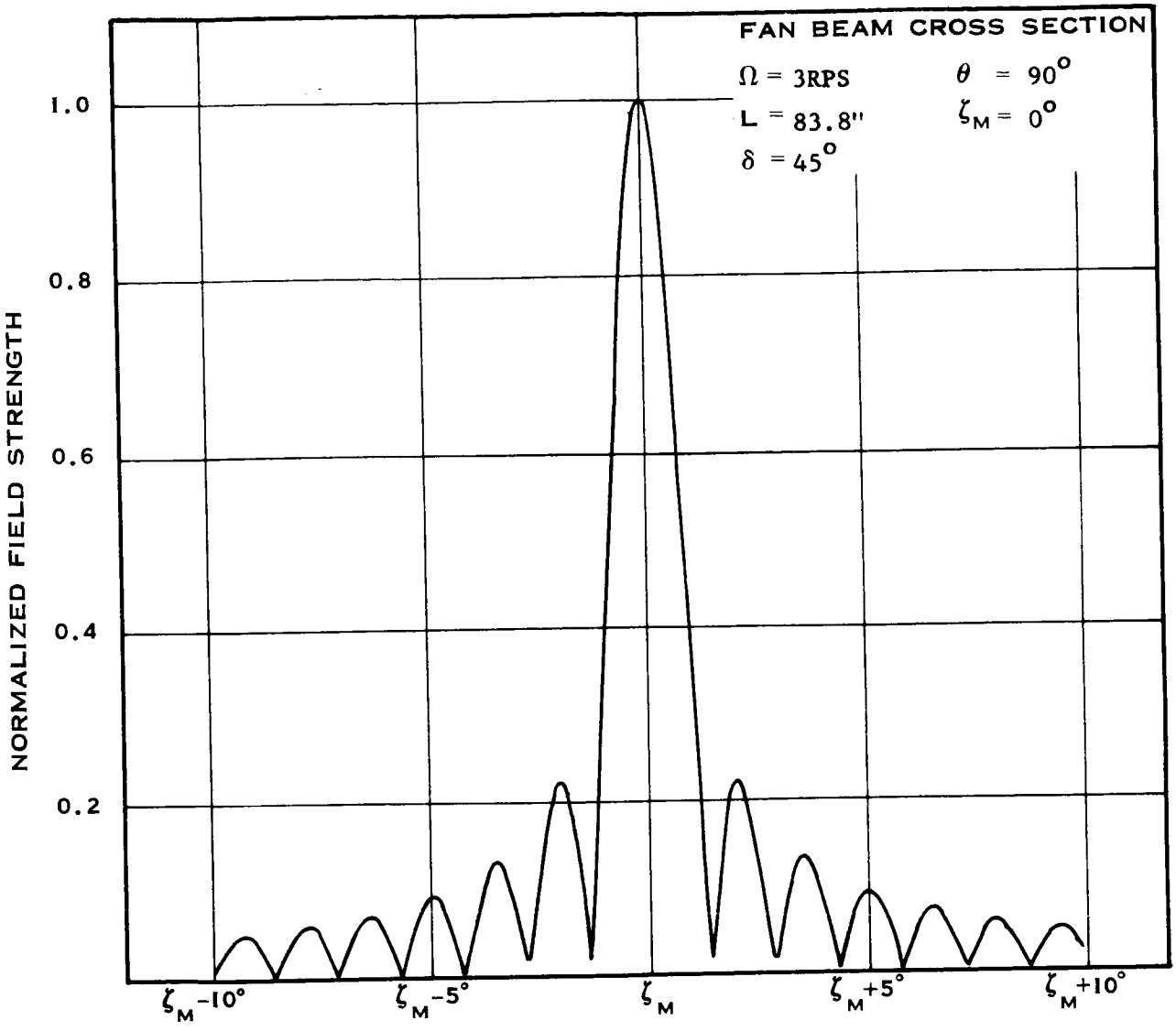

Figure C-22 Unguyed Antenna Pattern

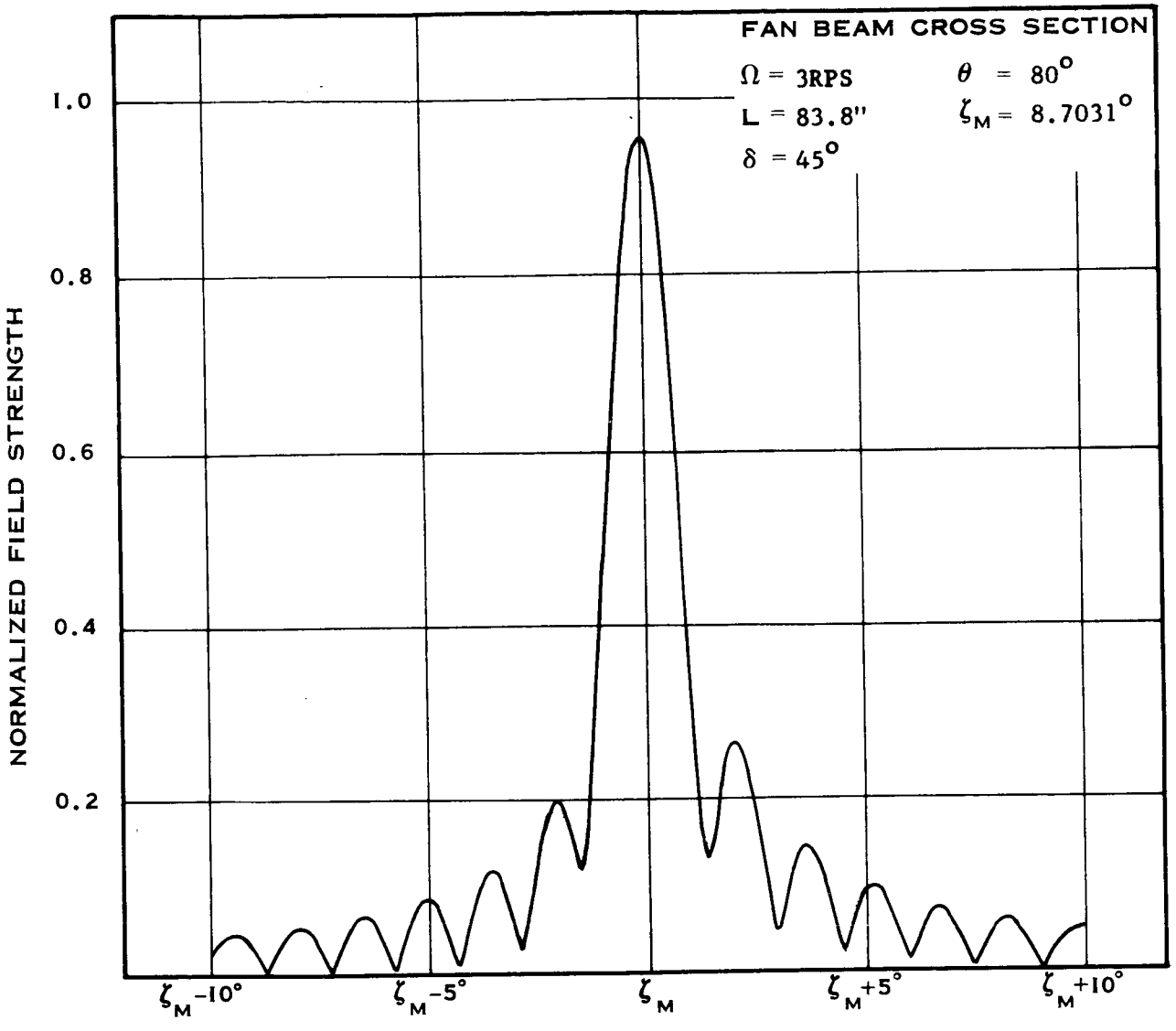

Figure C-23 Unguyed Antenna Pattern

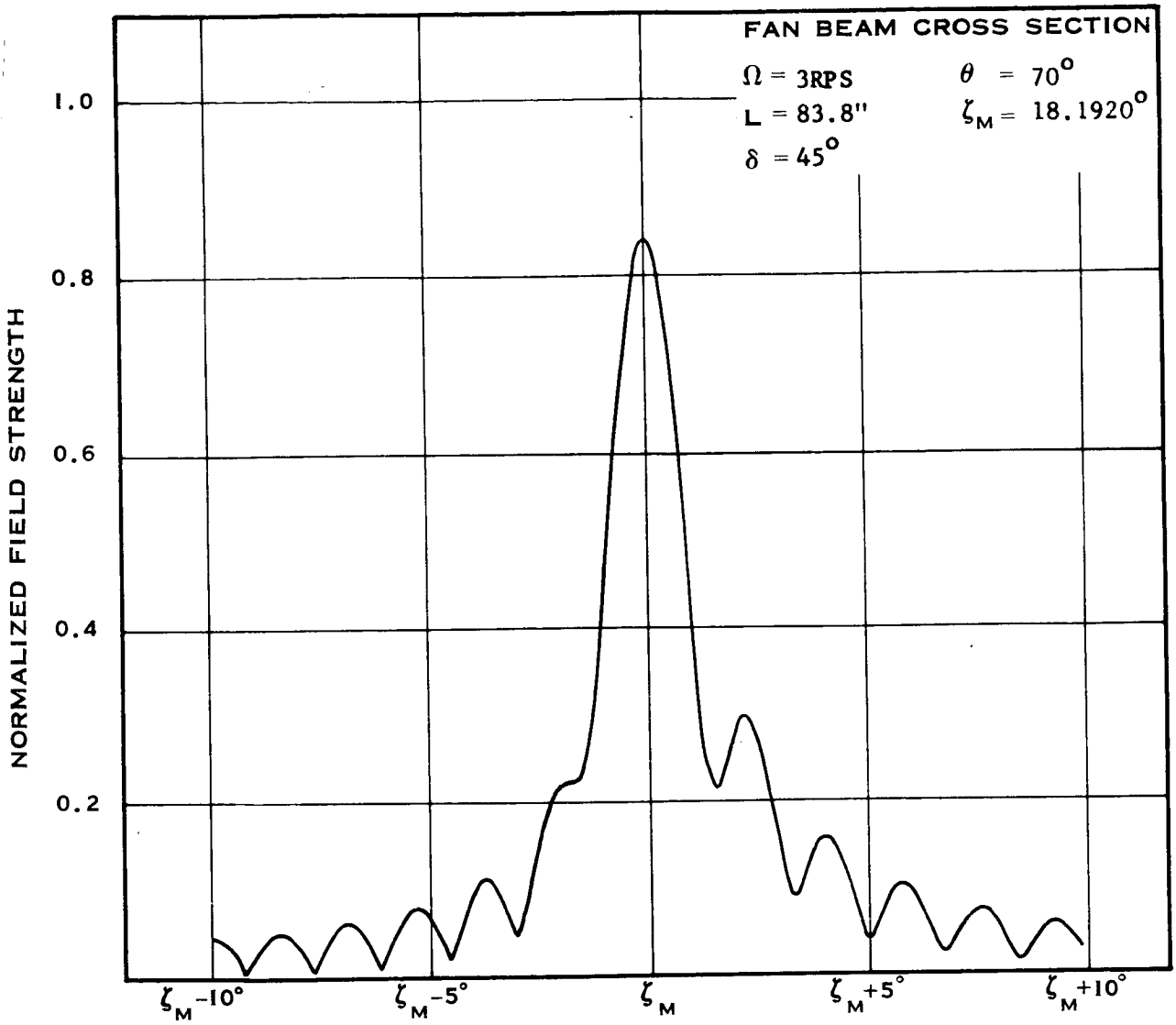

Figure C-24 Unguyed Antenna Pattern

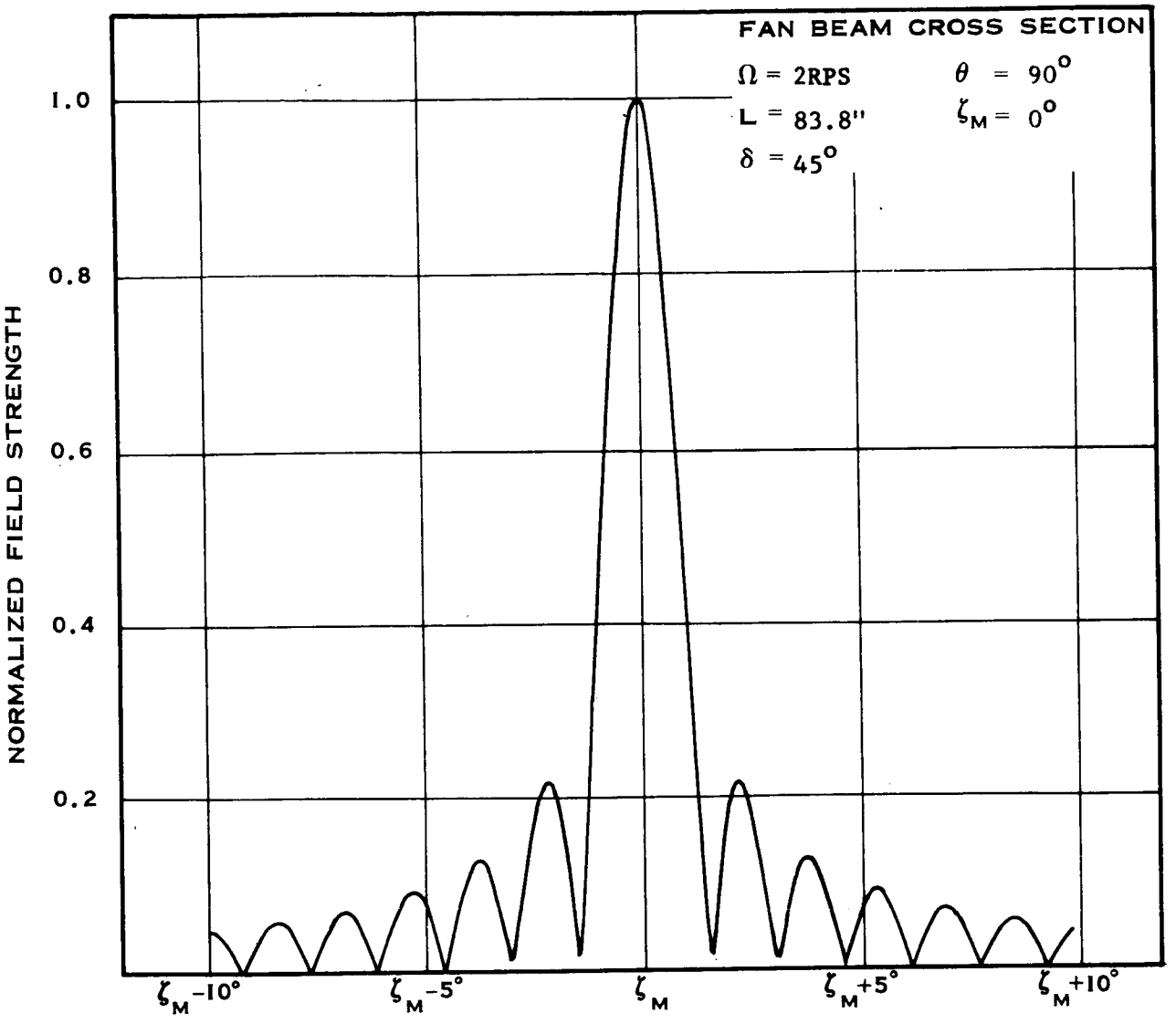

Figure C-25 Guyed Antenna Pattern

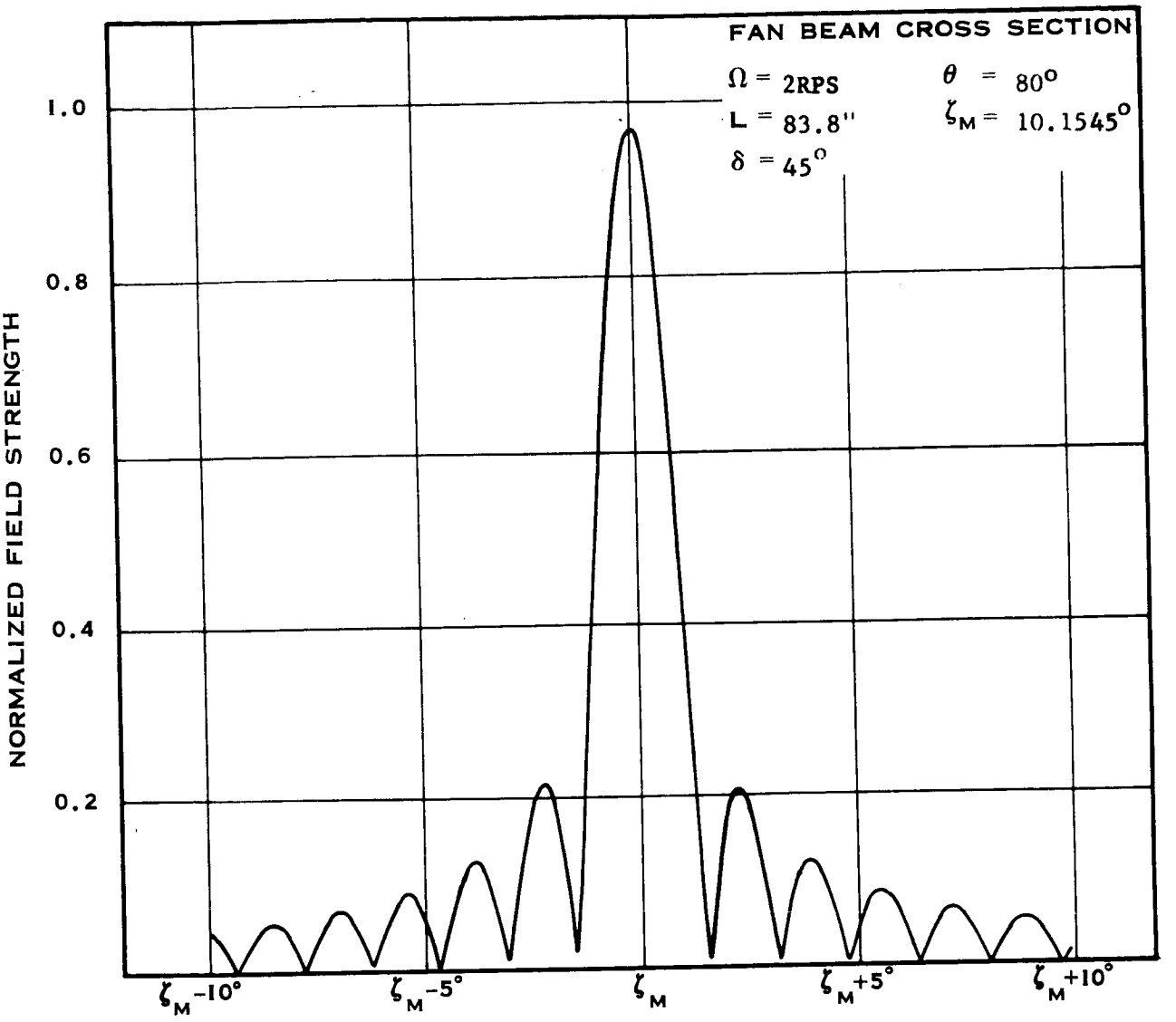

Figure C-26 Guyed Antenna Pattern

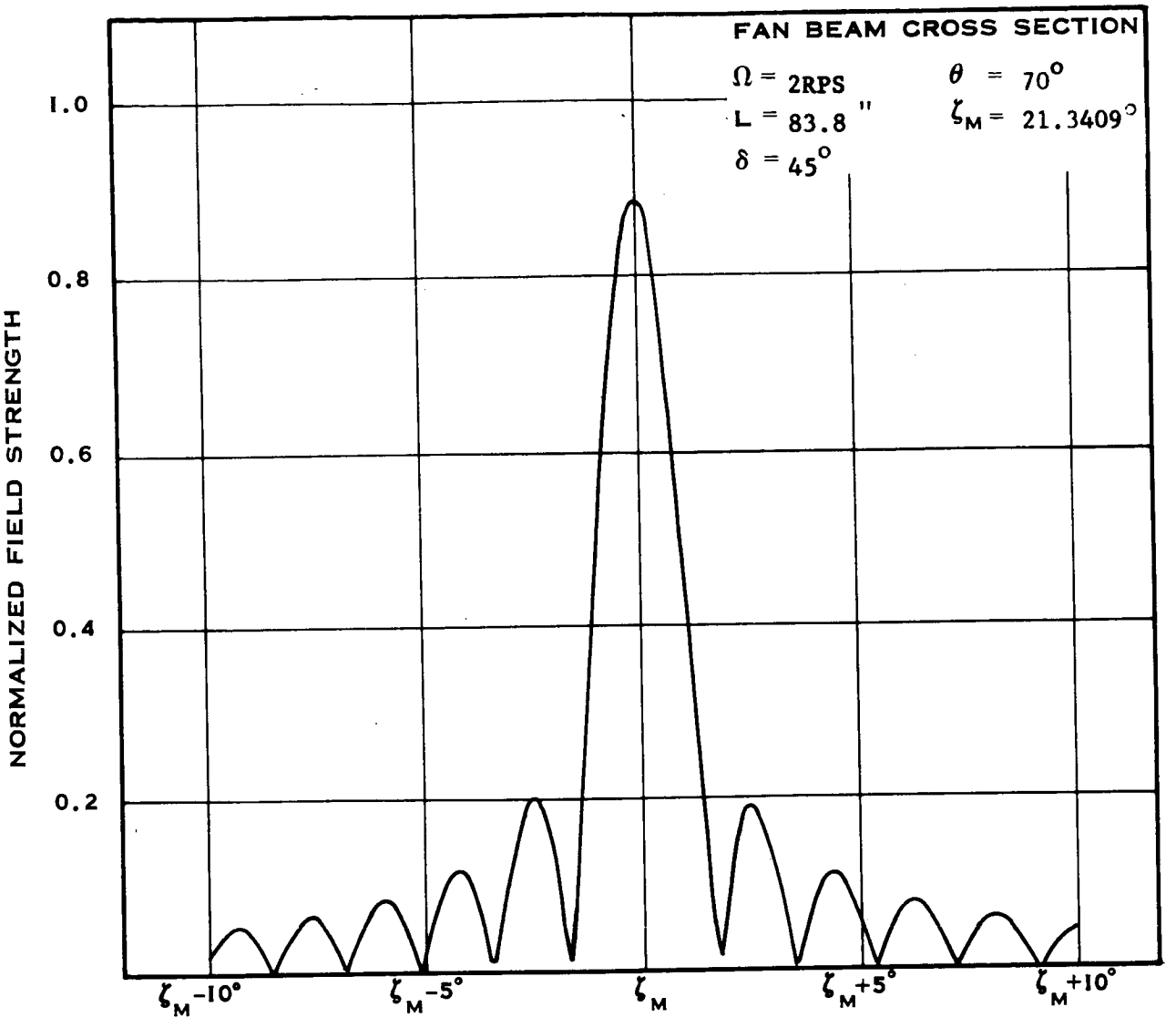

Figure C-27 Guyed Antenna Pattern

APPENDIX D

DOUBLE ANTENNA PATTERNS

This appendix contains a representative sampling of the profiles generated in the double antenna pattern evaluation. On each plot the number of slots M and N, the horizontal and vertical separation of the antennas H and V, the phase ($\Psi = 0^{\circ}$ or $\Psi = 180^{\circ}$), and the angle θ (as defined in the text) are given. Note that these patterns are not for deflected antennas.

Figures D-1 through D-7 show normal cross sections of a beam in 10° steps from the subsatellite point.

Figures D-8 through D-12 show similar cross sections with the number of slots, the antenna separation, and the phase varied.

Figures D-13 through D-18 show some typical pattern generated by a small number of elements widely separated.

Figures D-19 through D-21 give three different aspects of the same pattern.

Figure D-22 illustrates a pattern generated by a series of pairs of slots. The slots are spaced as though the antenna consisted of 40 slots of which slots 3, 4; 7, 8;, 11, 12; etc. were not operating.

Figure D-23 is the pattern formed by a 40 element antenna with a phase reversal at the midpoint.

Figure D-24 is the pattern formed by a 40 element antenna with a phase reversal at approximately 1/3 of the antenna length.

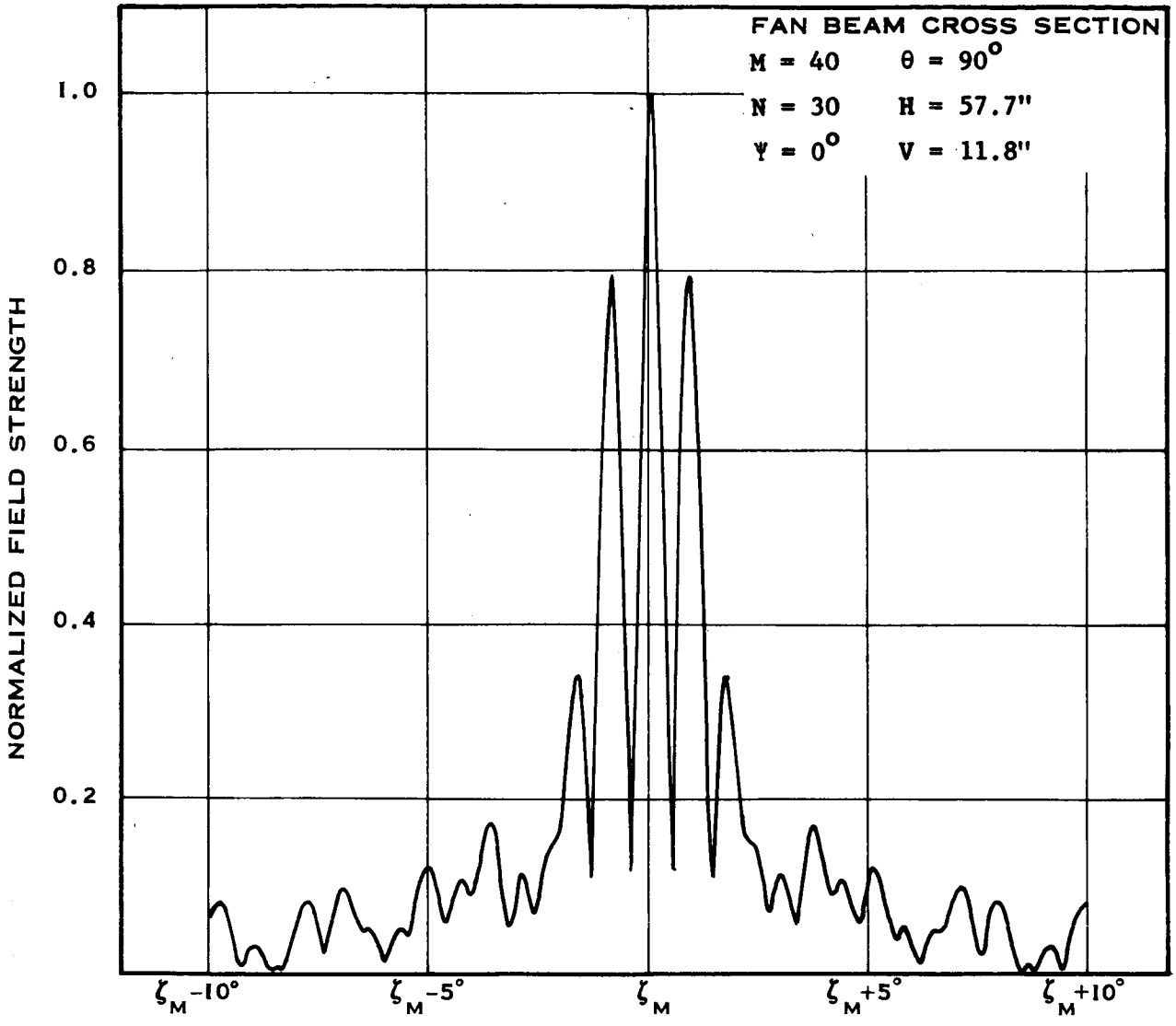

Figure D-1 Normal Cross Section Showing Effects of Separation and Misalignment

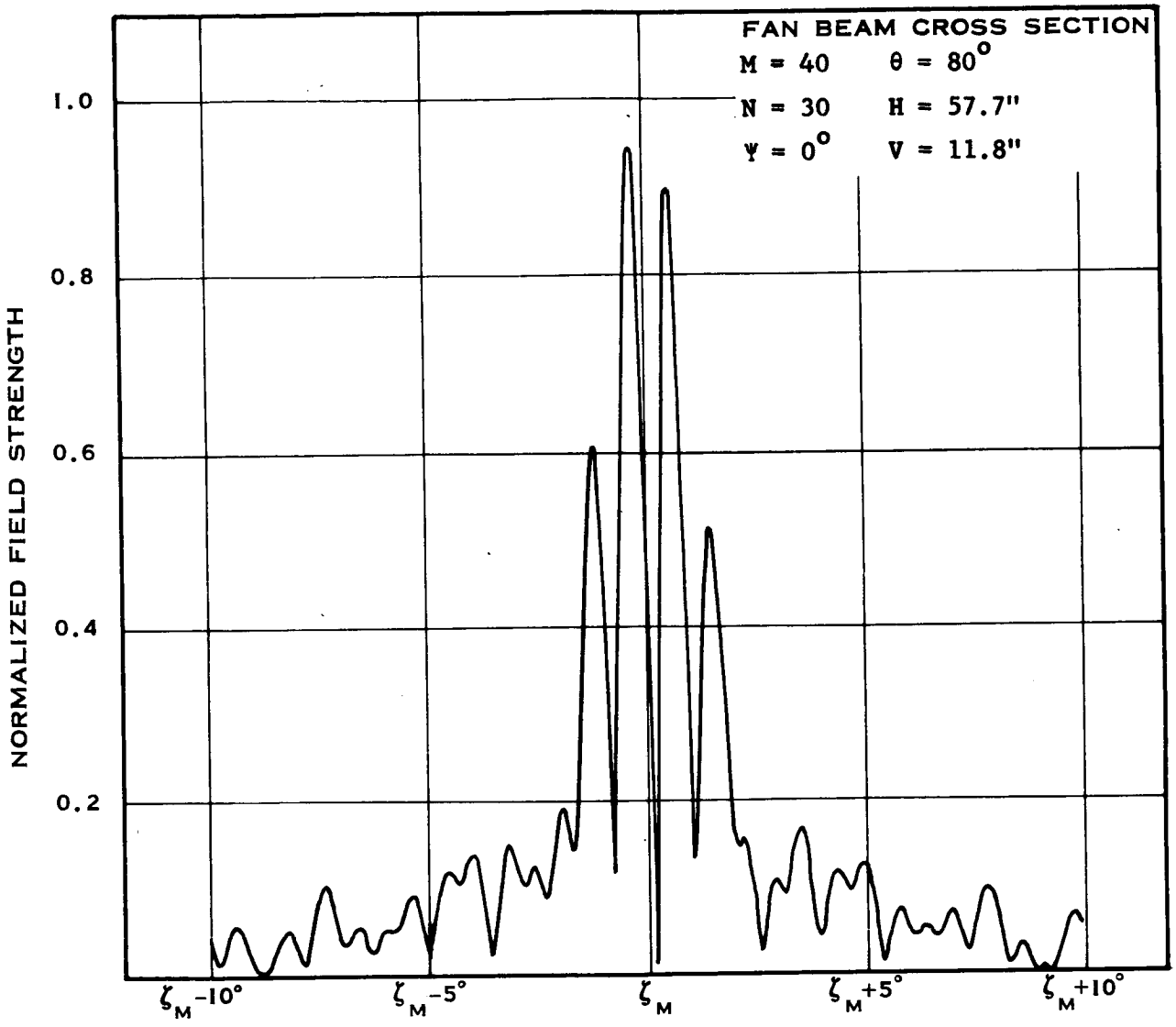

Figure D-2 Normal Cross Section Showing Effects of Separation and Misalignment

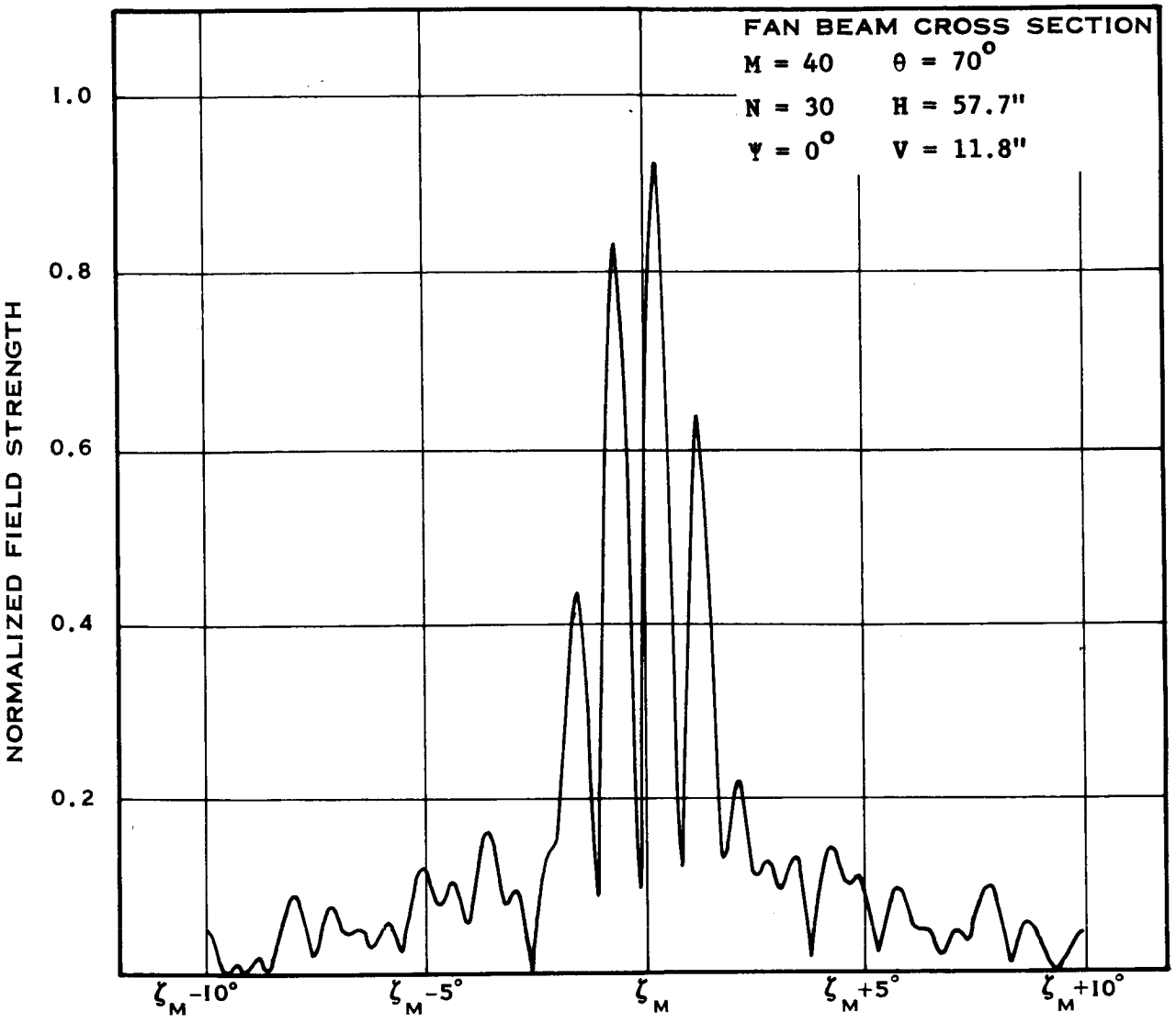

Figure D-3 Normal Cross Section Showing Effects of Separation and Misalignment

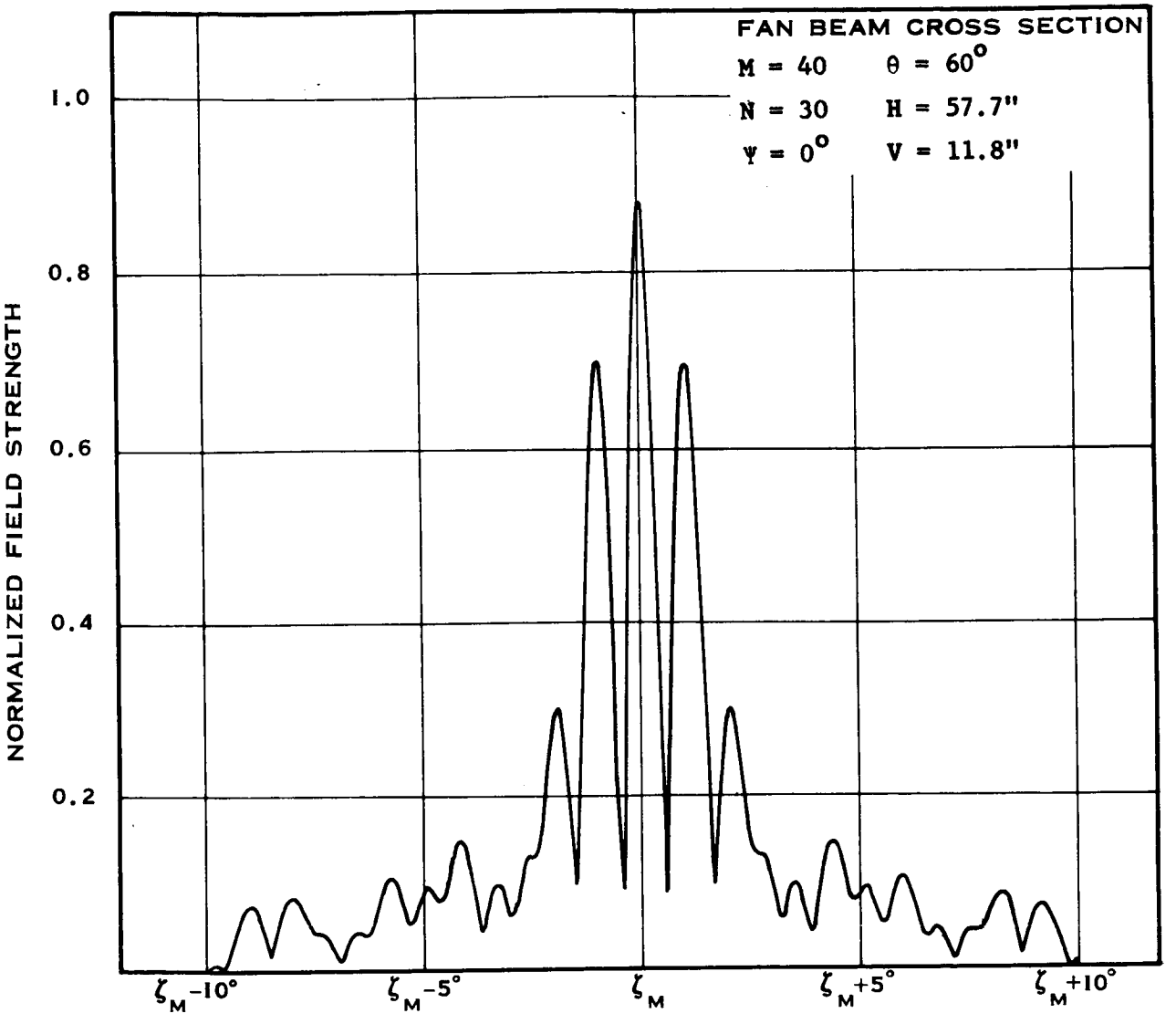

Figure D-4 Normal Cross Section Showing Effects of Separation and Misalignment

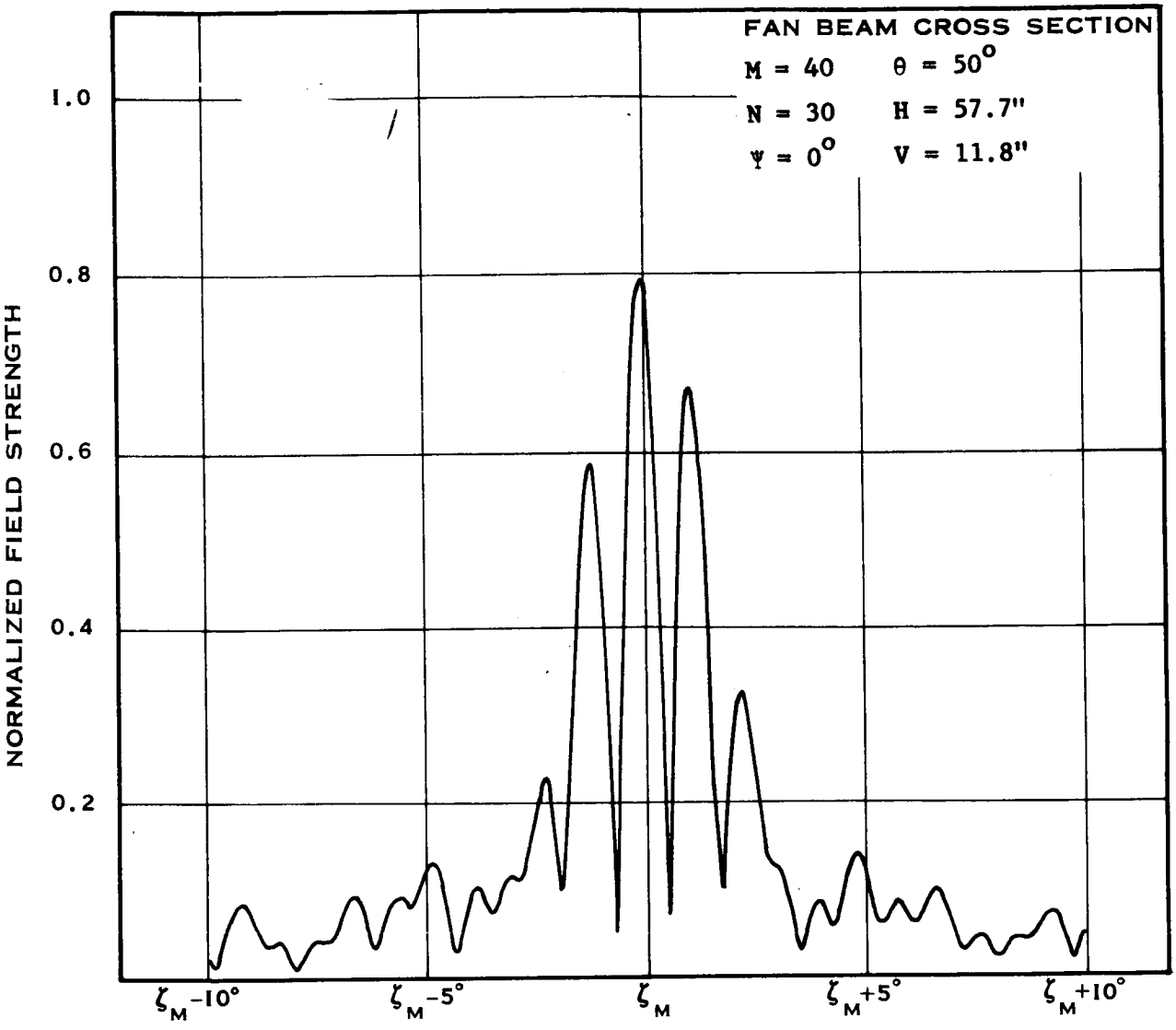

Figure D-5 Normal Cross Section Showing Effects of Separation and Misalignment

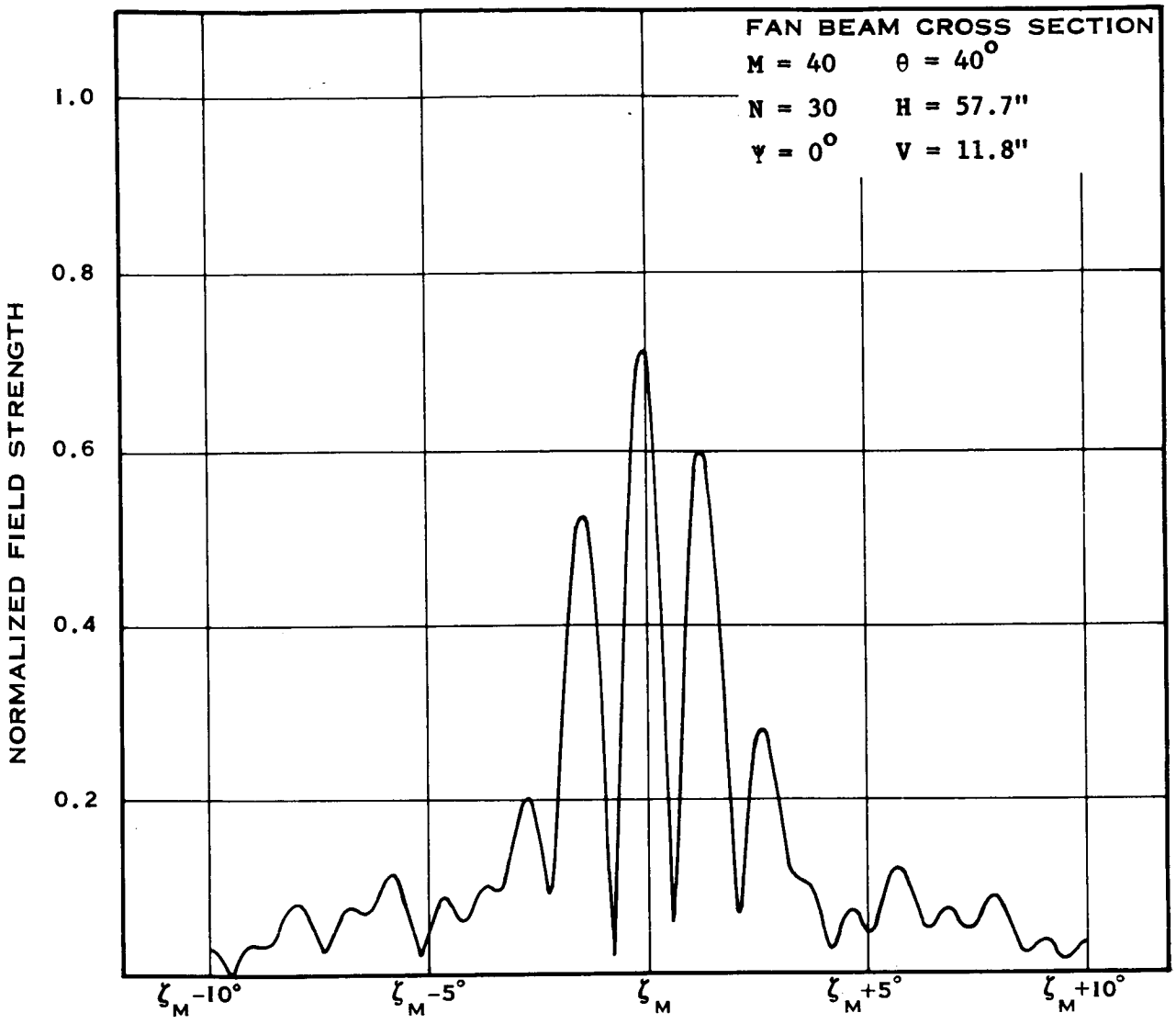

Figure D-6 Normal Cross Section Showing Effects of Separation and Misalignment

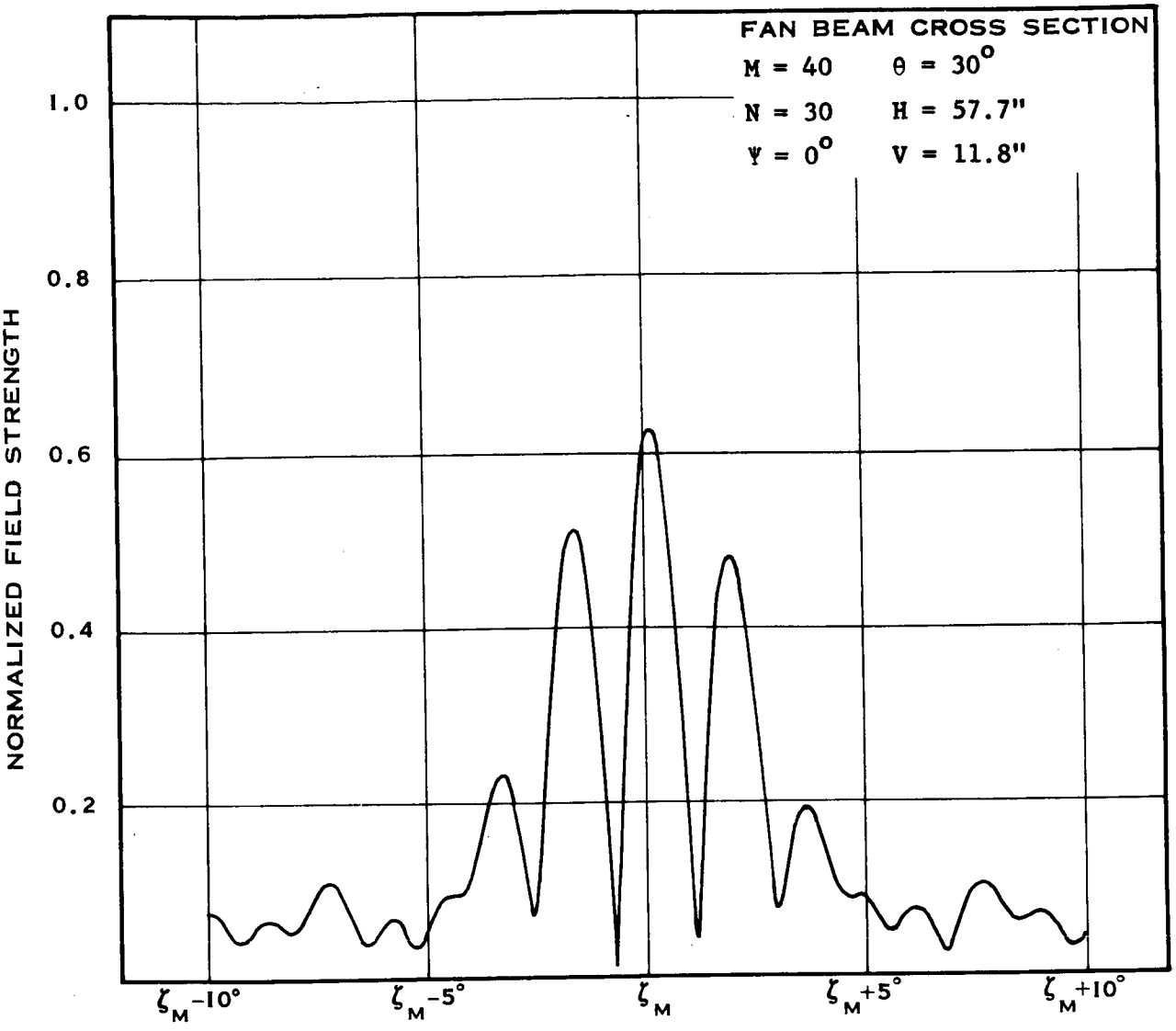

Figure D-7 Normal Cross Section Showing Effects of Separation and Misalignment

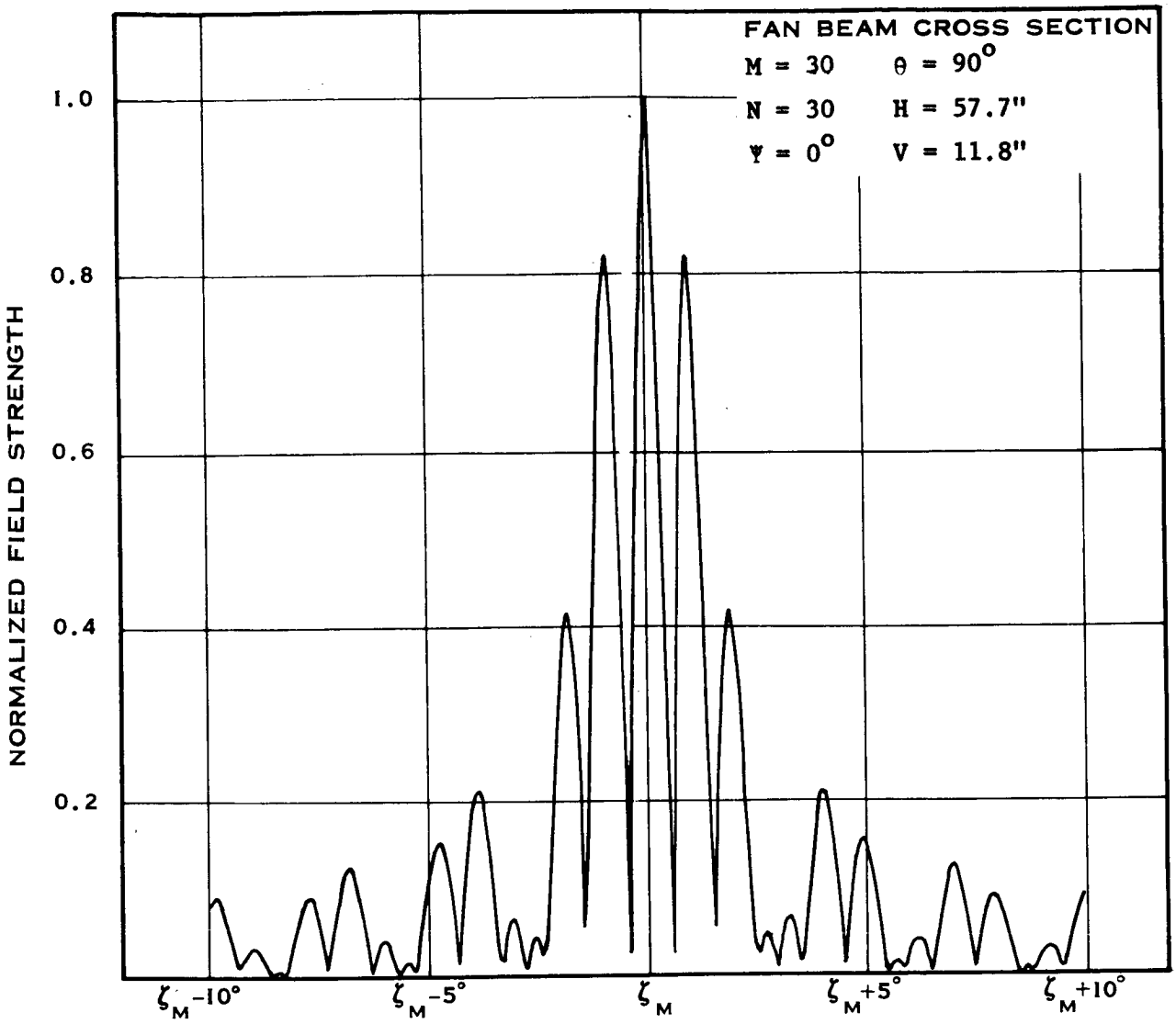

Figure D-8 Normal Cross Section Showing Effects of Separation and Misalignment

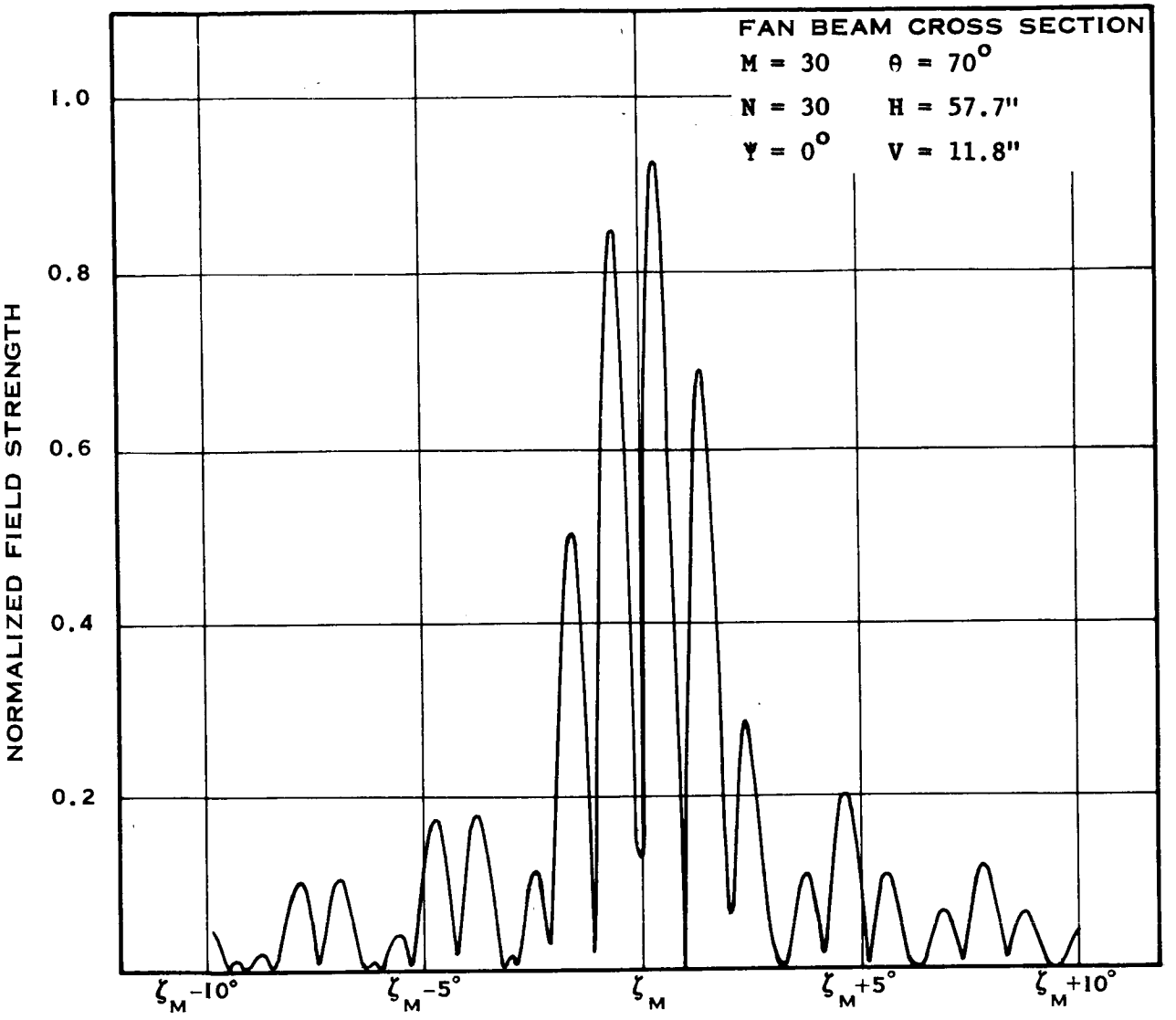

Figure D-9 Normal Cross Section Showing Effects of Separation and Misalignment

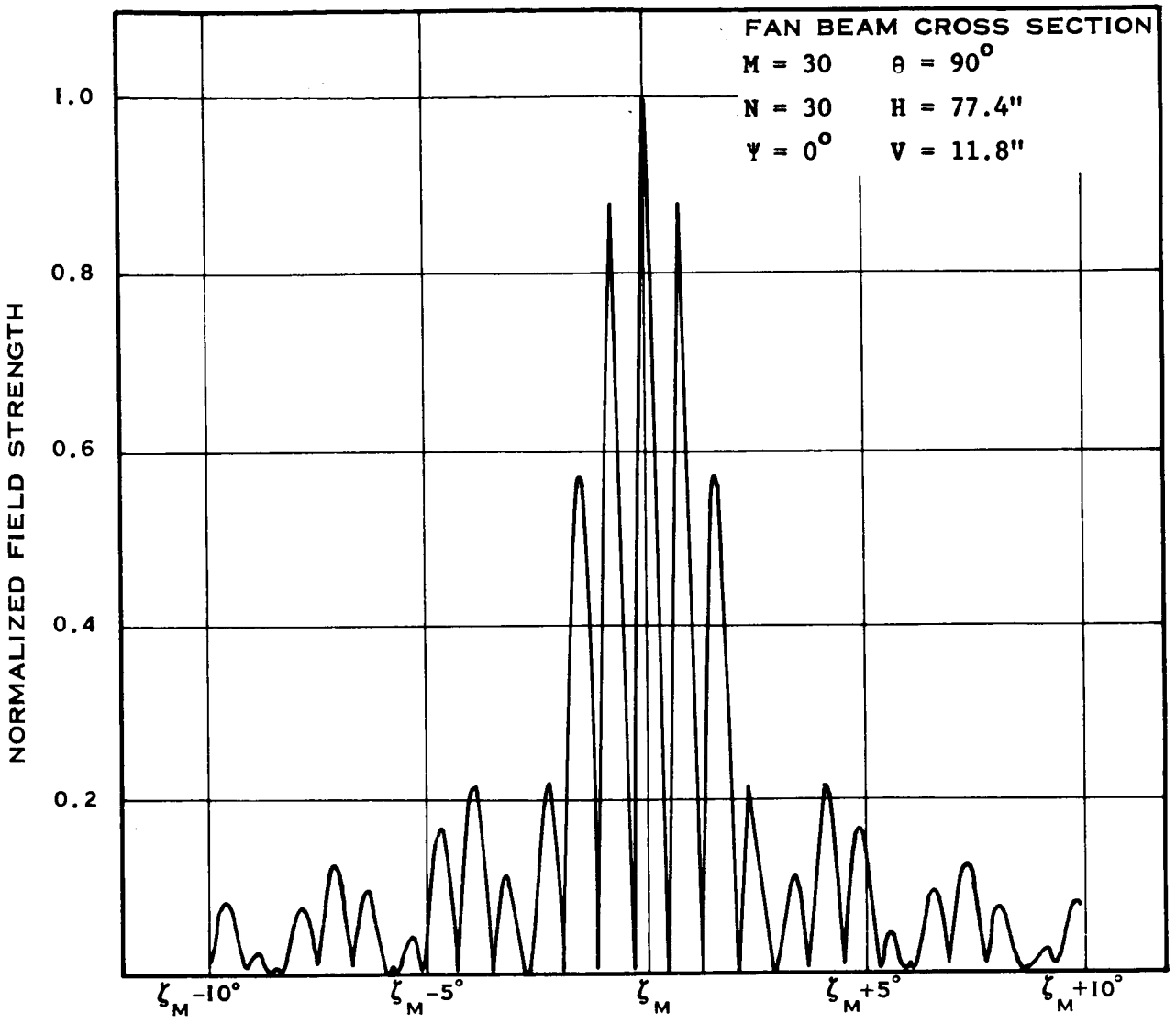

Figure D-10 Normal Cross Section Showing Effects of Separation and Misalignment

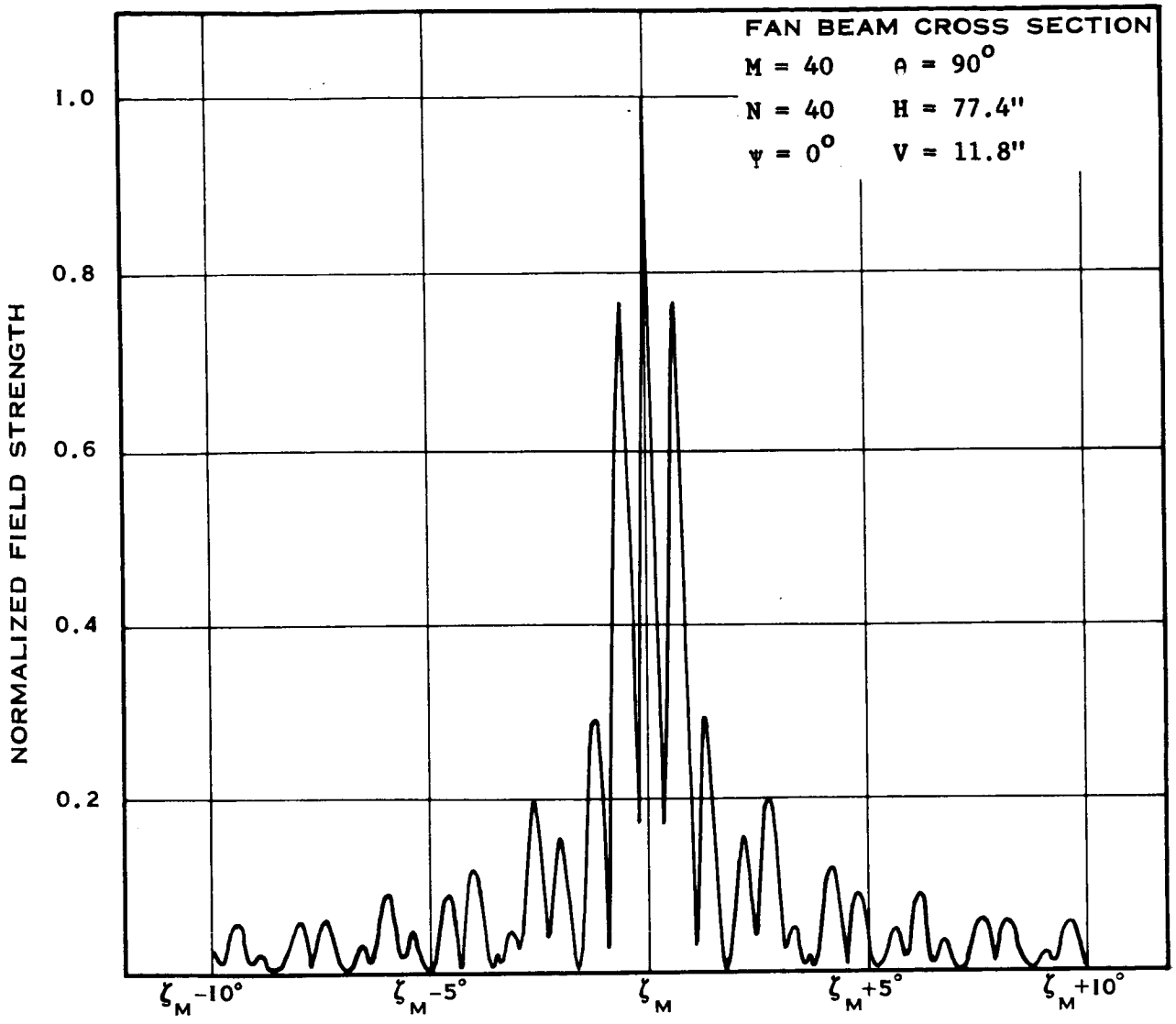

Figure D-11 Normal Cross Section Showing Effects of Separation and Misalignment

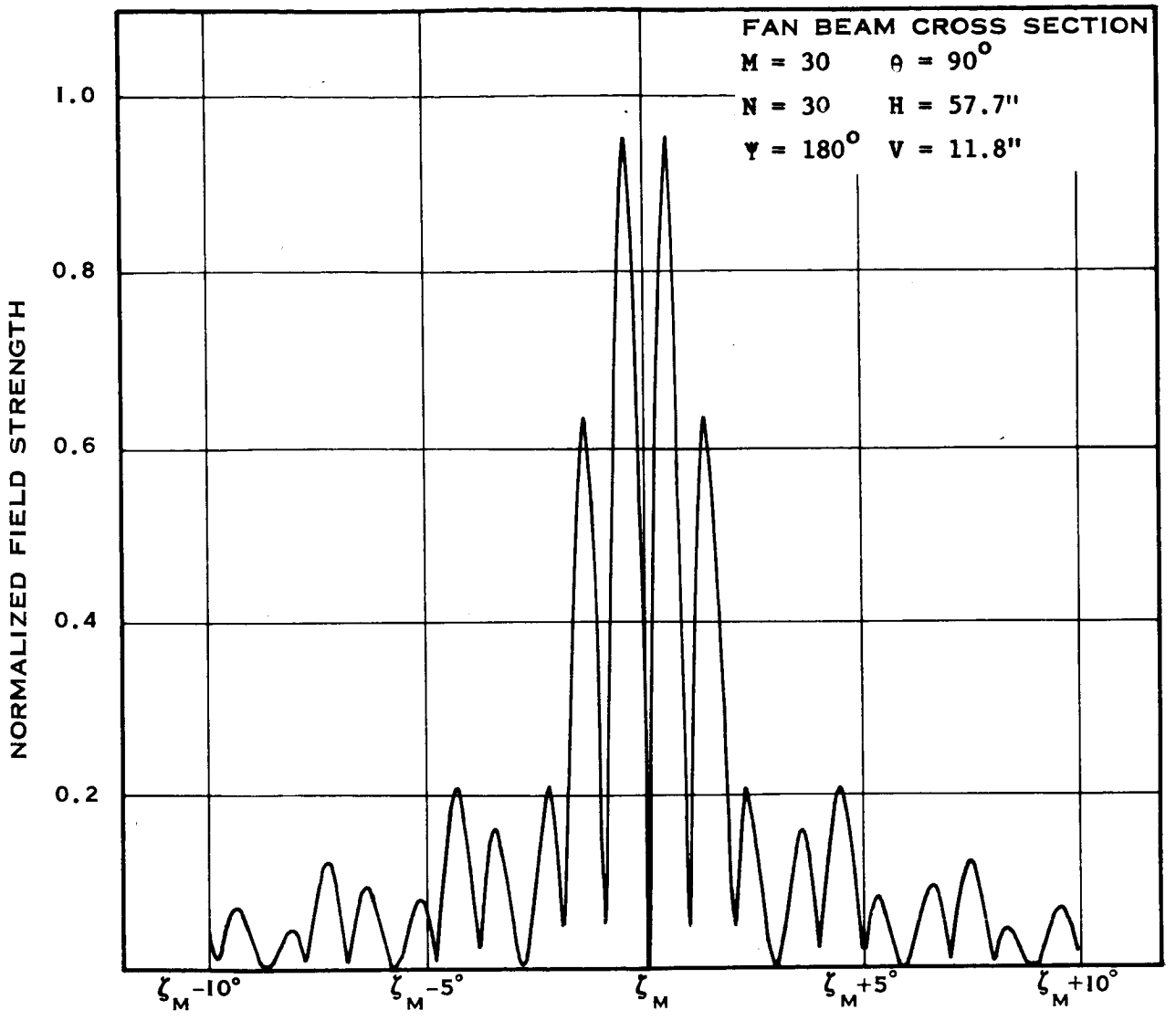

Figure D-12 Normal Cross Section Showing Effects of Separation and Misalignment

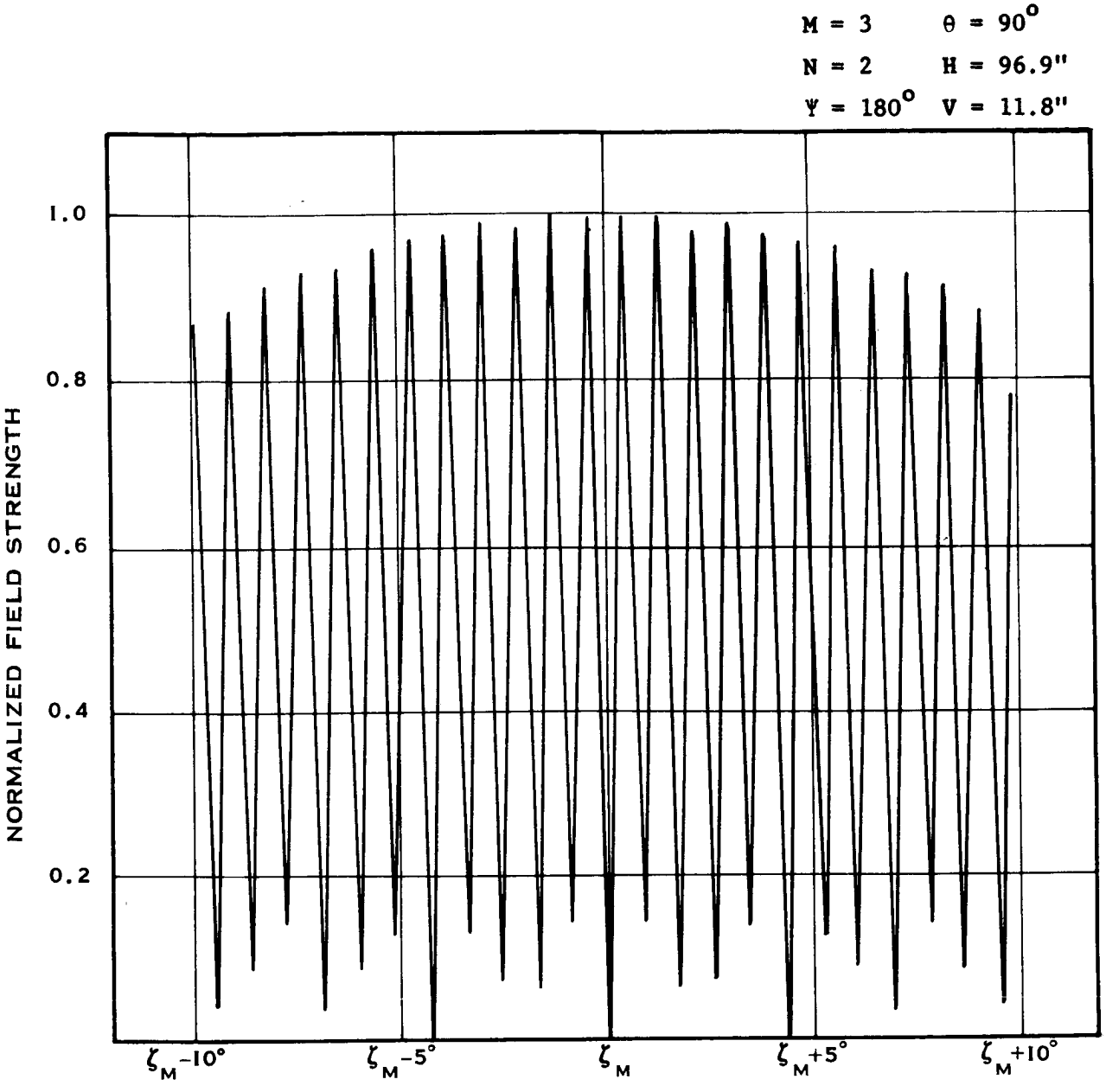

Figure D-13 Normal Cross Section of Typical Interference Pattern

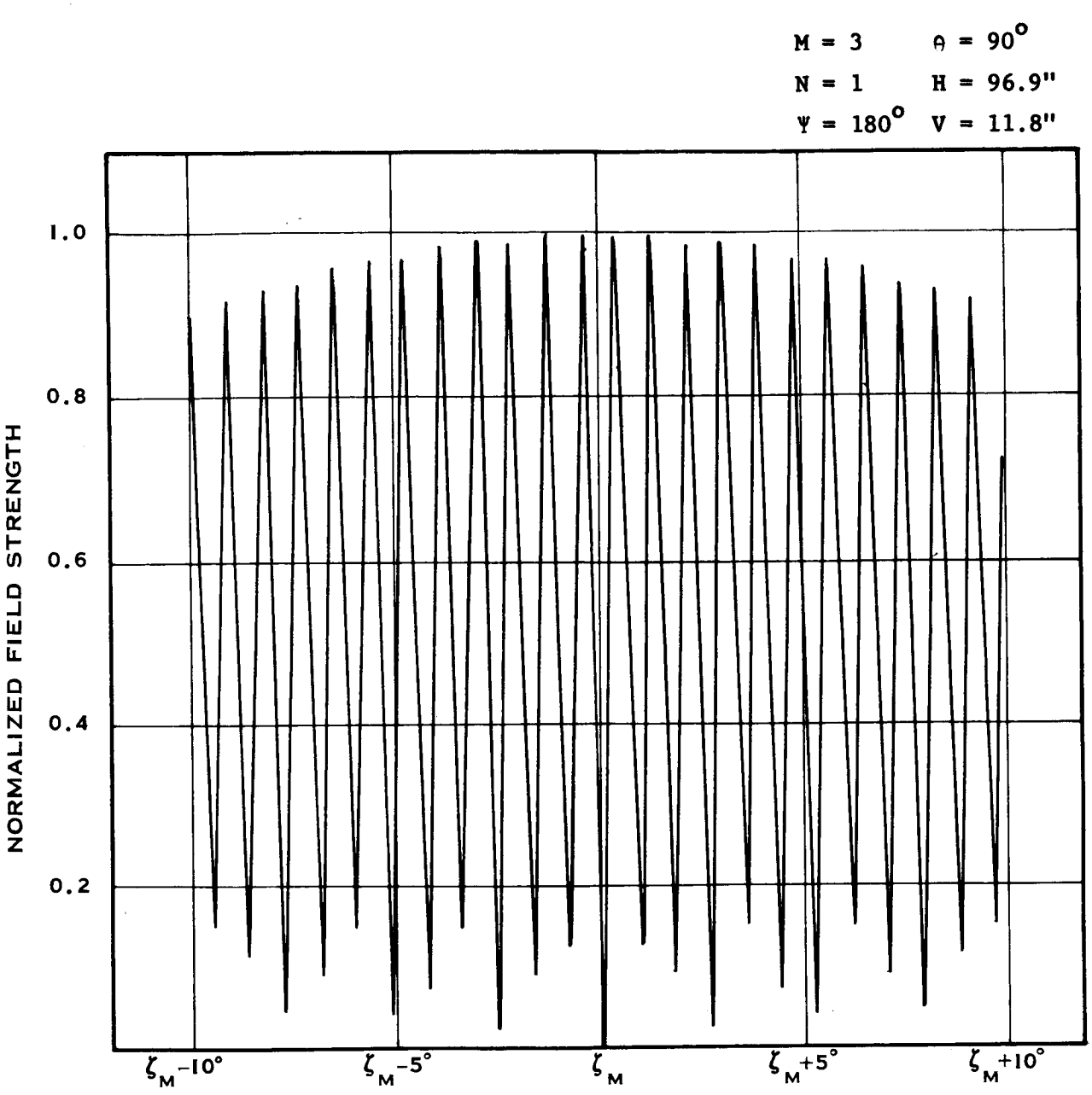

Figure D-14 Normal Cross Section of Typical Interference Pattern

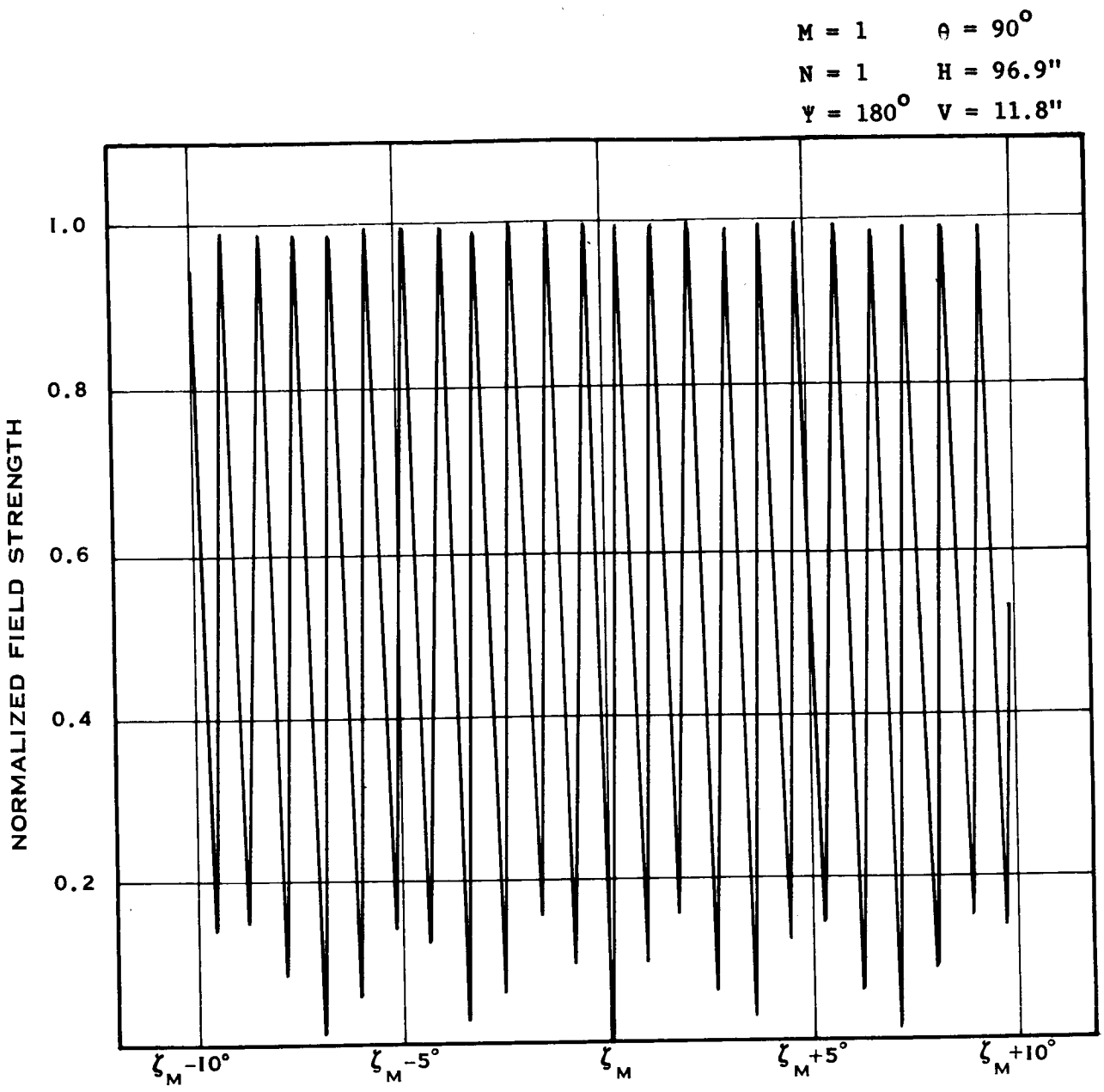

Figure D-15 Normal Cross Section of Typical Interference Pattern

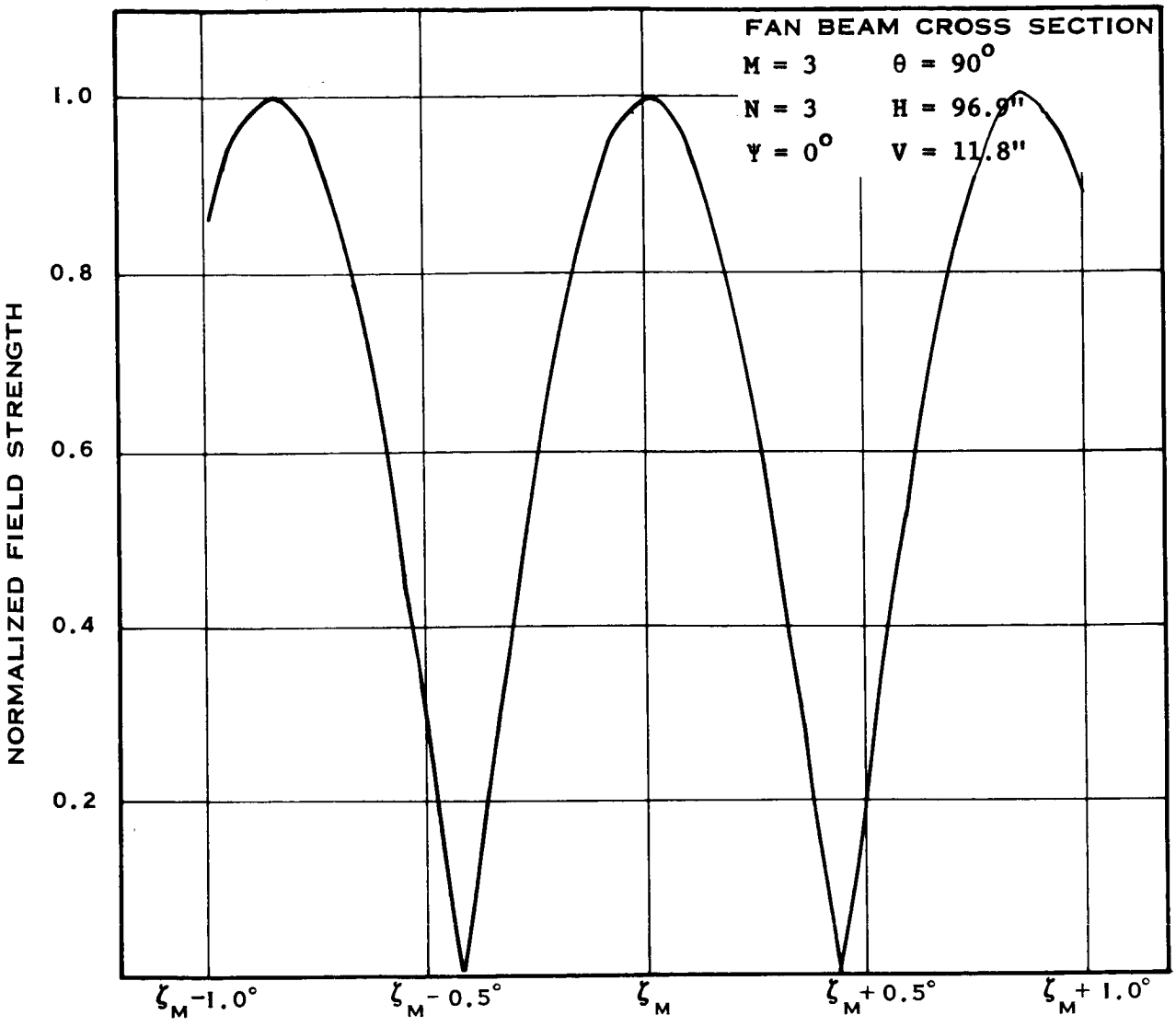

Figure D-16 Detail of Typical Interference Pattern

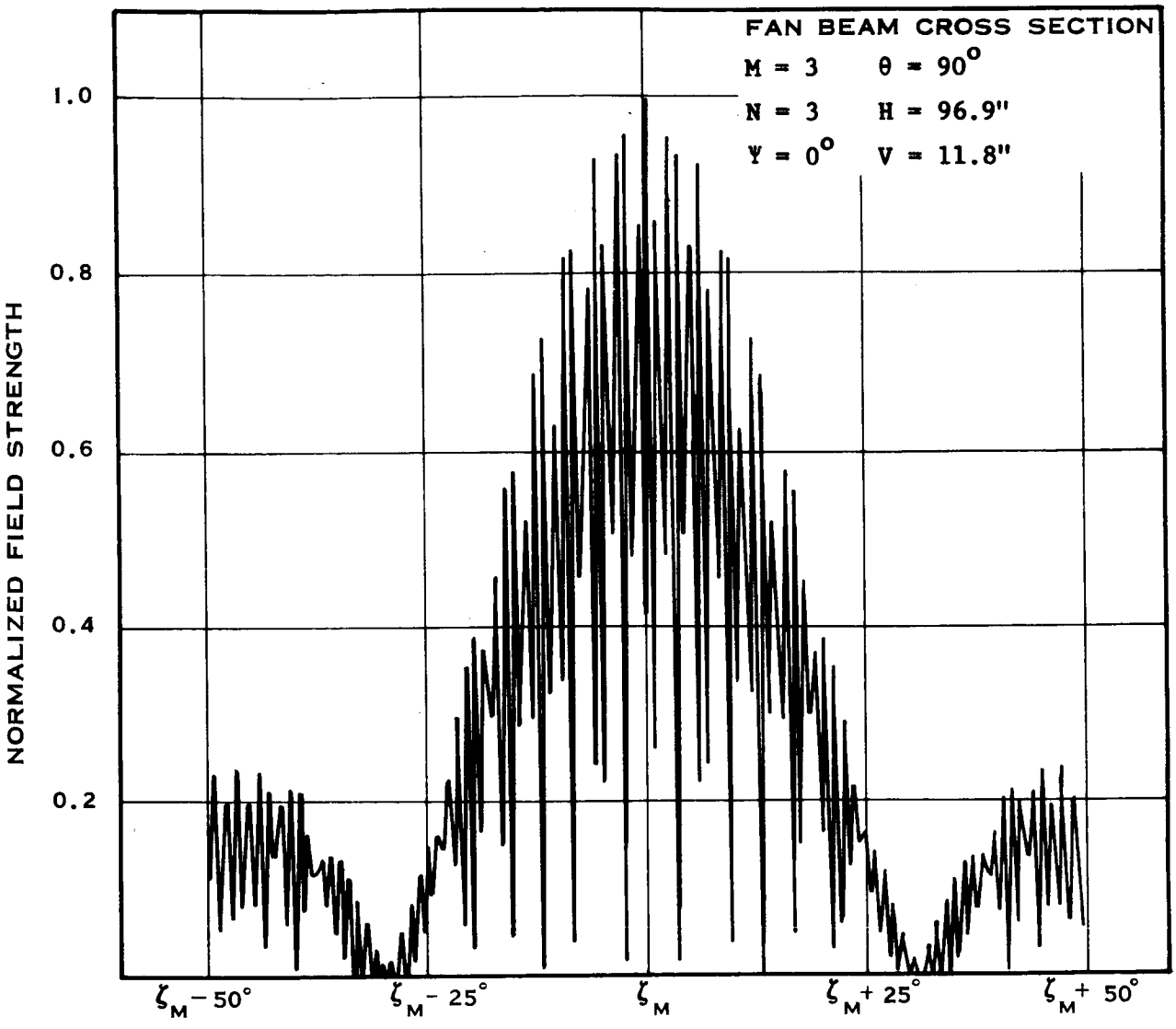

Figure D-17 Wide Range View Showing the Reference Envelope of the Interference Pattern

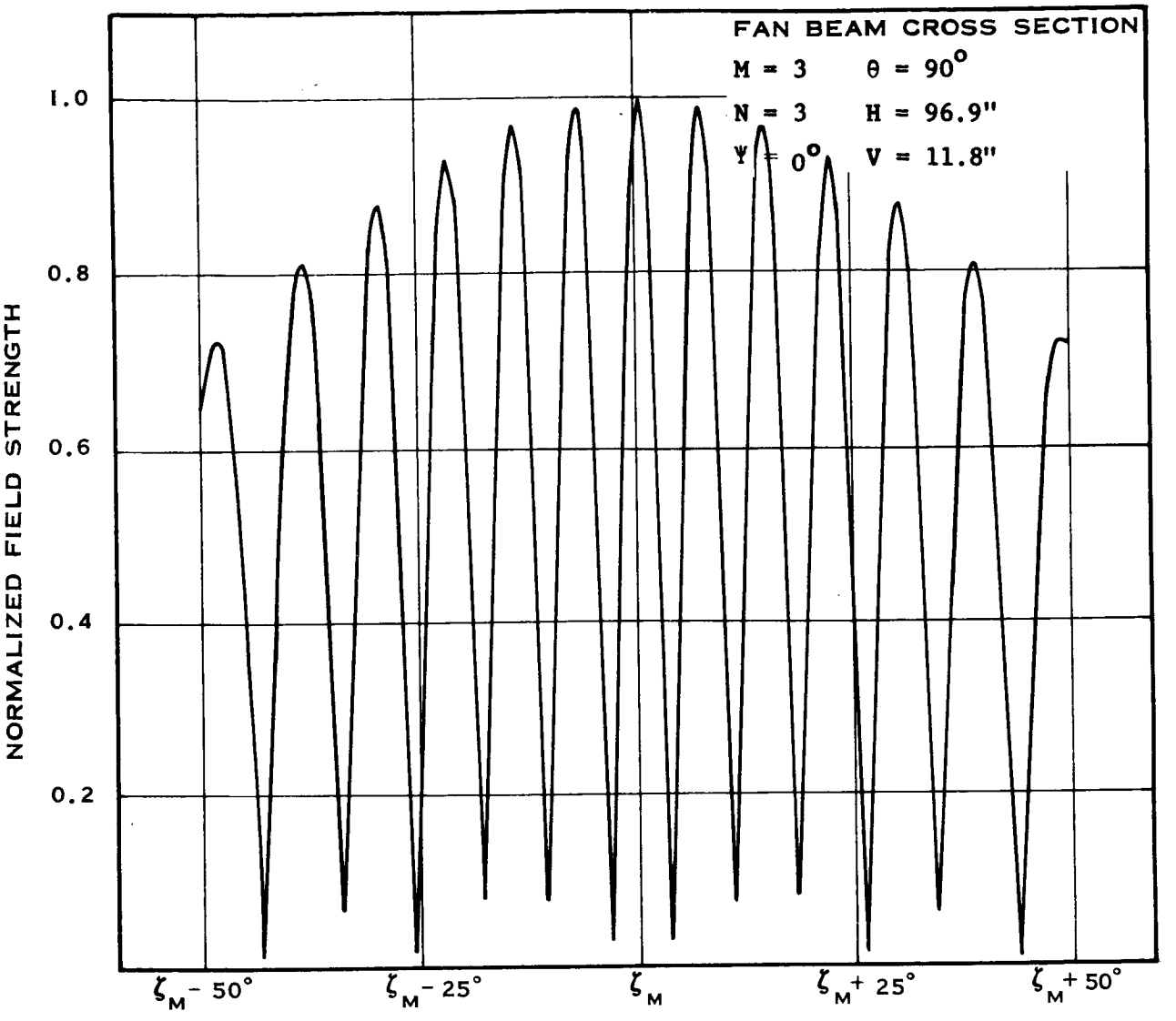

Figure D-18 Broad Beam Cross Section Showing How Misalignment Causes Interference in Long Dimensions

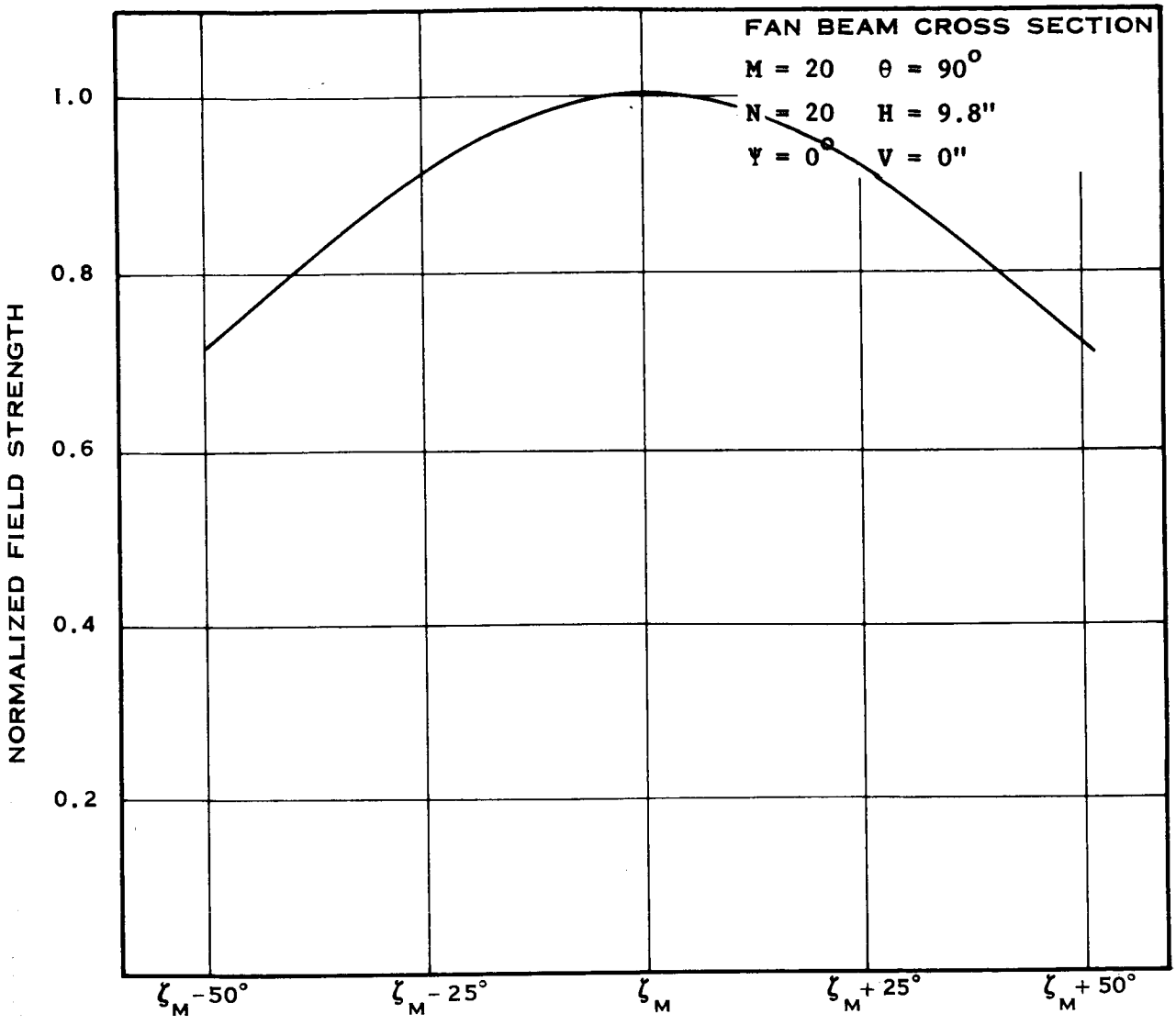

Figure D-19 Broad Beam Cross Section of Two Antennas With No Misalignment

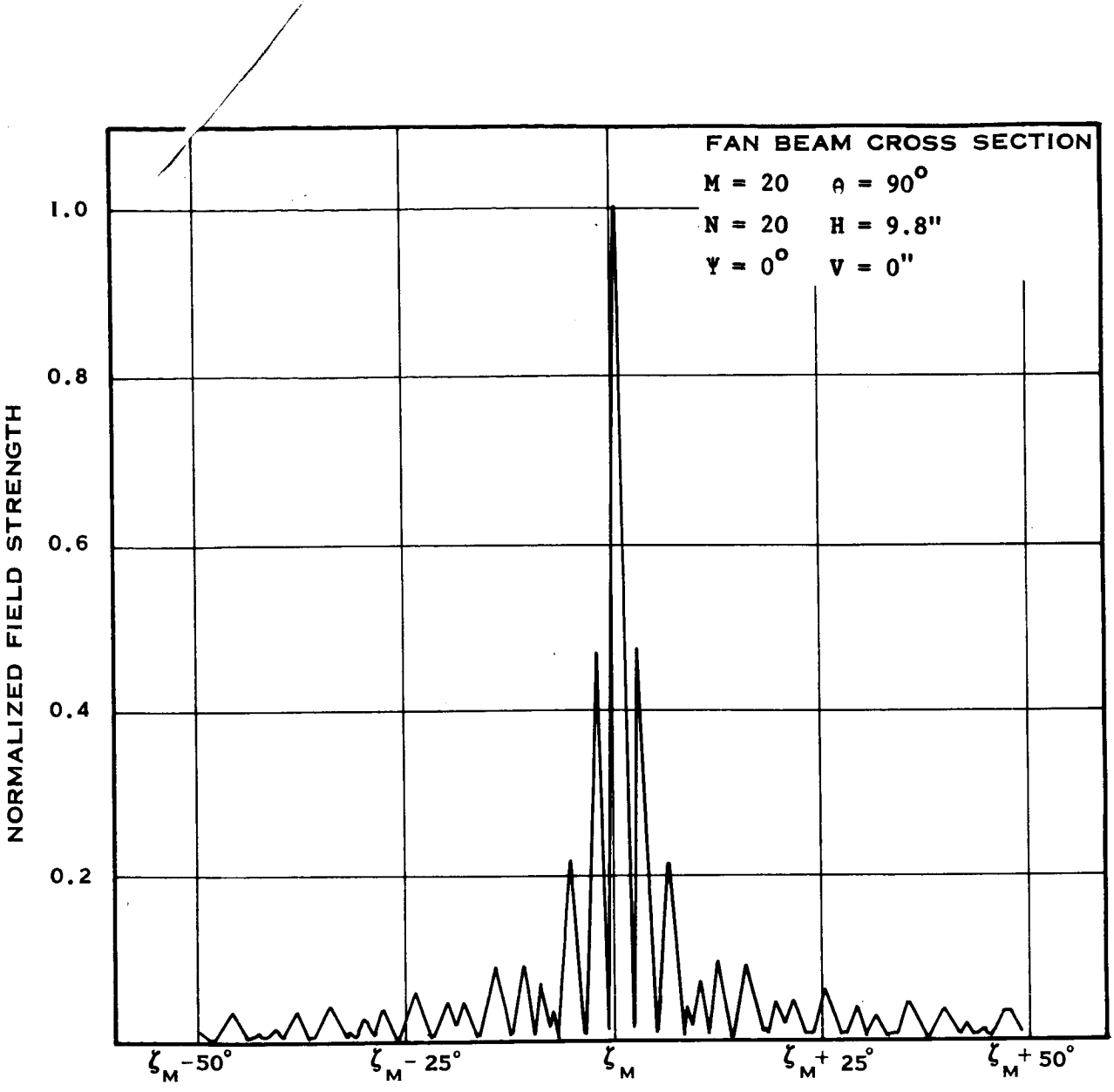

Figure D-20 Normal Cross Section of Antenna Pattern With No Misalignment

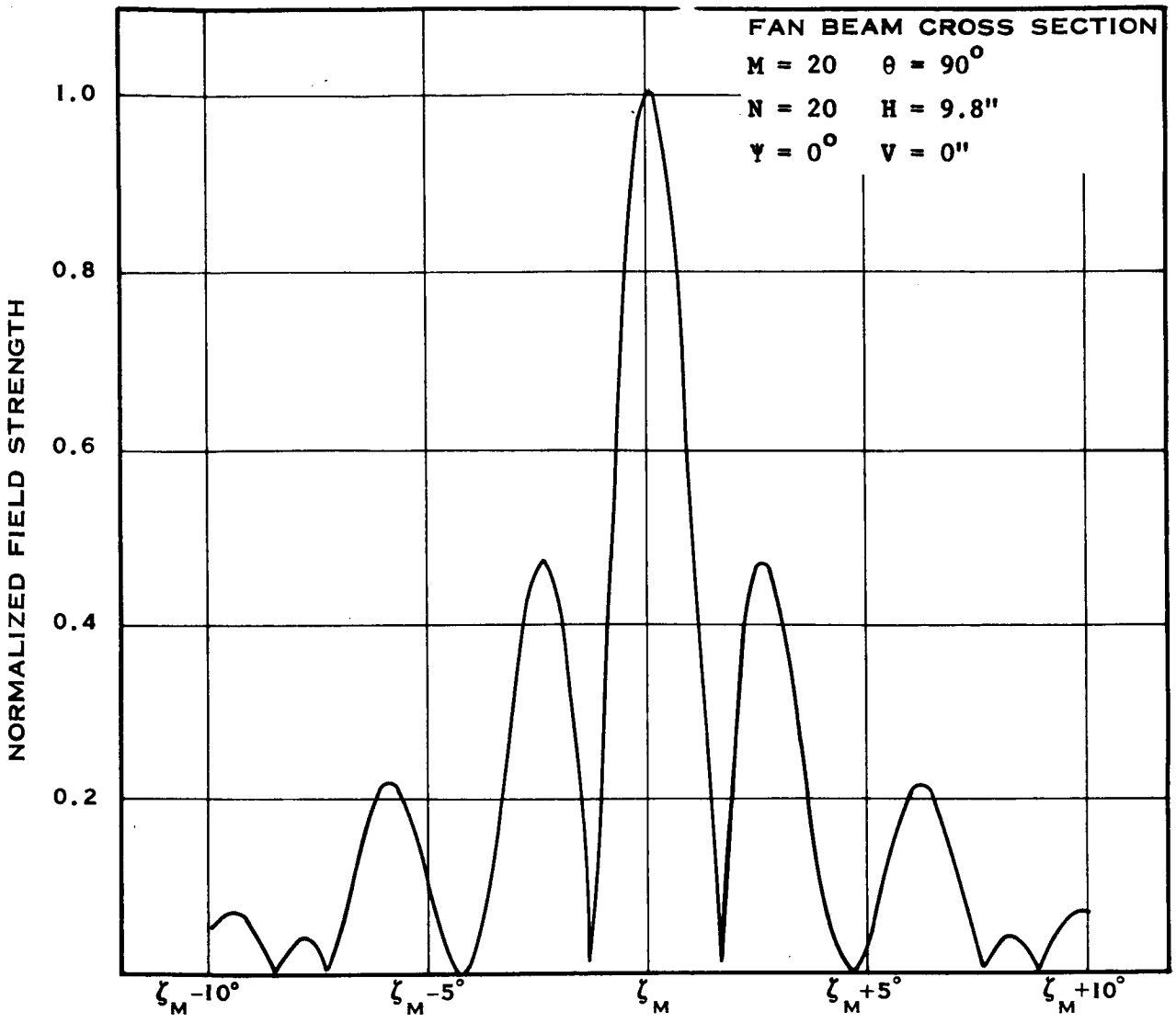

Figure D-21 Normal Cross Section of Antenna Pattern With No Misalignment

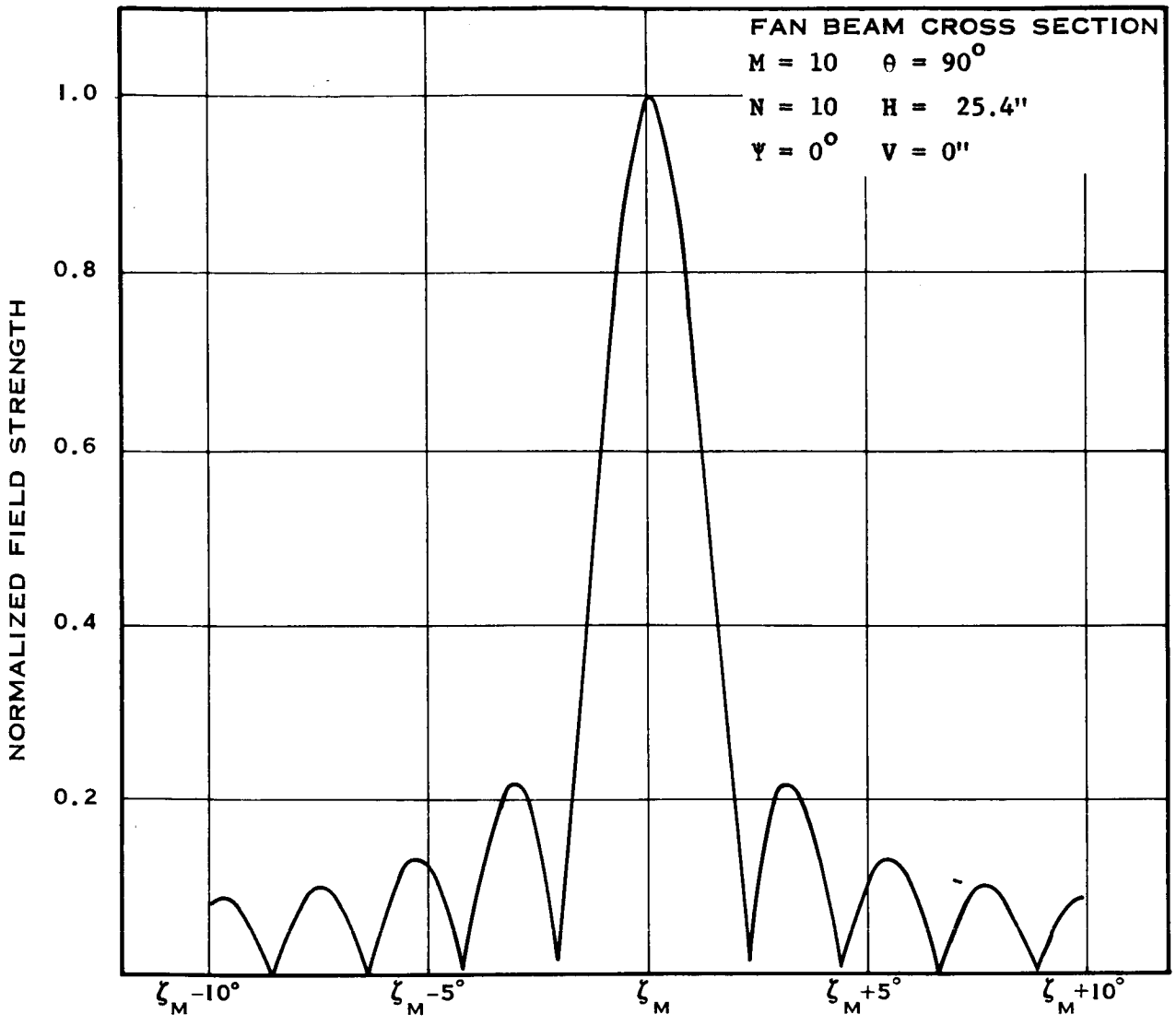

Figure D-22 Antenna Pattern Generated by a Sequence of Slot Pairs

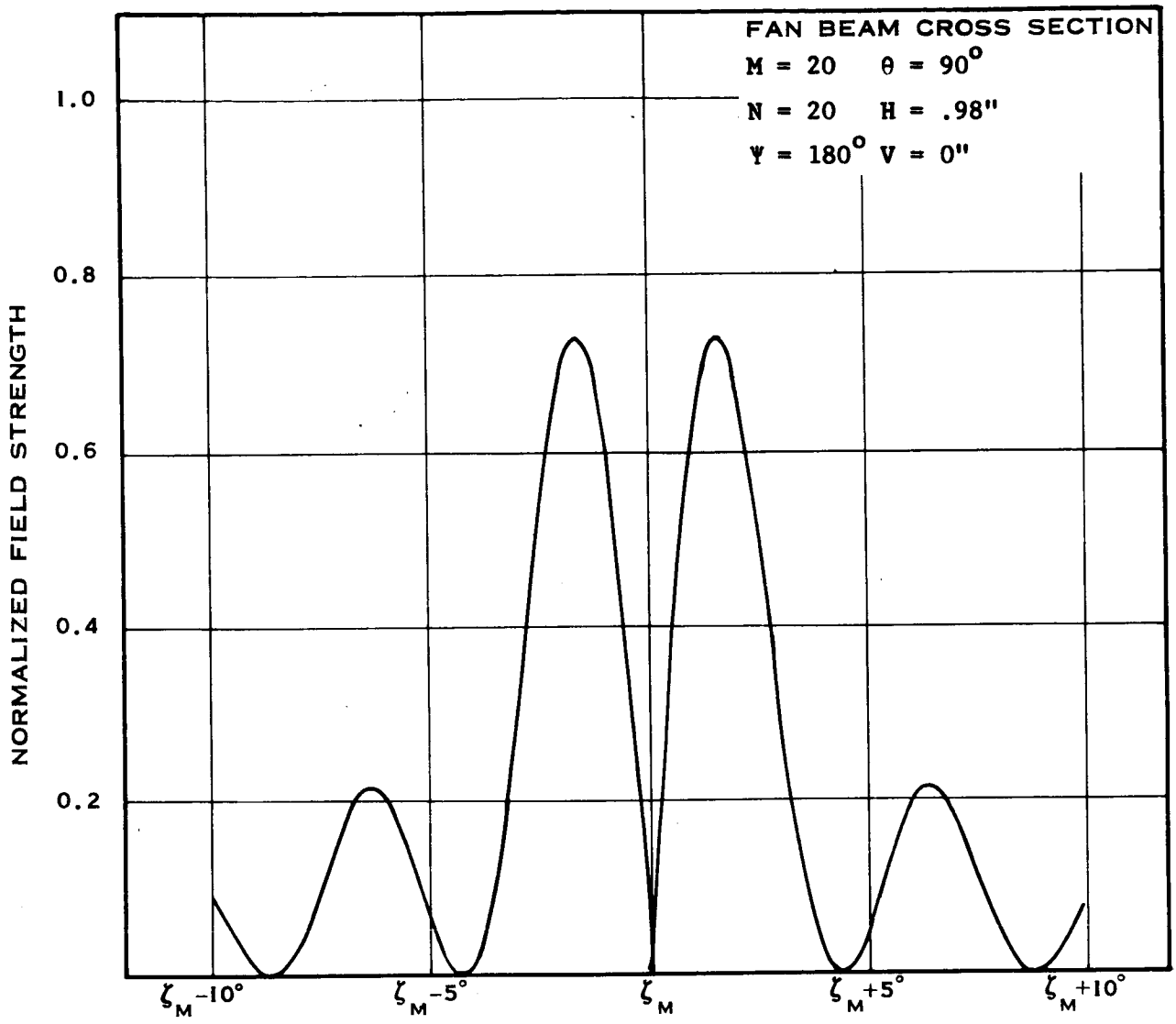

Figure D-23 Antenna Pattern With Phase Shift at Midpoint

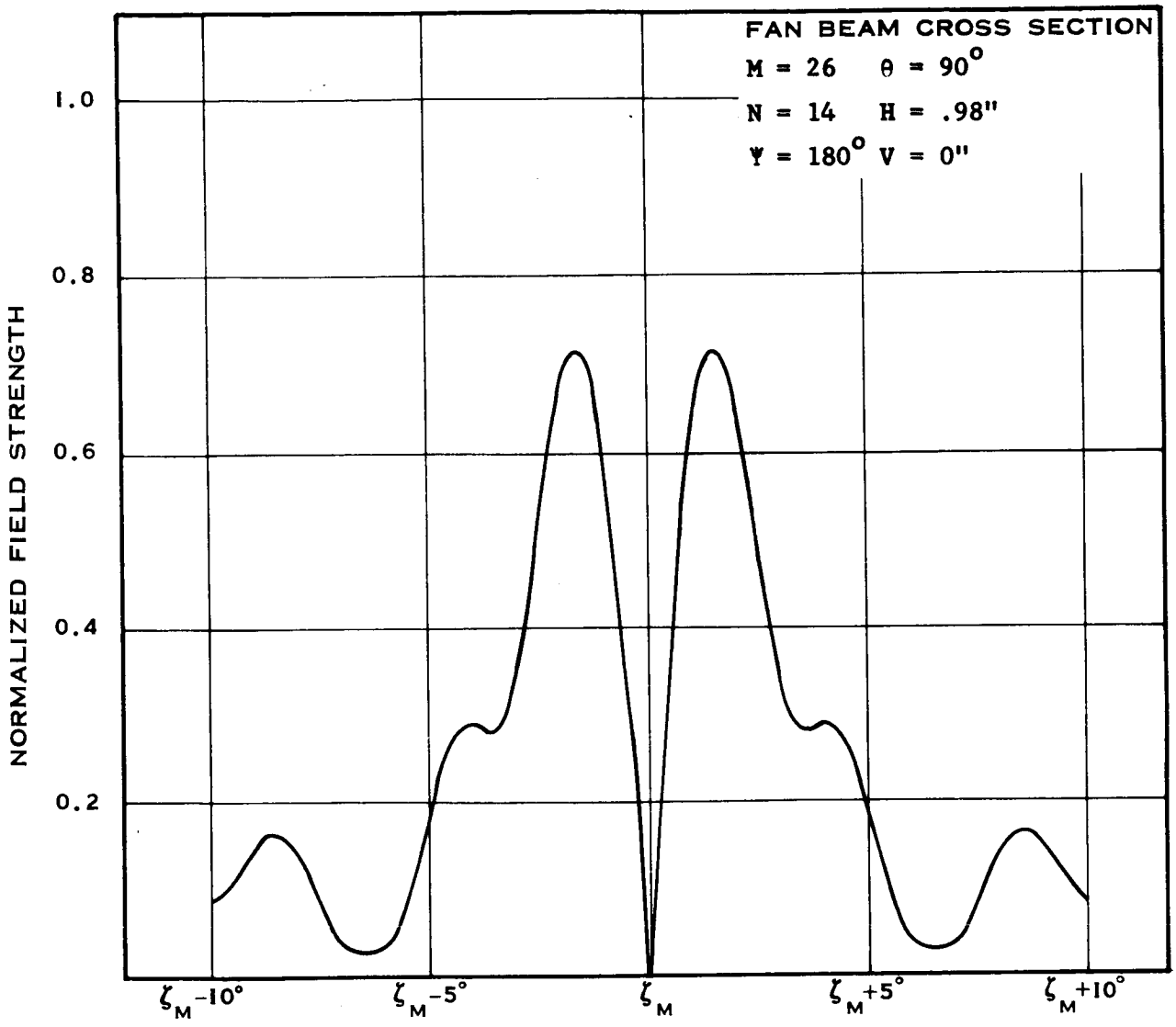

Figure D-24 Antenna Pattern With Phase Shift Not At Midpoint